ASPHALTENES CHARACTERIZATION BY NUCLEAR MAGNETIC RESONANCE SPECTROSCOPY

YEASMIN RATNA

Master of Science, Hyogo University, Japan 2014

A thesis submitted
in partial fulfilment of the requirements for the degree of

DOCTOR OF PHILOSOPHY

in

EARTH, SPACE, AND PHYSICAL SCIENCE

Department of Chemistry and Biochemistry
University of Lethbridge
LETHBRIDGE, ALBERTA, CANADA

ASPHALTENES CHARACTERIZATION BY NUCLEAR MAGNETIC RESONANCE SPECTROSCOPY

YEASMIN RATNA

Date of Defence: December 11, 2023

Dr. Paul Hazendonk Dr. Michael Gerken Thesis Co-Supervisors	Associate Professor Professor	Ph.D. Ph.D.
Dr. Nehal Thakor Thesis Examination Committee Member	Professor	Ph.D.
Dr. Peter Dibble Thesis Examination Committee Member	Associate Professor	Ph.D.
Dr. Arno De Klerk External Examiner University of Alberta Edmonton, Alberta	Professor	Ph.D.
Dr. Borries Demeler Chair, Thesis Examination Committee	Professor	Ph.D.

DEDICATION

This thesis is dedicated to my son for being so patient and understanding. To my parents and husband, who have given me their full support throughout my life.

ABSTRACT

Asphaltenes from various sources and processed in different ways were studied by nuclear magnetic resonance (NMR) relaxation and diffusion ordered spectroscopy (DOSY) methods. The study investigating samples obtained from various depths of an oil well from a Saudi Arabian deposit found those samples to exhibit increasing aggregate sizes with depths, with the molecular structure remaining essentially unchanged. DOSY experiments reveal three distinct asphaltene aggregation states in different solvents, with increasing particle sizes at greater depths. However, hardware limitations were observed in resolving particle sizes beyond 4 nm. Asphaltenes from *in-situ* pyrolyzed American oil shale were characterized with respect to maturity, showing that aggregate size increases with maturity. As part of an international effort to characterize one particular crude and sonicated sample from Colombia (PetroPhase 2017), this study found that sonication reduces the aggregate size. Three fluorinated probes were tested to study a Kuwaiti asphaltene sample by ^{19}F NMR spectroscopy and the results were compared to those obtained using the ^{1}H signals of the sample; perfluorooctanoic acid (PFOA) was found to be an effective probe for asphaltene aggregation, mirroring the results of the minor component of the ^{1}H relaxation dispersion analysis. In relaxation dispersion measurements of all four asphaltene types, two mobility regimes were observed with percentage contributions varying between asphaltene origins but being unchanged with respect to processing and sample depth. The behaviour of the contributions of the two mobility regimes in all samples cannot be explained by attributing them to different aggregation states, but a core-shell model is proposed with the more mobile component being on the outside ‘shell’ and the more rigid component constituting the core of a nanoparticle.

ACKNOWLEDGEMENTS

First and foremost, I give thanks to Allah, the most deserving of praise, the beneficent and merciful, for all his blessings throughout my life and for helping me overcome the challenges and difficulties of my work.

I want to give special thanks to my supervisors, Dr. Paul Hazendonk and Dr. Michael Gerken, without whom none of the work described here would have been possible. I would also like to thank my supervisory committee members, Dr. Peter Dibble and Dr. Nehal Thakor, for their support and insightful comments. Two individuals without whom this work would have been exponentially more difficult are Tony Montina and Michael "Mike" Opyr. Their hands-on experience with the spectrometer helped me gain practical knowledge.

I am extremely thankful to my parents and my parents-in-law for their constant love and prayers, helping me complete this work. I would like to thank my son Mubsir for being understanding even when mum has to stay late at school.

Lastly, I cannot express my appreciation for the support of my beloved husband, Mostafizur Rahman. He was always there for me to share my problems and gracefully endured every single concern I had during this work. I am grateful to him for his unyielding devotion and love.

TABLE OF CONTENTS

LIST OF TABLES

LIST OF FIGURES

LIST OF ABBREVIATIONS

AFM ..... Atomic Force Microscopy
API ..... American Petroleum Institute
AOSA ..... Athabasca Oil-Sands Asphaltene
CCC ..... Critical Cluster Concentration
CNAC .....Critical Nanoaggregate Concentration
COSY ..... Correlation Spectroscopy
CPMG ..... Carr-Purcell-Meiboom-Gill
CSA ..... Chemical Shift Anisotropy
CW ..... Continuous Wave
DC.....Direct Current
DEPT .....….Distortionless Enhancement by Polarization Transfer
DFA ..... Downhole Fluid Analysis
DOSY.....Diffusion-Ordered Spectroscopy
EA ..... Elemental Analysis
FD…… Fluorescence Depolarization
FID ..... Free Induction Decay
FT ..... Fourier Transform
FT-ICR…… Fourier-Transform Ion Cyclotron Resonance
FWHH ..... Full Width at Half Height
GOR ..... Gas-to-Oil Ratio
GPC ..... Gel Permeation Chromatography
HETCOR ..... Heteronuclear Correlation
HSQC ..... Heteronuclear Single Quantum Coherence
ICR ..... Ion Cyclotron Resonance
INEPT ..... Insensitive Nuclei Enhanced by Polarization Transfer
L^2MS ..... Two-Step Laser Mass Spectrometry
LDI……Laser Desorption Ionization
LDSPI ..... Laser Desorption Single-Photon Ionization
MRI ..... Magnetic Resonance Imaging
MALDI……..Matrix-Assisted Laser Desorption/Ionization
NMR ..... Nuclear Magnetic Resonance
NOE ..... Nuclear Overhauser Effect
NOESY ..... Nuclear Overhauser Effect Spectroscopy
OPEC ..... Organization of the Petroleum Exporting Countries
P ..... Petroleum
PAH..... Polyaromatic Hydrocarbon
PAS ..... Principal Axes System
PFOA ..... Perfluorooctanoic Acid
ppm ..... parts per million
RF or r.f..... Radio-Frequency
STE……. Stimulated Spin Echo
SANS ..... Small Angle Neutron Scattering
SARA ..... Saturates, Aromatics, Resins and Asphaltenes
SAXS ..... Small Angle X-ray Scattering

SALDI……Surface-Assisted Laser Desorption/Ionization
SEC ..... Size Exclusion Chromatography
SW..... Spectral Width
TMS ..... Tetramethylsilane
TRFD ..... Time-Resolved Fluorescence Depolarization
VPO..... Vapor Pressure Osmometry
WAXS……Wide-angle X-Ray Scattering

CHAPTER 1

1. ASPHALTENES

1.1. Introduction

Asphaltenes are the heaviest, most complicated, polar, and structurally mysterious component of petroleum, providing very little economic value and increasing negative consequences on the oil industry.[1,2] Asphaltenes are problematic for oil production in several distinct ways. A well-known property of asphaltene molecules is their ability to self-associate, resulting in aggregates that precipitate out of the oil under minimal pressure or temperature changes. Due to this, the result is blocking of well-bores, pipelines, and sometimes the deposition of sediments on the internal surface of reservoirs. Asphaltene deposition also caused coke deposition on catalysts during refining.[3] Asphaltenes, the most polar part of petroleum, are also infamous for stabilizing water-in-oil emulsions[1, 4] during crude oil production, which is undesirable from a processing and quality standpoint. Due to these issues, production costs are driven up, and the energy return on investment is lowered.[5] As an additional consequence, greenhouse gas emissions increase, and the environment is negatively affected.

Today, these challenges have become more apparent as we become increasingly dependent on heavier hydrocarbon resources, such as bitumen. Due to the depletion of our abundant light hydrocarbon reserves in the foreseeable future, we are now transitioning to heavier hydrocarbon reserves that are more difficult to extract. The new resource, known as 'heavy oils,' brings new problems and challenges to the petroleum sector, which is often ill-

prepared to deal with them. The petroleum industry has historically used various methods and techniques to extract crude oil, including drilling, pumping, and enhanced oil recovery methods such as steam or chemical injection.[6,7] A reservoirs characteristic, such as its size, depth, and viscosity, determine the methods available for extracting oil. Another factor that affects the choice of method is the location of the reservoir, as offshore drilling and extraction are typically more challenging and require specialized equipment and techniques. Mullins[1] does a fantastic job of detailing these strategies, including why they were employed and the resulting risks that come along with them. These methods served the industry well when crude oil was readily available and easy to extract; however, their effectiveness has been questioned as new petroleum resources have emerged. There is a great deal of risk involved in the exploration of heavy oil and shale oil, as well as great financial cost. Accurate reservoir modeling is needed to justify the billions of dollars in investments. Most of the time, theoretical approaches are not based on deep understanding of the structure and behavior of petroleum and its components, like asphaltenes, at the molecular level. A deep understanding of such principles is required for accurate reservoir modeling with contemporary methods like Downhole Fluid Analysis (DFA),[8,9] which is necessary for heavy-oil study.

In general, heavier oils have a higher proportion of asphaltenes. Asphaltene concentration in light crude oil, which has a low density, is less than 1%, while it can be over 20% in heavy crude oil, which has a high density.[1] Asphaltenes are expected to become increasingly problematic as the industry transitions to heavy oils. To avoid making mistakes that cost billions of dollars, reservoir models need to become more accurate, requiring a more accurate knowledge of asphaltene molecule structure and behavior. Over time, many

different analytical methods have been used to study the structure and aggregation behavior of asphaltene.[10-12] Nuclear magnetic resonance (NMR) spectroscopy has been applied extensively to study asphaltenes, although not to the fullest extent of its potential. Solution-state NMR spectroscopy has been widely used to characterize asphaltenes, yet the methods that have been used are essentially simple, leaving room for significant enhancements and developments. Solid-state NMR spectroscopy has had limited use in this field. When it comes to characterizing asphaltenes, the use of both of these spectroscopic methods leaves a lot of room for improvement to extract more detailed information.

This thesis aims to get a better understanding of asphaltene aggregation behavior using solution-state NMR spectroscopic techniques, including utilizing relaxation measurements.

1.2. Crude Oil

Crude oil is a mixture of hydrocarbons that form naturally and is found in underground reservoirs in liquid form.[13] It can appear as a thick tar-like substance or a highly viscous liquid. Additionally, the color of crude oil can range from pale yellow to dark brown or even black. It is one of the fuel sources that is used most extensively worldwide, and oil, in addition to oil derivatives, is traded worldwide in oil markets; however, oil reserves are limited.[14]

Unlike chemical compounds, crude oil is a complex mixture of molecules containing mostly 83-87% carbon, 11-16% hydrogen, 0-4% oxygen plus nitrogen, and 0-4% sulfur.[13, 15] The exact composition of crude oil depends largely on its geographic location. Due to this, its physical properties including density, viscosity, and color can be quite different.[16]

1.2.1. Compositions of Crude Oils

Crude oil is characterized by four fractions based on their solubility and polarity, namely Saturates, Aromatics, Resins and Asphaltenes. Together they are called the SARA fractions and the fractions can be separated in different stages.[16, 17] Figure 1.1. shows the separation steps of crude oil into the four SARA fractions.

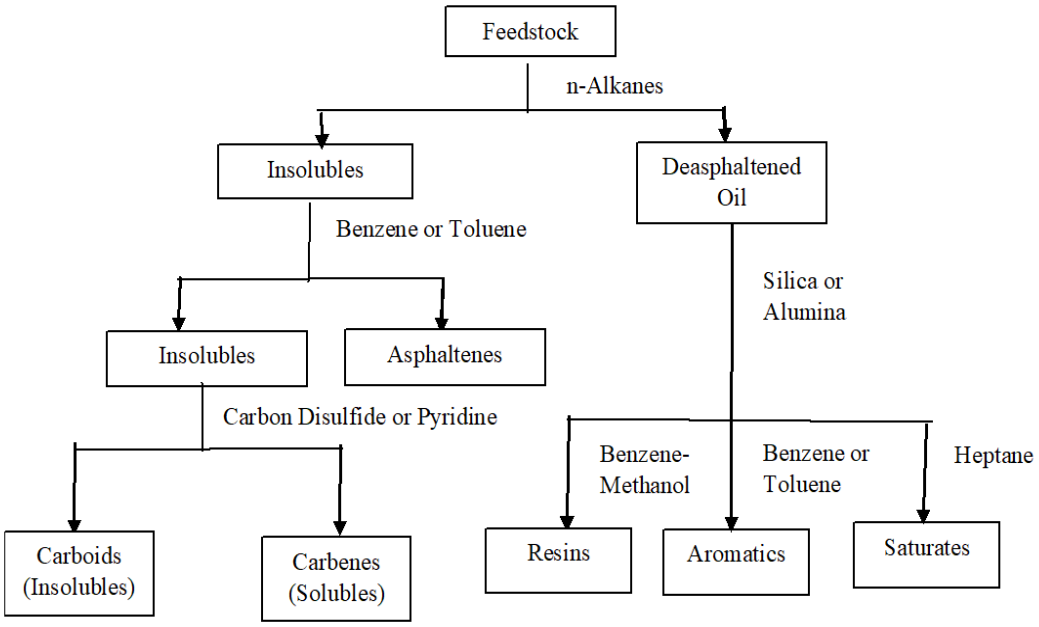

Figure 1.1. Crude oil is separated into four SARA fractions: saturates, aromatics, resins, and asphaltenes (Reproduced with permission from Fakher, S.; Ahdaya, M.; Elturki, M.; Imqam, A., Critical review of asphaltene properties and factors impacting its stability in crude oil. *Journal of Petroleum Exploration and Production Technology* **2020,** *10* (3), 1183-1200.)

The Saturates fraction mainly contain aliphatic compounds and they are soluble in paraffinic solvents like n-pentane, n-hexane, and n-heptane. Saturates are the lightest and least polar fraction in crude oil.[13] The Aromatics fraction consists of aromatic molecules that are highly polarizable and consist of one or more aromatic rings. These molecules are

soluble in paraffins like n-pentane, n-hexane, or n-heptane as well as toluene and dichloromethane.[18] The two remaining fractions, Asphaltenes and Resins, both contain polar substituents. The difference is that asphaltenes are insoluble in n-heptane (or n-pentane), whereas resins are miscible with n-heptane (or n-pentane).

1.3. Oil Shale

Oil shale reserves stand out as a significant alternative source of to petroleum. Oil shales are fine-grained rocks that contain organic material that can be transformed into fuel. About 20% percent of this organic substance is composed of a bitumen fraction that exhibits solubility in organic solvents like toluene, dichloromethane, or carbon disulfide. The remaining 80% consists of insoluble kerogen.[19, 20] Oil shales have been deposited in enormous lake basins, such as the Eocene Green River shales in Utah and Wyoming, in shallow oceans on stable platforms, such as the Permian Irati oil shale in Brazil, or in small lakes, bogs, and lagoons, sometimes with coal beds.[21] In order to extract usable oil from oil shale, the organic component, known as kerogen, needs to be heated to temperatures of about 500 °C. Even though oil shale can be used to produce oil, it has not been used extensively in the oil and gas industry because it is usually more expensive and requires more capital than conventional crude oil.

Before recovering and processing oil shale, the sedimentary rock must be extracted through surface or underground mining. The raw materials must then be sent to different processing facilities to get the kerogen out. In one type of processing technique, known as "*ex-situ* processing," the kerogen deposit is first extracted, and then the extracted material is transported to a different facility where it is processed. Other techniques, such as "*in-situ* processing," involve the extraction of kerogen directly from the ground.[22] The U.S. has the

most oil shale deposits in the world.[23] Most of them are in the Green River Formation in Colorado, Utah, and Wyoming.

1.4. Definitions of Asphaltenes

Asphaltenes are defined as the crude oil component that precipitates when excess n-heptane or n-pentane is added (typically 40 volumes of n-heptane or n-pentane to 1 volume of oil). They are insoluble in n-alkanes (typically n-heptane), but they show solubility in other solvents like toluene and chloroform.[24] Asphaltenes are a group of compounds with different chemical structures having one thing in common: their solubility behavior.[25] Solubility is a collective term for bulk behavior in asphaltene research and can be problematic at the molecular level. Due to their highly complex and diverse molecular compositions, asphaltenes have been the subject of a long-running debate concerning their actual structures and what drives their aggregation. Researchers who study asphaltenes often disagree on such questions even after studying it for many years. Asphaltenes can be extracted using several different methods described in the literature, including ultracentrifugation and Soxhlet extraction.[26] A small percentage of clay and paraffins are considered "impurities" after the extraction; several experiments have shown that asphaltene does not have a pure state.[27]

1.5. Impact of Asphaltene Precipitation and Deposition

Precipitation and consequent deposition of asphaltenes disrupt crude oil extraction in transport pipes and the refining process.[24, 28] In the underground reservoirs, asphaltenes are soluble, existing as stable solutions in crude oil under those conditions. However, once the reservoir conditions are disturbed, for example, by extraction of oil using different methods like solvent injection, the asphaltenes will begin to form solid particles in solution. The

solvent starts to interact with the oil and changes the pressure, temperature, and composition of the oil. As a result, the equilibrium conditions change and the asphaltenes no longer form stable solutions in crude oil.[29] This causes the aggregation and deposition of asphaltenes. Asphaltene deposits in the reservoir can create pore blockage, wellbore plugging, and other serious difficulties, all of which can lead to serious problems if not detected early. The cost of cleaning asphaltenes from the pipelines could be very expensive and significantly time-consuming, resulting in a large increase in the cost of oil production.[30] It is also considered difficult to upgrade asphaltenes, mainly due to their lower H:C ratio, higher heteroatom content, aggregating nature, and propensity to precipitate and to foul processing equipment.

The tendency of asphaltenes to aggregate and precipitate leads to various operational problems in the oil industry ranging from transportation to refining. Some of these problems include equipment plugging, fouling of heated surfaces, and catalyst deactivation. Thus, if asphaltene stability is not well managed, it can lead to an unplanned shutdown of plants, loss of production, and costly maintenance.

Saturates and Resins are waxy, soft, and low-melting materials and they are easily removed using a variety of different solvents or by mechanical processes.[31] However, the asphaltene that has formed inside the oil reservoir is of a complex character, which makes it difficult to remove them by mechanical methods, washing with solvents, or using hot well fluids.

Asphaltene deposits can be controlled chemically using asphaltene dispersants, asphaltene inhibitors, and dissolvers (solvents or oil).[32]Asphaltene inhibitors decrease the tendency of asphaltene molecules to aggregate by increasing stability of their solutions. Dispersants reduce particle sizes, allowing precipitated solids to disperse and remain suspended in the

oil.[33] Chemical treatments can only be effective with in a limited range of conditions, and even small changes in the oil composition can have a significant impact on dispersing asphaltenes. A higher level of structural information is needed to adjust processing processes, which can increase product quality and reduce energy usage, prices, and emissions.

1.6. Asphaltene Properties

Asphaltenes are characterized by their associational nature, which contributes to the complexity of the system. Asphaltene molecules have a strong tendency to stick together, form aggregates, and then precipitate out of solution. Because of their structural complexity, most of the methods are unable to effectively predict the association or aggregation behavior of asphaltenes. In order to understand and to better predict asphaltene aggregation behavior using analytical methods, it is essential to study the chemical, physical, and transport properties of asphaltenes. Knowing these properties will be essential for judging the results of tools designed to predict aggregation behavior.

1.6.1. Asphaltene Extraction using Different Paraffinic Solvents

Asphaltenes are separated from crude oil using a nonpolar solvent, such as petroleum naphtha, petroleum ether, n-pentane, iso-pentane, n-heptane, etc., in which asphaltenes are insoluble. [34] On the other hand, asphaltenes are soluble in solvents, including pyridine, toluene, and benzene. Asphaltene yield can be dramatically affected by which paraffinic solvents are used in the extraction process.[35] Different amounts of asphaltenes are produced when the solubility parameter of the hydrocarbon solvent changes. As the number of carbon atoms in the solvent decreases, asphaltene particles get bigger and flocculate more readily. For example, asphaltenes form much more precipitation in propane and butane than in n-

heptane. Compared with n-heptane asphaltenes, n-pentane asphaltenes show a significant difference in elemental composition.[36] In the n-heptane precipitate, the ratio of hydrogen to carbon is lower than in the n-pentane precipitate, but the ratios of nitrogen, oxygen, and sulfur to carbon are usually higher. The n-heptane precipitate has a higher aromaticity and hetero element content. Asphaltenes properties also change depending on how it is separated and how the properties are measured. Besides the type of solvent, contact time, the ratio of solvent to crude oil, and temperature are also very important.[37]

1.6.2. Molecular weight

Molecular weight (MW) is one of the most important physical properties of any material. The exact determination of asphaltene molecular weight has always been challenging owing to its polydispersity and its tendency to aggregate in solutions.

Asphaltene aggregation affects almost all analytical measurements. Asphaltene molecules form nanoaggregates at low concentration and the calculated MW will be higher than that of the monomer. So, it is difficult to differentiate monomers from aggregates and thus the debate on the monomer, aggregate, or cluster nature of asphaltenes has continued for decades. Vapor pressure osmometry (VPO) is a standard method to measure the molecular weight of asphaltenes and it requires high analyte concentrations; in that case, asphaltene self-association has been observed. Molecular weights from vapor pressure osmometry (VPO),[38-40] size exclusion chromatography (SEC),[40] and molecular film methods report average monomer asphaltene molecular weights of 1000 to 2000 g/mol.[41] Fluorescence depolarization (FD),[42,43] nuclear magnetic resonance (NMR),[44,45] and fluorescence correlation spectroscopy have reported monomer values between 500 to 1000 g/mol. Laser desorption ionization (LDI)[46] and matrix-assisted laser desorption ionization (MALDI)[46]

also have been used to analyze the MW of asphaltenes with monomer values of around 500 g/mol. More recently, results from time-resolved fluorescence depolarization (TRFD),[47, 48] two-step laser mass spectrometry (L^2MS),[49] and Fourier transform ion cyclotron resonance (FT-ICR) techniques[50,51] confirm that asphaltene molecular weights are distributed over a range of 400-1500 g/mol, with a mean between 700-800 g/mol.

1.6.3. Density and Viscosity

Density and viscosity are significant parameters for the characterization of asphaltenes and petroleum products. Gravimetric techniques are usually used to obtain the density of asphaltenes.[52] It has been reported that the average density of solid asphaltenes from crude oil is approximately 1200 kg/m^3. The density of asphaltenes is high when they contain large numbers of aromatic rings (smaller H/C ratio). Yarranton *et al*.[53] measured the liquid density of asphaltene solutions with different concentrations using indirect methods. The density of asphaltenes was measured backward, assuming no excess mixing volumes, and the densities obtained by this method vary between 1000 and 1200 kg/m^3 according to their source.[54]

1.6.4. Elemental Composition

Asphaltenes have no definite melting point and they are black and sticky solids. They are mainly composed of hydrogen and carbon, small quantities of sulfur, nitrogen, oxygen, and trace amounts of heavy metals like iron, vanadium, and nickel.[55,40,56] Asphaltene molecules include sulfur in the forms of sulfide and sulfoxide. Nitrogen can be found as pyrroles and pyridines, metals as porphyrins, and oxygen as carboxylic, phenolic, and ketonic sites. Generally, the hydrogen-to-carbon ratios of asphaltenes from different sources vary over a narrow range. For example, the H/C ratio of n-pentane extracted asphaltenes are typically

1.15±0.5%. In contrast, the proportions of heteroatom elements vary significantly: oxygen (0.2 - 4.9%), nitrogen (0.5 - 3.5%) and sulfur (0.3 -10.3%).[48,57]

1.6.5. Molecular Structure

In addition to measuring the molecular weight, it is also a challenge to determine the molecular structure of asphaltenes because they tend to self-associate in solution. The complexity of asphaltenes, due to their polydisperse nature, makes structural characterization difficult. For this reason, they do not have a precise structural definition.

The structural features of asphaltenes vary from one source of crude oil to another,[39,38] although asphaltenes do have some structural features in common. Asphaltenes are composed of fused polycyclic aromatic hydrocarbon (PAH) ring systems with pendant alkyl side chains. But the PAH size, architecture, and the number of PAHs remain unclear. In the literature published over the last 10 years, the PAH sizes vary from around 4 to 10 fused aromatic rings.[58] Morgan *et al*.[59] applied a method to study Maya crude oil fractions using a combination of liquid NMR and laser desorption-mass spectrometry to calculate the average PAH size of the asphaltene fraction as 8-10 fused rings. Dutta Majumdar *et al*.[28] have used solution-state ^{1}H and ^{13}C NMR spectroscopy to analyse heptane-extracted Athabasca oil-sands asphaltene (AOSA). The average polyaromatic hydrocarbon (PAH) and aliphatic chain length were determined, and they predicted that the structure of each molecule is composed of 6-7 pericondensed aromatic rings. High-resolution transmission electron microscopy (HRTEM)[60] is another method generally used to study the PAH size of asphaltene. This method reported that the PAH size is about 6 to 7 rings. Furthermore, direct molecular imaging using scanning tunnelling microscopy (STM)[61] and TRFD[61] showed that the average number of rings in petroleum asphaltene is ~7.

In addition to the PAH size, it is also necessary to know the type of condensation the PAH can exhibit. Pericondensation refers to an aromatic compound in which three or more rings share the same carbon atoms, while catacondensation refers to interconnecting carbons which do not exceed two rings. To determine what kinds of condensations are present in asphaltene, Raman spectroscopy and ^{13}C NMR spectroscopy have been employed.[62,58] Findings from these methods suggest that asphaltenes are dominated by pericondensation. There has been a major debate about the number of PAHs in an average asphaltene molecule. Currently, there are two models for asphaltenes: the island and the archipelago model.[63] The island model proposes one large condensed PAH core surrounded by aliphatic rings, with branched, mostly saturated, aliphatic chains. The mechanism of interactions for aggregation involves π-π stacking interaction between aromatic rings.[64,65]

The archipelago model proposes a large network of many cross-linked PAHs and aliphatic rings interconnected by aliphatic chains. In these models, heteroatoms such as O, N, and S are present in both the rings and chains.[66,67,68] Heavy metals are frequently found connected to the heteroatoms or the aromatic rings. The interactions leading to aggregation include hydrogen bonding, metal coordination complexes, π-π stacking, etc.[69,70] Both models are successful in explaining certain properties of asphaltenes, but neither is a comprehensive model accounting for all observations. The question that remains to be conclusively answered is whether one of these models predominates or whether the applicable model depends on the source of the asphaltenes. As an example, the island model is consistent with a 750 g/mol molecular weight for asphaltene, whereas the archipelago model is not. However, as several researchers have observed, the archipelago model supports the polymeric properties of asphaltenes. Thermal pyrolysis, thin-film pyrolysis, and oxidation experiments support the "archipelago" model.[71,72] Asphaltenes produce a wide range of

gas, liquid, and coke products in thermal and thin-film pyrolysis, which are considered to be consistent with the archipelago model. Fourier-transform ion cyclotron resonance mass spectrometry (FTICR-MS)[73] has been applied on asphaltene samples and fragmentation patterns provide clear evidence of archipelago structures. Experimental data from gel permeation, thermal oxidation, and small-angle neutron scattering have also supported the archipelago structure of asphaltenes.[74,75,76]

The experimental results from several techniques, however, suggest that the island model is the dominant framework. In the early 1960s, Yen *et al.*[77] used X-ray diffraction methods and they suggested that the island model more accurately represents the structure of asphaltenes. The method of atomic force microscopy (AFM)[78] shows that the structure in asphaltenes contains only one polycyclic aromatic hydrocarbon (PAH) center, consisting of around 7 fused rings. In time-resolved fluorescence depletion (TRFD) experiments, both island-type model compounds and petroleum asphaltenes have identical correlation times and these research results show that the PAHs are not cross-linked, which gives it its island architecture.[79] Several MS reports by Pomerantz *et al.*[50] support the predominant structure of single PAH per asphaltene molecule. They used a two-step laser desorption/ionization mass spectrometry (L^2MS) method to determine the molecular weight of asphaltene and the average molecular weight of approximately 600 g/mol. These experiments show that the fragmentation pattern of asphaltenes is similar to that of compounds that had island molecular structures. Moreover, scanning tunneling microscopy,[80] high-resolution transmission electron microscopy,[81] electronic triplet-state spectroscopy, laser-induced acoustic desorption (LIAD) and diffusion studies[82] show that the island type architecture is predominant. NMR spectroscopy[83] studies also support the island model for asphaltenes

structure. Despite continuous efforts, asphaltene molecular size and structure are still under active debate as these techniques report on disparate features of asphaltenes under dissimilar conditions.

1.6.6. Asphaltene Aggregation

The aggregation mechanism of asphaltenes is still not well understood, and the aggregation strongly depends on the solvent, concentration, and thermodynamic conditions. Changes in those conditions may destabilize solutions of asphaltenes in crude oil and result in aggregate formation.[84,85]

In the presence of a good solvent, such as toluene, asphaltene molecules self-associate with each other, forming stable aggregates. Yarranton *et al*.[53] argued that the initial asphaltene aggregate consists of only two to six asphaltene monomers, rendering the critical micelle concentration (CMC) not applicable for asphaltenes because of such a low aggregation number. In addition, in contrast to surfactants, asphaltenes lack an amphiphilic nature and head-head interactions may not be the driving force for asphaltene aggregation.

In recent years, it has been suggested that asphaltenes aggregate in a hierarchical model called the Yen-Mullins model, first suggested by Yen [77] and later updated by Mullins.[55] In the Yen-Mullins model, the primary interaction of asphaltene compounds is π- π stacking.[55] Pi (π) stacking is the attractive and non-covalent interaction between aromatic rings in a PAH. Different interactions are known to influence π stacking. This observation shows that asphaltene molecules consist mainly of island-type molecules. There are possible intermolecular and intramolecular attractive and repulsive interactions like hydrogen-bonding, polar–polar interactions, and electrostatic attractions that can be considered to also drive asphaltenes aggregation.[40] The PAH units in asphaltene molecules generate

attractive forces between aromatic cores by π-π interaction, these stacks consist of < 10 asphaltene molecules with 4−9 peri-condensed aromatic rings in each conjugated core. The alkyl side chains provide repulsion through steric hindrance, which prevents further π-π interactions and growth of the nanoaggregate. Findings from X-ray diffraction studies [86] supported the concept of π-π aromatic sheet interaction, and these sheets tend to stack together. Results from different techniques such as time-resolved fluorescence depolarization (TRFD),[87] DC conductivity,[88] and nuclear magnetic diffusion[89] show that asphaltene molecules are 1.5 nm in size. With increasing concentration, asphaltene molecules form nanoaggregates that can form clusters at higher concentrations, resulting in a structural hierarchy of three distinct phases (Fig.1.2).[55,90]

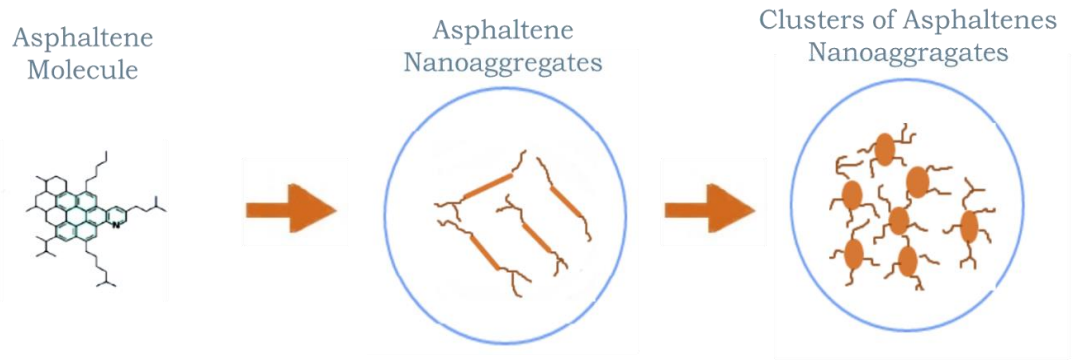

Figure 1.2. The "Yen-Mullins" model describing the hierarchical aggregation behavior of asphaltenes.

Critical nanoaggregate concentration (CNAC) and critical cluster concentration (CCC) are used to describe the asphaltene aggregation formation.[75,91,92] Mullins *et al.*[79] defined the asphaltene "critical nanoaggregate concentration" (CNAC) as a concentration at which the nanoaggregates stop their growth. At concentrations below CNAC, asphaltenes are present

as smaller multimers (dimers, trimers, etc.). Nanoaggregation of asphaltenes occurs at concentrations close to the CNAC. Different techniques such as centrifugation,[93] high-Q ultrasonic,[94] and electrical conductivity measurements (AC and DC) studies[88] have shown that aggregates form when the CNAC range between 0.05-0.15 g/L, as it varies based on the asphaltene source and thermodynamic conditions. Gas chromatography, mass spectrometry, NMR diffusion measurement, and fluorescence measurements have also been used to study the CNAC of asphaltenes.[92] Lisitza *et al.*[95] have shown that the average self-diffusion coefficient decreases above the CNAC.

At the critical clustering concentration (CCC), which is a significantly higher concentration than CNAC, asphaltenes have a strong tendency to form secondary aggregates, *i.e.*, clusters. Above the CCC, clusters of nanoaggregates become dominant, with asphaltene CCC at approximately 2.0-5 g/L. DC conductivity [88] and centrifugation [93] experiments were performed to determine the CCC values. The interactions between the asphaltene nanoaggregates are most likely dominated by alkyl−alkyl and alkyl−aromatic interactions. Furthermore, the small contribution of T-shaped interactions in cluster formation was indicated by Dutta Majumdar *et al.*[83] Molecular dynamics (MD) simulation studies have reproduced the full Yen–Mullins aggregation hierarchy for asphaltenes.[96,97] The sizes of such clusters are unknown, but they are bound by the nanoaggregates (~ 2 nm) and the smallest clusters grow to approximately 6 nm diameter.

The archipelago model invokes a network of smaller PAHs connected by aliphatic chains, with no hierarchy structure. Gray *et al.*[70] claims that experimental findings such as (a) molecular complexity (b) the different distribution of aggregate sizes; (c) the elastic

behavior of asphaltenes; and (d) the emulsion properties of nanoaggregates cannot be explained by the Yen-Mullins model.

The "supramolecular assembly" model proposed by Gray and co-workers,[70] suggested that asphaltene aggregates are porous, having a significant solvent content as supported by SANS and MD simulation studies. The introduction of this supramolecular network is the result of many different cooperative interactions, like aromatic π−π stacking, hydrogen bonding, hydrophobic pockets, and metal coordination complexes. They suggested that most molecules in asphaltenes contain several active sites, able to interact with other asphaltene molecules. Their aggregation behavior also depends on external forces and the solvent strength of the solution. This model can describe asphaltene properties such as aggregate sizes, adhesion to surfaces, emulsion properties, porosity, and elasticity.[98] However, the difference between nanoaggregates and clusters is not explained with this model.

More recently Zhang *et al.*,[27] proposed that a mechanism for asphaltene aggregation, suggesting that pancake bonding, involving radicals and polycyclic aromatic hydrocarbons (PAHs), could play a crucial role. This theory introduces the concept of hetero association between radical species and various PAHs or PAHs with heteroatoms, providing a unique perspective on the forces driving asphaltene nano aggregation. Supporting evidence from multiple analytical techniques, such as ultrahigh-resolution Fourier-transform ion cyclotron resonance mass spectrometry (FT-ICR MS), and atomic force microscopy (AFM) imaging, adds weight to this hypothesis. However, caution is warranted due to the lack of direct experimental validation and computational findings challenging specific bonding strengths. Computational analyses by Janesko *et al.*[99] particularly on 'half-pancake bonding', suggest

that this bonding type may not possess significant strength. The study implies that while pancake and half-pancake bonding might not be the sole drivers of asphaltene aggregation, interactions involving stable organic radicals, heteroatoms, and polar groups might still play a role. While the pancake bonding hypothesis offers intriguing insights, its lack of experimental support and computational challenges highlight the need for further investigation and scrutiny in the field.

1.7. NMR Spectroscopy for Characterization of Asphaltene

As outlined in the discussion so far, there is a need for a more comprehensive understanding of the structure and self-associate behavior of asphaltenes. Various analytical and spectroscopic data must be carefully considered and combined for a comprehensive analysis.

Numerous analytical techniques have been employed in asphaltenes research, with nuclear magnetic resonance (NMR)[10,100,101] and mass spectrometry (MS)[10,102,103] being the most widely used. Because of the excellent reproducibility of NMR techniques and the high sensitivity of MS techniques, these methods are superior to other analytical methods in characterization of asphaltenes. Each technology has advantages and liabilities and the techniques frequently complement one another.[59]

Mass spectrometry is the most prominent and essential way to obtain the molecular weight information of asphaltenes.[104,105] Multistage mass spectrometry (MS_n) is well-suited for researching asphaltenes because it can examine the structure of individual ionized molecules without separation. This approach estimates the total number of carbons in alkyl chains, aromatic core sizes, and molecular weight distributions (MWDs) for ionized asphaltene if an ionization method yields a single ion type per analyte without

fragmentation.[46] Boduszynski *et al.*[106] reported the average molecular weight of 850 g/mol for asphaltene using field ionization mass spectrometry (FIMS), which contradicted earlier records and has been criticized for failing to identify the molecular ion of the massive asphaltene molecules and their corresponding fragmentation patterns. No ionization method can produce ions from all asphaltene molecules by a single ionization approach,[107] such as electrospray ionization, atmospheric pressure chemical ionization (APCI), atmospheric pressure photoionization (APPI), laser desorption ionization, and matrix-assisted laser desorption/ionization (MALDI).[108] The main difficulty with using this array of ionization methods is the fragmentary nature of the information gathered which is at best a subset of all the species present in asphaltenes. It has been determined that studies of mass and methods of ionization are not yet exact; thus, it is essential to employ additional experimental methods.

Nuclear magnetic resonance (NMR) spectroscopy is a highly adaptable technique that can provide information on chemical functionalities and structural configurations at the molecular level.[109,110] There are many studies describing various applications of different NMR techniques for oil and petroleum fractions.[100,111] The NMR technique is non-destructive which offers specific information about the structure, size, shape, and dynamics of molecules. Researchers in protein and biomolecules employ this tool due to the high quality of information gained on conformation, dynamics, and structural details.[112]

In comparison with other analysis techniques, NMR spectroscopy has many advantages. Firstly, it enables the analysis of asphaltenes in a non-destructive way. NMR spectroscopy also offers a large variety of experiments with different capabilities. Beyond standard one-dimensional experiments that aid in identifying distinct chemical environments, two-

dimensional experiments reveal connectivity among these environments, offering insights into their spatial proximity. NMR relaxation measurements can provide information on the molecular reorientational dynamics of a system; those studies deal with the relaxation behaviour of the whole asphaltene system to study their dispersive and aggregation characteristics or molecular size. Diffusion-based experiments can probe the translational motion.[113,91] NMR spectroscopy also allows for the quantification of the different chemical species present. Another important aspect of NMR spectroscopy is the capability to study materials in all states, *i.e.*, the solid state, solution state, gel, and gas phase. NMR spectroscopy is a standard technique for studying asphaltenes because asphaltenes are solids that can be dissolved in appropriate solvents.

One drawback and difficulty in using NMR in petroleum research is its low sensitivity. NMR sensitivity has been vastly improved by the continuous developments in field strength and homogeneity, probe design, and the introduction of cryogenically cooled probes and microprobes. Typically a NMR sample should consist of a single phase as the presence of additional phases will introduce susceptibility broadening and, in the worst cases, field splitting giving rise to indistinct spectra, doubling of all the peaks that are present in the spectrum.[114]

NMR spectroscopy proves highly effective for investigating diamagnetic compounds, which possess paired electrons, thereby circumventing the predominant relaxation pathway associated with electron-nuclear coupling. This characteristic makes NMR spectra particularly well-resolved, especially for smaller molecules. Conversely paramagnetic substances, those which have unpaired electrons, are much more challenging to study owing to the consequent rapid relaxation or pseudo-contact shifts arising from the electron

magnetic moment.[115] This effect is not limited to the confines of the molecule but can severely affect nearby molecules. The number of NMR methods suitable for use with paramagnetic compounds is still somewhat limited. Structural information is often lost because the signals are extremely broad or in cover unusual wide chemical shift ranges.

Preparing NMR samples with solvents containing deuterium instead of hydrogen is necessary. The NMR signal from the deuterium nuclei is known as the NMR lock and is used to account for magnetic field instabilities. Many deuterated solvents are commercially available. Chloroform (as $CDCl_3$) is the most widely used solvent for non-hydrocarbons due to their high solubility. It has almost no effect on the chemical shifts of solutes and is the preferred solvent when shifts are required to be measured accurately. One of its potential problems is that it may trade its deuterium for exchangeable hydrogens, typically from residual water or OH groups in a sample, which will render the residual ^{1}H chloroform peak larger than usual and the exchangeable hydrogen (such as -OH signal) peak smaller.[114]

As NMR spectroscopy is the primary technique employed in this study, Chapter two presents the fundamental ideas and principles underlying NMR spectroscopy. In this thesis, NMR has been used only for ^{1}H and ^{19}F NMR spectroscopy, spin-lattice, or longitudinal relaxation time measurement experiments (T_1 measurement), spin-spin or transverse relaxation time measurement (T_2 measurement), and diffusion ordered spectroscopy (DOSY).

1.7.1. Solution-state NMR Spectroscopy

Solution-state NMR spectroscopy has been essential in developing an understanding of the structural motifs of asphaltenes. The majority of solution-state NMR spectroscopic studies on asphaltenes are based on one-dimensional techniques such as ^{1}H, ^{13}C, and ^{13}C DEPT

(Distortionless Enhancement by Polarization Transfer) NMR spectroscopy.[63,116] Friedel *et al.*[117] first recorded the solution-state ^{1}H NMR spectrum of a coal liquid asphaltene as early as 1959. They reported the detection of NMR signals in asphaltenes and recorded three separates ^{1}H NMR spectra, identifying the presence of polyaromatic hydrocarbon in asphaltene. The experiment was carried out in CS_2 as a solvent at 125°C. Carbon disulfide is an effective solvent for both hydrocarbon polymers and asphaltic substances, resulting in an excellent resolution for the given concentration, presumably because its solutions have lower viscosity and fewer sample aggregates. But CS_2 is hazardous because it is poisonous and highly flammable, thus it needs to be handled with special care. In the same year, Gardner[118] also used ^{1}H NMR to analyze asphaltene from the mid-continental U.S. They estimated the alkyl branches index as well as the relative concentrations of aromatic ring hydrogen and total alkyl hydrogen. Brown and Ladner have shown that structural parameters like aromaticity (f_A) (Eq. 1.1) for coal can be obtained using the ^{1}H NMR spectroscopy.[119] Many other structural parameters, such as the degree of aromatic ring substitution, naphthenic ring numbers, and the average PAH size can be calculated using the Brown and Ladner equation.[119,120] The aromaticity equation of Brown and Ladner can be written as:

$$f_A = \frac{\left\{\left(\frac{C}{H}\right) - \left(\frac{H_\alpha}{x}\right) - \frac{(H_\gamma + H_\beta)}{y}\right\}}{\frac{C}{H}} \qquad (1.1)$$

where C/H is the carbon to hydrogen atomic ratio calculated from elemental analysis; x is the average number of hydrogens atom per alkyl group (α) attached to an aromatic ring and y is the number of remaining alkyls substituents; and the normalised integrated intensities of the α, β, and γ-alkyl hydrogen atoms are expressed by H_α, H_β, and H_γ, respectively. Yen

and Erdman[77] used a modified Brown-Ladner method for the quantitative characterization of average asphaltene structure. To compare structural variations between the different asphaltenes, Girdler[121] used ^{1}H NMR spectroscopy. They were able to distinguish between n-pentane and n-heptane asphaltenes. n-Pentane asphaltenes were shown to have more hydrogen, lower aromaticity and apparent molecular weights, more aromatic substitution, shorter aliphatic chains, and less aromatic groupings than the corresponding n-heptane asphaltenes. Ramsey *et al.*[122] used the modified Brown-Ladner method to analyse asphaltenes, and they reported ^{1}H NMR spectra of asphaltenes, and they calculated a number of structural parameters including aromaticity, C/H ratio, and average molecular weight. Yen showed by ^{1}H NMR spectroscopy that thermal cracking can cleave alkyl side chains and aliphatic hydrocarbons and form aromatic structures from naphthenic structures.[123] Asphaltenes from Cold Lake heavy oil were fractionated by size exclusion chromatography and analysed using ^{1}H NMR spectroscopy by Semple *et al.*[124] determining fundamental features of asphaltene, such as average chemical structures in Cold Lake asphaltenes, aromatic core size, average C/H ratio, and alkyl side chains.

Furthermore, carbons with no attached protons are not shown in the ^{1}H spectra, which can distort aromaticity estimations. The development of high-resolution ^{13}C NMR spectroscopy was required to find solutions to these issues. ^{13}C NMR is used to gain information about the carbon backbone of a compounds chemical structure, but its applications are limited due to its low sensitivity, which results from ^{13}C's low natural abundance (1.1%), and the low gyromagnetic ratio of carbon-13 (6.7283×10^{7} rad/T s) compared to that of proton (26.7513×10^{7} rad/T s). Ignasiak[125] and Dereppe[126] published one of the first complete ^{13}C NMR studies of asphaltenes. Dereppe[127] developed a set of equations to calculate the

average structural parameters using integrated spectral areas, such as aromaticity, length of an alkyl chain, aromatic condensation. Dickinson[128] used a similar process to examine petroleum asphaltenes. By using ^{13}C NMR spectroscopy, Sklenar *et al.*[129] measured the aromaticity of coal asphaltenes using three separate methods: broadband decoupling, gated decoupling, and gated decoupling with relaxation reagent. They discovered that gated decoupling with the addition of a paramagnetic relaxation reagent allows for the most accurate measurements. Cookson[130] proposed gated spin-echo (GASPE) and conventional spin-echo ^{13}C NMR spectroscopy techniques to determine aromatic C or CH or aliphatic C, CH, CH_2, or CH_3 groups present in petroleum and coal liquids. Many groups used a combination of ^{13}C NMR spectral editing techniques, such as gated spin-echo and the DEPT process,[131] to define and predict the asphaltenes average structural parameters.[43,132] In the early days and up until the mid-90s, the majority of efforts in solution–state NMR spectroscopy for asphaltene characterization were based on one-dimensional techniques. The asphaltene system contains a wide range of carbon and proton environments, which can lead to signal misassignment if just one-dimensional approaches are used.

It is well-known that 2D NMR correlation techniques allow for more accurate assignments, however, a review of the literature shows that the use of 2D NMR spectroscopy has been limited in asphaltene characterization. The extended experimental time is one of the primary drawbacks of 2D NMR studies, particularly for asphaltene research due to its complex nature. Also, highly overlapping regions in the ^{1}H NMR spectra, like those in heavier petroleum fractions like asphaltene, cannot be clearly assigned or separated because the correlation contours in the 2D spectra are spread out and diffused.[133] Few studies have used ^{1}H Diffusion-Ordered Spectroscopy (DOSY) to investigate self-association behavior

in asphaltenes and to determine the molecular weight and size of aromatic cores.[134,135] Sarpal[136] used 2D-correlation spectroscopy (COSY) and heteronuclear correlation (HETCOR) to characterize hydrocracking base oil, which has a significantly lower molecular weight, is composed of paraffinic fractions, and is substantially different from asphaltenes. Furthermore, thermal cracking has been shown to generate archipelago-like structures.[71] Sheremata[137] then used Sarpal's[136] findings to analyse the ^{1}H and ^{13}C NMR spectra of asphaltenes.

NMR relaxation measurements offer insights into the molecular dynamics and aggregation behavior of asphaltenes.[138,139] NMR relaxation studies on the asphaltene molecules themselves are used in only a few studies because it is very labour and resource intensive. Pekerar *et al.*[135] measured ^{13}C T_1 values in solution to study the mobilities of asphaltene molecules. T_1 and T_2 measurements in solution give information about the mobility of asphaltene molecules and both are required to determine the motional timescale. A T_1/T_2 ratio approaching unity indicates a mobile system, whereas it is increasingly rigid as the ratio becomes larger. Ostlund *et al.*[140] conducted an investigation into asphaltene deposition by employing relaxation dispersion measurements of ^{1}H T_1 and T_2 on asphaltene molecules. Focusing on the 0.7–2.1 ppm range, representing the aliphatic region in the ^{1}H NMR spectrum, the study identified two different T_2 relaxation times, namely 0.6 and 7.0 ms. These times were associated with protons situated either in proximity or at a distance from the aromatic core, offering limited insights into the molecular architecture. Lisitza[95] studied the aggregation behaviour of asphaltenes using the spin-echo technique but did not describe T_2 values. Gizatullin *et al.*[141] studied the NMR relaxation (T_1 and T_2) and translational diffusion (D) properties of several maltenes with and without asphaltene. Experiments on

relaxation showed that in the absence of asphaltene, T_1 and T_2 are similar in maltenes, however in the presence of asphaltene, relaxation time constants are significantly longer, as is the slowing of the maltenes motion. As T_2 is more influenced than T_1, the slowdown is significant. When asphaltene is present, the ratio between T_1 and T_2 increases more, usually by about 50%. Furthermore, they observed lower maltene diffusion coefficients in the presence of asphaltenes. In addition to this method, low-field NMR relaxometry has been used to study the behavior of asphaltene in native crude oil.[136,142,143] All of these investigations are valuable in their own right and shed light on asphaltene behavior, but the relaxation behavior of certain chemical groups within asphaltenes remains unanswered.

1.7.2. Solid-state NMR Spectroscopy

Basic solution-state NMR spectroscopy is widely used to characterize asphaltene, whereas solid-state NMR has rarely been applied. The reason for this is that solid-state NMR investigations demand more spectroscopic expertise than normal routine solution-state NMR studies. Solid-state NMR requires pure materials, as complicated materials broaden the lines. The presence of broad lines indicates a lack of sensitivity and poor resolution (many peaks overlap at low resolution). Whereas improper interpretation of solid-state NMR results may lead to flawed results, solid-state NMR can potentially offer significant advantages over solution-state methods.

Typically, solid-state NMR spectroscopy observables are orientation dependent. In general, solid-state NMR spectroscopy can provide precise structural information since the orientation dependency of the chemical shift can be determined with low interference from the chemical exchange and rapid motion. This contrasts with solution-state NMR, where valuable detailed structural information is compromised by isotropic motion and

interactions between the system and the solvent. This is particularly true for complex mixtures with hierarchical structural patterns, like asphaltenes monomer-nanoaggregate-cluster hierarchy, whereas solid-state NMR methods are well suitable to investigate phase structures. Solid-state ^{1}H and ^{13}C NMR studies of coal-derived asphaltenes applying the dipolar dephasing technique[144] were reported by the group of Murphy, Gerstein, Weinberg, and Yen between 1981 and 1983.[145, 146] These early studies are characterized by poor resolution due to ineffective ^{1}H decoupling caused by a low magnetic field, low power, and inhomogeneity in the radio-frequency (rf) field. Experiments using ^{13}C cross-polarization magic angle spinning (CP-MAS) were carried out by Cyr *et al.*[147] and Semple *et al.*[124] to describe asphaltenes produced from bitumen and heavy oil, respectively. They made the common mistake of extracting quantitative results from ^{13}C CP-MAS NMR signal intensities, especially on material with long networks of non-protonated aromatic carbons. Particularly for asphaltenes, integration values from a ^{13}C CP-MAS NMR spectrum should not be used to obtain quantitative information due to the large variation in proton-to-carbon CP efficiency among various carbons. These efficiencies depend on the carbons proximity to the system's protons, which may result in the absence of specific carbon signals. Cyr,[147] on the other hand, noticed this problem in their work but did not discuss it in detail. Storm *et al.*[148] and Pekerar *et al.*[135] studied petroleum-derived asphaltenes using CP-MAS techniques. They carry out relaxation and CP time measurements in the solid state, but these measurements appear to be fundamentally flawed, because the measurements were carried out just for the strong signals, and they entirely ignored the underlying resonances that were present in the broad background. By applying deconvolution (peak-fitting) analysis to the solid-state ^{13}C NMR spectra, Douda *et al.*[149], Daaou *et al.*[150], and Bouhadda *et al.*[151] demonstrated that these underlying resonances make up a significant part of the

spectrum and should not be ignored. Storm[148] carried out one of the earliest studies of CP-dynamics and reported the cross-polarization time constants (T_{CP}) and the ^{1}H spin-lattice relaxation time in the rotating frame ($T_{1\rho}$), which are useful parameters needed to understand the structure and mobility. Since the CP-dynamics model that Storm used to obtain these numbers is different from the CP models such as the classical I-S model and the I-I*-S model that have been used for a long time in the solid-state NMR spectroscopy literature,[152] its accuracy could be called into question. Pekerar[135] also reported T_{CP} values, but neither their CP-dynamics model nor the CP-dynamics were discussed in detail. Another mistake found in some MAS studies[149, 153, 154] is that they do not take into account the aromatic spinning sidebands that overlap with the aliphatic signals. This can lead to mistakes in assignments and measurement. Specifically, the 8 kHz MAS rate applied by Douda *et al.*[149] to deconvolve the aliphatic part of the ^{13}C NMR spectra ignored the spinning sidebands of the aromatic region. At a 14 kHz MAS rate, Daaou *et al.*[153] made the same mistake, leading to inaccurate integration values. These studies only present a deconvolution model for the aliphatic region and integrate the aromatic portion of the spectrum. Bouhadda *et al.*[151] performed a deconvolution study of the full ^{13}C NMR spectra by comparing single-pulse excitation (SPE), cross-polarization, and Hahn-echo sequences to assess the aromaticity of an Algerian crude. They observed that SPE provided the best measure of aromaticity. Quantitative single-pulse excitation (SPE) MAS NMR spectra of asphaltenes were also reported by Hauser *et al.*[155], who employed a CP-polarization inversion (CP/PI) technique for spectral editing. They studied how stable heavy oil asphaltenes are at high temperatures during pyrolysis and found that dealkylation or dehydrogenation is more likely to happen than the formation of larger polyaromatic rings

as the pyrolysis temperature rises. Dutta Majumdar *et al.*[156] employed solid-state ^{1}H NMR spectroscopy under ultrafast magic angle spinning (60 kHz) to examine the solid phase aggregate structure of a petroleum asphaltene. They used a dipolar filter and DQ-MAS experiments and showed that nanoaggregates form clusters through alkyl-alkyl interactions and T-shaped interactions with aromatic proton environments, as these were shielded and deshielded by ring currents. This interpretation is similar to the clusters posited by the Yen-Mullins model, but, instead of exclusive alkyl-alkyl interactions within the clusters, T-shaped interactions were shown to also play a role. Alemany *et al.*[63] studied solid-state and solution-state NMR spectra of six Ecuadorian asphaltenes. For these asphaltenes, they obtained meaningful carbon aromaticity values using direct polarization with ^{13}C pulse excitation. In comparison to a single contact time CP-MAS spectrum, it was found that multiple contact times are more beneficial when studying asphaltene. By utilizing CP-MAS and direct ^{13}C pulses they stated that, condensed aromatic ring systems become larger as aromaticity increases, which is consistent with "island" rather than "archipelago" aromatic structures. Bouhadda *et al.*[157] employed liquid ^{1}H and solid ^{13}C CP-MAS NMR spectroscopy in combination with qualitative DEPT to investigate the molecular structural parameters of Algerian asphaltenes. From the solid-state ^{13}C CP-MAS NMR spectrum, a value for aromaticity was calculated and they conclude that these asphaltenes have a small condensed aromatic ring system (four or five rings per sheet). While CP-MAS has been widely employed, CP dynamics analysis and relaxation investigations are few. Solid-state ^{1}H NMR spectra inherently exhibit broad signals owing to the robust ^{1}H-^{1}H homonuclear dipolar couplings, which persist even at elevated spinning speeds. However, resolving resonances in such spectra and deducing any relevant information from them requires very specific pulse sequences, which are challenging to conduct.

1.8. Thesis Objectives

The objective of this thesis is to investigate asphaltene aggregation behavior using solution-state ^{1}H and ^{19}F NMR spectroscopy techniques. A protocol for reliably characterizing asphaltene structure by ^{1}H NMR spectroscopy needs to be developed using deconvolution analysis that will be applicable for a range of asphaltenes. In addition, measurements of ^{1}H T_1 and T_2 measurements will be carried out for various asphaltenes, resulting in T_1/T_2 ratios that will yield mobility information, potentially enabling the calculation of hydrodynamic radii of aggregates that predominate in solutions. These aggregate sizes will be compared to those obtained from DOSY experiments. The study encompasses the characterization of asphaltene samples obtained at different depths from an oil well, providing insights into the impact of varying conditions on aggregation behaviors. Additionally, the study extends to the analysis of *in-situ* pyrolyzed oil shale asphaltenes, exploring the relationship between asphaltene aggregation and maturity. The investigation of the asphaltene sample PetroPhase 2017, which has been studied by a number of research groups around the world using different techniques, will contribute insights into how asphaltene aggregation changes upon sonication. Furthermore, the potential application of ^{19}F NMR spectroscopy, including relaxation dispersion measurements, using fluorine-containing probe molecules will be studied, offering a unique perspective and enhanced sensitivity for dynamic and structural investigations.

REFERENCES

1. Mullins, O. C.; Sheu, E. Y.; Hammami, A.; Marshall, A. G., Asphaltenes, heavy oils, and petroleomics. Springer Science & Business Media: 2007.

2. Chilingarian, G.; Yen, T., Asphaltenes and Asphalts, 1. Elsevier: 1994.

3. Ancheyta, J., Asphaltenes: chemical transformation during hydroprocessing of heavy oils. CRC press: 2010.

4. Becker, J., Crude oil waxes, emulsions, and asphaltenes. Pennwell Books Tulsa, OK: 1997.

5. Murphy, D. J.; Raugei, M.; Carbajales-Dale, M.; Rubio Estrada, B., Energy Return on Investment of Major Energy Carriers: Review and Harmonization. Sustainability 2022, 14 (12), 7098.

6. Vishnyakov, V.; Suleimanov, B.; Salmanov, A.; Zeynalov, E., Primer on enhanced oil recovery. Gulf Professional Publishing: 2019.

7. Ericson, S. J.; Engel-Cox, J.; Arent, D. J. Approaches for integrating renewable energy technologies in oil and gas operations; National Renewable Energy Lab.(NREL), Golden, CO (United States): 2019.

8. Mullins, O. C.; Pomerantz, A. E.; Zuo, J. Y.; Dong, C., Downhole fluid analysis and asphaltene science for petroleum reservoir evaluation. Annual review of chemical and biomolecular engineering 2014, 5, 325-345.

9. Mullins, O. C.; Chen, L.; Betancourt, S. S.; Achourov, V.; Dumont, H.; Cañas, J. A.; Forsythe, J. C.; Pomerantz, A. E., Reservoir fluid geodynamics. In Fluid Chemistry, Drilling and Completion, Elsevier: 2022; pp 1-39.

10. Hassanzadeh, M.; Abdouss, M., A comprehensive review on the significant tools of asphaltene investigation. Analysis and characterization techniques and computational methods. Journal of Petroleum Science and Engineering 2022, 208, 109611.

11. Mullins, O. C.; Sheu, E. Y., Structures and dynamics of asphaltenes. Springer Science & Business Media: 1999.

12. Rashid, Z.; Wilfred, C. D.; Gnanasundaram, N.; Arunagiri, A.; Murugesan, T., A comprehensive review on the recent advances on the petroleum asphaltene aggregation. Journal of Petroleum Science and Engineering 2019, 176, 249-268.

13. Simanzhenkov, V.; Idem, R., Crude oil chemistry. Crc Press: 2003.

14. Johnson, O.; ProQuest, 40 classic crude oil trades: real-life examples of innovative trading. Routledge: Abingdon, Oxon;New York, NY;, 2022.

15. Manning, F.; Thompson, R., Oilfield Processing of Petroleum, Vol 2: Crude Oil. Tulsa, OK: PennWell Books 1995.

16. Abdel-Raouf, M., Crude oil emulsions: Composition stability and characterization. BoD–Books on Demand: 2012.

17. Fakher, S.; Ahdaya, M.; Elturki, M.; Imqam, A., Critical review of asphaltene properties and factors impacting its stability in crude oil. Journal of Petroleum Exploration and Production Technology 2020, 10 (3), 1183-1200.

18. Wauquier, J.-P., Petroleum refining 1 crude oil petroleum products-Technip. 1996.

19. Yen, T. F.; Chilingarian, G. V., Oil shale. 1976.

20. Kang, Z.; Zhao, Y.; Yang, D., Review of oil shale in-situ conversion technology. Applied Energy 2020, 269, 115121.

21. Speight, J. G., Shale oil and gas production processes. Gulf Professional Publishing: 2019.

22. Speight, J. G., Shale oil production processes. Gulf Professional Publishing: 2012.

23. Bartis, J. T.; LaTourrette, T.; Dixon, L.; Peterson, D.; Cecchine, G., Oil shale development in the United States: prospects and policy issues. Rand Corporation: 2005.

24. Vargas, F. M.; Tavakkoli, M., Asphaltene deposition: fundamentals, prediction, prevention, and remediation. CRC Press: 2018.

25. Yen, T. F.; Chilingarian, G. V., Asphaltenes and asphalts, 2: Part B. Elsevier: 2000.

26. Ancheyta, J.; Centeno, G.; Trejo, F.; Marroquin, G.; García, J.; Tenorio, E.; Torres, A., Extraction and characterization of asphaltenes from different crude oils and solvents. Energy & Fuels 2002, 16 (5), 1121-1127.

27. Zhang, Y.; Siskin, M.; Gray, M. R.; Walters, C. C.; Rodgers, R. P., Mechanisms of asphaltene aggregation: puzzles and a new hypothesis. Energy & Fuels 2020, 34 (8), 9094-9107.

28. Dutta Majumdar, R.; Gerken, M.; Mikula, R.; Hazendonk, P., Validation of the Yen-Mullins Model of Athabasca Oil-Sands Asphaltenes using Solution-State 1H NMR Relaxation and 2D HSQC Spectroscopy. Energy Fuels 2013, 27 (11), 6528-6537.

29. Mustafiz, S.; Islam, M. R., State-of-the-art Petroleum Reservoir Simulation. Petroleum science and technology 2008, 26 (10-11), 1303-1329.

30. El-Bassoussi, A. A.; Ahmed, M. H. M.; Sayed, S. M. E.; Basta, J. S.; Attia, E. S. K., Characterization of Some Local Petroleum Residues by Spectroscopic Techniques. Petroleum Science and Technology 2010, 28 (5), 430-444.

31. Evdokimov, I. N.; Eliseev, N. Y.; Akhmetov, B. R., Asphaltene dispersions in dilute oil solutions. Fuel 2006, 85 (10-11), 1465-1472.

32. Fan, T.; Buckley, J. S., Rapid and Accurate SARA Analysis of Medium Gravity Crude Oils. Energy Fuels 2002, 16 (6), 1571-1575.

33. Kelland, M. A., Production chemicals for the oil and gas industry. CRC press: 2016.

34. Sheu, E. Y.; Mullins, O. C., Fundamentals and applications. Springer: 1995.

35. Mougnol, J.-B. B.; Rabiu, A.; Obanijesu, E.; Sam, Z. In Asphaltene Extraction Capacity of Different Solvents, Proceedings of the 7th International Conference on Informatics, Environment, Energy and Applications, 2018; pp 114-118.

36. Speight, J., Petroleum Asphaltenes-Part 1: Asphaltenes, resins and the structure of petroleum. Oil & gas science and technology 2004, 59 (5), 467-477.

37. Mokhtari, R.; Hosseini, A.; Fatemi, M.; Andersen, S. I.; Ayatollahi, S., Asphaltene destabilization in the presence of an aqueous phase: The effects of salinity, ion type, and contact time. Journal of Petroleum Science and Engineering 2022, 208, 109757.

38. Groenzin, H.; Mullins, O. C., Molecular Size and Structure of Asphaltenes from Various Sources. Energy Fuels 2000, 14 (3), 677-684.

39. Hosseini-Dastgerdi, Z.; Tabatabaei-Nejad, S. A. R.; Khodapanah, E.; Sahraei, E., A comprehensive study on mechanism of formation and techniques to diagnose asphaltene structure; molecular and aggregates: a review. Asia-Pacific Journal of Chemical Engineering 2015, 10 (1), 1-14.

40. Mullins, O. C., The Modified Yen Model. Energy Fuels 2010, 24 (4), 2179-2207.

41. Yarranton, H.; Powers, D.; Okafor, J.; van den Berg, F., Regular solution based approach to modeling asphaltene precipitation from native and reacted oils: Part 2, molecular weight, density, and solubility parameter of saturates, aromatics, and resins. Fuel 2018, 215, 766-777.

42. Zheng, C.; Zhu, M.; Zareie, R.; Zhang, D., Characterisation of subfractions of asphaltenes extracted from an oil sand using NMR, DEPT and MALDI-TOF. Journal of Petroleum Science and Engineering 2018, 168, 148-155.

43. V. Calemma, R. R., P. D'Antona, and L. Montanari, Characterization of Asphaltenes Molecular Structure. Energy & Fuels 1998, 12 (1998), 422-428.

44. Snyder, D. A.; Zhang, F.; Bruschweiler, R., Covariance NMR in higher dimensions: application to 4D NOESY spectroscopy of proteins. J Biomol NMR 2007, 39 (3), 165-75.

45. R. C. Silva*, P. R. S., 1H and 13C NMR for Determining Average Molecular Parameters of Asphaltenes from Vacuum Residue Distillation. Ann. Magn. Reson. 2004, 3 (2004), 63-67.

46. Fergoug, T.; Boukratem, C.; Bounaceur, B.; Bouhadda, Y., Laser Desorption/Ionization-Time of Flight (LDI-TOF) and Matrix-Assisted Laser

Desorption/Ionization - Time of Flight (MALDI – TOF) mass spectrometry of an Algerian asphaltene. Egyptian Journal of Petroleum 2017, 26 (3), 803-810.

47. Storm, D. A.; Edwards, J. C.; DeCanio, S. J.; Sheu, E. Y., Molecular Representations of Ratawi and Alaska North Slope Asphaltenes Based on Liquid- and Solid-State NMR. Energy Fuels 1994, 8 (3), 561-6.

48. Speight, J. G., Petroleum Asphaltenes - Part 1: Asphaltenes, Resins and the Structure of Petroleum. Oil & Gas Science and Technology 2006, 59 (5), 467-477.

49. Sabbah, H.; Morrow, A. L.; Pomerantz, A. E.; Mullins, O. C.; Tan, X.; Gray, M. R.; Azyat, K.; Tykwinski, R. R.; Zare, R. N., Comparing Laser Desorption/Laser Ionization Mass Spectra of Asphaltenes and Model Compounds. Energy & fuels 2010, 24 (6), 3589-3594.

50. Pomerantz, A. E.; Hammond, M. R.; Morrow, A. L.; Mullins, O. C.; Zare, R. N., Two-Step Laser Mass Spectrometry of Asphaltenes. J. Am. Chem. Soc. 2008, 130 (23), 7216-7217.

51. Parlov Vuković, J.; Novak, P.; Plavec, J.; Friedrich, M.; Marinić Pajc, L.; Hrenar, T., NMR and Chemometric Characterization of Vacuum Residues and Vacuum Gas Oils from Crude Oils of Different Origin. Croatica Chemica Acta 2015, 88 (1), 89-95.

52. Soleymanzadeh, A.; Soleymanzadeh, A.; Yousefi, M.; Yousefi, M.; Kord, S.; Kord, S.; Mohammadzadeh, O.; Mohammadzadeh, O., A review on methods of determining onset of asphaltene precipitation. Journal of petroleum exploration and production technology 2019, 9 (2), 1375-1396.

53. Yarranton, H. W.; Fox, W. A.; Svrcek, W. Y., Effect of Resins on Asphaltene Self-Association and Solubility. Canadian journal of chemical engineering 2007, 85 (5), 635-642.

54. Asprino, O. J.; Elliott, J. A.; McCaffrey, W. C.; Gray, M. R., Fluid properties of asphaltenes at 310− 530 C. Energy & fuels 2005, 19 (5), 2026-2033.

55. Mullins, O. C.; Sabbah, H.; Eyssautier, J.; Pomerantz, A. E.; Barre, L.; Andrews, A. B.; Ruiz-Morales, Y.; Mostowfi, F.; McFarlane, R.; Goual, L.; Lepkowicz, R.; Cooper, T.; Orbulescu, J.; Leblanc, R. M.; Edwards, J.; Zare, R. N., Advances

in Asphaltene Science and the Yen-Mullins Model. Energy Fuels 2012, 26 (7), 3986-4003.

56. Poveda, J. C.; Molina, D. R., Average molecular parameters of heavy crude oils and their fractions using NMR spectroscopy. Journal of Petroleum Science and Engineering 2012, 84-85, 1-7.

57. Zhao, S.; Kotlyar, L. S.; Woods, J. R.; Sparks, B. D.; Chung, K. H., Molecular Nature of Athabasca Bitumen. Petroleum Science and Technology 2000, 18 (5-6), 587-606.

58. Ruiz-Morales, Y.; Mullins, O. C., Polycyclic Aromatic Hydrocarbons of Asphaltenes Analyzed by Molecular Orbital Calculations with Optical Spectroscopy. Energy & fuels 2007, 21 (1), 256-265.

59. Morgan, T. J.; Alvarez-Rodriguez, P.; George, A.; Herod, A. A.; Kandiyoti, R., Characterization of Maya Crude Oil Maltenes and Asphaltenes in Terms of Structural Parameters Calculated from Nuclear Magnetic Resonance (NMR) Spectroscopy and Laser Desorption−Mass Spectroscopy (LD−MS). Energy & Fuels 2010, 24 (7), 3977-3989.

60. Trejo, F.; Ancheyta, J.; Rana, M. S., Structural Characterization of Asphaltenes Obtained from Hydroprocessed Crude Oils by SEM and TEM. Energy & fuels 2009, 23 (1), 429-439.

61. Betancourt, S. S.; Ventura, G. T.; Pomerantz, A. E.; Viloria, O.; Dubost, F. X.; Zuo, J.; Monson, G.; Bustamante, D.; Purcell, J. M.; Nelson, R. K.; Rodgers, R. P.; Reddy, C. M.; Marshall, A. G.; Mullins, O. C., Nanoaggregates of Asphaltenes in a Reservoir Crude Oil and Reservoir Connectivity. Energy & fuels 2009, 23 (3), 1178-1188.

62. Ruiz-Morales, Y., Molecular Orbital Calculations and Optical Transitions of PAHs and Asphaltenes. Springer New York: New York, NY, pp 95-137.

63. Alemany, L. B.; Verma, M.; Billups, W. E.; Wellington, S. L.; Shammai, M., Solid- and Solution-State Nuclear Magnetic Resonance Analyses of Ecuadorian Asphaltenes: Quantitative Solid-State Aromaticity Determination Supporting the "Island" Structural Model. Aliphatic Structural Information from Solution-State 1H–13C Heteronuclear Single-Quantum Coherence Experiments. Energy & Fuels 2015, 29 (10), 6317-6329.

64. Calemma, V.; Iwanski, P.; Nali, M.; Scotti, R.; Montanari, L., Structural Characterization of Asphaltenes of Different Origins. Energy Fuels 1995, 9 (2), 225-30.

65. Castro Díaz, M.; Uguna, C. N.; Cheeseman, B.; Barker, J.; Snape, C. E., Investigation of the Fluid Behavior of Asphaltenes and Toluene Insolubles by High-Temperature Proton Nuclear Magnetic Resonance and Rheometry and Their Application to Visbreaking. Energy & Fuels 2016, 30 (3), 2012-2020.

66. Cyr, N.; McIntyre, D. D.; Toth, G.; Strausz, O. P., Hydrocarbon structural group analysis of Athabasca asphaltene and its GPC fractions by carbon-13 NMR. Fuel 1987, 66 (12), 1709-14.

67. Douda, J.; Alvarez, R.; Navarrete Bolanos, J., Characterization of Maya Asphaltene and Maltene by Means of Pyrolysis Application. Energy Fuels 2008, 22 (4), 2619-2628.

68. AlHumaidan, F. S.; Hauser, A.; Rana, M. S.; Lababidi, H. M. S., NMR Characterization of Asphaltene Derived from Residual Oils and Their Thermal Decomposition. Energy & Fuels 2017, 31 (4), 3812-3820.

69. Carvalho, V. V.; Vasconcelos, G. A.; Tose, L. V.; Santos, H.; Cardoso, F. M. R.; Fleming, F.; Romão, W.; Vaz, B. G., Revealing the chemical characterization of asphaltenes fractions produced by N-methylpyrrolidone using FTIR, molecular fluorescence, 1H NMR, and ESI(±)FT-ICR MS. Fuel 2017, 210, 514-526.

70. Gray, M. R.; Tykwinski, R. R.; Stryker, J. M.; Tan, X., Supramolecular assembly model for aggregation of petroleum asphaltenes. Energy & Fuels 2011, 25 (7), 3125-3134.

71. Alshareef, A. H.; Scherer, A.; Tan, X.; Azyat, K.; Stryker, J. M.; Tykwinski, R. R.; Gray, M. R., Formation of Archipelago Structures during Thermal Cracking Implicates a Chemical Mechanism for the Formation of Petroleum Asphaltenes. Energy & fuels 2011, 25 (5), 2130-2136.

72. Tatiana Montoya Blanca, L. A. N. N. N. C. A. F. F. B. C., Kinetics and mechanisms of the catalytic thermal cracking of asphaltenes adsorbed on supported nanoparticles. Petroleum science 2016, 13 (3), 561-571.

73. Chacón-Patiño, M. L.; Rowland, S. M.; Rodgers, R. P., Advances in Asphaltene Petroleomics. Part 3. Dominance of Island or Archipelago Structural Motif Is Sample Dependent. Energy & fuels 2018, 32 (9), 9106-9120.

74. Zaytseva, O. V.; Magomadov, E. E.; Kadiev, K. M.; Chernysheva, E. A.; Kapustin, V. M.; Khadzhiev, S. N., A study of structural transformations of asphaltene molecules during hydroconversion of vacuum residue at various temperatures in the presence of nanosized molybdenum disulfide particles. Petroleum Chemistry 2013, 53 (5), 309-315.

75. Sheu, E. Y.; De Tar, M. M.; Storm, D. A.; DeCanio, S. J., Aggregation and kinetics of asphaltenes in organic solvents. Fuel 1992, 71 (3), 299-302.

76. Mullins, O. C.; Rodgers, R. P.; Weinheber, P.; Klein, G. C.; Venkataramanan, L.; Andrews, A. B.; Marshall, A. G., Oil Reservoir Characterization via Crude Oil Analysis by Downhole Fluid Analysis in Oil Wells with Visible-Near-Infrared Spectroscopy and by Laboratory Analysis with Electrospray Ionization Fourier Transform Ion Cyclotron Resonance Mass Spectrometry. Energy Fuels 2006, 20 (6), 2448-2456.

77. Yen, T. F.; Erdman, J. G.; Saraceno, A. J., Investigation of the Nature of Free Radicals in Petroleum Asphaltenes and Related Substances by Electron Spin Resonance. Analytical chemistry (Washington) 1962, 34 (6), 694-700.

78. Schuler, B.; Meyer, G.; Peña, D.; Mullins, O. C.; Gross, L., Unraveling the Molecular Structures of Asphaltenes by Atomic Force Microscopy. Journal of the American Chemical Society 1900, 137 (31), 9870-9876.

79. Mullins, O. C., The Asphaltenes. Annual review of analytical chemistry (Palo Alto, Calif.) 2011, 4 (1), 393-418.

80. F. Trejo, J. A., *,† T. J. Morgan,‡ A. A. Herod,‡ and R. Kandiyoti‡, Characterization of Asphaltenes from Hydrotreated Products by SEC, LDMS, MALDI, NMR, and XRD. Energy & Fuels 2007, 21, 2121-2128.

81. Eskin, D.; Mohammadzadeh, O.; Akbarzadeh, K.; Taylor, S. D.; Ratulowski, J., Reservoir impairment by asphaltenes: A critical review. The Canadian Journal of Chemical Engineering 2016, 94 (6), 1202-1217.

82. Durand, E.; Clemancey, M.; Lancelin, J.-M.; Verstraete, J.; Espinat, D.; Quoineaud, A.-A., Effect of Chemical Composition on Asphaltenes Aggregation. Energy Fuels 2010, 24 (2), 1051-1062.

83. Dutta Majumdar, R.; Gerken, M.; Hazendonk, P., Solid-State 1H and 13C Nuclear Magnetic Resonance Spectroscopy of Athabasca Oil Sands Asphaltenes: Evidence for Interlocking π-Stacked Nanoaggregates with Intercalated Alkyl Side Chains. Energy Fuels 2015, 29 (5), 2790-2800.

84. Haji-Akbari, N.; Teeraphapkul, P.; Fogler, H. S., Effect of Asphaltene Concentration on the Aggregation and Precipitation Tendency of Asphaltenes. Energy & Fuels 2014, 28 (2), 909-919.

85. Gray, M. R.; Yarranton, H. W.; Chacon-Patino, M. L.; Rodgers, R. P.; Bouyssiere, B.; Giusti, P., Distributed properties of asphaltene nanoaggregates in crude oils: A review. Energy & Fuels 2021, 35 (22), 18078-18103.

86. Zheng, F.; Shi, Q.; Vallverdu, G.; Giusti, P.; Bouyssière, B., Fractionation and Characterization of Petroleum Asphaltene: Focus on Metalopetroleomics. Processes 2020, 8 (1504), 1504.

87. Mullins, O. C., Rebuttal to Strausz et al. Regarding Time-Resolved Fluorescence Depolarization of Asphaltenes. Energy & fuels 2009, 23 (5), 2845-2854.

88. Zeng, H.; Song, Y.-Q.; Johnson, D. L.; Mullins, O. C., Critical Nanoaggregate Concentration of Asphaltenes by Direct-Current (DC) Electrical Conductivity. Energy & fuels 2009, 23 (3), 1201-1208.

89. Jia, Z.; Xiao, L.; Wang, Z.; Liao, G.; Zhang, Y.; Liang, C., Molecular dynamics and composition of crude oil by low-field nuclear magnetic resonance. Magnetic resonance in chemistry 2016, 54 (8), 650-655.

90. Murgich, J.; Abanero, J. A.; Strausz, O. P., Molecular Recognition in Aggregates Formed by Asphaltene and Resin Molecules from the Athabasca Oil Sand. Energy Fuels 1999, 13 (2), 278-286.

91. Vorapalawut, N.; Nicot, B.; Louis-Joseph, A.; Korb, J.-P., Probing Dynamics and Interaction of Maltenes with Asphaltene Aggregates in Crude Oils by Multiscale NMR. Energy Fuels 2015, 29 (8), 4911-4920.

92. Wu, Q.; Seifert, D. J.; Pomerantz, A. E.; Mullins, O. C.; Zare, R. N., Constant Asphaltene Molecular and Nanoaggregate Mass in a Gravitationally Segregated Reservoir. Energy & Fuels 2014, 28 (5), 3010-3015.

93. Mostowfi, F.; Indo, K.; Mullins, O. C.; McFarlane, R., Asphaltene Nanoaggregates Studied by Centrifugation. Energy & fuels 2009, 23 (3), 1194-1200.

94. Andreatta, G.; Bostrom, N.; Mullins, O. C., High-Q Ultrasonic Determination of the Critical Nanoaggregate Concentration of Asphaltenes and the Critical Micelle Concentration of Standard Surfactants. Langmuir 2005, 21 (7), 2728-2736.

95. Freed, D. E.; Lisitza, N. V.; Sen, P. N.; Song, Y.-Q., Molecular Composition and Dynamics of Oils from Diffusion Measurements. Springer New York: New York, NY, pp 279-299.

96. Almusallam, A. S.; Shaaban, M.; Nettem, K.; Fahim, M. A., Delayed Aggregation of Asphaltenes in the Presence of Alcohols by Dynamic Light Scattering. Journal of Dispersion Science and Technology 2013, 34 (6), 809-817.

97. da Silva Oliveira, E. C.; Neto, Á. C.; Júnior, V. L.; de Castro, E. V. R.; de Menezes, S. M. C., Study of Brazilian asphaltene aggregation by Nuclear Magnetic Resonance spectroscopy. Fuel 2014, 117, 146-151.

98. Shutkova, S. A.; Dolomatov, M. Y., Study of a supramolecular structure of continental type petroleum asphaltenes. Journal of structural chemistry 2017, 58 (7), 1270-1274.

99. Janesko, B. G.; Brothers, E. N., Half-Pancake Bonding in Asphaltenes. Energy & Fuels 2021, 35 (19), 15657-15662.

100. Ok, S.; Mal, T. K., NMR spectroscopy analysis of asphaltenes. Energy & Fuels 2019, 33 (11), 10391-10414.

101. Mullins, O. C., The asphaltenes. Annual review of analytical chemistry 2011, 4 (1), 393.

102. Niyonsaba, E.; Manheim, J. M.; Yerabolu, R.; Kenttämaa, H. I., Recent advances in petroleum analysis by mass spectrometry. Analytical Chemistry 2018, 91 (1), 156-177.

103. Ryan, D. J.; Qian, K., Laser-Based Ionization: A Review on the Use of Matrix-Assisted Laser Desorption/Ionization and Laser Desorption/Ionization Mass Spectrometry in Petroleum Research. Energy & Fuels 2020, 34 (10), 11887-11896.

104. Pomerantz, A. E.; Wu, Q.; Mullins, O. C.; Zare, R. N., Laser-based mass spectrometric assessment of asphaltene molecular weight, molecular architecture, and nanoaggregate number. Energy & Fuels 2015, 29 (5), 2833-2842.

105. Zuo, P.; Qu, S.; Shen, W., Asphaltenes: Separations, structural analysis and applications. Journal of Energy Chemistry 2019, 34, 186-207.

106. Boduszynski, M. M., Composition of heavy petroleums. 1. Molecular weight, hydrogen deficiency, and heteroatom concentration as a function of atmospheric equivalent boiling point up to 1400. degree. F (760. degree. C). Energy & Fuels 1987, 1 (1), 2-11.

107. Koolen, H. H.; Gomes, A. F.; de Moura, L. G.; Marcano, F.; Cardoso, F. M.; Klitzke, C. F.; Wojcik, R.; Binkley, J.; Patrick, J. S.; Swarthout, R. F., Integrative mass spectrometry strategy for fingerprinting and tentative structural characterization of asphaltenes. Fuel 2018, 220, 717-724.

108. Pereira, T. M.; Vanini, G.; Tose, L. V.; Cardoso, F. M.; Fleming, F. P.; Rosa, P. T.; Thompson, C. J.; Castro, E. V.; Vaz, B. G.; Romao, W., FT-ICR MS analysis of asphaltenes: Asphaltenes go in, fullerenes come out. Fuel 2014, 131, 49-58.

109. Vukovic, J. P.; Novak, P.; Jednacak, T., NMR Spectroscopy as a Tool for Studying Asphaltene Composition. Croatica Chemica Acta 2019, 92 (3), 1G-1G.

110. Emsley, J. W.; Lindon, J. C., NMR spectroscopy using liquid crystal solvents. Elsevier: 2018.

111. Rakhmatullin, I. Z.; Efimov, S. V.; Klochkov, A. V.; Gnezdilov, O. I.; Varfolomeev, M. A.; Klochkov, V. V., NMR chemical shifts of carbon atoms and characteristic shift ranges in the oil sample. Petroleum Research 2022, 7 (2), 269-274.

112. I. Schwager, P. A. F., 2 J. T. Kwan,3 V. A. Weinberg, and T. F. Yen*, Characterization of the Microstructure and Macrostructure of Coal-Derived Asphaltenes by Nuclear Magnetic Resonance Spectrometry and X-ray Diffraction. Anal. Chem. 1983, 55, 42-45.

113. Shikhov, I.; Li, R.; Arns, C. H., Relaxation and relaxation exchange NMR to characterise asphaltene adsorption and wettability dynamics in siliceous systems. Fuel 2018, 220, 692-705.

114. Chamberlain, N. F., The practice of NMR spectroscopy: with spectra-structure correlations for hydrogen-1. Plenum Press: New York, 1974.

115. Bertini, I.; Turano, P.; Vila, A. J., Nuclear magnetic resonance of paramagnetic metalloproteins. Chemical reviews 1993, 93 (8), 2833-2932.

116. Andrews, A. B.; Edwards, J. C.; Pomerantz, A. E.; Mullins, O. C.; Nordlund, D.; Norinaga, K., Comparison of Coal-Derived and Petroleum Asphaltenes by 13C Nuclear Magnetic Resonance, DEPT, and XRS. Energy Fuels 2011, 25 (7), 3068-3076.

117. Friedel, R. A., Absorption Spectra and Magnetic Resonance Spectra of Asphaltene. The Journal of chemical physics 1959, 31 (1), 280-281.

118. Gardner, R. A.; Hardman, H. F.; Jones, A. L.; Williams, R. B., Characterization of Thermal Diffusion Fractions of Petrolenes from a Mid-Continent Asphalt. Journal of chemical and engineering data 1959, 4 (2), 155-159.

119. Brown, J.; Ladner, W., A study of the hydrogen distribution in coal-like materials by high-resolution nuclear magnetic resonance spectroscopy. 2. A comparison with infra-red measurement and the conversion to carbon structure. Fuel 1960, 39 (1), 87-96.

120. Brown, J., A Study of the Hydrogen Distribution in Coal-like Materials by High-resolution Nuclear Magnetic Resonance Spectroscopy I-The Measurement and Interpreatation of the Spectra. Fuel 1960, 39, 79-86.

121. Girdler, R. In Constitution of asphaltenes and related studies, Assoc Asphalt Paving Technol Proc, 1965.

122. Ramsey, J. W.; McDonald, F. R.; Petersen, J. C., Structural Study of Asphalts by Nuclear Magnetic Resonance. I&EC Product Research and Development 1967, 6 (4), 231-236.

123. Yen, T. F.; Wu, W. H.; Chilingar, G. V., A study of the structure of petroleum asphaltenes and related substances by infrared spectroscopy. Energy Sources 1984, 7 (3), 203-235.

124. Semple, K. M.; Cyr, N.; Fedorak, P. M.; Westlake, D. W., Characterization of asphaltenes from Cold Lake heavy oil: variations in chemical structure and composition with molecular size. Canadian journal of chemistry 1990, 68 (7), 1092-1099.

125. Ignasiak, T.; Kemp-Jones, A.; Strausz, O., The molecular structure of Athabasca asphaltene. Cleavage of the carbon-sulfur bonds by radical ion electron transfer reactions. The Journal of organic chemistry 1977, 42 (2), 312-320.

126. Dereppe, J.-M.; Moreaux, C.; Castex, H., Analysis of asphaltenes by carbon and proton nuclear magnetic resonance spectroscopy. Fuel 1978, 57 (7), 435-441.

127. Dereppe, J. M.; Moreaux, C.; Castex, H., Analysis of asphaltenes by carbon and proton nuclear magnetic resonance spectroscopy. Fuel 1978, 57 (7), 435-41.

128. Dickinson, E. M., Structural comparison of petroleum fractions using proton and 13C nmr spectroscopy. Fuel 1980, 59 (5), 290-294.

129. Sklenar, V.; Hajek, M.; Sebor, G.; Lang, I.; Suchanek, M.; Starcuk, Z., Analysis of coal asphaltenes by carbon-13 Fourier transform nuclear magnetic resonance spectrometry. Analytical Chemistry 1980, 52 (12), 1794-1797.

130. Cookson, D. J.; Smith, B. E., Determination of carbon C, CH, CH2 and CH3 group abundances in liquids derived from petroleum and coal using selected multiplet 13C NMR spectroscopy. Fuel 1983, 62 (1), 34-38.

131. Doddrell, D.; Pegg, D.; Bendall, M. R., Distortionless enhancement of NMR signals by polarization transfer. Journal of Magnetic Resonance (1969) 1982, 48 (2), 323-327.

132. Christopher, J.; Sarpal, A. S.; Kapur, G. S.; Krishna, A.; Tyagi, B. R.; Jain, M. C.; Jain, S. K.; Bhatnagar, A. K., Chemical structure of bitumen-derived asphaltenes by nuclear magnetic resonance spectroscopy and x-ray diffractometry. Fuel 1996, 75 (8), 999-1008.

133. Kapur, G. S.; Berger, S., Unambiguous Resolution of α-Methyl and α-Methylene Protons in 1H NMR Spectra of Heavy Petroleum Fractions. Energy & Fuels 2005, 19 (2), 508-511.

134. Masuda, K.; Okuma, O.; Nishizawa, T.; Kanaji, M.; Matsumura, T., High-temperature nmr analysis of aromatic units in asphaltenes and preasphaltenes derived from Victorian brown coal. Fuel 1996, 75 (3), 295-299.

135. Pekerar, S.; Lehmann, T.; Méndez, B.; Acevedo, S., Mobility of asphaltene samples studied by 13C NMR spectroscopy. Energy & fuels 1999, 13 (2), 305-308.

136. Sarpal, A. S.; Kapur, G. S.; Chopra, A.; Jain, S. K.; Srivastava, S. P.; Bhatnagar, A. K., Hydrocarbon characterization of hydrocracked base stocks by one- and two-dimensional n.m.r. spectroscopy. Fuel 1996, 75 (4), 483-490.

137. Sheremata, J. M.; Gray, M. R.; Dettman, H. D.; McCaffrey, W. C., Quantitative Molecular Representation and Sequential Optimization of Athabasca Asphaltenes. Energy Fuels 2004, 18 (5), 1377-1384.

138. Evdokimov, I. N.; Eliseev, N. Y.; Akhmetov, B. R., Initial stages of asphaltene aggregation in dilute crude oil solutions: studies of viscosity and NMR relaxation. Fuel 2003, 82 (7), 817-823.

139. Durand, E.; Clemancey, M.; Lancelin, J.-M.; Verstraete, J.; Espinat, D.; Quoineaud, A.-A., Aggregation states of asphaltenes: Evidence of two chemical behaviors by 1H diffusion-ordered spectroscopy nuclear magnetic resonance. The Journal of Physical Chemistry C 2009, 113 (36), 16266-16276.

140. Ostlund, J. A.; Lofroth, J. E.; Holmberg, K.; Nyden, M., Flocculation behavior of asphaltenes in solvent/nonsolvent systems. J Colloid Interface Sci 2002, 253 (1), 150-8.

141. Lindt, K.; Gizatullin, B.; Mattea, C.; Stapf, S., Non-Exponential 1H and 2H NMR Relaxation and Self-Diffusion in Asphaltene-Maltene Solutions. Molecules 2021, 26 (17), 5218.

142. Morgan, V. G.; Bastos, T. M.; Sad, C. M.; Leite, J. S.; Castro, E. R.; Barbosa, L. L., Application of low-field nuclear magnetic resonance to assess the onset of asphaltene precipitation in petroleum. Fuel 2020, 265, 116955.

143. Norinaga, K.; Wargardalam, V. J.; Takasugi, S.; Iino, M.; Matsukawa, S., Measurement of Self-Diffusion Coefficient of Asphaltene in Pyridine by Pulsed Field Gradient Spin− Echo 1H NMR. Energy & Fuels 2001, 15 (5), 1317-1318.

144. Opella, S.; Frey, M., Selection of nonprotonated carbon resonances in solid-state nuclear magnetic resonance. Journal of the American Chemical Society 1979, 101 (19), 5854-5856.

145. Weinberg, V.; Yen, T.; Gerstein, B.; Murphy, P., Characterization of pyrolyzed asphaltenes by diffuse reflectance-Fourier transform infrared and dipolar desphasing-solid state/sup 13/C nuclear magnetic resonance spectroscopy. Am. Chem. Soc., Div. Pet. Chem., Prepr.;(United States) 1981, 26 (CONF-810813-(Vol. 2)).

146. Murphy, P. D.; Gerstein, B.; Weinberg, V. L.; Yen, T., Determination of chemical functionality in asphaltenes by high-resolution solid-state carbon-13 nuclear magnetic resonance spectrometry. Analytical Chemistry 1982, 54 (3), 522-525.

147. Cyr, N.; McIntyre, D.; Toth, G.; Strausz, O., Hydrocarbon structural group analysis of Athabasca asphaltene and its gpc fractions by 13C nmr. Fuel 1987, 66 (12), 1709-1714.

148. Storm, D.; Edwards, J.; DeCanio, S.; Sheu, E. Y., Molecular representations of Ratawi and Alaska north slope asphaltenes based on liquid-and solid-state NMR. Energy & fuels 1994, 8 (3), 561-566.

149. Douda, J.; Alvarez, R.; Navarrete Bolaños, J., Characterization of Maya asphaltene and maltene by means of pyrolysis application. Energy & fuels 2008, 22 (4), 2619-2628.

150. Daaou, M.; Bendedouch, D.; Bouhadda, Y.; Vernex-Loset, L.; Modaressi, A.; Rogalski, M., Explaining the flocculation of Hassi Messaoud asphaltenes in terms of structural characteristics of monomers and aggregates. Energy & Fuels 2009, 23 (11), 5556-5563.

151. Bouhadda, Y.; Florian, P.; Bendedouch, D.; Fergoug, T.; Bormann, D., Determination of Algerian Hassi-Messaoud asphaltene aromaticity with different solid-state NMR sequences. Fuel 2010, 89 (2), 522-526.

152. Kolodziejski, W.; Klinowski, J., Kinetics of cross-polarization in solid-state NMR: a guide for chemists. Chemical Reviews 2002, 102 (3), 613-628.

153. Daaou, M.; Bendedouch, D.; Modarressi, A.; Rogalski, M., Properties of the polar fraction of Hassi-Messaoud asphaltenes. Energy & fuels 2012, 26 (9), 5672-5678.

154. Siskin, M.; Kelemen, S.; Eppig, C.; Brown, L.; Afeworki, M., Asphaltene molecular structure and chemical influences on the morphology of coke produced in delayed coking. Energy & Fuels 2006, 20 (3), 1227-1234.

155. Hauser, A.; Bahzad, D.; Stanislaus, A.; Behbahani, M., Thermogravimetric analysis studies on the thermal stability of asphaltenes: pyrolysis behavior of heavy oil asphaltenes. Energy & fuels 2008, 22 (1), 449-454.

156. Majumdar, R. D.; Montina, T.; Mullins, O.; Gerken, M.; Hazendonk, P., Insights into asphaltene aggregate structure using ultrafast MAS solid-state 1H NMR spectroscopy. *Fuel* **2017,** *193*, 359-368.

157. Djendara, A.; Bouhadda, Y.; Fergoug, T.; Djabeur, M.; Bellil, A., Characterisation of an algerian asphaltene by 1H and 13C CPMAS NMR, DEPT and ESI mass spectroscopy. *Egyptian Journal of Petroleum* **2021,** *30* (2), 17-22.

CHAPTER 2

NUCLEAR MAGNETIC RESONANCE SPECTROSCOPY

2.1. Overview

Nuclear magnetic resonance (NMR) spectroscopy is a widely applicable and versatile analytical technique that is used to study the structure and molecular dynamics of different classes of materials in the liquid, solution, and solid states. The first experiments with NMR were conducted in 1945 by Stanford University's Felix Bloch and Harvard University's Edward Purcell. [1,2]

For organic chemists, NMR spectroscopy is an important analytical tool which allows for the determination of not only the composition and structure of the molecule, but also the sample's properties, contents, and purity level. The most common type of NMR spectroscopy used by chemists is one-dimensional ^{1}H NMR spectroscopy.[3] For determining specific structural properties, a wide range of NMR techniques has been developed over time, including basic one-dimensional techniques and multidimensional correlation techniques.[4] NMR spectroscopy is widely used in physical and biological sciences as well.

In this thesis, the structure and aggregation behaviour of asphaltenes were studied using solution-state NMR spectroscopy methods. As an introduction to this chapter, some basic and general principles will be introduced followed by a description of the pulse-sequence techniques employed in these studies, as well as an overview of why they are useful for studying asphaltenes.

2.2. NMR Spectroscopy Fundamentals

2.2.1. Nuclear Magnetic Spin

NMR spectroscopy utilizes the magnetic properties of atomic nuclei, as most nuclei have a nuclear magnetic moment (μ). The atom's nucleus is made up of protons and neutrons. Neutrons have no charge and protons have a positive charge (+1). The number of protons and neutrons together make up the atomic mass number. Nuclei with odd numbers of neutrons and protons have a non-zero nuclear spin quantum number and a magnetic moment.

Nuclei with a non-zero spin have an intrinsic angular momentum $\vec{P}$ that is related to the spin quantum number *I* which is expressed by Eq. 2.1:

$$\vec{P} = \hbar\sqrt{I\,(I+1)} \qquad (2.1)$$

where $\hbar = \frac{h}{2\pi}$, h is Planck's constant, and *I* is the spin quantum number. The spin quantum number *I* can take on positive integer values (0, 1, 2…, n) or half-integer values (1/2, 3/2, …, n/2). Based on classical electromagnetism, the magnetic dipole moment ($\vec{\mu}$) of a nucleus arises because of rotation associated with the spin angular momentum ($\vec{P}$) of the nucleus which is expressed by Eq.2.2

$$\vec{\mu} = \gamma\vec{P} \qquad (2.2)$$

where γ is the magnetogyric ratio, which is specific for a certain nucleus. A spin angular momentum of the nucleus is projected along the z-axis (conventionally) giving the z-component of the magnetic moment μ_z according to Eq.2.3.

$$\mu_z = \gamma P_z \qquad (2.3)$$

where $P_z = \hbar m_{I,}$ in which m_I is the magnetic quantum number, and this number takes on $2I+1$ values from $-I$ to $+I$ in integer steps.

The energy of interaction between an applied magnetic field $\overrightarrow{B_0}$ and a magnetic moment $\vec{\mu}$ can be expressed as follows:

$$E = -\overrightarrow{\mu}.\overrightarrow{B_0} \tag{2.4}$$

Consider a magnetic field of magnitude $\overrightarrow{B_0}$ oriented along the z-axis, the energy is written as a function of the z-component of magnetization:

$$E = -\gamma P_z B_0 \tag{2.5}$$

In the absence of an applied magnetic field $\overrightarrow{B_0}$, the distribution of nuclear spins is random in directions, resulting in a zero net magnetization for the bulk system and degenerate energy levels. (Fig.2.1)

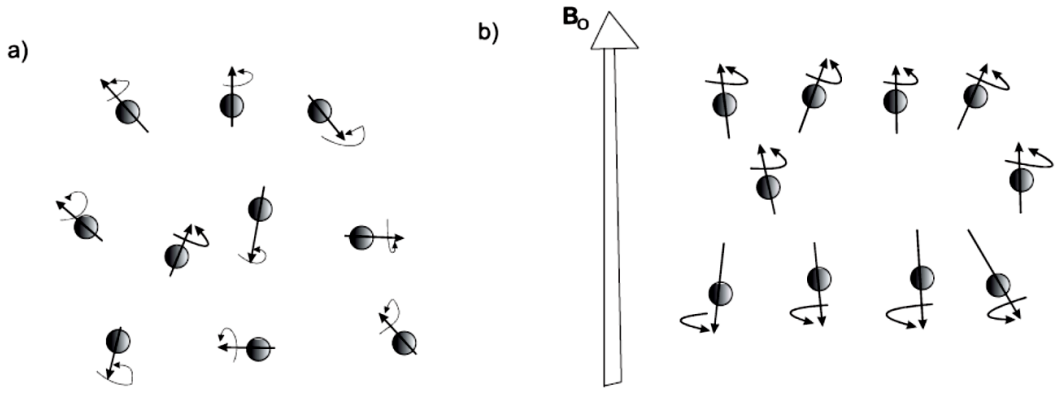

Figure 2.1. Distribution of spin magnetic moments in the a) absence and b) presence of an external magnetic field $\overrightarrow{B_0}$

But when a B_0 is applied, the nuclei align with or against it, and an energy transfer takes place between the ground state and the excited state. Two spin states are possible, one that is aligned with the magnetic field is called the α state ($m_I = +1/2$) which is the more stable state, and the other that is aligned in the direction opposite to the field is called the β state ($m_I = -1/2$) which is the less stable state. The Boltzmann distribution describes the population differences between the two spin states:

$$\frac{N_\beta}{N_\alpha} = e^{-\left(\frac{\Delta E}{kT}\right)} \tag{2.6}$$

where N_α and N_β are the numbers of nuclei in lower and upper energy states, ΔE is the energy difference between the states, temperature (T) in K and the Boltzmann constant ($k=1.3805 \times 10^{-23}$ J/K). At room temperature, $\Delta E \ll kT$, so the difference in the population of up and down states is very small and is typically on the order of ppm.

A torque is generated when the magnetic moment $\vec{\mu}$ interacts with the magnetic field $\overrightarrow{B_0}$ (Eq. 2.7):

$$\tau = \vec{\mu} \times \overrightarrow{B_0} \tag{2.7}$$

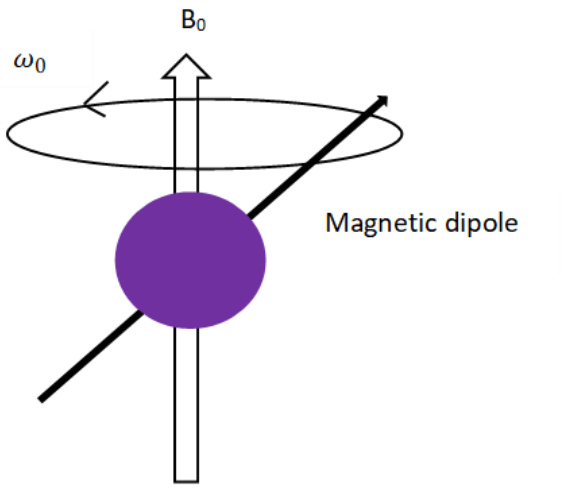

Figure 2.2. Nuclear magnetic moment precession with frequency ω_0 around an external magnetic field $\overrightarrow{B_0}$.

The torque changes the direction of the magnetic moment and causes the nucleus to precess around the field's axis, a process known as Larmor precession. The frequency of the precession is given by Eq. 2.8:

$$\omega_0 = -\gamma B_0 \qquad (2.8)$$

The frequency ω_0 is the resonance frequency in radians per second, also known as Larmor frequency. Therefore, the Larmor frequency is dependent on the local magnetic field strength, as well as the nature of the nucleus.

The frequency can also be expressed in cycles per second, or Hz. It is written as follows:

$$\omega_o = -\frac{\gamma B_O}{2\pi} \qquad (2.9)$$

2.2.2. Signal Generation, Relaxation, and NMR Experiment

The longitudinal magnetization M_z , i.e., the sum of all μ_z, at equilibrium does not change with time. However, the time dependence of the magnetization is needed to get a NMR signal. The longitudinal magnetization needs to be transferred to the transverse (xy) plane to get the time dependence. When a high radio frequency (r.f.) pulse resonating at the Larmor frequency is applied along either of the transverse axes, all the spins precess coherently, resulting in an overall transverse magnetization precessing at the Larmor frequency.

In the xy plane, a coil generates the radio frequency pulse. The oscillations in the magnetic field caused by the precession of the transverse magnetization $\overrightarrow{M_{x,y}}$ induce a current that can be observed using the same coil that applied the r.f. pulse, producing the NMR signal.

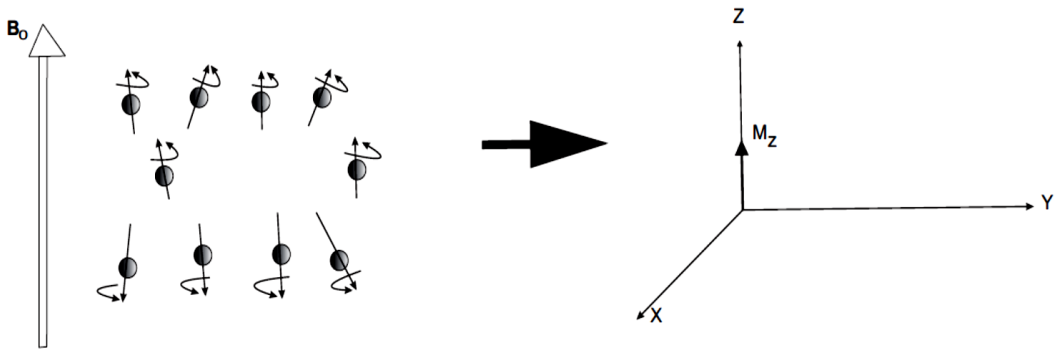

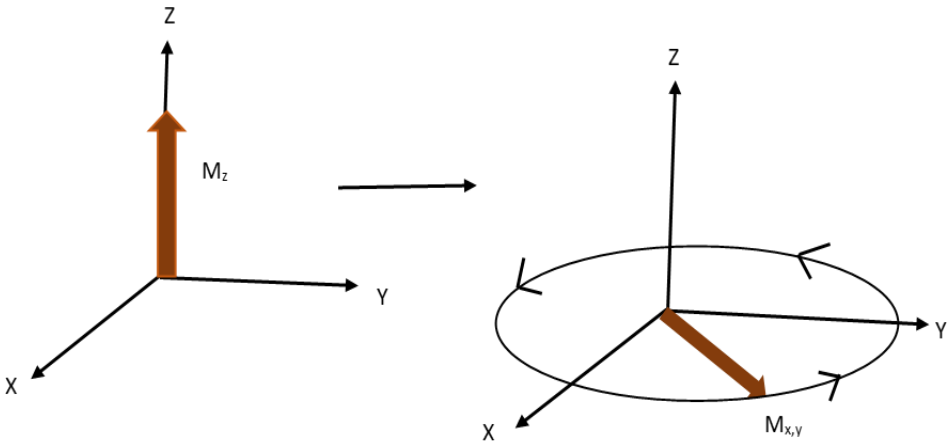

Figure 2.3. An r.f. pulse rotated longitudinal magnetization (M_z) to the transverse plane, and precession of the transverse magnetization $M_{x,y}$ at the Larmor frequency ω_0.

After the termination of the r.f. pulse, the transverse magnetization gradually returns to equilibrium over time via a process much like Brownian motion due to the influence of randomly fluctuating local fields, a phenomenon known as transverse-relaxation.

A diamagnetic sample outside of a magnetic field is not magnetized. When the sample is positioned inside a magnet, the induced magnetization will not appear instantly, but will appear over time determined by the spin-lattice relaxation time. In the Bloch theory of NMR, the relaxation time is simplified by assuming that equilibrium will be attained exponentially, treating its time constant as a parameter.[5]

This theory offers two relaxation processes for the induced magnetization to return to the equilibrium state: transverse relaxation is caused by the dephasing of the transverse component, which occurs at a rate determined by the time constant of T_2 (and rate, R_2); and longitudinal relaxation, where the longitudinal component is returned to its equilibrium value, which occurs at a rate determined by the time constant T_1 (or rate, R_1). Both

relaxation processes are time dependent. Transverse relaxation results in the loss of the bulk transverse magnetization due to the loss of phase coherence amongst the individual spins in the ensemble. Longitudinal relaxation returns the system to the equilibrium state predicated by the Boltzmann distribution.

It is important to know how long it takes for this spin alignment process to reach equilibrium. Bloch Equations are applied to answer this question. In the absence of a pulse, the rate of change of M_z is given by:

$$\frac{dM_z}{dt} = \frac{-(M_z - M_0)}{T_1} \tag{2.10}$$

Solving this differential equation by integration gives the M_z value at the time t,

$$M_z = M_0(1 - exp^{-t/T_1}) \tag{2.11}$$

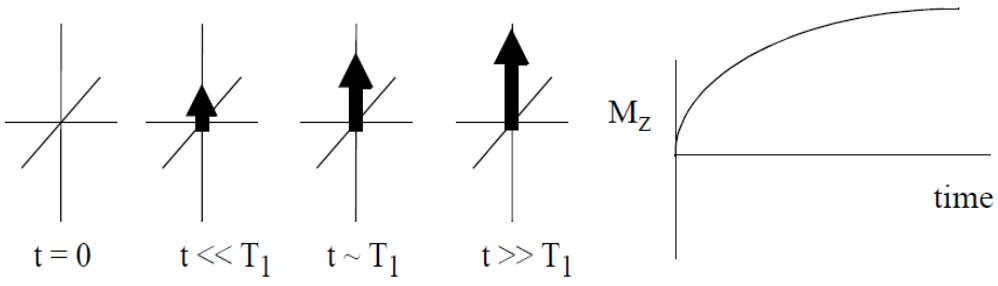

Figure 2.4 Under longitudinal T_1 relaxation, the longitudinal magnetization Mz returns to equilibrium.

M_0 is the equilibrium magnetization before applying the r.f. pulse. From these equations, T_1 is the time needed to (re)establish (e – 1)/ e of total magnetization along the z-axis. T_1 has a time scale that can range from milliseconds to days, depending on several factors including solvent viscosity, temperature, molecule size, mobility, and structure.

When a r.f. field is applied in the xy direction, the magnetic moment precesses about the field direction, resulting in phase-coherent spin. But if the r.f. field is turned off, coherence is lost due to randomly fluctuating local fields, which causes M_x and M_y to disperse as shown in Figure 2.5.

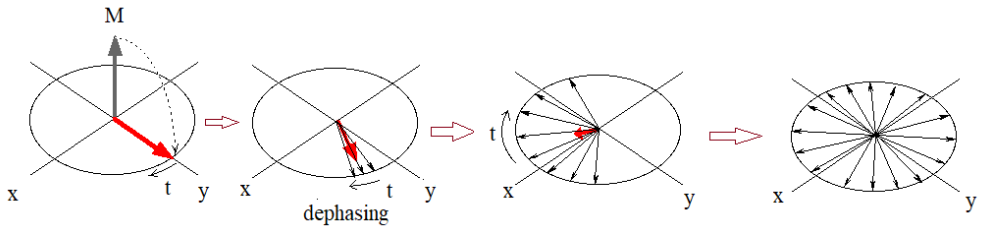

Figure 2.5. Coherence distribution at M_x and M_y plane, which leads to net transverse magnetization processing at the Larmor frequency.

The transverse relaxation time is the rate at which the transverse components in the x-y plane decay. Bloch equations determine M_x+M_y's dynamic on resonance:

$$\frac{dM_x}{dt} = -\frac{M_x}{T_2}, \frac{dM_y}{dt} = -\frac{M_y}{T_2} \tag{2.12}$$

$$M_{x,y} = M_0 exp\left(-\frac{t}{T_2}\right) \tag{2.13}$$

where T_2 is the transverse relaxation time constant, and M_0 is the transverse magnetization's initial intensity.

During longitudinal and transverse relaxation, random magnetic field fluctuations can cause spin flips (i.e., relaxation). Longitudinal relaxation generates a flow of energy out of the excited spin system and re-establish the Boltzmann distribution. Transverse relaxation eliminates phase coherence without affecting the overall energy of the system (i.e., without re-establishing the Boltzmann distribution).

The transverse magnetization rotates at the Larmor frequency, causing an oscillating magnetic field that causes a current in the signal detection coil. Considering relaxation effects, the rotating magnetization trajectory is a collapsing helix. Under T_2 relaxation, transverse magnetization decays in a spiral trajectory in the transverse plane (Fig. 2.6a). Under T_1 relaxation, longitudinal magnetization recovers, yielding the helical trajectory. The NMR signal is produced by the induced current generated by this oscillation, which is known as the free induction decay or FID.

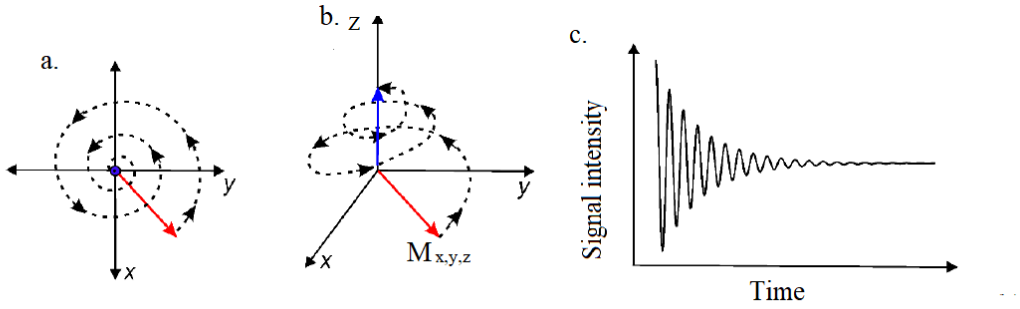

Figure 2.6. a) The spiral trajectory of the transverse magnetization under T_2 relaxation; b) the overall helical trajectory of the longitudinal and transverse magnetization; c) The FID signal.

The FID can be described by Eq. 2.14:

$$S_t = S_0 exp(i\omega_0 t) exp\left(-\frac{t}{T_2}\right) \quad (2.14)$$

where S_0 is the initial intensity and S_t is the signal intensity at time t. The signal intensity is measured as a time function, which is then transformed to the frequency domain using Fourier transform (FT), generating the NMR spectrum. The NMR spectrum will be a plot of signal intensity vs. frequency with a peak centered at the Larmor frequency (ω_0) and a half-line width determined by the $1/\pi T_2$.

$$\Delta\upsilon_{\frac{1}{2}} = \frac{1}{\pi T_2} \tag{2.15}$$

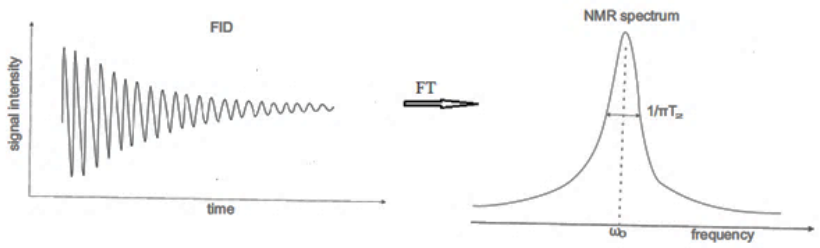

Figure 2.7. The FID is digitized, and the NMR spectrum is then generated using the Fourier Transform. $1/\pi T_2$ gives the full width at half height.

A pulse sequence diagram is used to represent the NMR experiment, such as pulses and delays. Figure 2.8 represents a very simple NMR pulse sequence.

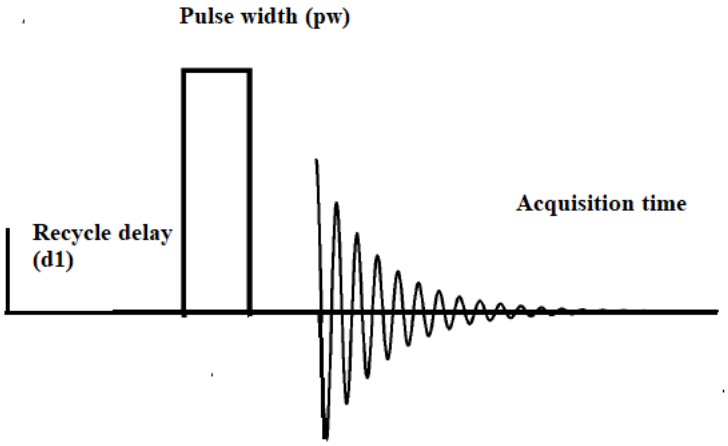

Figure 2.8. A basic 1D NMR pulse sequence diagram.

It consists of an initial pre-scan delay, also known as relaxation delay or recycle delay, followed by an excitation r.f. pulse, the duration of which determines the angle at which it rotates the longitudinal magnetization, and ending with the acquisition time.

2.2.3. Nuclear Shielding, Chemical Shift and *J* Coupling

The power of NMR spectroscopy originates from the combination of nuclear shielding and coupling, making it possible to identify individual spin environments and how they relate to each other proximally. An atom consists of a nucleus and negatively charged electrons that surround the nucleus. The electron densities surrounding the nuclei, such as protons, vary depending on the chemical environment. When a molecule is exposed to a uniform external magnetic field, the valence electrons surrounding the protons are induced to circulate, resulting in the generation of a secondary magnetic field, known as the induced magnetic field. The movement of electrons (especially π electrons) around neighboring nuclei generates a field that can oppose or enhance the applied field at that proton. The proton is shielded when the induced field opposes the applied field. On the other hand, the proton is said to be deshielded if the induced field enhances the applied field. As a result, the various protons in a molecule do not have the same frequency of resonance. Historically, it is said that shielding moves the signal upfield, while deshielding moves it downfield. The difference in the signal position is called the chemical shift and is defined in parts per million (ppm) by the reference frequency, as shown in the equation.

$$\delta = \frac{\omega_o - \omega_{ref}}{\omega_{ref}} \qquad (2.16)$$

where ω_o is the Larmor frequency of the sample and ω_{ref} is the Larmor frequency of the reference compound.

The effective local magnetic field is related to the applied external magnetic field by the following relationship.

$$\vec{B}_{ind.} = \hat{\sigma}\overrightarrow{B_0} \tag{2.17}$$

where $\hat{\sigma}$ is called the chemical shielding tensor. The chemical shielding tensor provides the relationship between the induced field and the molecule's orientation with respect to $\overrightarrow{B_0}$. Mathematically, shielding is express as a 3×3 matrix given by:

$$\hat{\sigma} = \begin{pmatrix} \sigma_{xx} & \sigma_{xy} & \sigma_{xz} \\ \sigma_{yx} & \sigma_{yy} & \sigma_{yz} \\ \sigma_{zx} & \sigma_{zy} & \sigma_{zz} \end{pmatrix} \tag{2.18}$$

The chemical shift can also be represented as a tensor in matrix form. Choosing a coordinate system with B_0 pointing in its z direction,

$$\delta = \begin{pmatrix} \delta_{xx} & \delta_{xy} & \delta_{xz} \\ \delta_{yx} & \delta_{yy} & \delta_{yz} \\ \delta_{zx} & \delta_{zy} & \delta_{zz} \end{pmatrix} \tag{2.19}$$

This tensor representation is in the laboratory (LAB) frame, but it is often converted to its own frame of reference, known as the Principal Axes System (PAS), for easier manipulation. In the PAS method, the tensor is a 3×3 diagonal matrix given by:

$$\delta = \begin{pmatrix} \delta_{xx} & 0 & 0 \\ 0 & \delta_{yy} & 0 \\ 0 & 0 & \delta_{zz} \end{pmatrix} \tag{2.20}$$

when the B_0 field is parallel to x, y, z of the PAS.

In isotropic liquids, the result is an averaging of all three main components of the PAS frame and is given by:

$$\delta_{iso} = \frac{1}{3}\left(\delta_{xx} + \delta_{yy} + \delta_{zz}\right) \quad (2.21)$$

This is applicable for solution-state NMR spectroscopy, where fast reorientational molecular motion averages the principal components and make them equal. But this equation is not applicable for solid-state NMR spectroscopy because of limited reorientational motion in solids.

Different types of electronic environments are responsible for different chemical shifts among protons in a molecule. The following factors contribute to a proton's shielding or deshielding in a magnetic field: local diamagnetic effect, diamagnetic and paramagnetic effects due to neighbouring atoms or groups of atoms, effects from interatomic ring current.

The diamagnetic shielding effect is due to the circulation of valence electrons or π electrons in the system under an external field, which produces a local magnetic field. The new induced field is opposing the external magnetic field B_0. This means that the higher the electron density, the stronger the shielding effect. Except for protons, this effect is negligible in other nuclei.

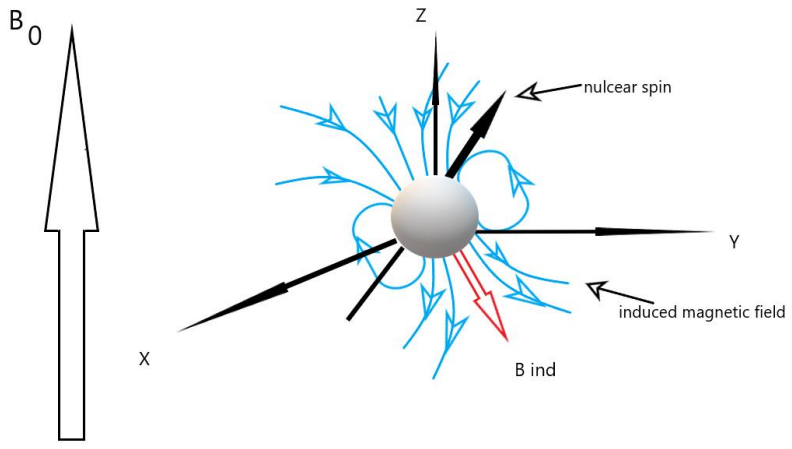

Figure 2.9. In the presence of an external magnetic field $\overrightarrow{B_0}$, an induced magnetic field is produced by diamagnetic current induced by circulating electrons around the nucleus.

The electronic environment of the nucleus of interest and thus the neighbouring groups, influence the chemical shift change. When the neighbouring groups net effect is to reduce electron density, the induced field is decreased, resulting in deshielding. Deshielding allows the nuclei to be exposed to a larger fraction of the external field, increasing the resonance frequency.

Accordingly, the ring-current effect is most often seen in aromatic ring systems with π electrons, which causes a deshielding effect in proton resonances. When an external magnetic field B_0 is applied to benzene, where the π electrons move freely across the ring, the circulating π electrons generate their own local field in aromatic rings, creating shielding and deshielding zones for surrounding nuclei depending on their position relative to the ring. This is called ring-current effect, illustrated in Figure 2.10.

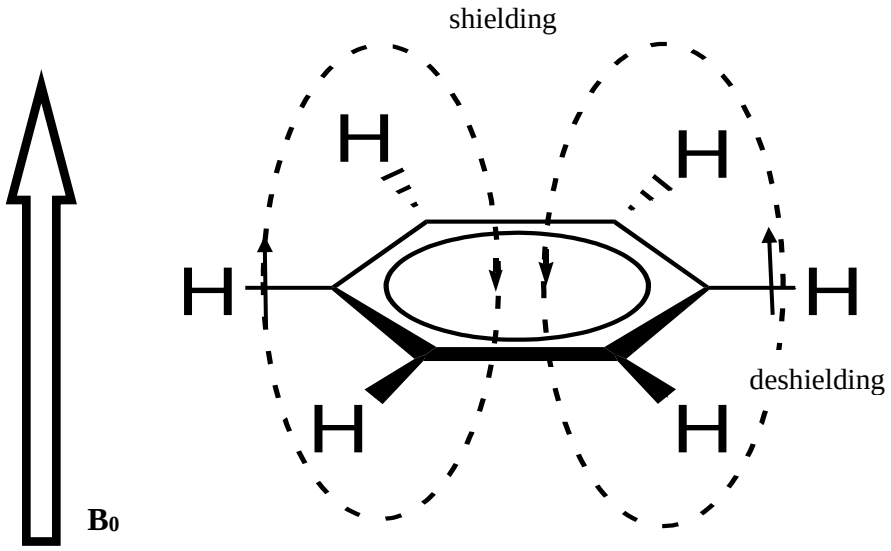

Figure 2.10. The ring current effect in benzene rings.

The external magnetic field generates a local field that acts along the external field on the periphery of the rings, as well as against it above and below the plane of the ring. As a result, any nuclei on the ring's periphery, such as aromatic protons or any other substituent, will be introduced to an effective field equivalent to the total of the external and induced fields, resulting in deshielding, i.e., a larger chemical shift. On the other hand, nuclei above or below the planes of the ring will have a reduced effective field or will be shielded, reducing their chemical shift.

In addition to chemical shielding, nuclear spins are influenced by the interaction between the magnetic moments of nearby mediated by the surrounding electron density. This interaction is known as scalar spin-spin coupling or *J*-coupling giving rise to splitting in the NMR lines. The number of neighbouring nuclei determines the multiplicity of the splitting pattern arising from *J*-couplings, and the magnitude is determined by their relative orientation.

Two types of coupling interactions occur between nuclei: direct dipolar coupling and indirect scalar coupling. The direct dipolar coupling interactions depends on the orientation of the internuclear vector with respect to the static field. Under normal isotropic motion this interaction averages to zero in solution. In contrast, the dipole-dipole interaction can be observed in liquid crystal solvents and in the solid state.

During scalar coupling the nuclear dipole polarization polarizes nearby electrons. This polarization is transmitted throughout the electron density of the molecule via the σ MO network. The electron polarization interacts with nuclear moments throughout the molecule and as the relative orientation of the electron density remains unchanged with respect to the nuclei this interaction does not vanish under isotropic averaging.

The coupling constant is often written as ${}^{n}J_{AB}$, with n indicating the number of intervening bonds and A and B indicating the two coupled spins. The term "multiplet" refers to a resonance line that has been split due to *J*-coupling. For example, in the ^{1}H NMR spectrum of an ethyl group (-CH_2-CH_3) the -CH_3 signal is split into a triplet by the 3-bond ^{1}H-^{1}H homonuclear *J*-coupling (${}^{3}J_{HH}$) to the –CH_2 group protons, while the –CH_2 signal is split into a quartet by the same interaction (n+1 rule).

2.2.4. Relaxation and Molecular Motion

Relaxation dispersion is a consequence of the difference in which T_1 and T_2 depend on molecular motion, and thus it can be an important source of information in studying factors that influence affect molecular motion. Transverse and longitudinal relaxation of spin-½ nuclei can take place via nuclear dipole-dipole or chemical shift anisotropy (CSA) mechanisms. The dipolar mechanism is the dominant relaxation mechanism for protons in diamagnetic systems, owing to their high natural abundance and strong magnetic dipole moments. The CSA mechanism contributed negligibly. Consequently, only the dipole-dipole mechanism needs to be considered ^{1}H. The relaxation takes place under the influence of the magnetic field produced by a nearby nucleus, which modulates in time rapidly due to molecular reorientational motion.

As a result of molecular motion, the local field experienced by a nucleus is time-dependent **f**(t). The fluctuations are essentially random and thus average is zero over long time periods. Therefore, its magnitude is usually measured by its mean square value, defined by Eq 2.22

$$\langle f^2(t) \rangle \neq 0 \qquad (2.22)$$

An autocorrelation function, G(τ), is used to define the time dependency of **f**(t), also known as the rate at which the local field fluctuates over time. The formula for this function is as follows:

$$G(\tau) = \langle f(t+\tau)\, f(t)\rangle \approx \langle f^2(t)\rangle \exp\left(-\frac{|\tau|}{\tau_c}\right) \quad (2.23)$$

A correlation between the same function at different times is called an autocorrelation function. For small τ the field does not have much time to move so G(τ) is large. As τ increases the field will have reoriented significantly and thus does not have much overlap with its original vector, hence G(τ) decays over time eventually converging to zero. The decay time constant τ_c is called a correlation time and is defined as the time taken for a molecule to rotate by one radiant.

For small molecules (which are rapidly tumbling), the fluctuations are fast, so τ_c is short, and for large molecules (which are more slowly tumbling), the fluctuations are slow, so τ_c is longer.

In the theory of NMR relaxation, the spectral density *J*(ω) plays a significant role. Spectral density functions are Fourier transforms of the time-correlation functions.

$$J(\omega) = 2\int_0^\infty G(\tau) exp\{-i\omega\tau\} d\tau \quad (2.24)$$

Changing the perspective from time dependence to frequency dependence, the Fourier Transformation of the correlation function is used and obtained a Lorentzian spectral density.

$$\exp\left(-\frac{|\tau|}{\tau_c}\right) \overset{FT}{\rightarrow} \frac{2\tau_c}{(1+\omega^2\tau_c^2)} = J(\omega) \quad (2.25)$$

The spectral density gives information about the intensity or power of fluctuations at given frequencies.

A fast-fluctuating fields will have a short correlation time, and the spectral density will be broad, as is represented in Figure 2.11.

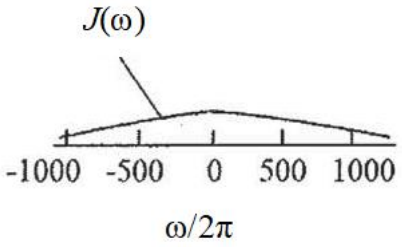

Figure 2.11. Spectra density of a rapid fluctuating field

Conversely, when a magnetic field undergoes slow fluctuations, the correlation time becomes long, resulting in a narrow spectral density, as illustrated in Figure 2.12.

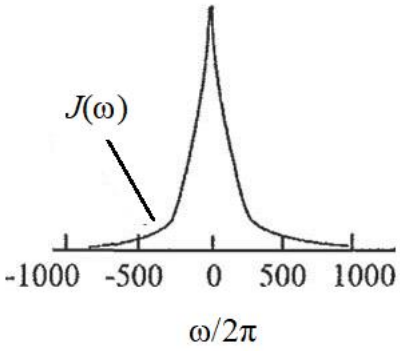

Figure 2.12. Spectral density of a slowly fluctuating field

The fast motion regime occurs when $\omega_0\tau_c << 1$. In this regime, it is presumed that $1+\omega_0^2\tau_c^2 \approx 1$ and therefore the spectral density is not dependent of the Larmor frequency:

$$J(\omega_0) = 2\tau_c \tag{2.24}$$

The slow-motion limit is defined as when $\omega_0\tau_c >> 1$. Under the condition $1+\omega_0^2\tau_c^2 \approx \omega_0^2\tau_c^2$ and since $J(0) = 2\tau_c$ the spectral density in this regime is:

$$J(\omega_0) = \frac{J(0)}{\omega_0^2\tau_c^2} \tag{2.25}$$

The effect of molecular motion on relaxation depends upon spectral density and this relation comes from transitions between all four energy levels of a two-spin system.

Transition Probabilities:

A dipolar-coupled two-spin system has 4 energy levels. The dipolar interaction between the two spins can cause relaxation-induced transitions between any of these energy levels. As illustrated in Figure 2.13, there are six possible transitions categorized as single-quantum, double-quantum, and zero-quantum transitions, each with different probabilities: W_1, W_2, and W_0, respectively. The W_2 transition involves simultaneous flipping of two aligned spins, W_0 is similar but with anti-parallel spins, and W_1 involves the flipping of only one spin.

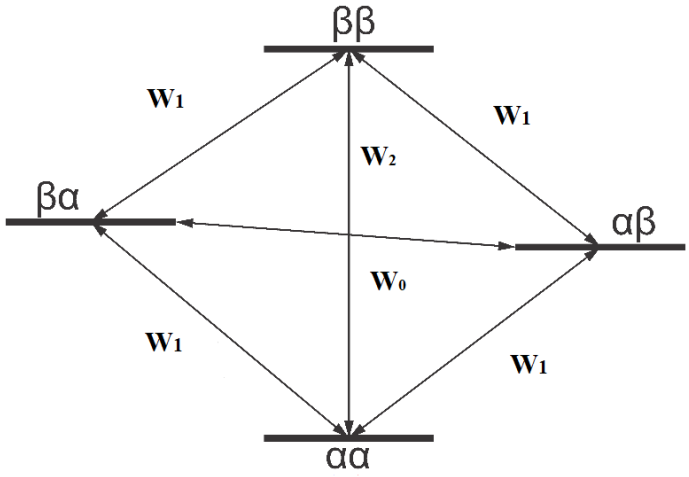

Figure 2.13. The six possible transitions in a two-spin system: four single-quantum transition, with rate constant W_1, one double-quantum transition, with rate constant W_2 and one zero-quantum transition, with rate constant W_0. The spins in higher energy states are aligned against the B_0 magnetic field.

The probability of a single-quantum transition for spin j in a dipolar-coupled two-spin system is expressed by Equation 2.26.[6]

$$W_1 = \frac{3}{20} b^2 J(\omega_0) \tag{2.26}$$

where $J(\omega_0)$ is the spectral density and b is the dipolar coupling constant [6] defined by:

$$b = -\frac{\mu_0}{4\pi} \frac{\gamma_1 \gamma_2 h}{r^3} \tag{2.27}$$

where μ_0 is a physical constant, $\gamma_1 \, and \, \gamma_2$ are spin gyromagnetic ratios, and r is the internuclear distance.

The double-quantum transition probability is given by Eq.2.28.[6]

$$W_2 = \frac{3}{5} b^2 J(2\omega_0) \tag{2.28}$$

The spectral density of the dipolar coupling at twice the Larmor frequency is denoted by $J(2\omega_0)$.

The zero-quantum transition probability is given by Eq.2.29.[6]

$$W_0 = \frac{1}{10} b^2 J(0) \tag{2.29}$$

The spectral density of the dipolar coupling at a frequency of zero is represented by $J(0)$. For homonuclear spin systems, the dipolar relaxation rates ($1/T_1$ and $1/T_2$) are given by Eq.2.30 and 2.31.[6]

$$\frac{1}{T_1} = \frac{3}{10} b^2 \{J(\omega_0) + 4J(2\omega_0)\} \tag{2.30}$$

$$\frac{1}{T_2} = \frac{3}{20} b^2 \{3J(0) + 5J(\omega_0) + 2J(2\omega_0)\} \tag{2.31}$$

Since the spectral density is a function of the correlation time τ_c. Accordingly, T_1/T_2 can be expressed as:

$$\frac{T_1}{T_2} = \frac{1}{2} \frac{\left[10+37\omega^2\tau_c^2+12\omega^4\tau_c^4\right]}{\left[5+8\omega^2\tau_c^2\right]} \tag{2.32}$$

The longitudinal relaxation time T_1 is dependent on correlation time τ_c.[7] Correlation times are inversely proportional to the rate of reorientational motion. Small molecules that move quickly have very short correlation times and corresponding long T_1. For large molecules that move slowly, τ_c is long and T_1 is short, T_1 goes down until it reaches ($\tau_c=1/\omega_0$), at that point T_1 increases slowly with τ_c, as shown in the curve in Fig. 2.14.

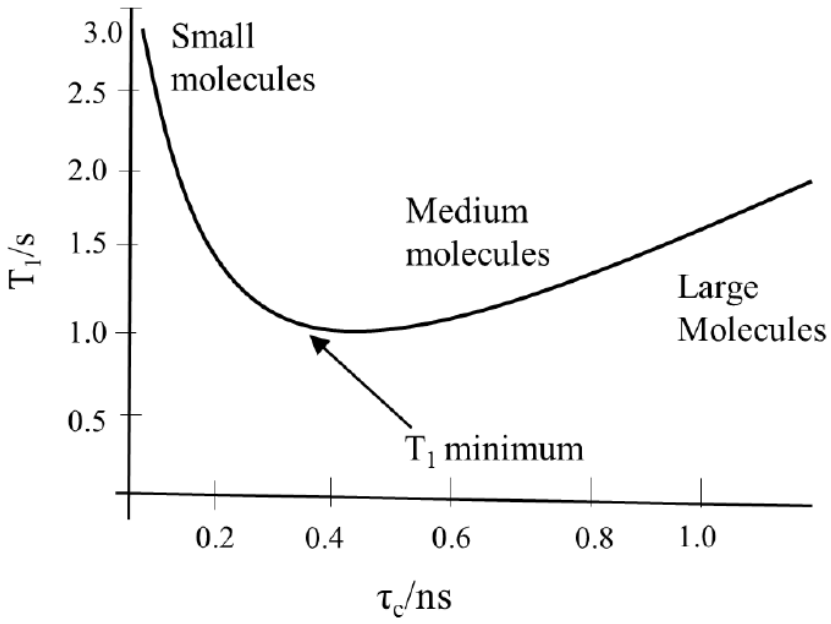

Figure 2.14. Longitudinal relaxation time constant in relation to correlation time.

This curve shows that at room temperature, small or gaseous molecules have a short correlation time, followed by a liquid with no viscosity. The correlation times are longer when the molecule is bigger or when it is in a viscous liquid.

The longitudinal relaxation times are also affected by the temperature.[7] This is because the random fluctuations start around the molecule, and correlation times also depend on temperature. Increasing the temperature of the sample causes the motion to speed up, which results in a short τ_c. The effect of the T_1 relaxation time on temperature depends on where τ_c is. Therefore, when a sample has a long τ_c, heating the sample results in a decrease in T_1. When a sample has a short τ_c , increasing the sample's temperature results in a rise in T_1, as seen in Fig. 2.15.

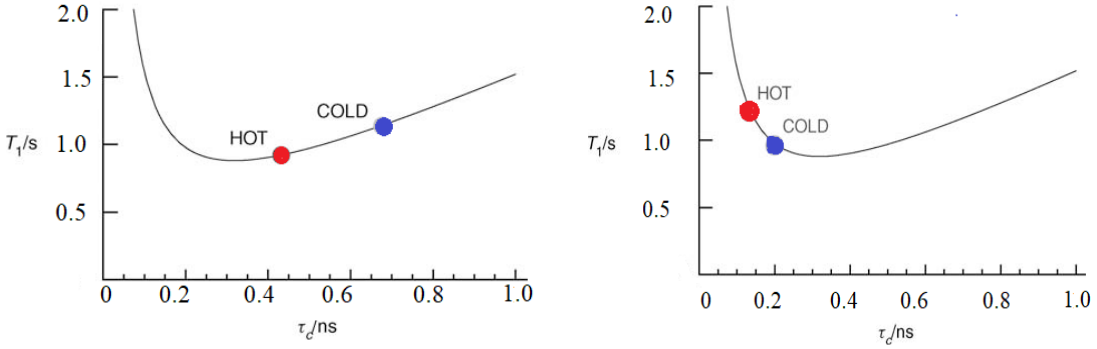

Figure 2.15. (a) Long correlation times, elevating the sample temperature reduces T_1 (b) Short correlation times, increasing the sample temperature leads to higher T_1.

The relaxation times T_1 and T_2 are plotted as a function of correlation time in Fig. 2.16.

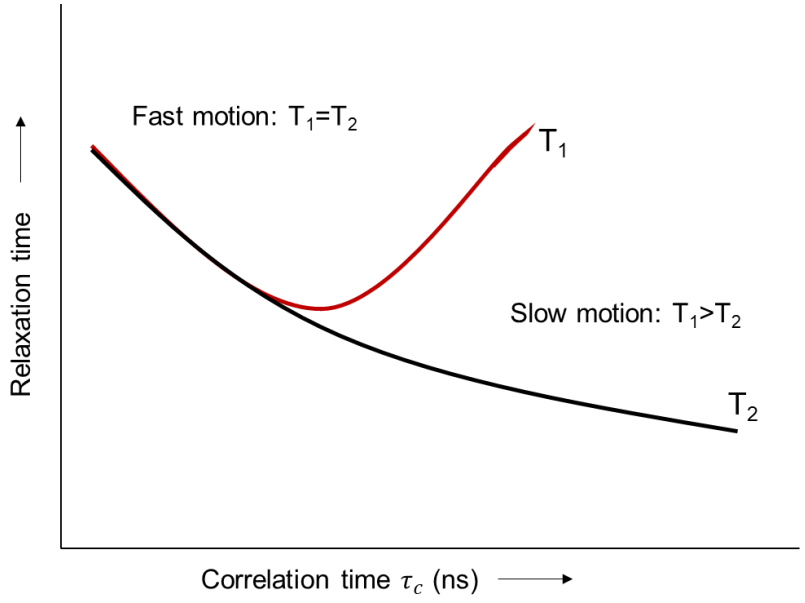

Figure 2.16. Relaxation times plotted against correlation time τ_c. Short τ_c values represent rapid molecular motion while longer values indicate slower motion.

The correlation time represents local magnetic field fluctuation, which depends on molecular motion. For small molecules, the molecular motion is fast enough and the frequency of reorientational motion ($1/\tau_c$) exceeds the Larmor frequency, such that $\omega << 1/\tau_c$. Conversely, for rigid, slow-tumbling molecules, the rate of reorientational motion is much slower than ω where $\omega >> 1/\tau_c$. In the fast-motion regime, T_1 and T_2 are similar, resulting in minimal relaxation dispersion where the ratio gradually decreases with increasing τ_c; however, they separate as they enter the slow-motion system, where T_1 continuously increases while T_2 decreases. Overall, the T_1/T_2 ratios increase with increasing τ_c and increased relaxation dispersion is observed.

For studies of asphaltenes, relaxation (T_1 and T_2) measurements can give information about the mobility of asphaltene molecules in solution and both are required to determine the motional timescale.

The rotational correlation time can be related to measurable variables through the hydrodynamic radius, r.

$$\tau_c = \left[\frac{4\pi\eta}{3kT}\right] r^3 \tag{2.33}$$

Where η is the viscosity, k is the Boltzmann constant, and T is the absolute temperature. Thus, it is evident that the measurement of T_1 and T_2 relaxation dispersions, which determine τ_c, can yield insight into molecular sizes.

2.3. Selected NMR Spectroscopic Experiments

2.3.1 One dimensional ^{1}H NMR Spectroscopy

Proton nuclear magnetic resonance (^{1}H NMR) is a spectroscopic technique that is commonly used for structural analysis of chemicals and compounds. This method has been used to characterize crude oil and related products. Usually, it is a fast and simple experiment that can be completed in a short amount of time and only requires a basic understanding of NMR methodology on the part of the users. A ^{1}H NMR spectrum provides information on the different types of ^{1}H presence in the structure that resonate at specific chemical shifts over a narrow chemical shift range, usually 0-20 ppm. Splitting patterns affected by scalar *J*-coupling between the ^{1}H nuclei (J_{HH}) can also be seen in ^{1}H NMR spectra, which can help with nuclei connectivity and signal assignment. In addition, if the experimental settings (long recycle delay) are set correctly, ^{1}H NMR signals are proportional to the sample's hydrogen nuclei. Chemical shifts and coupling show which functional groups are present and how they are connected to one another. Large molecules that are present in asphaltenes have a vast range of structural variations. They have different resonance frequencies and multiple chemically inequivalent protons in different chemical environments. The ^{1}H NMR signals are extremely crowded with many overlapping signals, leading to heterogeneous broadening and *J*-coupling information is lost in these ^{1}H NMR spectra, making spectral analysis difficult. In these cases, spectral assignments must be made using deconvolution analysis instead of integration. One disadvantage of ^{1}H NMR spectroscopy is that it cannot provide information about the presence of carbons without attached protons (quaternary carbons). These carbons can only be detected using ^{13}C NMR spectroscopy.

2.3.2. One dimensional ^{13}C NMR Spectroscopy

The ^{13}C NMR spectroscopy method is used to characterise carbon-containing molecules. The ^{13}C NMR experiment is much less sensitive than ^{1}H because the spin-active nucleus is approximately 1% abundant and the remaining 99% are inactive because it has a spin of zero. A ^{1}H NMR spectrum can be acquired in around 3 to 5 minutes with a good signal-to-noise ratio; ^{13}C NMR spectra normally take a couple of hours (or overnight) and have a much lower signal-to-noise ratio. In contrast to ^{1}H NMR experiments, obtaining high-quality ^{13}C NMR spectra with a suitable signal-to-noise ratio requires collecting more scans or preparing a highly concentrated sample.

As a result of low natural abundance of ^{13}C, splitting due to *J*-coupling between carbon nuclei (J_{CC}) is rarely observed. This is because the chance of two ^{13}C nuclei being next to each other is very small. Furthermore, it lengthens the T_1 relaxation time of carbon, requiring long recycling times. However, unless the ^{1}H spins are decoupled, heteronuclear *J*-coupling between ^{1}H and ^{13}C (J_{CH}) can be observed, which can complicate the spectrum. ^{13}C NMR gives more information about the backbone of molecules, rather than about the periphery. Since the chemical shift range for most organic compounds is 200 ppm for ^{13}C NMR compared to 10–15 ppm for ^{1}H, peaks overlap less in ^{13}C NMR spectra. The sensitivity of ^{13}C NMR must be increased to obtain a qualitative assignment, which can be performed using a polarization transfer pulse sequence (INEPT and DEPT).

Polarization is often transferred from ^{1}H to ^{13}C in the Insensitive Nuclei Enhancement by Polarization Transfer (INEPT) experiment, resulting in an increase in the intensity of the ^{13}C signal. In INEPT, scalar coupling between sensitive nuclei (^{1}H) and insensitive nuclei (^{13}C) is mainly used. In comparison to the INEPT experiment, another experiment known

as Distortionless Enhancement by Polarization Transfer (DEPT) can be used to increase ^{13}C NMR sensitivity. This method utilizes the fact that different CH function behave differently in an experiment. DEPT is used to differentiate between three types of groups: CH_3, CH_2, and CH. In each of the three experiments, the proton pulse is set at 45°, 90°, or 135°. The number of protons bound to a carbon atom determines the different pulses. In the case of a 45° pulse (DEPT-45), all carbons with directly attached proton(s) appear. At 90°(DEPT-90), only signals from CH groups are detected, while at 135°(DEPT-135), signals from CH and CH_3 carbons with opposite phases to those of CH_2 groups. Running a complete set of DEPT experiments allows for complete group assignment.

2.3.3. T_1 and T_2 Relaxation Experiments

Relaxation experiments in NMR spectroscopy are one of the most important and valuable used methods to obtain useful information about the dynamics of the molecules.

T_1 relaxation:

T_1 relaxation, also called longitudinal relaxation, is the process by which the net longitudinal component of the magnetization returns to equilibrium over time and energy is transferred from the spin system to it immediate surroundings, referred to as the lattice.

In the experiment used to determine the T_1 constant known as the inversion recovery method, first an inversion pulse (180°) is applied that rotates the magnetization M_z into the negative z-axis, which is followed by a delay (τ) during which the magnetization is allowed to relax for a fixed time period towards the positive z-axis. Finally, a 90° observation pulse is applied that flips the longitudinal magnetization to the transverse(xy)

plane, and subsequently the signal is recorded, Fig. 2.17**.** This experiment is repeated for a series of fixed delay periods.

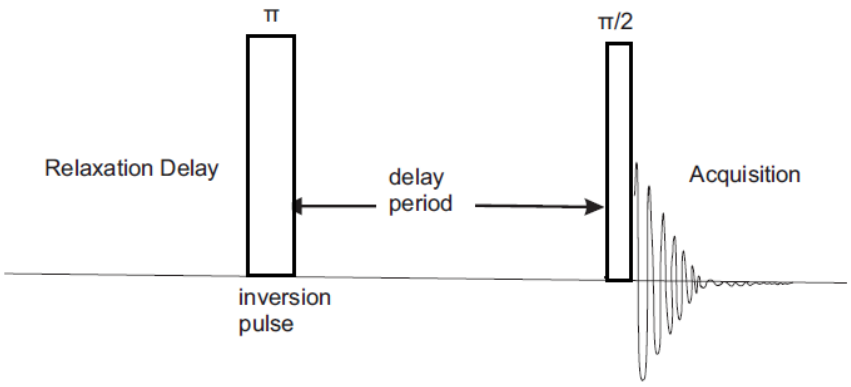

Figure 2.17. Pulse-sequence of Inversion recovery experiments

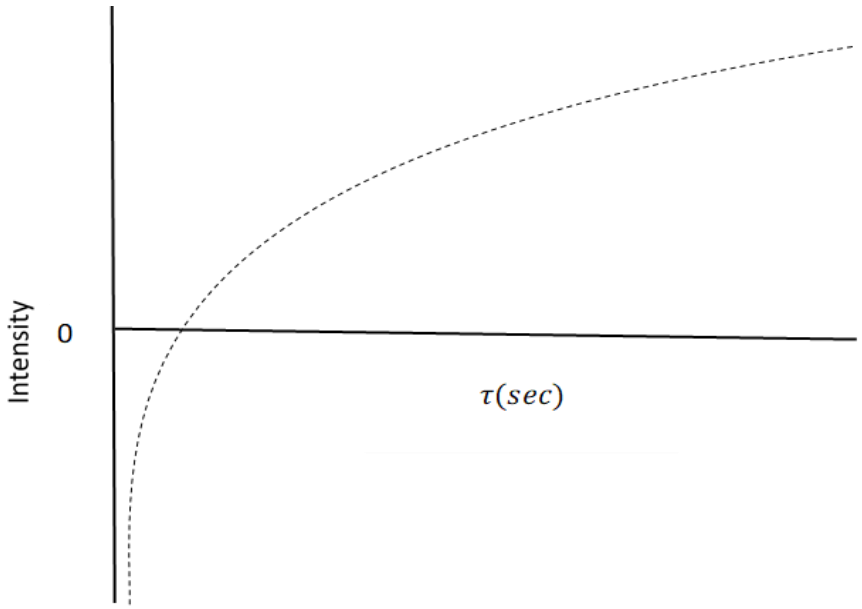

Figure 2.18. Inversion recovery curve for T_1 experiment.

To determine T_1, the signal intensities are fitted to the following equation:

$$M_z(\tau) = M_\infty + (M_0 - M_\infty) \exp\left(-\frac{\tau}{T_1}\right) \quad (2.34)$$

where M_z is the intensity of the magnetization at time τ following the pulse, M_∞ is the intensity of the magnetization at equilibrium and M_0 is the intensity of the inverted magnetization at $\tau = 0$.

T_2 relaxation:

Transverse relaxation or T_2 relaxation determines the rate at which the transverse magnetization decays in the transverse plane. In the experiment used to determine the T_2 constant, first a 90^o (excitation) pulse is applied, followed by a fixed time delay (τ), after which a 180^o (inversion) pulse is applied followed by a second delay with the same τ period. During the first delay period, both coherent and incoherent processes dephase the magnetization. During the second delay period, coherently dephased components of the transverse magnetization to refocus, resulting in the formation of an echo at 2τ. However, due to incoherent systems, the loss of magnetization is irreversible, resulting in signal intensity decay. A series of spectra with increasing delay periods are collected, and the signal intensity is extracted as a function of τ. T_2 is calculated by fitting the experimental data to an exponential decay curve given by Eq. 2.35:

$$M(\tau) = M_0 exp\left(-\frac{\tau}{T_2}\right) \quad (2.35)$$

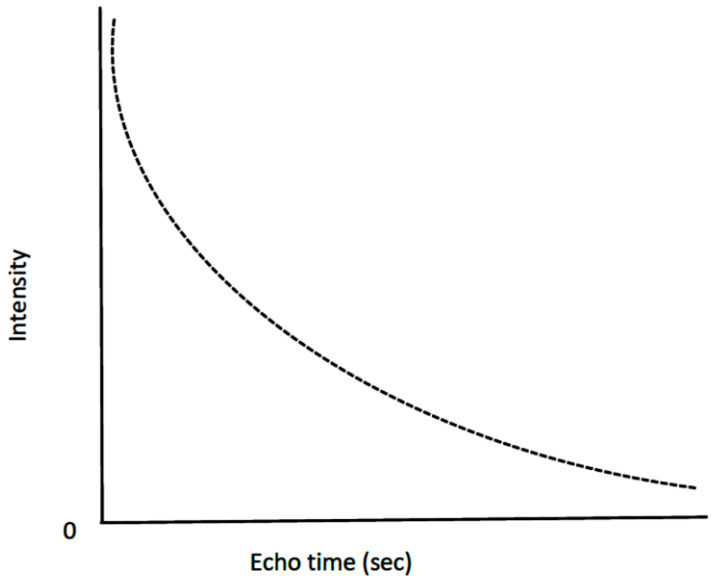

Figure 2.19. Hahn-echo T_2 relaxation experiment, the decay of signal intensity is plotted against the echo time.

Two components with similar intensities characterize a bi-exponential decay, but different T_2 values.

Carr-Purcell-Meiboom-Gill (CPMG) experiment:

The CPMG experiment is similar to the Hahn-Echo experiment, except that after the first 180^o pulse, additional 180^o pulses are applied to analyze the decaying echo response. Instead of gradually increasing the value of τ, it is maintained constant at a small value in this experiment, a train of $\tau/2$-$180°$-$\tau/2$ echo sequences is applied n times, only incoherent processes dephase the transverse magnetization during this period. To prevent phase distortions, the n is always an even integer, and T_2 is obtained by fitting an exponential

decay curve as for the Hahn-echo sequence. The CPMG series will be employed for all T_2 relaxation measurements in this thesis.

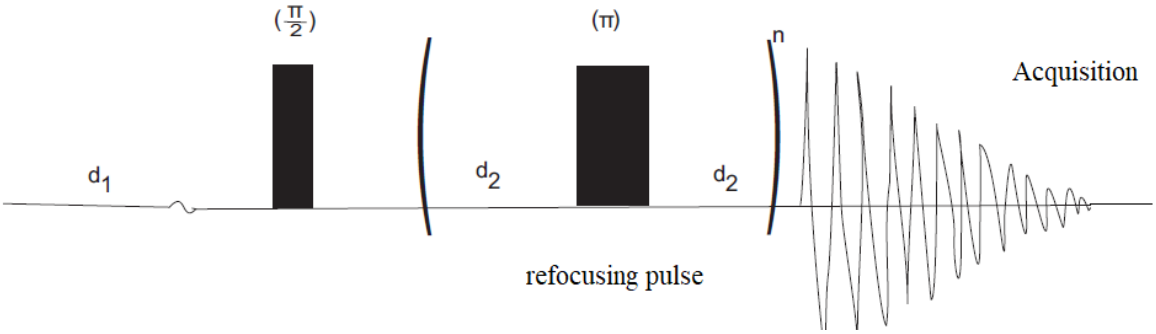

Figure 2.20. Pulse sequences of CPMG experiment.

2.3.4. Diffusion-Ordered NMR Spectroscopy

The objective of the DOSY NMR technique is to separate NMR signals originating from a mixture of molecules based on the variations in the molecular translational diffusion of each of the molecules. DOSY NMR has been used a lot in routine NMR analysis of chemical mixtures for chemical identification. The molecular diffusion coefficient of a sample is calculated with this technique, and the molecular size is then able to estimate based on the measured diffusion coefficient. The diffusion coefficient is influenced by molecular size and shape, as well as temperature, solvent viscosity, and other variables, according to the Debye-Einstein equation:

$$D = \frac{k_B T}{6\pi\eta r_H} \tag{2.36}$$

where the molecule is approximated as a spherical particle of hydrodynamic radius r_H in a solvent of viscosity η, k_B is the Boltzmann constant, and T is the absolute temperature (^{o}K).

Based on the DOSY NMR theory described in the literature, two fundamental pulse sequences are presented in Fig. 2.21.[8] The pulse sequence is recorded using a spin echo (SE) at the top and a stimulated spin echo at the bottom (STE). In both situations, the initial step is to use a 90° radio-frequency (RF) pulse to excite the spins. Spins are now relaxed in the x and y-plane according to the transverse relaxation time T_2. A gradient pulse with an intensity g and a duration δ is applied after this RF pulse. The spin spatial position is encoded inside the spin phase shift at the end of this gradient pulse. During the time interval denoted by Δ, the molecules are allowed to diffuse. During this time of diffusion, the magnetization will take on either a transversal or longitudinal direction, depending on whether the SE or STE pulse sequence is used. When the diffusion time Δ has ended, a second gradient pulse is applied with the same magnitude and duration as the previous one. In order to rephase the spins, the second gradient pulse has the opposite "effective sign" as the first. There are two ways for the spectroscopist to create a gradient pulse with the opposite "effective sign" from the first pulse. Either it is a gradient pulse with an actual current flowing in the opposite direction (opposite sign), or it is a gradient pulse with the same sign as the first one because an RF pulse reversed the spins. The SE sequence provides a clear illustration of this (Fig. 2.21A). A gradient pulse with the same sign, intensity, and length must be used to unwrap the spin phase caused by the gradient pulse because the 180° RF pulse inverts the spin-dephasing.

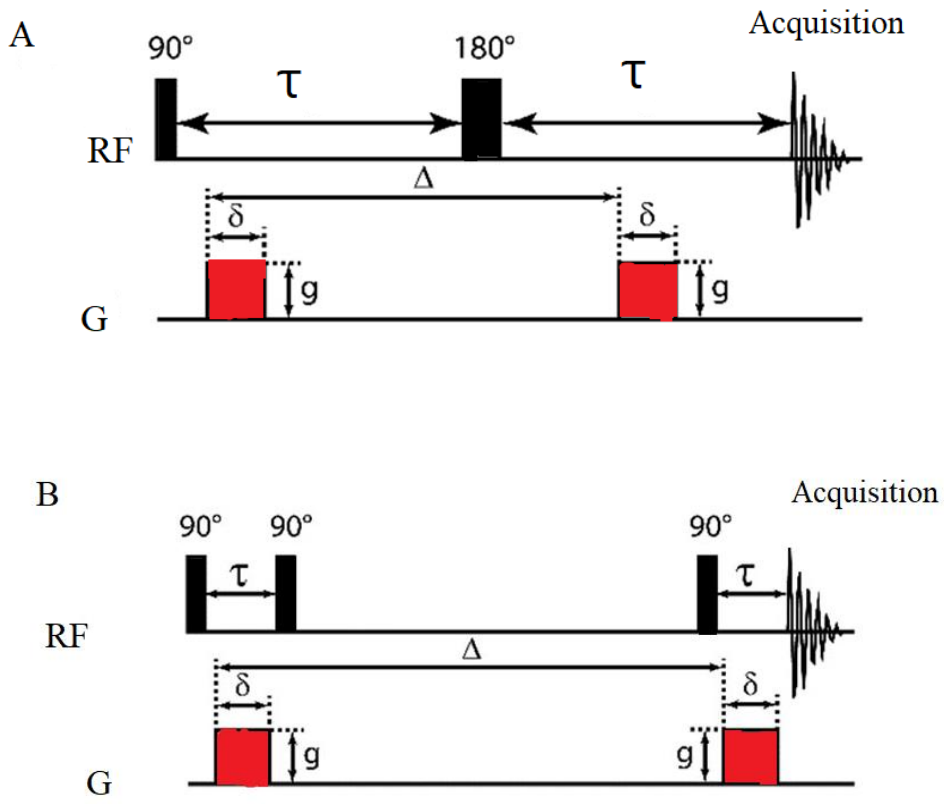

Figure 2.21. The two pulse sequences of DOSY NMR experiments. The pulse sequences are based on a spin-echo (A) or stimulated-echo (B). The main diffusion-related parameters *(g, δ, Δ)* are presented in the figure.

Intensity of NMR signal depends on gradient pulse area (*g* and *δ*), diffusion time *Δ*, and diffusion coefficient D. In the Stejskal-Tanner formula,[9] the NMR signal is written as follows:

$$S = S_0 e^{-(\gamma g \delta)^2 \Delta' D} \qquad (2.37)$$

where Δ' is a corrected diffusion time dependent on the pulse sequence and gradient form. It is essential to remember that, except for the diffusion coefficient D, all other parameters are either established by the pulse sequence itself (*δ*,*g* and *Δ*) or measured (S and S_0). In

order to estimate the diffusion coefficient, one fixed parameter must be adjusted discretely to fit experimental results. In most cases, the experimentalist will change the intensity of the pulsed gradients g to maintain consistency in the timings throughout the different experiments.

REFERENCES

1. Bloch, F., Nuclear induction. Physical review 1946, 70 (7-8), 460.

2. Purcell, E. M.; Torrey, H. C.; Pound, R. V., Resonance absorption by nuclear magnetic moments in a solid. Physical review 1946, 69 (1-2), 37.

3. Becker, E. D., A brief history of nuclear magnetic resonance. Analytical chemistry 1993, 65 (6), 295A-302A.

4. Tjandra, N.; Bax, A., Direct measurement of distances and angles in biomolecules by NMR in a dilute liquid crystalline medium. Science 1997, 278 (5340), 1111-1114.

5. Derome, A. E., Modern NMR techniques for chemistry research. 1st -- ed.; Pergamon Press: New York;Oxford [Oxfordshire];, 1987; Vol. 6.

6. Levitt, M. H., Spin dynamics: basics of nuclear magnetic resonance. John Wiley & Sons: New York;Toronto;, 2001.

7. Levitt, M. H., Spin dynamics: basics of nuclear magnetic resonance. John Wiley & Sons: 2013.

8. Johnson, C. S., Diffusion ordered nuclear magnetic resonance spectroscopy: principles and applications. Progress in Nuclear Magnetic Resonance Spectroscopy 1999, 34 (3), 203-256.

9. Pagès, G.; Gilard, V.; Martino, R.; Malet-Martino, M., Pulsed-field gradient nuclear magnetic resonance measurements (PFG NMR) for diffusion ordered spectroscopy (DOSY) mapping. Analyst 2017, 142 (20), 3771-3796.

CHAPTER 3

STUDY OF ASPHALTENE PHASE COMPOSITION AT VARIOUS DEPTHS IN RESERVOIRS USING SOLUTION-STATE NMR SPECTROSCOPY

3.1. Introduction

Crude oil reservoirs are composed of solids, liquids, and gases. In a reservoir, the aggregation state of asphaltenes remains stable but when the oil is extracted, changes in reservoir conditions, such as pressure or temperature, cause phase instability and result in precipitation and deposition of asphaltene, thus causing flow assurance problems.[1,2] Understanding the structural composition of asphaltene and its aggregation behavior in different depths is thus helpful for findings ways to resolve these problems. The composition of asphaltene in a reservoir fluid varies with depth in many reservoirs (within a single reservoir).[3] In most cases, oil density and viscosity increase with depth in a reservoir.[4] Oil becomes highly dense and viscous, because of higher asphaltene content. With the advancement of the science of asphaltenes, it is now possible to understand how those compounds affect some oilfield issues, such as heavy oil production and fluid flow assurance in pipelines.

Asphaltene structure and aggregation mechanisms in reservoirs have been studied, and several experimental approaches have been described in the literature. Mass spectrometry has proven to be one effective tool for determining asphaltene composition. Andrew *et al.*[3] used two-step laser mass spectrometry (L^2MS) and surface-assisted laser

desorption/ionization (SALDI) to examine the chemical composition of asphaltene molecules in a reservoir. Their study found that the asphaltene component increases slightly with depth throughout the reservoir.

This chapter presents the characterization of asphaltenes collected from different depths within the stacked reservoirs of the Manifa oilfield in Saudi Arabia using solution-state NMR spectroscopy techniques. Several questions immediately arise: (i) does the asphaltene structure change with depth in the same reservoir, or does only the aggregation behavior change? and (ii) if structural changes occur, can NMR spectroscopy be used to identify these changes? In general, NMR spectroscopy can provide information about the different types of chemical groups present, such as aromatic and aliphatic groups. This information can help to identify structural changes in asphaltenes at different depths and better understand their aggregation behavior.

The present work employs a detailed analysis of T_1 and T_2 relaxation behaviour of asphaltenes from different depths in the reservoir. Based on the analysis of T_1 and T_2 relaxation behavior, it is possible to obtain information about the mobility and interactions between the different molecular components. These parameters can provide insights into the size of the asphaltene aggregates, which is closely related to their degree of aggregation. Higher T_1/T_2 ratios suggest larger and more compact aggregates, whereas and lower T_1/T_2 ratios indicating smaller and less compact aggregates.

In the analysis of ^{1}H NMR spectra, deconvolution methods will be used. This method can separate the different overlapping peaks in a spectrum, which allows for the determination of important parameters such as the number of chemically distinct groups present, the relative intensities of each peak, and the chemical shifts of each peak.

3.2. Experimental section

3.2.1. Asphaltene (Manifa) samples

The five asphaltene samples used in this study were supplied by the Schlumberger Doll Research Center (USA), each with a different phase composition and physical properties. The samples came from an oilfield in Saudi Arabia and were identified by the moniker, Manifa. The samples are taken from a reservoir whose asphaltene content changes significantly with depth, from about 2 wt% asphaltene at the top to more than 30 wt% asphaltene at the bottom, as shown in Fig. 3.1.[4,5] The Manifa asphaltene samples were collected from a single reservoir with five different depths ranging from 7700 to 8080 feet.

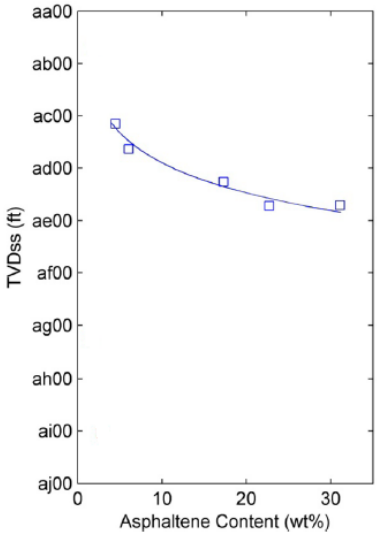

Figure 3.1. Asphaltene content gradient in single reservoir.[5] The y axis indicates reservoir depth, represented as true vertical depth subsea (TVD_{ss}). To preserve the anonymity of the reservoir, the initial digits of the depths have been obscured, and relative depths increase from top to bottom. (Reproduced with permission from Pomerantz, A. E.; Mullins, O. C.; Zare, R. N., Constant asphaltene molecular and nanoaggregate mass in a gravitationally segregated reservoir. *Energy & Fuels* **2014,** *28* (5), 3010-3015.)

The elemental composition of the Manifa asphaltenes had been determined using conventional combustion analysis (carbon, hydrogen, nitrogen, sulfur) and pyrolysis (oxygen).[6] Figure 3.2 presents the elemental compositions of these five asphaltene samples.

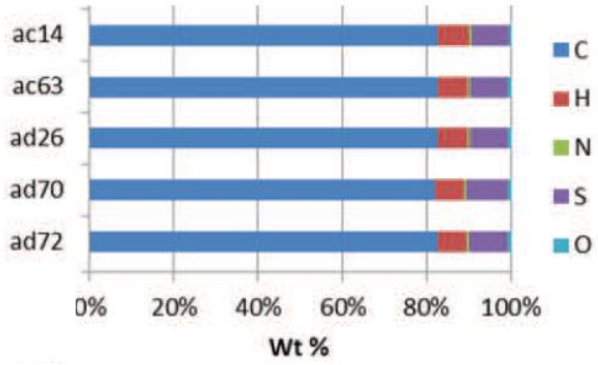

Figure 3.2. Elemental compositions of asphaltenes from variable reservoir depths. Elements are presented in the order carbon, hydrogen, nitrogen, sulfur, oxygen. To preserve the anonymity of the reservoir, the initial digits of the depths have been obscured, and relative depths increase from top to bottom. (Reproduced with permission from Pomerantz, A. E.; Seifert, D. J.; Qureshi, A.; Zeybek, M.; Mullins, O. C., The molecular composition of asphaltenes in a highly compositionally graded column. *Petrophysics-The SPWLA Journal of Formation Evaluation and Reservoir Description* **2013,** *54* (05), 427-438.)

As can be seen in this graph, the asphaltenes have a predominant carbon content (80 to 85 wt%), and its heteroatom content (which includes nitrogen, sulfur, and oxygen) sums up to approximately 10 wt%. The proportions of nitrogen, sulfur, and oxygen in asphaltenes from different depths vary only slightly within that range. Little change in elemental composition was found and no trend with depth was observed within this reservoir.

3.2.2. Sample preparation:

Asphaltene samples for NMR analysis were prepared at 50 g/L concentration. All NMR experiments were carried out at room temperature (25°C). The NMR samples were made using toluene-d_8 and $CDCl_3$ as solvents, which were purchased from Sigma-Aldrich and used as received. First, 50 mg of asphaltene was weighed out in a plastic weighing dish using an electronic analytical balance (Mettler Toledo, accuracy: 0.1 mg). The sample was then transferred into a small vial and dissolved in 1 mL of a deuterated solvent ($CDCl_3$ or toluene-d_8). A vial was used to ensure more effective mixing of the sample compared to using an NMR tube. The samples were treated with vortexing (VWR mini vortexer) for one minute in order to get thorough dissolution. However, due to the high concentration of asphaltene, incomplete dissolution occurs, leading to the presence of precipitates at the bottom of the vial. The solution is transferred to an NMR tube for analysis. All of the analyses were done with 5-mm NMR tubes, which were supplied by Wilmad Lab Glass. Based on the line width of the residual solvent signal, it was not deemed necessary to purge the samples with N_2 gas. The presence of oxygen was not controlled because the effect of oxygen on the relaxation rate was negligible. The influence of oxygen is only noticeable in systems with low molecular weight and solvents with extremely low viscosity.

After the samples were prepared for NMR experiments, the outside of the tube was cleaned with acetone. In the NMR lab, Kimwipes were used to clean the bottom of the tube before placing it in a sample changer.

3.2.3. ^{1}H NMR experiment

All NMR spectra were obtained using a Bruker Avance III HD 700 MHz NMR spectrometer operating at 16.4 T and a triple resonance Bruker TXO-Z (C/F-H-2H) probe equipped with a ^{2}H lock channel, automatic tuning and matching, and Z-gradient. Experiments were performed at room temperature, and the sample appeared to be completely dissolved. No evidence for phase inhomogeneity was found, since throughout the NMR investigations the reference signals always had a symmetric and narrow line shape. Any phase inhomogeneity present on the microscopic scale would have resulted in difficulties shimming the spectrum. The 1D ^{1}H NMR spectra were recorded with a 90° pulse width of 12.4 μs, and 128 transients. Two recycle delays (5 and 120 s) were used to ascertain the quantitative nature of the results. Many previous research studies used a shorter recycle delay (e.g., 2 s, 3 s, and 5 s), which resulted in signal saturation.[7-10] Any significantly longer delay than 120 s was deemed impracticable due to the length of time required to get an acceptable signal-to-noise ratio.

3.2.4. Relaxation experiment

For ^{1}H T_1 and T_2 NMR measurements, samples were prepared in both solvents ($CDCl_3$ and toluene-d_8). The relaxation experiment used the same samples as were used in the ^{1}H NMR experiment. ^{1}H NMR relaxation data were obtained using a Bruker Avance III HD 700 MHz spectrometer operating in a four high power channels (HFXY) mode using a triple resonance Bruker TXO-Z (C/F-H-2H) probe equipped with a ^{2}H lock channel, automatic tuning and matching, Z-gradient, and VT capabilities. All spectra were obtained using a sweep width of 700 kHz, data points were zero-filled to 64k data points, unless stated otherwise. All relaxation data were acquired at room temperature. T_1 relaxation times were

obtained using the inversion recovery pulse sequence[11] of the form {–RD–p_1(180°)–τ–p_2(90°)–aq(acquire)}; the phase cycles were: p_1: {x, –x}$_4$; p_2: {x_2, –x_2, y_2, –y_2}; aq: {x_2, –x_2, y_2, –y_2} and the recycle delay used was 120 s. The delay array used was 0.001, 0.35, 0.75, 1.5, 2, 2.2, 2.5, 2.7, 3, 3.2, 3.5, 4, 4.5, 5, 10, 20, 30, 45, 60, 75, 90 and 120 s with 8 scans for each delay.

The saturation–recovery (SR) method[12] is another technique for T_1 measurement, in which the longitudinal magnetization is set to zero and then measured after a delay time τ. The SR sequence is the multiple-pulse sequence: {90°– τ – 90° –τ – 90°– acquisition}. Saturation was achieved by an aperiodic sequence with a train of 90° pulses separated by decreasing delays. The delay array used was 0, 1, 2, 3, 4, 5, 10, 20, 30, 45, 60, 90, 120, 240, 360, 480, 600,7 20, 840 and 960 s with 8 scans for each delay.

T_2 relaxation data were obtained using the CPMG (Carr- Purcell- Meiboom -Gill) pulse sequence[13] of the form [–RD–p_1(90°)–{τ–p_2(180°)–τ}$_n$–aq(acquire)]; the phase cycles were: p_1: {x, x, –x, –x, y, y, –y, –y}; p_2: {y, –y, y, –y, x, –x, x, –x}; aq:{ x, x, –x, –x, y, y, –y, –y}; the time delay between the pulses was 2 ms and the recycle delay was 120 s. The delay array was: 4, 6, 8, 10, 16, 20, 24, 36, 60, 70, 80, 120, 180, 250, 350, 450, 500, 750, 1000 and 1250 ms with 8 scans for each delay. Data were Fourier-transformed, baseline-corrected, and phased. The integration and deconvolution analysis were performed by MestRenova software (version 14.2.0).

3.2.5. Bi-exponential fits

The analysis of the bi-exponential behavior of the T_1 and T_2 spectra is an important mathematical tool for NMR relaxation studies of complex samples. Generally, a standard linear regression method is used to obtain T_1 and T_2 values if the data exhibit mono-exponential behavior. Bi-exponential data sets cannot be analyzed in this manner owing to large systemic errors being introduced, even when the second component is very small. This study uses the nonlinear fitting optimization method to model the relaxation curves, which allows for two independent relaxation times, one relative composition ratio, and two initial conditions.[14] This nonlinear optimization was carried out with the Levenberg-Marquardt optimization method.[15]

3.2.6. DOSY experiment

Proton diffusion ordered NMR (DOSY) experiments were performed on a Bruker Avance 700 MHz spectrometer, which operates at 16.4 T and uses a triple-resonance Bruker TXO-Z (C/F-H-2H) probe equipped with a ^{2}H lock channel and Z-gradient. Each sample was obtained by mixing 50 mg of asphaltene dissolved in 1 mL of a deuterated solvent ($CDCl_3$ or toluene-d_8). A series of NMR spectra is generally collected in a stimulated echo as a function of pulsed-field gradient intensity in a DOSY experiment. The intensity of each signal decreases at a rate determined by the diffusion coefficient, independent of T_2 relaxation time. The stebpgp1s pulse sequence was used in the diffusion-ordered spectroscopy (DOSY) experiments.[16] Spectra were obtained with 32 scans in an increasing linear gradient ranging from 2% to 95% with a pulsed gradient time δ of 3.6 ms and diffusion times Δ of 50 -100 ms during the DOSY experiment. The spectra were then analysed using the Bruker Dynamics Suite using two processing methods, where the first

is the standard routine allowing up to three components, the second method involves an inverse Laplace transform. The former method utilizes nonlinear optimization to $A_{\text{diffusion}}(\delta, \Delta, D)$ in Equation 3.6 and thus provides diffusion constants and intensities for each component along with their 95% confidence limits.

3.2.7. Error considerations

In this work, the amount of supplied sample was limited, allowing for the preparation of one NMR sample per asphaltene sample. In order to produce accurate and exact findings in the NMR analysis, it is necessary to consider a number of different potential sources of error. In this study, two types of errors need to be considered: errors associated with the relative method and those associated with the absolute method. The errors in the relative method arise from the measurement and analysis of the spectral data, such as deconvolution of overlapping peaks or regression analysis, and can lead to uncertainties in quantification of the different chemical components present in the sample. In the case of ^{1}H NMR studies, the error for the relative method comes from the deconvolution of the peak fitting, and a residual error (RE) was obtained from (χ^2/N) values. The relative error in peak area was then calculated using Eq. 3.1

$$\text{Relative error} = \frac{100 \times N \times \sqrt{(RE)}}{A} \% \quad (3.1)$$

where N is the number of data points in the interval and A is the peak area.

The errors for the absolute method depend on the measurements and scale. In the study, a fundamental error comes from measuring the sample weight, solvent volume, and deconvolution of the NMR spectrum. To measure the sample mass, an analytical balance was used with an accuracy of 0.1 mg. To measure the volume of the solvent, a sealed 1 mL

ampule supplied by Sigma Aldrich was used; it is, however, impossible to transfer exactly 1 mL due to small 'losses' of injection of the solvent on the inside surfaces of the ampule. The estimated error in volume is around 1%.

3.3. Results and Discussion

The ^{1}H NMR spectra of five asphaltenes collected at different reservoir depths were recorded. All spectra are composed of overlapping signals. Instead of analyzing the full spectra, three regions containing signals of interest were primarily focused on, because limiting the region reduces the possibility of signal contamination from different structural environments with similar chemical shifts. Signals in specific chemical shift regions (aromatic, alicyclic, aliphatic) of the asphaltenes were deconvolved using the smallest number of deconvolution components, providing quantitative information about NMR parameters for each signal. The deconvolved components have their individual chemical shifts, line widths, signal intensities, areas, and Lorentzian/Gaussian (L/G) ratios. The same sets of chemical shifts, line widths, and L/G ratios were used for all five samples to ensure reliable and consistent analysis.

Fig. 3.3 presents the ^{1}H NMR spectra of the five asphaltenes collected at different reservoir depths.

a)

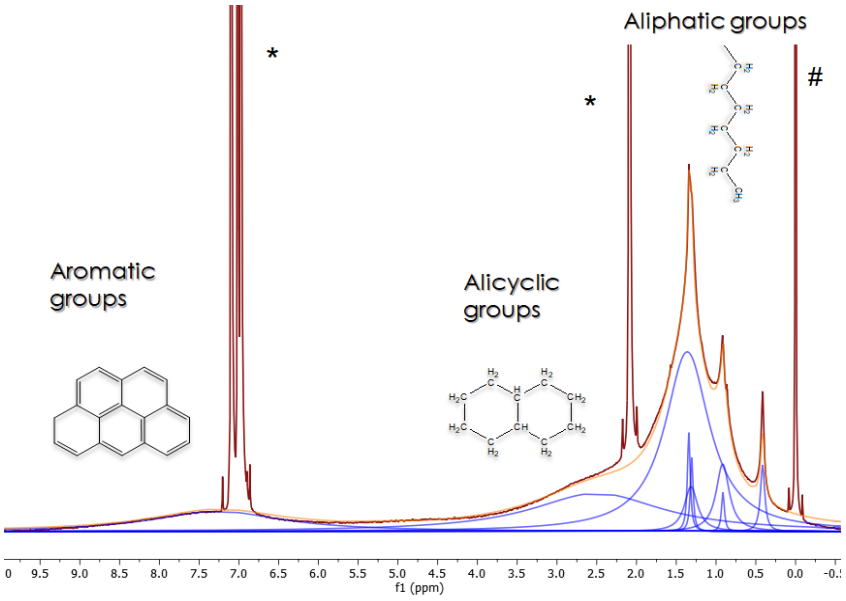
Aliphatic groups
*
*
#
Aromatic groups
Alicyclic groups
f1 (ppm)

b)

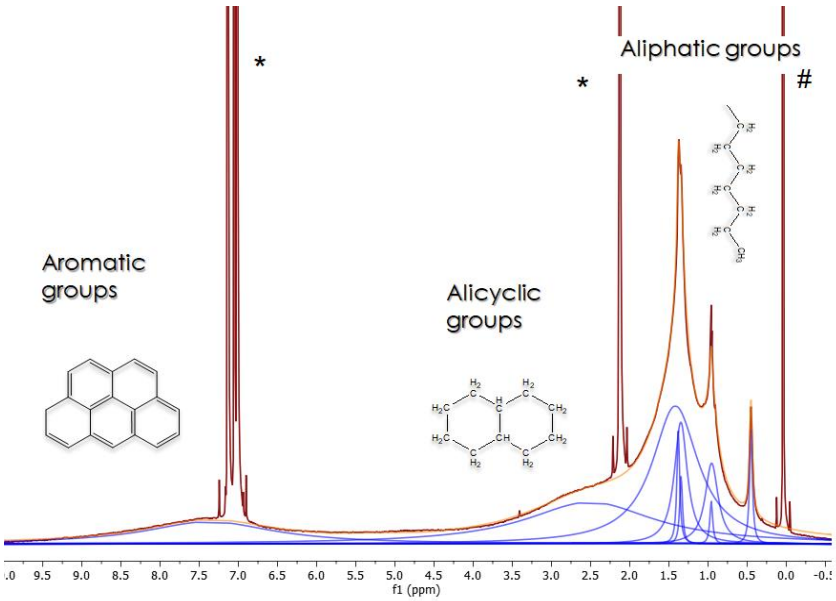
Aliphatic groups
*
*
#
Aromatic groups
Alicyclic groups
f1 (ppm)

c)

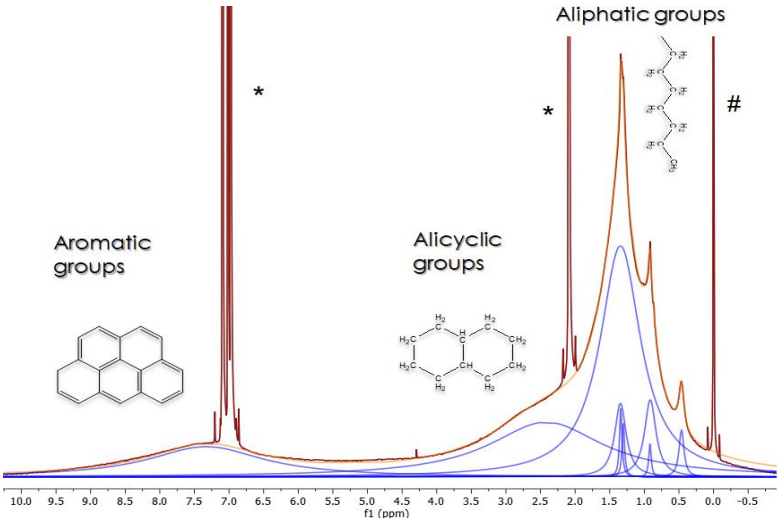
Aliphatic groups
*
*
#
Aromatic groups
Alicyclic groups
10.0 9.5 9.0 8.5 8.0 7.5 7.0 6.5 6.0 5.5 5.0 4.5 4.0 3.5 3.0 2.5 2.0 1.5 1.0 0.5 0.0 -0.5
f1 (ppm)

d)

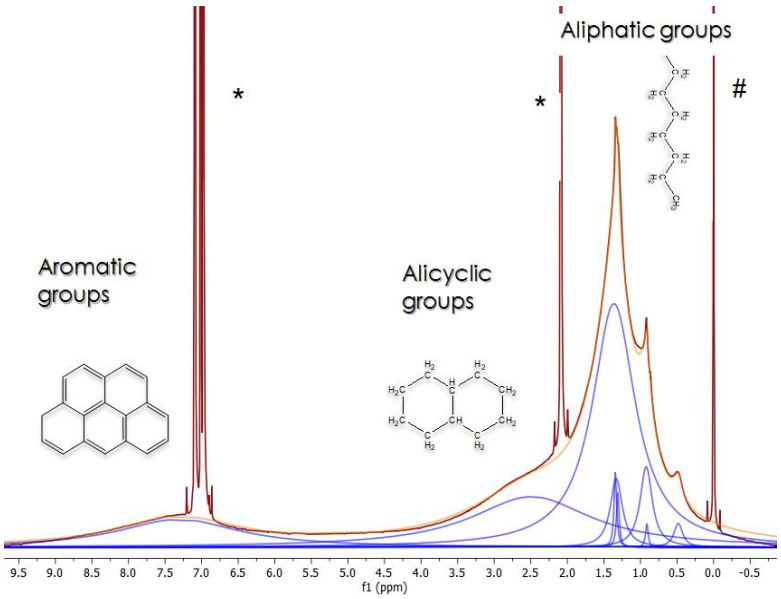
Aliphatic groups
*
*
#
Aromatic groups
Alicyclic groups
9.5 9.0 8.5 8.0 7.5 7.0 6.5 6.0 5.5 5.0 4.5 4.0 3.5 3.0 2.5 2.0 1.5 1.0 0.5 0.0 -0.5
f1 (ppm)

e)

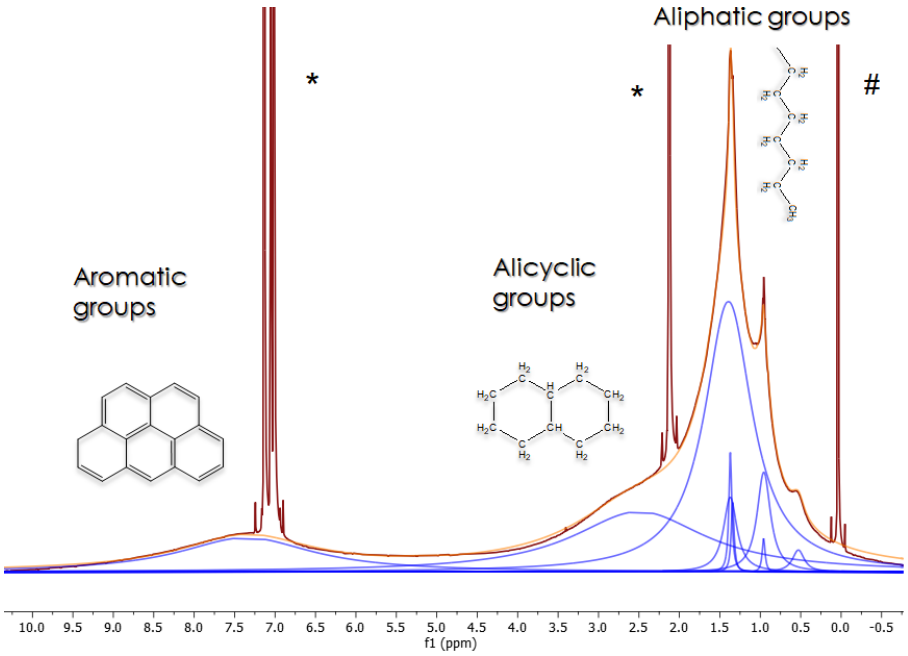

Figure 3.3. 700 MHz ^{1}H NMR spectra of the Manifa asphaltene samples at reservoir depths of (a) 7767.6 ft; (b) 7963.5 ft; (c) 8026.3 ft; (d) 8070.9 ft; (e) 8072.1 ft. The maroon traces are the experimental spectra, the blue traces are the deconvoluted signals, and the orange traces are the sum of the deconvoluted components. All ^{1}H NMR spectra were recorded at ambient temperature in toluene-d_8 (residual solvent signals are denoted by *) using TMS (denoted by $^{\#}$) as the internal reference with a 90° pulse during acquisition and a recycle delay of 120 s and 16 scans.

In the present study, purely Lorentzian lineshapes were used to deconvolve the ^{1}H NMR spectra because the lineshapes were found to be homogenous in the solution state. Deconvolution involved determining each sub-peak's areas, chemical shifts, and linewidths within the spectrum by applying a Lorentzian function to it. Table 3.1 lists typical deconvolution parameters associated with characteristic spectral areas and their functional groups.

Table 3.1. Chemical shift assignments for fitted peaks in the ^{1}H NMR spectra of asphaltenes.

Functional group	Chemical shift (ppm)	Linewidth (Hz)
Aromatic hydrogens (H_{ar})	9.00-7.30	1400
Alicyclic hydrogens (H_{alc})	3.50-2.50	1400
Aliphatic chain	1.80-0.50	500,140,30

In NMR spectroscopy, accurate knowledge of the longitudinal relaxation time is essential to ensure the spectral intensities are not attenuated due to saturation. Hence, it is critical to choose the recycle delay carefully to ensure quantitative results. Between each scan in the NMR experiment, a delay 5 to 7 times T_1 should be used. This study analysed the NMR signals of asphaltenes with two different recycle delays, *i.e.*, 5 s and 120 s. The main objective was to explore the effect of saturation on the NMR signals by using a relatively short recycle delay of 5 s. The use of a 5 s recycle delay has been common in previous studies of asphaltenes, making it a representative value for comparison and analysis.

The composition of the different spectral environments (aromatic, alicyclic and aromatic) in this study was determined using the relative and absolute methods. In the relative method, the percentage of each region was obtained from the peak areas with respect to the sum of all asphaltene peak areas.

To calculate the absolute composition, the integral of each chemical shift area was divided by the residual ^{1}H signal of a standard solvent (toluene-d_8). When using the absolute method, the amount of water present in the sample can be calculated, which is the most important information received by this method.

The deconvolution results for the five asphaltene samples are listed in Tables 3.2 and 3.3 using a 5 s recycle delay. Figure 3.4 shows the relative composition of asphaltenes obtained at different reservoir depths when a recycle delay of 5 s is used. When the short 5 s recycle delay was used, the percentage of aromatic and alicyclic components appear to decrease with depth. The opposite trend was observed for the aliphatic component.

When a long delay (120 s) was used for the investigation, different compositional information was obtained as presented in Tables 3.4 and 3.5 and Figure 3.5. The trend obtained form the data using a long recycle delay of 120 s was reversed with respect to the data using a 5 s recycle delay. The aromatic and alicyclic fractions increased with increasing depth, while the aliphatic fraction decreased. This result clearly shows the importance of using the longer recycle delay and that incorrect information is obtain from spectral data using a recycle delay of 5 s.

Table 3.2. The deconvolution (peak-fitting) models used for the solution-state ^{1}H NMR spectra of Manifa asphaltenes at ambient temperature in toluene-d_8 using a 5 s recycle delay. This deconvolution model used purely Lorentzian lineshapes.

$\delta(^{1}H)$ (ppm)	Width (Hz)	Area	$\delta(^{1}H)$ (ppm)	Width (Hz)	Area
Depth: 7767.6 ft			Depth: 7963.5 ft		
7.37	1400	12600	7.41	1400	21400
2.50	1400	13900	2.52	1400	24700
1.38	500	21900	1.36	600	49400
1.32	140	4920	1.34	140	741
0.92	30	530	0.92	30	399
1.33	30	829	1.33	30	783
1.29	30	588	1.29	30	637
0.91	140	2690	0.92	140	4480
Depth: 8026.3 ft			Depth: 8070.9 ft		
7.45	1400	19000	7.39	1400	10500
2.56	1400	22600	2.57	1400	12000
1.35	600	51900	1.35	600	30000
1.34	140	5930	1.32	140	3230
0.92	30	386	0.92	30	331
1.33	30	545	1.34	30	692
1.29	30	494	1.29	30	471
0.93	140	3480	0.91	140	2450
Depth: 8072.1 ft					
7.4	1400	15100			
2.56	1400	17300			
1.35	600	43700			
1.33	140	5300			
0.92	30	265			
1.33	30	559			
1.29	30	466			
0.92	140	3530			

Table 3.3. Relative composition for the fitted peaks of the ^{1}H NMR spectra of Manifa asphaltenes at ambient temperature in toluene-d_8 using a 5 s recycle delay. The percentage of relative errors were calculated from the residual error (χ^2/N) in the deconvolution analysis.

Depth (ft)	Total area	% Aromatic	%Alicyclic	% Aliphatic
7767.6	58100	21.7 (± 0.05)	24.0 (± 0.03)	54.2 (± 0.02)
7963.5	109000	19.6 (± 0.03)	22.6 (± 0.03)	57.8 (± 0.03)
8026.3	104000	18.2 (± 0.04)	21.6 (± 0.04)	60.1 (± 0.03)
8070.9	59700	17.6 (± 0.03)	20.1 (± 0.05)	62.3 (± 0.03)
8072.1	86300	17.5 (± 0.05)	20.0 (± 0.03)	62.4 (± 0.04)

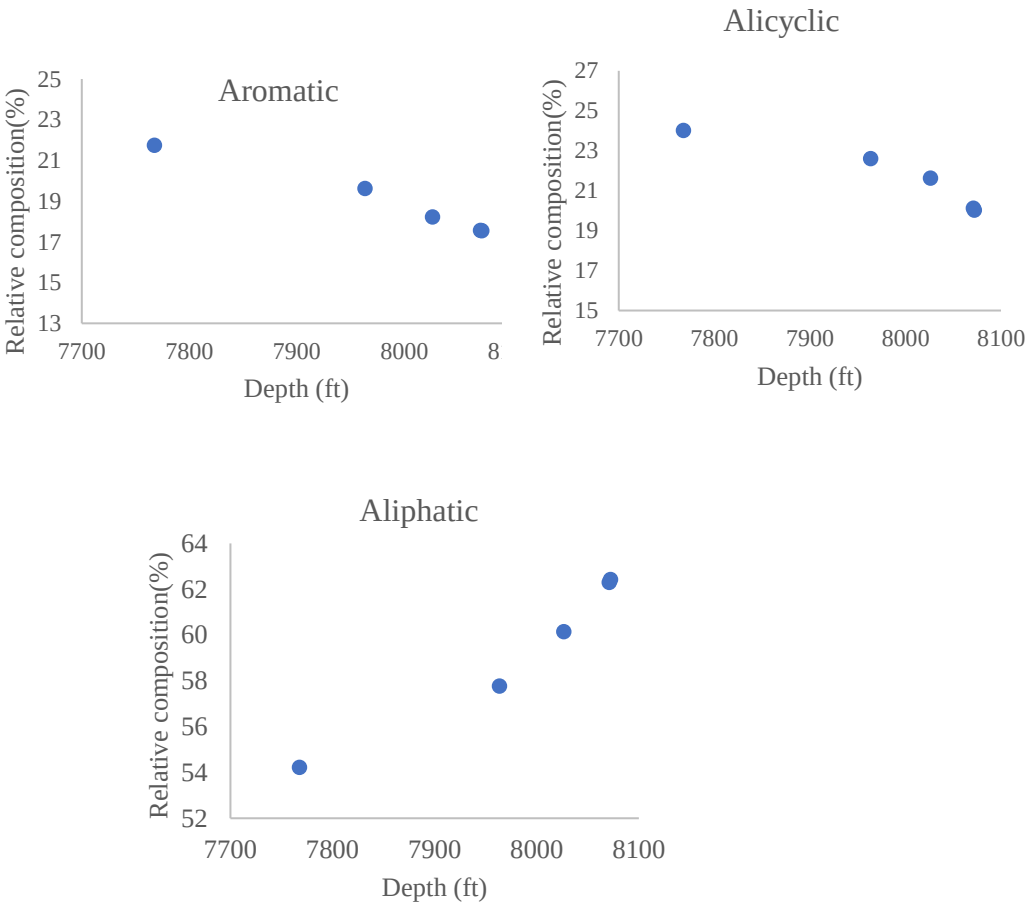

Figure 3.4. Effect of reservoir depth on the relative composition of Manifa asphaltenes at ambient temperature in toluene-d_8 using a recycle delay of 5 s.

Table 3.4. The deconvolution (peak-fitting) models used for the solution-state ^{1}H NMR spectra of Manifa asphaltenes at ambient temperature in toluene-d_8 using a 120 s recycle delay. This deconvolution model used purely Lorentzian lineshapes.

δ(^{1}H) (ppm)	Width (Hz)	Area	δ(^{1}H) (ppm)	Width (Hz)	Area
Depth: 7767.6 ft			Depth: 7963.5 ft		
7.37	1400	31500	7.31	1400	40400
2.51	1400	32900	2.49	1400	42700
1.43	500	72800	1.36	500	79000
1.35	140	2300	1.31	140	3350
1.33	30	980	1.34	30	995
1.29	30	531	1.30	30	623
0.96	140	4470	0.93	140	5350
0.95	30	680	0.92	30	700
Depth: 8026.3 ft			Depth: 8070.9 ft		
7.36	1400	54000	7.35	1400	62000
2.47	1400	58000	2.49	1400	64000
1.37	500	97500	1.37	500	98800
1.36	140	4030	1.36	140	4770
1.30	30	1000	1.30	30	1010
1.29	30	680	1.29	30	790
0.95	140	6650	0.93	140	7230
0.92	30	780	0.92	30	880
Depth: 8072.1 ft					
7.36	1400	67400			
2.47	1400	71400			
1.38	500	103000			
1.36	140	5180			
1.32	30	1230			
1.30	30	800			
0.95	140	8120			
0.92	30	920			

Table 3.5. Relative composition for the fitted peaks of the ^{1}H NMR spectra of Manifa asphaltenes at ambient temperature in toluene-d_8 using a 120 s recycle delay. The percentage of relative errors were calculated from the residual error (χ^2/N) in the deconvolution analysis.

Depth (ft)	Total area	% Aromatic	% Alicyclic	% Aliphatic
7767.6	146000	21.5 (± 0.05)	22.5 (± 0.02)	55.9 (± 0.03)
7963.5	173000	23.3 (± 0.04)	24.7 (± 0.03)	52.0 (± 0.03)
8026.3	223000	24.2 (± 0.03)	26.1 (± 0.03)	49.7 (± 0.02)
8070.9	243000	25.5 (± 0.03)	26.5 (± 0.02)	48.0 (± 0.03)
8072.1	964000	26.1 (± 0.05)	27.6 (± 0.02)	46.3 (± 0.04)

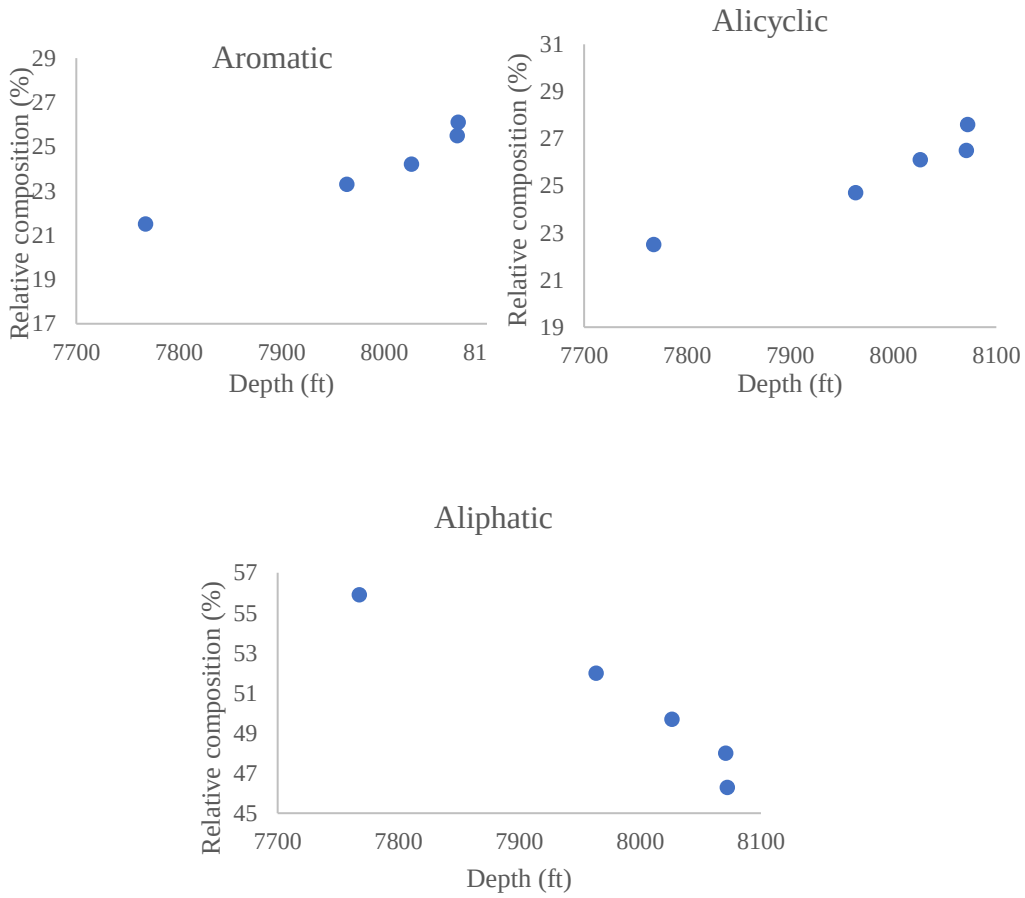

Figure 3.5. Effect of relative composition of of Manifa asphaltenes at ambient temperature in toluene-d_8 using a 120 s recycle delay.

The absolute composition of the asphaltene samples with respect to aromatic, alicyclic and aliphatic hydrogens was determined using a 120 s recycle delay, and the results are presented in Table 3.6. A systematic variation of composition was observed with sample depth, paralleling the data of the relative method.

Table 3.6. Absolute composition of Manifa asphaltenes at ambient temperature in toluene-d_8. The errors were calculated from the relative errors in the deconvolution analysis.

Depth (ft)	Aromatic	Alicyclic	Aliphatic
7767.6	19.5 ± 0.7	21.5 ± 0.6	52.9 ± 0.5
7963.5	22.1 ± 0.9	24.4 ± 0.7	49.7 ± 1.0
8026.3	24.1 ± 0.9	26.1 ± 0.5	48.7 ± 0.5
8070.9	25.5 ± 1.0	27.7 ± 0.8	45.9 ± 0.9
8072.1	26.2 ± 0.9	28.0 ± 0.8	45.6 ± 0.7

Table 3.6 shows a trend for the increased aromatic and alicyclic absolute composition of the asphaltene fraction with depth. The asphaltenes contain water, and the water content varies from sample to sample, as shown in Figure 3.6. The contributions of the water signals are listed in Table 3.7. A decrease in water content was found for deeper depths.

(a) 7767.6 ft depth (b) 8070.9 ft depth

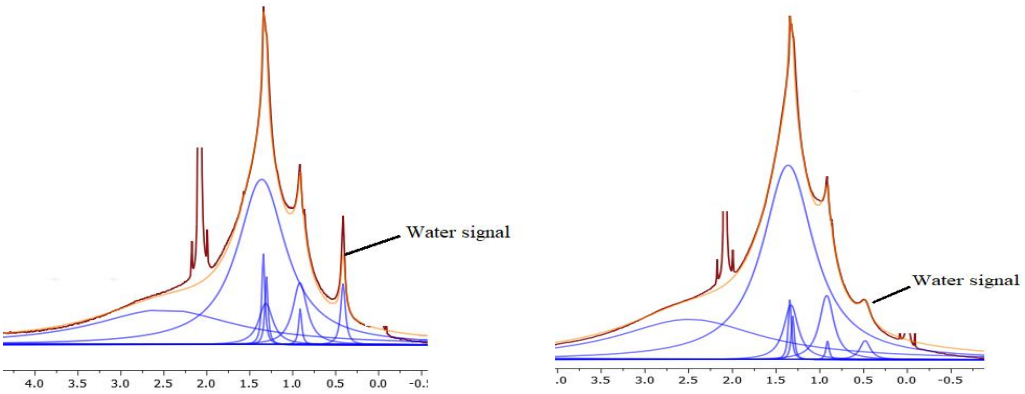

Figure 3.6. Alicyclic and aliphatic regions of the solution-state ^{1}H NMR spectra of different reservoir depths (7767.6 ft and 8070.9 ft) asphaltenes in toluene-d_8. The percentage of water signal varies from sample to sample as highlighted in a and b.

Table 3.7. Water signal of asphaltenes in toluene-d_8 solvent.

Depth (ft)	Total Signal/Solvent	Water/Solvent
7767.6	93.9 ± 1.5	4.8 ± 0.06
7963.5	96.2 ± 1.2	2.2 ± 0.04
8026.3	98.9 ± 0.8	0.3 ± 0.01
8070.9	99.2 ± 0.4	0.04 ± 0.001
8072.1	99.8 ± 0.002	-

Whereas the absolute method is used to determine the amount of water in a sample, the relative method provides more information about the structure of a typical asphaltene molecule. As discussed above, the errors of the absolute method are larger than the one of the relative methods, because the sample preparation and experimental procedure determine the error; on the other hand, sample preparation does not affect the relative method. Because the absolute method has limitations, the relative method determines the Manifa asphaltenes composition more accurately, despite the fact that it does not provide information about water content.

3.3.2. T_2 and T_1 relaxation measurements

Three types of measurements of relaxation times for the Manifa samples were carried out, *i.e.*, saturation recovery (T_1), inversion recovery (T_1) and CPMG (T_2).

The advantage of using the saturation recovery (SR) technique is that the recycle delay can be avoided between scans, thereby cutting the experiment time down by a factor of 2 to 3 compared to the inversion–recovery method. Hence, the SR experiment is particularly important for samples with long T_1 values, as this experiment can estimate T_1. Additionally, the number of components contributing to T_1 can be determined using the SR experiment. In such an experiment, longitudinal magnetization is set to zero and then measured after a delay time τ. The delay time τ is referred to as the recovery time.

The saturation recovery experiment was conducted on a single Manifa sample (8070.9 feet) focussing on the aromatic region. When accurately determining T_1 values, the saturation recovery experiment is not recommended because achieving 100% saturation is not possible, resulting in a higher noise level and larger errors. Therefore, doing an inversion recovery (IR) experiment is still necessary for quantitative purposes to obtain the precise T_1 values.

As shown in Fig. 3.7, two components were apparent up to 120 s. At longer delay times, however, further increase in signal was observed (Figure 3.8), indicating the presence of at least an additional component with a very long T_1. The recovery of this third component was observed up to 960 s, where it still had not returned to spin equilibrium. The decision was made to use a 120 s recovery delay in the inversion recovery experiment where the third component would be saturated, leading to loss of 2-3% of the total asphaltene signal (based on the measurements made at 960 s).

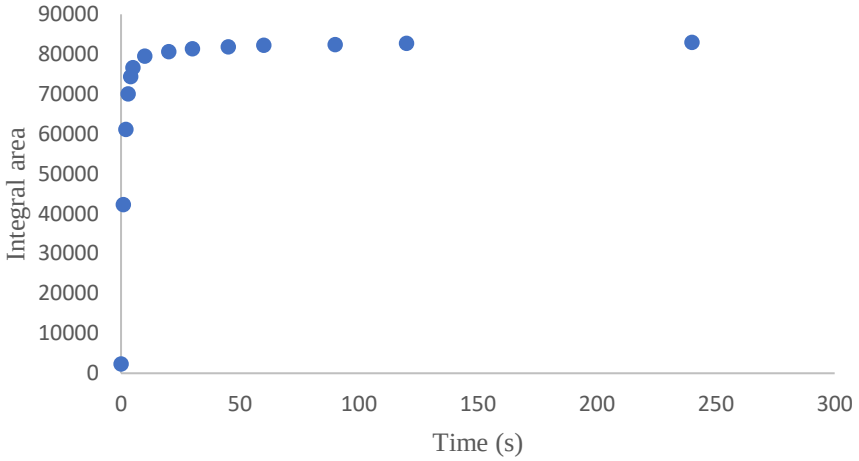

Figure 3.7. The integrated aromatic area measured in a SR experiment as a function of time (T), T is the repetition time between two 90° pulses.

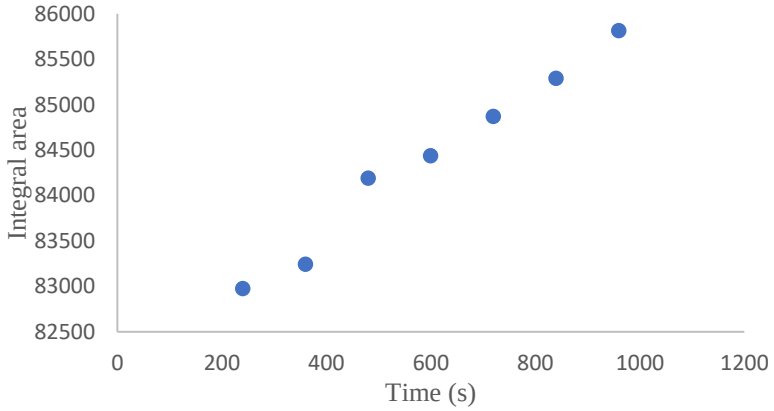

Figure 3.8. The integrated aromatic area measured in a SR experiment as a function of time (T), T is the repetition time between two 90° pulses. The y-axis is depicted with integration values from 82500 to 86000 to show the trend for longer delay times.

To obtain T_1 and T_2 relaxation times, the experimental relaxation curves obtained from inversion recovery and CPMG experiments, respectively, were processed using the Levenberg-Marquardt algorithm to find the best fitting non-linear curves. A peak-fitting model was used to identify types of proton environments with different chemical shift ranges in the ^{1}H NMR spectrum.

The bi-exponential recovery curves from the inversion recovery experiments are shown in Figure 3.9 for the sample at 8072.1 ft of depth (the other curves are shown in Appendix 1). The raw data obtained from the inversion recovery experiment were normalized and plotted against time.

The raw data for the T_2 determination were obtained from CPMG experiments and were normalized and plotted against time (Figure 3.10 for 8072.1 ft depth). The T_2 values were obtained by fitting using the Levenberg - Marquardt algorithm.

Aliphatic

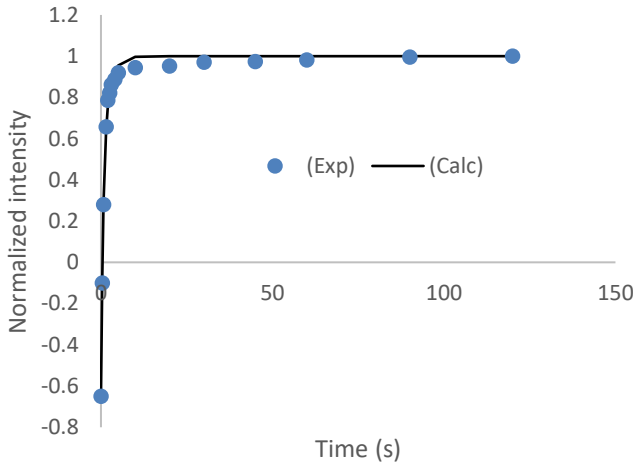

Alicyclic

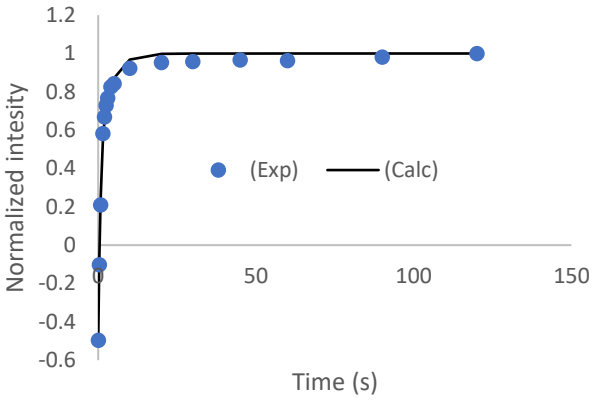

Aromatic

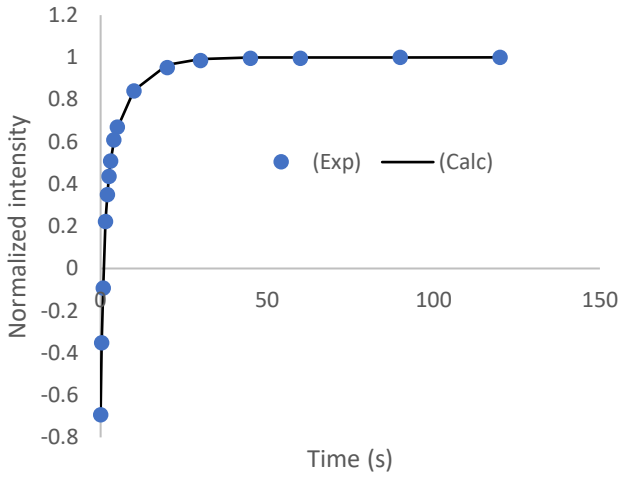

Figure 3.9. Non-linear regressive line-fitting of the T_1 data of the ^1H signal at a reservoir depth of 8072.1 ft in toluene-d_8. The blue points are the inversion recovery data, and the black line shows the exponential recovery curve fitted to the data.

Aliphatic

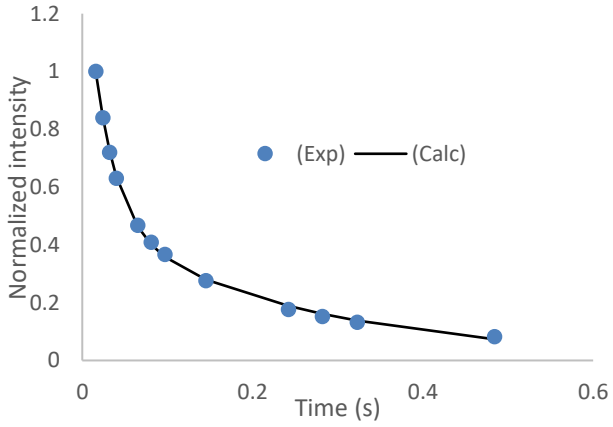

Alicyclic

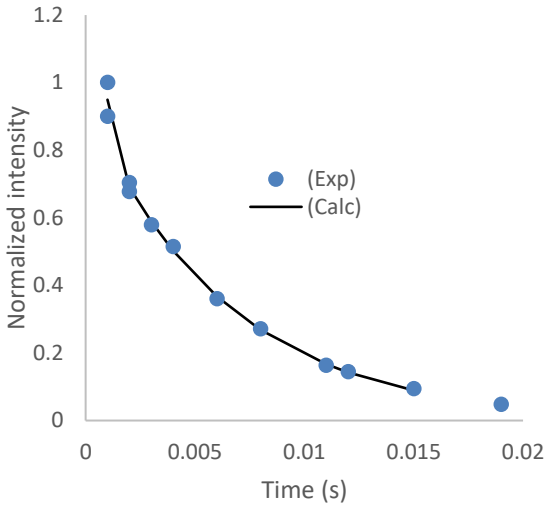

Aromatic

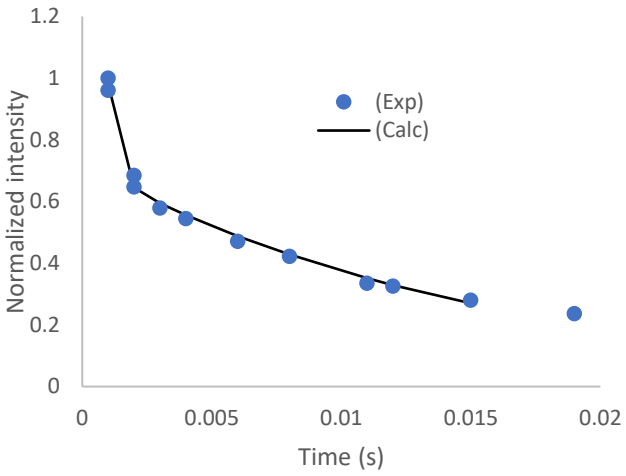

Figure 3.10. CPMG curve from the Manifa sample (8072.1 ft) at 700 MHz. The blue data points are the CPMG data, and the black line shows the exponential decay curve fitted to the echo envelope.

Table 3.8 lists the T_1 and T_2 relaxation time constants of ^1H resonances of the Manifa asphaltene sample at a depth of 8072.1 ft using a 120 s recycle delay.

In the inversion recovery experiments, two components, one with a short T_1 and the other with a long T_1, were found. Bi-exponential relaxation behaviour has been observed in many cases for complex materials, hence, it is not unexpected to be observed for asphaltenes.[17,

[18] The relaxation analysis in this study is based on the ratio of the two relaxation parameters T_1 and T_2. The size of both relaxation times is determined by the characteristic molecular dynamics, as established in the research by Bloembergen, Purcell, and Pound (BPP theory).[19] To summarize the theory, the two relaxation times T_1 and T_2 are equal for molecules with rapid isotropic motion, hence the T_1/T_2 ratio is 1 in such cases. The T_1 and T_2 values diverge as molecular dynamics slows down. In fact, for complex and solid materials, T_2 is often quite short while T_1 is typically extremely long, ranging several orders of magnitude. Note that in NMR terminology, "rapid" and "slow" are always used with respect to the nuclear precession (Larmor frequency). "Rapid" dynamics refers to motion in which the typical correlation time τ_c is significantly shorter than the precession period T = $1/\omega_o$, where ω_o is the Larmor frequency.

Table 3.8. ^{1}H NMR Relaxation times of reservoir depth (8072.1 ft) asphaltene in toluene-d_8. The values in parentheses represent the percentage of protons having the corresponding T_1 and T_2. The standard deviations for both T_1 and T_2 have been calculated.

^{1}H ppm	assignment	T_1 (s)	T_2 (ms)	T_1/T_2
1.5-0.8	aliphatic chain	0.57 ± 0.03 (65 ± 4.2%)	27.1 ± 1.1 (68 ± 4.4%)	21 ± 1.38
		1.40 ± 0.04 (35 ± 4.2%)	260 ± 1.7 (32 ± 4.2%)	5 ± 0.15
3.5-2.4	alicyclic	3.2 ± 0.05 (68 ± 5.4%)	0.25 ± 0.01 (65 ± 4.5%)	13000 ± 550
		1.5 ± 0.03 (32 ± 4.5%)	16.0 ± 0.8 (35 ± 4.2%)	100 ± 5.3
9.0-7.6	aromatic CH	6.50 ± 0.05 (68 ± 5.5%)	0.32 ± 0.02 (70 ± 5.0%)	20000 ± 640
		1.50 ± 0.03 (32 ± 4.5%)	15.0 ± 0.8 (30 ± 4.5%)	100 ± 5.6

In the study of the Manifa asphaltene sample, two T_1/T_2 ratios were obtained for each of the selected proton environment types with relative contribution of approximately 2:1, indicating the presence of two distinct motional timescales. For the calculations of the T_1/T_2 ratios, the T_1 and T_2 values of the components with similar % contributions were taken. For

the aliphatic groups, the shorter T_1 values were paired with the shorter T_2 values, which is consistent with the higher mobility of these groups. On the other hand, the shorter T_1 values were paired with the longer T_2 values for alicyclic and aromatic ^1H signals, consistent with the divergent behaviour of these relaxation times for longer correlation times (See Figure 2.16 in Chapter 2). The different kinds of ratios indicate that these protons have distinctly different mobilities. The major component of each type of ^1H signal has a larger T_1/T_2 ratio. Aliphatic groups are generally capable of more internal mobility than alicyclic and aromatic groups, resulting in substantially smaller T_1/T_2 ratios. The minor component of the aliphatic groups with T_1/T_2 ratios close to five, whereas a larger ratio of 21 was found for the major component.

Alicyclic signals exhibit T_1/T_2 ratios of 13,000 and 100. Both ratios indicate the restricted mobility of these protons compared to the aliphatics for both the long and short components. This is consistent with the alicyclics being adjacent to stacked aromatic cores where a significant reduction in mobility would be anticipated as opposed to those on the periphery of the aggregates.

The T_1/T_2 ratios of the aromatic components of the Manifa asphaltenes are 20,000 and 100. The aromatic hydrogens mostly reflect the mobility of the whole aggregate and thus the corresponding ratio is expected to be very large.

Parallel behavior to that observed in toluene was seen with the T_1/T_2 ratios for the aliphatic, alicyclic, and aromatic components in $CDCl_3$ (Table 3.9). The biexponential fitting curves for selective inversion experiments on the Manifa sample at a reservoir depth of 8072.1 ft in $CDCl_3$ are shown in Fig. 3.11.

Table 3.9. ^{1}H NMR relaxation times of a Manifa asphaltene sample at a reservoir depth of 8072.1 ft in $CDCl_3$. The values in parentheses represent the percentage of protons having the corresponding T_2 and T_1. The standard deviations for the T_1 and T_2 values are provided.

^{1}H ppm	assignment	T_1 (s)	T_2 (ms)	T_1/T_2
1.5-0.8	aliphatic	0.50 ± 0.03 (70 ± 4.5%) 1.60 ± 0.04 (30 ± 3.5%)	30.0 ± 1.0 (68 ± 5.5%) 280 ± 2.0 (32 ± 3.7%)	16.7 ± 1.2 5.5 ± 0.14
3.5-2.4	alicyclic	2.80 ± 0.05 (65 ± 4.5%) 1.60 ± 0.03 (35 ± 4.5%)	4.60 ± 0.06 (68 ± 4.0%) 17.0 ± 0.8 (32 ± 3.8%)	600 ± 13 90 ± 4.5
9.0-7.6	aromatic	3.30 ± 0.05 (72 ± 5.5%) 1.50 ± 0.03 (28 ± 4.5%)	0.30 ± 0.02 (70 ± 5.0%) 16.0 ± 0.8 (30 ± 4.0%)	11000 ± 660 93 ± 4.8

Aliphatic

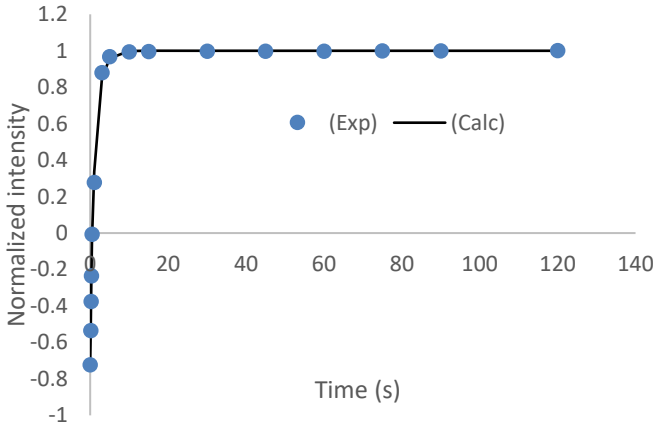

Alicyclic

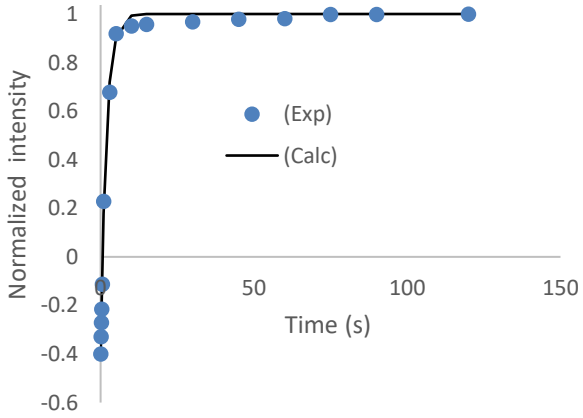

Aromatic

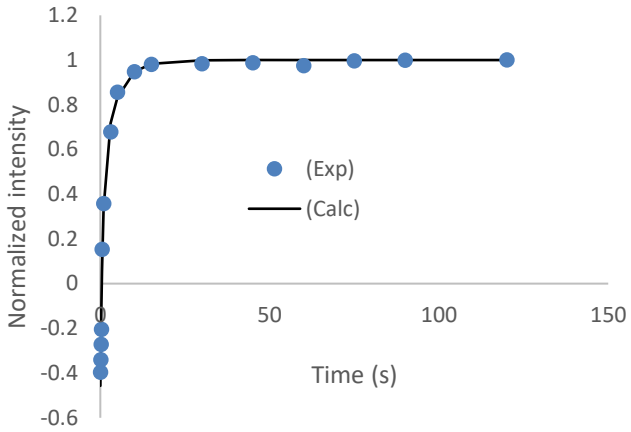

Figure 3.11. Non-linear regressive line-fitting of the T_1 data of the ^1H signal at a reservoir depth of 8072.1 ft in $CDCl_3$. The blue points are the inversion recovery data, and the black line shows the exponential recovery curve fitted to the data.

The raw data for the T_2 determination were obtained from CPMG experiments and were normalized and plotted against time. The CPMG curves for the sample from the 8072.1 ft depth are shown in Fig. 3.12.

Aliphatic

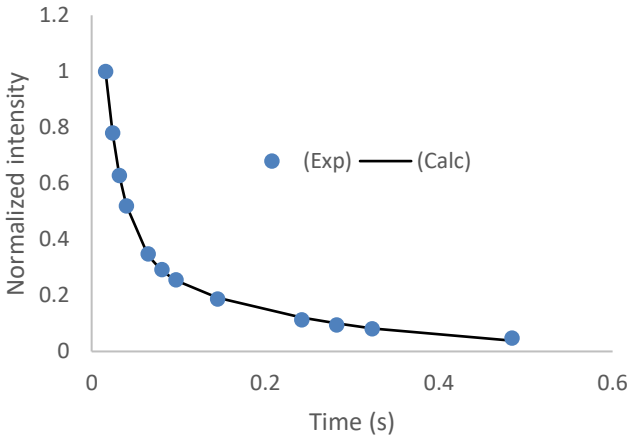

Alicyclic

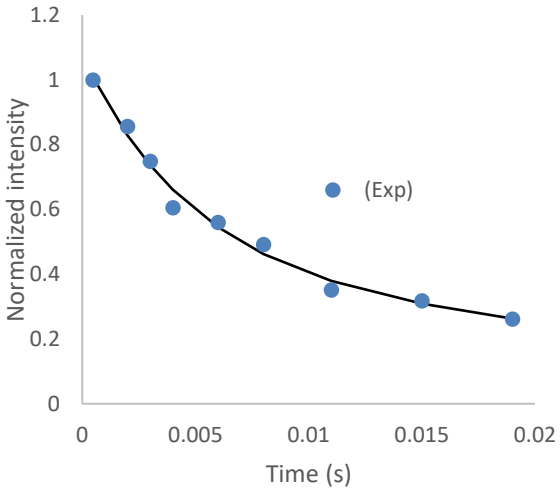

Aromatic

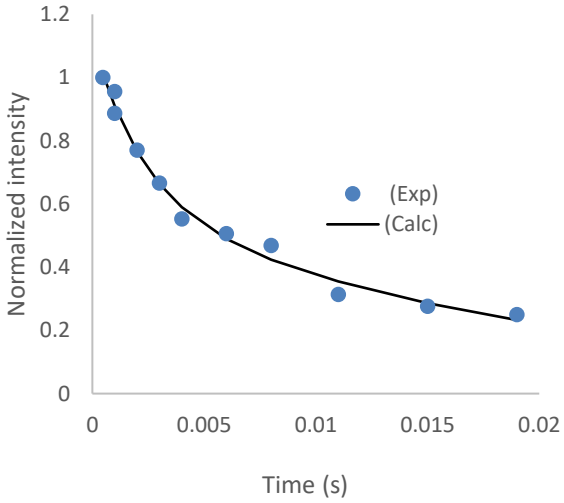

Figure 3.12. CPMG curve from the Manifa sample (8072.1 ft) at 700 MHz. The blue data points are the CPMG data, and the black line shows the exponential decay curve fitted to the echo envelope.

There are striking changes in the relaxation dispersion values for the alicyclic and aromatic signals in $CDCl_3$ with respect to the data from toluene-d_8 solutions. For the alicyclic, the T_1/T_2 ratio of the major component, with the larger T_1/T_2 value, decreased by a factor of 20 when compared to toluene-d_8, whereas the major component of the aromatic was lowered only by a factor of 2. Also note that the ratio of major to minor remains effectively constant between the three structural features and seems to be unaffected by solvent.

Table 3.10. T_1/T_2 ratios of asphaltenes from different reservoir depths using 120 s delays in toluene-d_8.

Depth (ft)	Toluene-d_8 (T_1/T_2)		
	Aliphatic	Alicyclic	Aromatic
7767.6	13.0 ± 0.78 (60-75%) 1.8 ± 0.06 (25-40%)	5000 ± 220 (60-75%) 65 ± 3.0 (25-40%)	10000 ± 390 (60-75%) 68 ± 3.1 (25-40%)
7963.5	15.5 ± 0.83 (60-75%) 2.9 ± 0.07 (25-40%)	7500 ± 290 (60-75%) 69 ± 3.2 (25-40%)	15000 ± 570 (60-75%) 70 ± 3.3 (25-40%)
8026.3	16.8 ± 0.86 (60-75%) 4.7 ± 0.12 (25-40%)	9000 ± 327 (60-75%) 76 ± 3.7 (25-40%)	17000 ± 610 (60-75%) 80 ± 3.8 (25-40%)
8070.9	17 ± 1.0 (60-75%) 5.2 ± 0.18 (25-40%)	11000 ± 430 (60-75%) 80 ± 3.7 (25-40%)	18000 ± 720 (60-75%) 85 ± 3.8 (25-40%)
8072.1	21 ± 1.38 (60-75%) 5.0 ± 0.15 (25-40%)	13000 ± 550 (60-75%) 100 ± 5.3 (25-40%)	20000 ± 640 (60-75%) 100 ± 5.6 (25-40%)

The values in parentheses represent the relative percentage of each signal having the corresponding T_1 and T_2. (See appendix for fitting curves)

The variation of T_1/T_2 ratios with increasing depth of Manifa asphaltenes dissolved in toluene-d_8 and $CDCl_3$ are shown in Tables 3.10 and 3.11, respectively. The relaxation analysis of all samples showed that each signal has two components: a major component with larger T_1/T_2 ratios and a minor component with smaller T_1/T_2 ratios. These ratios will be subsequently used to determine the size of the nanoaggregates at the various reservoir depths.

Table 3.11. T_1/T_2 ratios of asphaltenes from different reservoir depths using 120 s delays in $CDCl_3$.

Depth (ft)	$CDCl_3$ (T_1/T_2)		
	Aliphatic	Alicyclic	Aromatic
7767.6	9.8 ± 0.6 (60-75%) 1.1 ± 0.03 (25-40%)	200 ± 10 (60-75%) 73 ± 3.7 (25-40%)	6200 ± 300 (60-75%) 64 ± 3.2 (25-40%)
7963.5	11 ± 0.72 (60-75%) 1.2 ± 0.03 (25-40%)	410 ± 20 (75-85%) 80 ± 4.2 (15-25%)	8200 ± 400 (70-80%) 79 ± 4.2 (20-30%)
8026.3	11 ± 0.74 (60-75%) 1.1 ± 0.03 (25-40%)	500 ± 25 (60-75%) 88 ± 4.4 (25-40%)	9800 ± 500 (60-75%) 90 ± 4.5 (25-40%)
8070.9	12 ± 0.72 (60-75%) 4.5 ± 0.12 (25-40%)	590 ± 28 (60-75%) 90 ± 4.2 (25-40%)	11000 ± 650 (60-75%) 90 ± 4.3 (25-40%)
8072.1	17 ± 1.2 (60-75%) 5.5 ± 0.14 (25-40%)	600 ± 30 (60-75%) 90 ± 4.5 (25-40%)	11000 ± 660 (65-78%) 93 ± 4.8 (22-35%)

The values in parentheses represent the relative percentage of each signal having the corresponding T_1 and T_2.

Tables 3.10 and 3.11 show that the T_1/T_2 ratios of a major components increase significantly with depth. Figure 3.13 shows the T_1/T_2 ratios of the major components for aromatic and alicyclic signals with well depth in toluene-d_8 and $CDCl_3$.

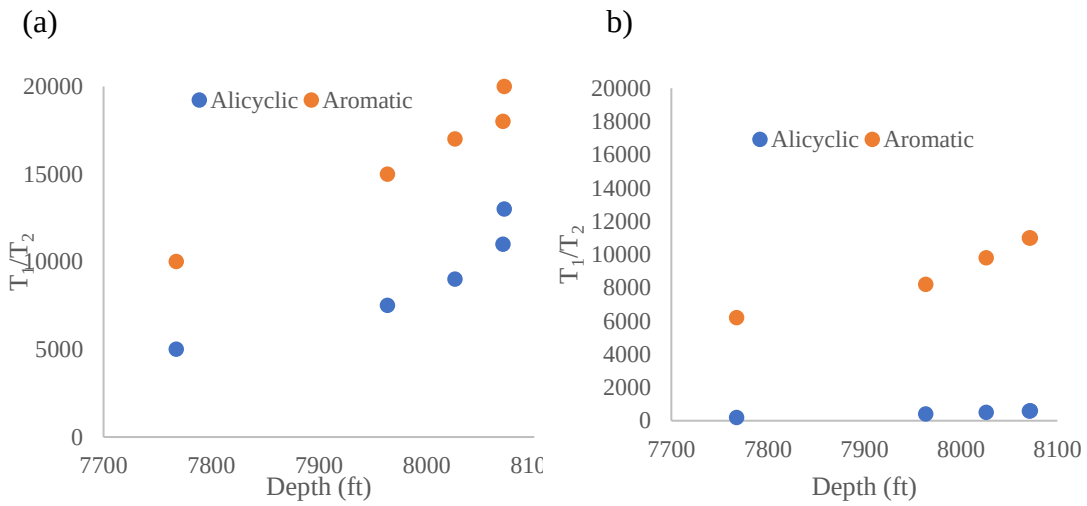

Figure 3.13. The relationship between alicyclic and aromatic T_1/T_2 ratios of component with larger T_1/T_2 values and reservoir depth in (a) toluene-d_8 and (b) $CDCl_3$.

In toluene-d_8 the increase in the ratio for aromatics is most dramatic rising from 10,000 to 20,000, while the absolute increase of the ratio for the alicyclic groups is smaller from 5000 to 13,000. In $CDCl_3$, however, the increase of T_1/T_2 ratios are smaller in absolute terms for both groups, where that of the aromatics increase from 6,200 to 11,000 and that of the alicyclic groups rise from 200 to 600. When considering the relative change, the aromatic T_1/T_2 ratios approximately double between the highest and lowest depth in both solvents, while the alicyclic T_1/T_2 ratios approximately triple. In toluene, the tighter clustering of asphaltenes may result in a more constricted environment, which can enhance steric congestion for the alicyclics and possibly cause the observed disproportionate influence on the T_1/T_2 ratios.

Furthermore, it should be noted that the relative contributions of major to the minor components remain essentially constant between depths. Also, the relative difference in T_1/T_2 ratios between solvents also remain the same for all three environments where the

$CDCl_3$ values are smaller than those of toluene-d_8 by a factor of approximately 0.7, 0.05, and 0.50 for the aliphatics, alicyclics and aromatics, respectively.

Two possible explanations are possible for the two components with different T_1/T_2 ratios. The first possible explanation is attributing the larger T_1/T_2 ratio of the three groups (aliphatic, alicyclic, and aromatic) with them being located inside the stacked cores of nanoaggregates. The component with the smaller T_1/T_2 ratio could be attributed to the groups on the periphery, providing them with an increased mobility. Some subsets of the asphaltene molecules possibly accumulate on the periphery of the stacked aggregates, being loosely bound to the stacked aromatic cores.

The second possible explanation would employ the structural hierarchy of the "island" model. The two distinct T_1/T_2 ratios of the aromatic, alicyclic and aliphatic signals indicate distinct time scales of motion and are consistent with two sizes of the asphaltene units, *i.e.*, nanoaggregates, and clusters. The large size of the T_1/T_2 ratios suggests that the latter model is valid, with the larger T_1/T_2 ratios reflecting cluster. In invariance of the percent composition between the two solvent systems, however, is not consistent with this interpretation. The T_1/T_2 ratio of the major component is still representing the motional regime of the entire aggregate/ cluster.

The relaxation rate is determined by the correlation time, τ_c, of rotational motion. In general, the ratio of T_1/T_2 increases with increasing correlation time; however, initially it seems independent of τ_c until it reaches $1/\omega_o$, after which it increases dramatically. Hence for slow motion, the T_1/T_2 ratio is an effective proxy for the timescale of motion. The relaxation of the ^1H nuclear spin polarization occurs primarily through dipole-dipole

relaxation and thus chemical shielding anisotropy mechanism can be ignored.[20] In this case, the relationship between correlation time τ_c and T_1/T_2 has been shown to be:[20]

$$\frac{T_1}{T_2} = \frac{1}{2}\frac{\left[10+37\omega^2\tau_c^2+12\omega^4\tau_c^4\right]}{\left[5+8\omega^2\tau_c^2\right]} \quad (3.2)$$

When motion is fast and the correlation time is small (*e.g.*, 1.0 ns), the T_1/T_2 approaches unity for modest magnetic field strengths. For the Manifa asphaltene samples in toluene-d_8, T_1/T_2 ratios for aromatics 20,000 correspond to correlation times 37 ns at 700 MHz, which is two to three times slower than that for the low-molecular-weight system. According to these results, asphaltene molecules form clusters instead of small aggregates, limiting their reorientation ability and supporting the island model.

The hydrodynamic radii of asphaltenes are calculated from the correlation time τ_c, using Eq. 3.3 with T = 298 K and η(toluene) = 0.56 mPa/s, and η($CHCl_3$) = 0.54 mPa/s.[21]

$$\tau_c = \left[\frac{4\pi\eta}{3kT}\right] {r_H}^3 \quad (3.3)$$

As shown in Fig. 3.14, the hydrodynamic radii calculated from the aromatic signal increase with depth. The relaxation dispersion of the aromatic signals is the most likely to represent the mobility regime of the entire aggregate, hence, the hydrodynamic radii obtained from the aromatic signals will be discussed further. The T_1/T_2 ratios of the major components for aromatics and r_H values with increasing depth of Manifa asphaltenes dissolved in toluene-d_8 and $CDCl_3$ are shown in Table 3.12. The hydrodynamic radii in $CDCl_3$, increase from 3.2 nm to 3.6 nm and those in toluene, which are larger from the onset, increase from 3.6 nm to 4 nm with depth. Thus, for both solvents particle size increases with depth while the particles in toluene are consistently larger.

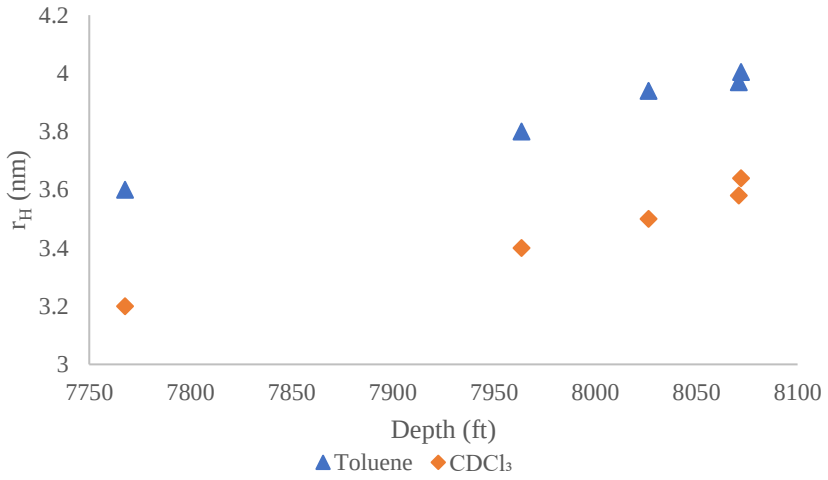

Figure 3.14. The relationship between hydrodynamic radii and reservoir depth in toluene-d_8 and $CDCl_3$, using a recycle delay of 120 s.

Table 3.12. T_1/T_2 ratios of aromatics major component and r_H values from different reservoir depths of Manifa asphaltenes.

	Toluene (T_1/T_2)		$CDCl_3$(T_1/T_2)	
Depth (ft)	Aromatic	r_H (nm)	Aromatic	r_H (nm)
7767.6	10000 ± 390	3.6 ± 0.3	6200 ± 300	3.2 ± 0.5
7963.5	15000 ± 570	3.8 ± 0.4	8200 ± 400	3.4 ± 0.5
8026.3	17000 ± 610	3.9 ± 0.4	9800 ± 500	3.5 ± 0.5
8070.9	18000 ± 720	3.9 ± 0.4	11000 ± 650	3.6 ± 0.6
8072.1	20000 ± 640	4.0 ± 0.3	11000 ± 660	3.6 ± 0.6

Hydrogen-1 NMR diffusion-ordered spectroscopy (DOSY) experiments were carried out on the Manifa asphaltene samples providing translational diffusion coefficients for the various components, thereby ideally offering supplementary information about the aggregates sizes in solution. DOSY experiments were conducted on solutions of asphaltenes in deuterated chloroform and toluene. Figures 3.15 and 3.16 show the DOSY spectra of Manifa asphaltene in deuterated chloroform and toluene, processed using the conventional algorithm and using the inverse Laplace transform (ILT).

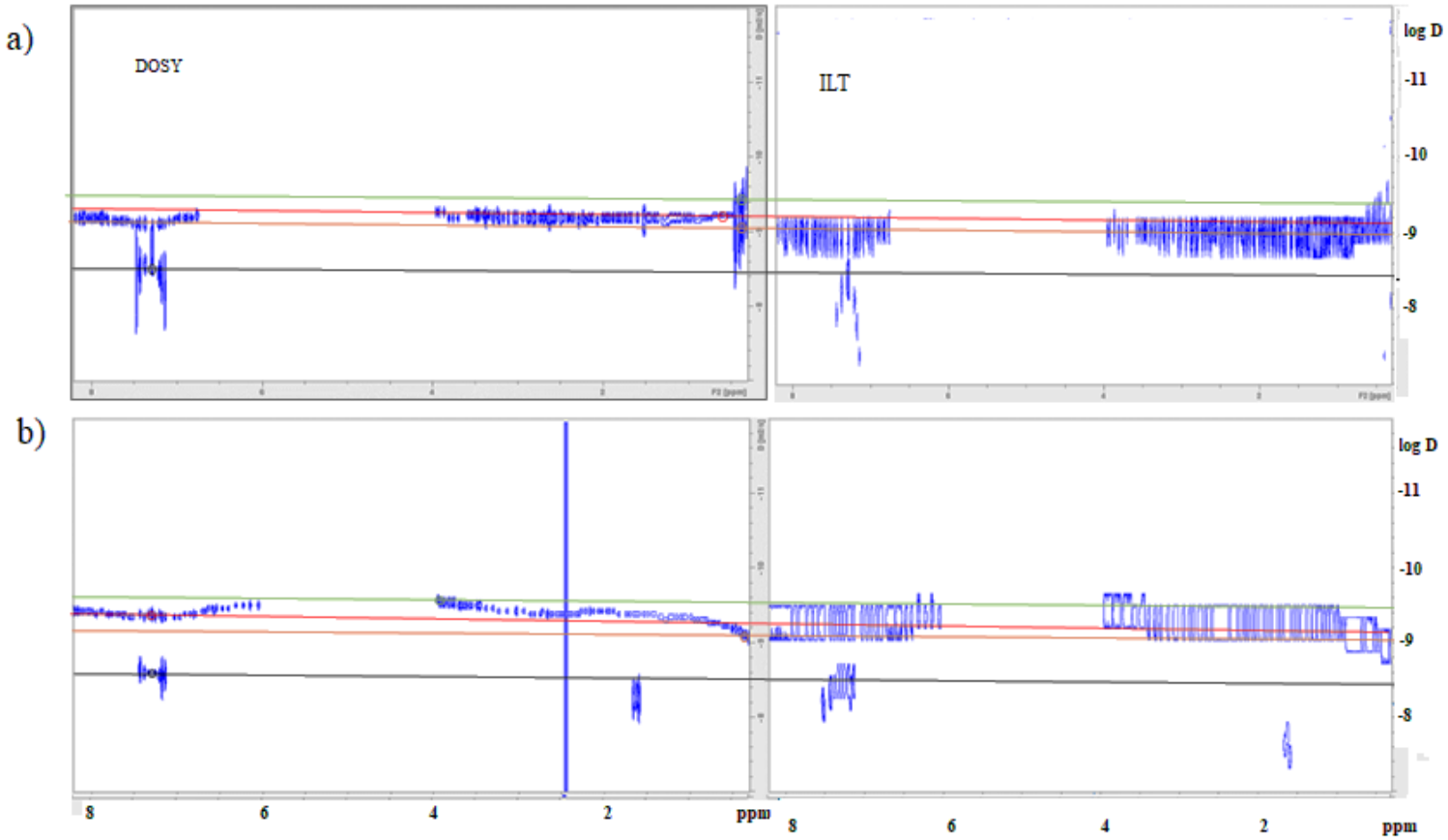
a)
DOSY
ILT
log D
-11
-10
-9
-8
b)
log D
-11
-10
-9
-8
8
6
4
2
ppm
8
6
4
2
ppm

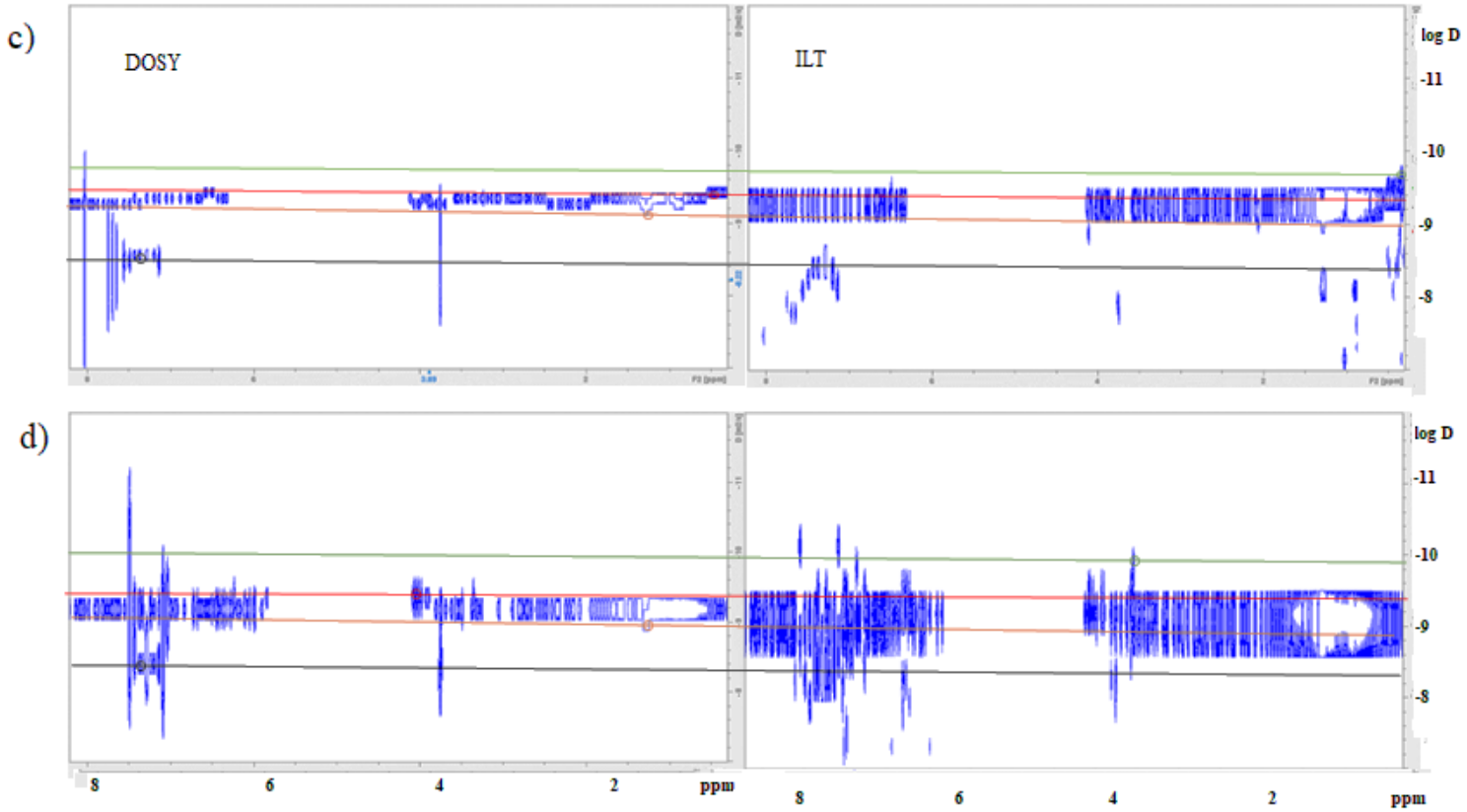

Figure 3.15. ^{1}H DOSY and the corresponding Inverse Laplace Transform (ILT) spectra of Manifa asphaltene in $CDCl_3$ at reservoir depths of (a) 7963.5 ft; (b) 8026.3 ft; (c) 8070.9 ft; (d) 8072.1 ft. X-axis represents the chemical shift in ppm and Y-axis represents the diffusion coefficient value in log form. The coloured horizontal lines indicate the components (orange-, red- and green-colored lines), as well as the solvent (black colored line), characterized by their different diffusion coefficients.

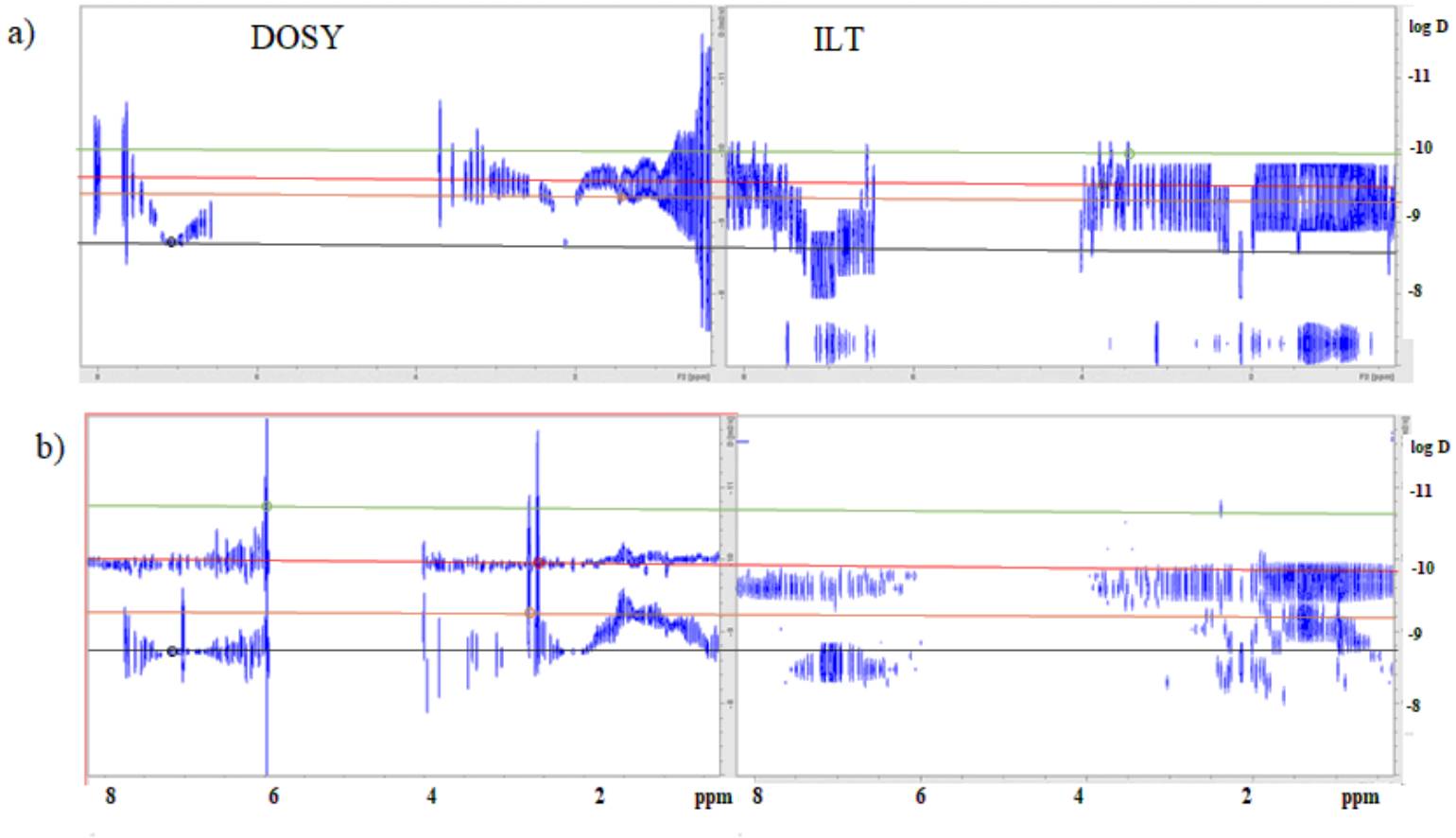
a)
DOSY
ILT
log D
-11
-10
-9
-8
b)
log D
-11
-10
-9
-8
8
6
4
2
ppm
8
6
4
2
ppm

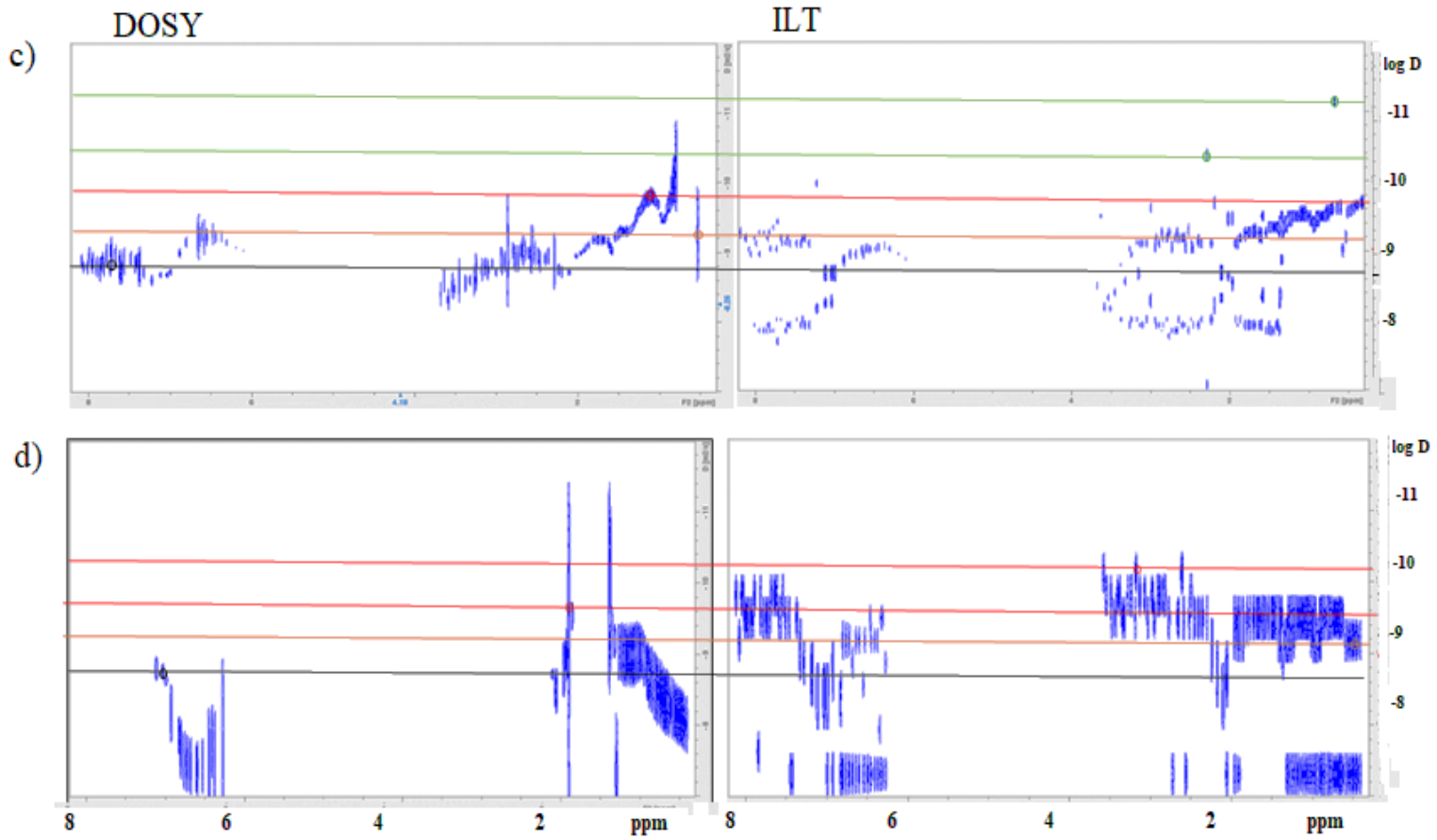

Figure 3.16. ^{1}H DOSY and the corresponding Inverse Laplace Transform (ILT) spectra of Manifa asphaltene in toluene-d_8 at reservoir depths of (a) 7963.5 ft; (b) 8026.3 ft; (c) 8070.9 ft; (d) 8072.1 ft. X-axis represents the chemical shift in ppm and Y-axis represents the diffusion coefficient value in log form. The coloured horizontal lines indicate the components (orange-, red- and green-colored lines), as well as the solvent (black colored line), characterized by their different diffusion coefficients.

In Figures 3.15 and 3.16 three groupings of cross peaks are selected (indicated by the colored lines), representing high, medium, and low diffusion coefficients; for each line one representative cross peak is shown in Figures 3.15 and 3.16 by the colored circle. The diffusion constants are tabulated for each group in Table 3.13, adjusted to 298 K and to the viscosity of the pure solvent, and the corresponding hydrodynamic radii are calculated.

Diffusion coefficients depend on sample concentration, solvent viscosity, and temperature. As solvent and solute are both influenced by these factors the relative diffusion coefficient is used, which is the ratio of the diffusion coefficient of the solute to the solvent. The benefit of using the relative diffusion coefficients (DR) is that it removes the effect of variations in viscosity and temperature. The adjusted diffusion coefficient is computed from DR using the self diffusion coefficients (D_0) of the pure solvents at 298 K, which are 2.28×10^{-9} and 3.96×10^{-9} m^2/s for toluene and chloroform, respectively (Eq. 3.4).[22,23]

$$D^* = D_o \times DR \tag{3.4}$$

Once the D* values are calculated, the Stokes-Einstein equation (Eq. 3.5) is used to calculate the samples' hydrodynamic radii (r_H).

$$D^* = \frac{kT}{6\pi\eta r_H} \tag{3.5}$$

The D* and r_H values with increasing depth of Manifa asphaltenes dissolved in $CDCl_3$ and toluene-d_8 are listed in Tables 3.13 and 3.14, respectively. The same color coding is used for the components as in Fig. 3.15 and 3.16.

Table 3.13. The diffusion coefficients (D), solvent diffusion coefficients (SD), relative diffusion coefficients (DR), adjusted diffusion coefficients (D*) and r_H values for Manifa asphaltenes in $CDCl_3$. Assuming the self-diffusion constant for chloroform is $D_o = 3.96 \times 10^{-9}$ m^2/s.

Depth (ft)	D[a] (m^2/s) × 10^{-10}	SD (m^2/s) x10^{-10}	DR	D* (m^2/s) × 10^{-10}	r_H (nm) subnano, nano
	9.33 ± 0.32		0.31 ± 0.014	12.5 ± 0.51	0.31 ± 0.02
7963.5	5.94 ± 0.16	29.5 ± 0.18	0.20 ± 0.01	7.96 ± 0.40	0.49 ± 0.05
	3.80 ± 0.11		0.12 ± 0.005	5.09 ± 0.19	0.76 ± 0.14
8026.3	8.51 ± 0.21		0.34 ± 0.009	13.4 ± 0.36	0.29 ± 0.02
	4.16 ± 0.15	25.1 ± 0.11	0.16 ± 0.007	6.59 ± 0.11	0.59 ± 0.02
	2.63 ± 0.12		0.10 ± 0.005	4.16 ± 0.21	0.94 ± 0.18
8070.9	6.45 ± 0.22		0.23 ± 0.009	9.36 ± 0.35	0.42 ± 0.02
	3.80 ± 0.12	27.5 ± 0.15	0.14 ± 0.005	5.51 ± 0.20	0.71 ± 0.05
	2.18 ± 0.08		0.08 ± 0.003	3.17 ± 0.12	1.23 ± 0.32
8072.1	9.33 ± 0.24		0.23 ± 0.01	9.33 ± 0.40	0.42 ± 0.05
	4.46 ± 0.15	39.8 ± 0.17	0.11 ± 0.006	4.47 ± 0.24	0.87 ± 0.12
	1.51 ± 0.09		0.04 ± 0.005	1.51 ± 0.17	2.58 ± 0.63

[a] Error analysis for D is based on the three-component fit performed in the dynamic center during the DOSY analysis.

Table 3.14. The diffusion coefficients (D), solvent diffusion coefficients (SD), relative diffusion coefficients (DR), adjusted diffusion coefficients (D*) and r_H values for Manifa asphaltenes in toluene-d_8. Assuming the self-diffusion constant for toluene is $D_o = 2.28 \times 10^{-9}$ m^2/s.

Depth (ft)	D[a] (m^2/s) × 10^{-10}	SD (m^2/s) × 10^{-10}	DR	D* (m^2/s) × 10^{-10}	r_H (nm) subnano, nano, and micro
	6.45 ± 0.41		0.34 ± 0.023	7.88 ± 0.53	0.50 ± 0.03
7963.5	4.07 ± 0.29	18.7 ± 0.13	0.22 ± 0.016	4.97 ± 0.37	0.78 ± 0.26
	1.54 ± 0.21		0.08 ± 0.012	1.89 ± 0.28	2.06 ± 0.79
	7.08 ± 0.39		0.34 ± 0.021	7.72 ± 0.48	0.51 ± 0.04
8026.3	2.29 ± 0.18	20.8 ± 0.12	0.11 ± 0.009	2.50 ± 0.20	1.56 ± 0.42
	0.32 ± 0.14		0.02 ± 0.007	0.35 ± 0.18	11.3 ± 2.18
	5.62 ± 0.32		0.29 ± 0.017	6.71 ± 0.39	0.58 ± 0.05
8070.9	1.58 ± 0.12	19.1 ± 0.12	0.08 ± 0.007	1.89 ± 0.16	2.06 ± 0.47
	0.39 ± 0.08		0.02 ± 0.003	0.47 ± 0.07	8.20 ± 2.01
	0.07 ± 0.01		0.004 ± 0.0008	0.086 ± 0.009	45.0 ± 9.82
	6.30 ± 0.43		0.33 ± 0.025	7.34 ± 0.50	0.53 ± 0.04
8072.1	2.08 ± 0.15	19.1 ± 0.12	0.11 ± 0.009	2.49 ± 0.21	1.56 ± 0.47
	0.74 ± 0.09		0.04 ± 0.008	0.88 ± 0.18	4.41 ± 1.41
	—		—	—	—

[a] Error analysis for D is based on the three-component fit performed in the dynamic center during the DOSY analysis.

The choice of the diffusion constants requires some comment, as at first sight they may seem somewhat inconsistent. For these samples and the limitations imposed by the spectrometer operational parameters it was not possible to meet the full dephasing conditions equally for all signals of interest. As a result, only the alkyl signals and the minor components of the alicyclic and aromatic would be considered. Even for these signals the amplitudes of the cross peaks do not reflect the relative composition. The major contributions are severely underrepresented, especially at diffusion constants smaller than 10^{-10} m^2/s. It was not possible to get consistent amplitudes for the entire range of D from 10^{-7} to 10^{-12} m^2/s. A brief account of this situation is discussed below.

The version of the DOSY pulse sequence used in these experiments is provided in Figure 3.17 and a summary of the acquisition parameters is reported in Table 3.15.

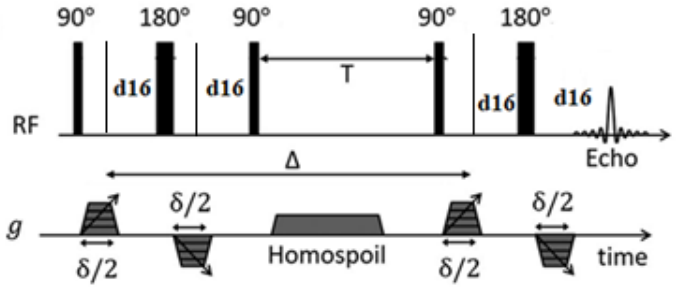

Figure 3.17. NMR diffusion pulse sequence diagrams for Pulse Field Gradient Stimulated Echo (PGSTE) experiments. Radiofrequency (RF axis) pulses are indicated by vertical bars; thin and thick bars represent 90° and 180° RF pulses respectively. Gradient pulses of incremental magnitude *g* are shown with effective pulse durations δ/2 for the PGSTE sequences, respectively. Homospoil gradients are also shown and are applied during the longitudinal storage period T to remove any residual transverse magnetisation. The diffusion time is Δ.

.

Table 3.15. Summary of PFG NMR acquisition parameters.

Pulse sequence	PGSTE
Diffusion time, Δ/ms	50-100
Maximum gradient strength/G cm^{-1}	56
Effective gradient pulse duration, δ/μs	3200-3600
Gradient recovery delay, d_{16}/μs	200
Homospoil gradient duration/μs	600
Recycle delay d_1/s	20-60
No. of scans	32

The amplitude factor associated with a given cross peak ultimately determines the intensity and diffusion constant in the DOSY spectrum. It is important that the magnetization is fully dephased with the gradient strengths applied. Dephasing must be predominantly due to diffusion, despite significant loss of signal intensity due to transverse and longitudinal

relaxation. For the Pulse Field Gradient Stimulated Echo (PGSTE) sequence with bilinear gradients the total amplitude A (δ, Δ, D, T_1, T_2) is the product of three amplitude factors[24]:

$$A(\delta, \Delta, D, T_1, T_2) = A_{transverse}(\delta, T_2) \times A_{longitudinal}(\delta, \Delta, T_1) \times A_{diffusion}(\delta, \Delta, D)$$

$$= e^{-(2\delta+4d_{16})/T_2} \times e^{-\frac{\Delta-(\delta+2d_{16})}{T_1}} \times e^{-(\Delta-\frac{\delta}{3})D(\gamma G\delta)^2} \quad (3.6)$$

Figure 3.18 shows the behaviour of the transverse amplitude factors under the experimental conditions as a function of the gradient pulse duration (δ) for the relaxation times provided in Table 3.16.

Table 3. 16. ^{1}H NMR relaxation times of Manifa asphaltene in toluene-d_8.

Depth (ft)	Aliphatic		Alicyclic		Aromatic	
	T_1 (s)	T_2(ms)	T_1 (s)	T_2 (ms)	T_1 (s)	T_2 (ms)
7767.6	0.38 ± 0.02 (65 ± 4.5%) 1.20 ± 0.04 (35 ± 3.5%)	29.2 ± 0.9 (68 ± 3.5%) 650 ± 4.2 (32 ± 4.0%)	2.38 ± 0.05 (70 ± 5.5%) 1.24 ± 0.03 (30 ± 5.0%)	0.48 ± 0.02 (65 ± 5.8%) 19.0 ± 0.8 (35 ± 3.5%)	3.50 ± 0.06 (72 ± 5.8%) 1.25 ± 0.04 (28 ± 4.5%)	0.35 ± 0.02 (68 ± 5.5%) 18.3 ± 0.9 (32 ± 4.0%)
7963.5	0.40 ± 0.02 (70 ± 3.5%) 1.20 ± 0.03 (30 ± 3.5%)	25.8 ± 0.9 (68 ± 4.0%) 414 ± 3.50 (32 ± 3.5%)	2.40 ± 0.06 (68 ± 5.5%) 1.21 ± 0.03 (32 ± 4.0%)	0.32 ± 0.01 (65 ± 5.8%) 17.5 ± 0.7 (35 ± 4.5%)	4.04 ± 0.06 (70 ± 5.5%) 1.30 ± 0.03 (30 ± 4.5%)	0.27 ± 0.01 (72 ± 4.5%) 18.5 ± 0.8 (28 ± 5.0%)
8026.3	0.46 ± 0.02 (70 ± 4.5%) 1.20 ± 0.03 (30 ± 3.5%)	28.1 ± 0.8 (68 ± 4.0%) 254 ± 1.5 (32 ± 3.0%)	2.91 ± 0.06 (68 ± 5.5%) 1.23 ± 0.04 (32 ± 4.0%)	0.32 ± 0.01 (70 ± 5.0%) 16.2 ± 0.6 (30 ± 4.5%)	4.81 ± 0.07 (70 ± 5.8%) 1.23 ± 0.04 (30 ± 3.5%)	0.29 ± 0.01 (72 ± 4.5 %) 15.1 ± 0.5 (28 ± 4.5%)
8070.9	0.51 ± 0.02 (65 ± 4.5%) 1.40 ± 0.05 (35 ± 3.5%)	29.9 ± 0.9 (70 ± 4.0%) 264 ± 1.5 (30 ± 4.5%)	3.15 ± 0.05 (65 ± 5.5%) 1.30 ± 0.03 (35 ± 4.5%)	0.28 ± 0.01 (68 ± 5.0%) 15.2 ± 0.6 (32 ± 4.0%)	6.14 ± 0.05 (73 ± 5.8%) 1.30 ± 0.04 (27 ± 4.4%)	0.34 ± 0.01 (75 ± 5.5%) 15.1 ± 0.5 (25 ± 4.0%)
8072.1	0.57 ± 0.03 (65 ± 4.2%) 1.40 ± 0.04 (35 ± 4.2%)	27.1 ± 1.1 (68 ± 4.4%) 260 ± 1.7 (32 ± 4.2%)	3.2 ± 0.05 (68 ± 5.4%) 1.5 ± 0.03 (32 ± 4.5%)	0.25 ± 0.01 (65 ± 4.5%) 16.0 ± 0.8 (35 ± 4.2%)	6.50 ± 0.05 (68 ± 5.5%) 1.50 ± 0.03 (32 ± 4.5%)	0.32 ± 0.02 (70 ± 5.0%) 15.0 ± 0.8 (30 ± 4.5%)

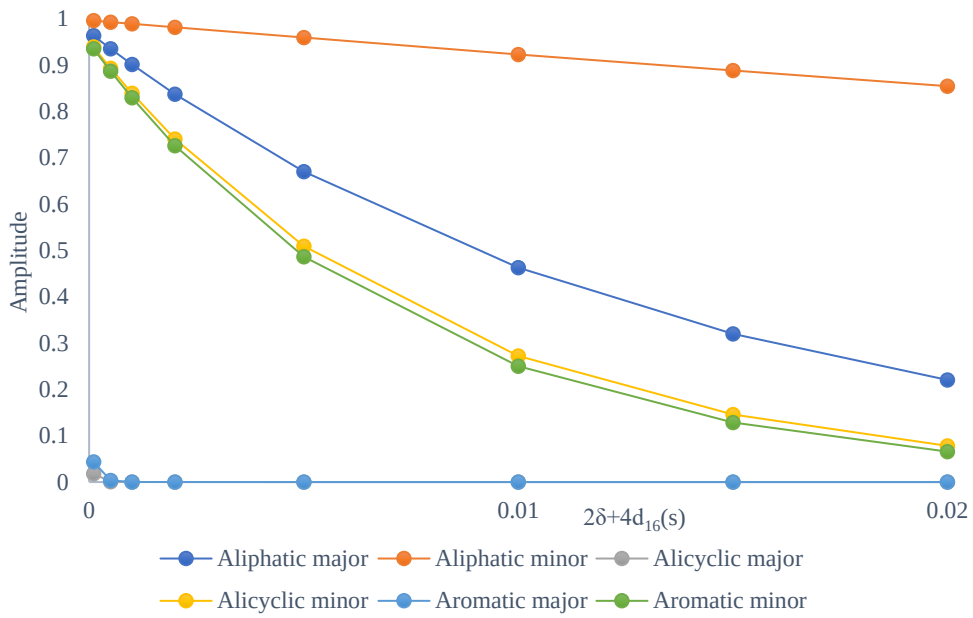

Figure 3.18. Transverse Relaxation Amplitude factors as a function of dephasing time $2\delta + 4d_{16}$, for the different T_1/T_2 components of the Manifa in toluene for $\Delta = 100$ ms.

The total dephasing time is $2\delta + 4d_{16}$, which falls within the range of 7.2 to 8 ms. For an 8 ms dephasing time, any signal with a T_2 less than 2 ms will experience significant dephasing, making it challenging to observe and analyze such signals. This means the major signals for the alicyclic and aromatic environments are lost completely, leaving the aliphatic environment as the only one with both signals observed. Shorter gradient pulse durations that would make it possible to observe the two lost signals would have to be 100 to 300 ms, which would lower the limit of diffusion constants to greater than 10^{-9} m^2/s. To maximize the range of observable diffusion constants, δ must be as large as the probe will allow which in this case is 3.6 ms. At a total dephasing time of 8 ms, the aliphatic major and minor signals will be at 55% and 93% of their original intensities.

Figure 3.19 shows the behaviour of the longitudinal relaxation amplitude factor under the experimental conditions as a function of diffusion time (Δ). At 100 ms diffusion time, all the signals show little attenuation. Note that the aliphatic signals differ dramatically, where the major signal decays rapidly compared to the minor. Thus, a window from 100 to 500 ms is available before the major signal decays too severely from ≈ 85% to ≈ 45%, where the DOSY cross peak intensity will still be sufficiently large to determine the smaller diffusion constants. Much longer diffusion times, greater than 1 s, will render the signal too weak to give clearly defined cross peaks.

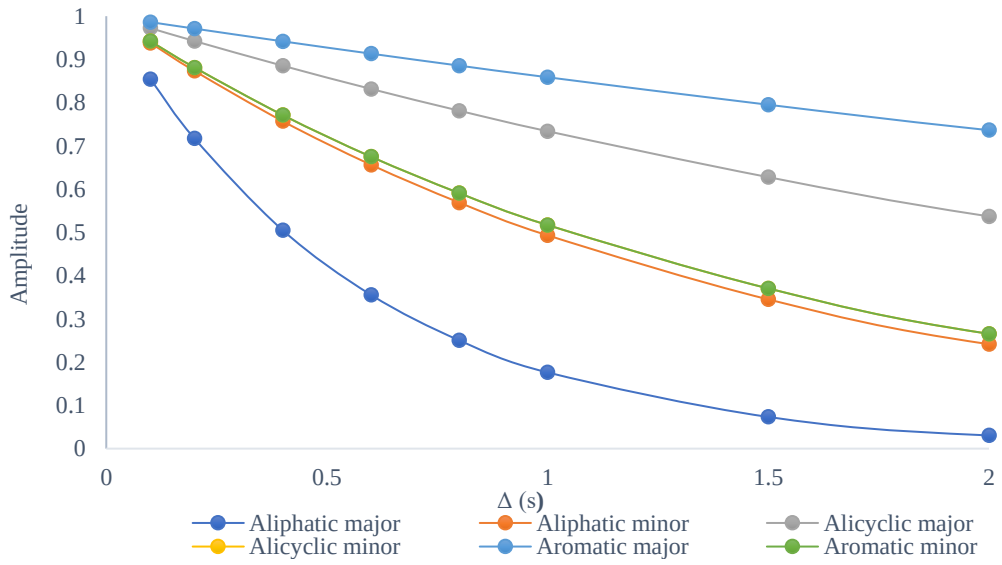

Figure 3.19. Longitudinal Relaxation Amplitude factors as a function of diffusion time Δ, for Manifa in toluene with δ = 3.6 ms.

Figure 3.20 shows the behavior of the diffusion amplitude factor as a function of diffusion constant in toluene under the experimental conditions. For addressing the choice of diffusion time, diffusion times of 100 to 5000 ms are compared. Note that the degree of dephasing during the diffusion time determines the intensity of the cross peak. Consider

the aliphatic major and minor signals at 100 ms diffusion and 3.6 ms gradient pulse times, accounting for initial relative populations (66 to 34 %), transverse (54 to 93.5%) and longitudinal (85.5 to 94.2 %) relaxation amplitudes the major and minor signal will be at 30.5 and 30.0%, respectively. For a diffusion constant of 10^{-10}, 10^{-11} and 10^{-12} m^2/s the attenuation factors will be 10, 75 and 97%. Correspondingly, for the faster diffusion rate 90% of the initial amplitude is dephased, i.e., 27.5% (30.5 × 0.9) and 27% (30.0 × 0.9) for major and minor signals, respectively, giving strong cross peaks for both signals. At the slowest diffusion rate only 3% of the initial amplitude is dephased giving very weak cross peaks for both signals (major: 30.5 × 0.03 = 0.9%; minor: 30.0 × 0.03 = 0.9%). In contrast the initial amplitudes at 500 ms will be 16.0 and 22.3% where again strong cross peaks will be seen for D = 10^{-10} m^2/s (14.4 and 20.7%) but very weak ones for 10^{-12} m^2/s (0.48 and 0.67%). In the end, not much is gained by increasing the diffusion to time to 500 ms in terms of sensitivity at the lower diffusion times in this case, which would come at a cost of 30 to 50% of the signal intensity.

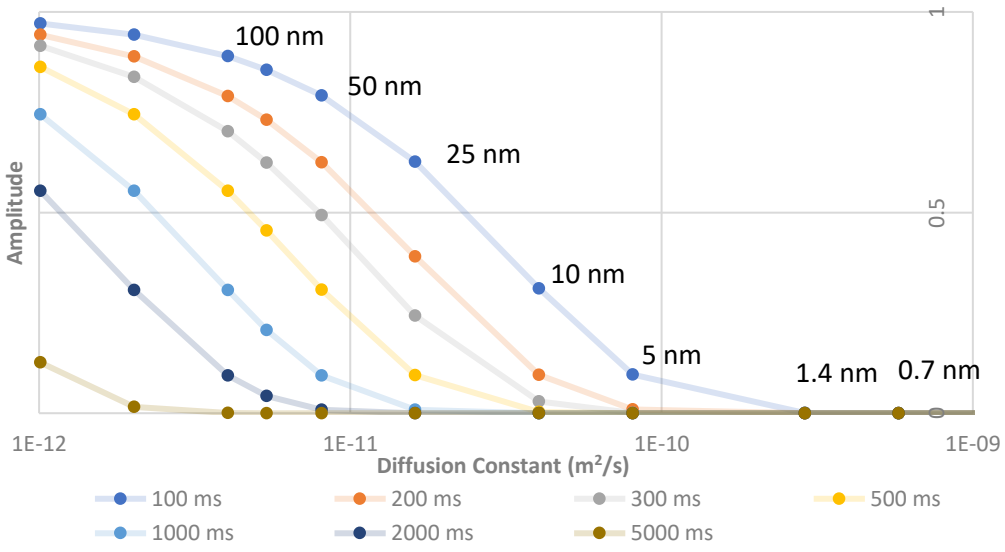

Figure 3.20. Diffusion amplitude factor as a function of hydrodynamic radius (nm) and diffusion constant for various diffusion times (Δ = 100 to 5000 ms) in toluene under the experimental conditions.

One possible interpretation of the relaxation dispersion results would correlate two particle sizes of the major and minor components to two diffusion constants. Also, one should note, that since the contribution from internal motion cannot be separately determined, these predicted diffusion constants would therefore represent the upper limit to the average for each component. Recall that hydrodynamic radii range from 3.2 to 4 nm (Table 3.12) and Table 3.17 gives those calculated for the minor component ranging from 1.5 to 1.7 nm. These radii correspond to adjusted diffusion constants of 1.0 to 1.3 × 10^{-10} m^2/s for the major and 2.4 to 2.5 × 10^{-10} m^2/s for the minor components, respectively. Experimental diffusion constants will therefore be anywhere between 20 to 50% smaller. Furthermore, the lower range of these distributions will readily approach values on the order of 10^{-11} m^2/s. Hence, robust sensitivity in the DOSY experiments to diffusion coefficients must be

achievable well into the 10^{-11} m^2/s range, which, considering the relevant relaxations times, imposes pulse field gradient strengths well beyond the limits of the probes currently in use. To attain reliable cross peak intensities over the whole range of diffusion constants anticipated dephasing curves, as seen in Fig. 3.19, for diffusion times of 1000 to 2000 ms would be ideal; therefore, the gradient strength would have to be 10 to 20 times stronger.

Table 3.17. T_1/T_2 ratios of aromatics of the minor component, D and r_H values from different reservoir depths of Manifa asphaltenes.

Depth (ft)	Toluene-d_8			$CDCl_3$		
	T_1/T_2 minor	r_H (nm)	D $\times 10^{-10}$ (m^2/s)	T_1/T_2 minor	r_H (nm)	D $\times 10^{-10}$ (m^2/s)
7767.6	68	1.53	2.52	64	1.52	2.53
7963.5	70	1.56	2.47	79	1.58	2.44
8026.3	80	1.59	2.43	90	1.62	2.38
8070.9	85	1.61	2.4	90	1.62	2.38
8072.1	100	1.65	2.34	93	1.63	2.36

DOSY studies by Oliveira *et al.*[8] on Brazilian samples collected from three distinct offshore sources, distinguishes between three aggregation states, which they labeled as nanoaggregates, microaggregates, and macroaggregates. These DOSY experiments, were performed in deuterated toluene (99.5% D) on a Varian 400 MHz spectrometer, with a gradient strength of 18 G cm^{-1}. The gradient pulse durations (δ) were within the 1.5 to 3 ms, while the diffusion delays (Δ) spanned from 0.05 to 0.45 s. The authors observed diffusion constants up to 10^{-10} m^2/s; however, they did not obtain evidence for large clusters which would have had much smaller diffusion constants.

Keeping the aforementioned caveats regarding the DOSY signal intensities in mind, the DOSY cross-peaks in both solvents were be grouped into three categories in line with Oliviera's approach, where the cross peaks with the lowest D values have particularly low intensities when compared to those at middle and higher D's. In Tables 3.13 and 3.14 the presumed sub nanoaggregates (monomers, dimers, trimers etc.) are indicated in orange, the nanoaggregates in red and the microaggregates are green.

Upon closer inspection the three categories do not align between the solvents. The first two in chloroform (orange, red), from 0.31 to 0.87 nm, and the first (orange), 0.5 to 0.6 in toluene seem to agree, and thus are considered nano. The remaining category in chloroform (green), 0.76 to 2.58 nm, is most comparable to the second in toluene (red), 0.78 to 2.06 nm; however, the alternative largest value is much greater at 4.41 nm. These will be considered microaggregates. The largest category in toluene (green) has no counterparts in chloroform, and completely disappear below at 8070 ft depth, will be referred to a macroaggregates.

A small angle X-ray scattering (SAXS) study of asphaltenes, extracted from a Saudi heavy crude, in toluene at 5 mg/ml by Eyssautier *et al.*[25] found that sub nanoaggregates reach a stable size with a hydrodynamic radius of 1.4 nm. The nano category the hydrodynamic radii (r_H) correspond to suboptimal aggregates such as monomers, dimers, trimers, *etc*. The r_H's in the micro category suggest that that the optimal size is reached, and the onset of clustering takes place up to about 3 nanoaggregates (based on the ratios of the hydrodynamic volumes) and possibly as high as 33 aggregates. The macro category is composed of clusters from 3 to 200 aggregates. The extreme values cast serious doubt on the reliability of the cross peaks at the higher D's.

In summary, DOSY analysis reveals a dynamic interplay of varying populations with different sizes, showing differences between solvents and variations with depth. Across both solvents, there is a consistent trend of increasing particle sizes with depth, observed for nano-, micro-, or macro-aggregates, with the aggregates consistently larger in toluene.

These trends are consistent with those from the T_1/T_2 ratios; however, there are some notable differences. In contrast, the relaxation dispersion results show only two categories, mainly because of the limitation of a biexponential analysis. Triexponential analysis of the relaxation data would not provide reliable data and a larger component was allowed to saturate (see above). The hydrodynamic radii derived from the T_1/T_2 of the major component in toluene range from 3.6 to 4 nm, indicating cluster sizes between 17 and 23 nanoaggregates. This is akin to the DOSY results for the micro category, but not identical where r_H increases from 0.78 to 4.41 nm. The hydrodynamic radii from the T_1/T_2 values in toluene for the minor component fall within the 1.5 to 1.7 nm range, suggestive of the stable nanoaggregates and small clusters of 2 to 3 nanoaggregates, which is in line with the nano category for DOSY. The question therefore remains as to how the major and minor components of T_1/T_2 parse into the size categories for DOSY. This would depend on the relative contributions from each category which cannot be determined from the DOSY data. If the sub-nano and macro are relatively minor contributions, they will have little impact on the average size. In this case the major component should be dominated by the micro and the minor by the nano.

3.4. Conclusion

1) The structural composition of asphaltenes at varying reservoir depths was assessed using a quantitative ^{1}H NMR spectroscopic method. All ^{1}H NMR experiments required extended recycle delays (120 s) to prevent signal saturation, particularly for the two components of interest. A third very low intensity long-lived component was allowed to saturate.

The spectral data was analyzed using a deconvolution model, which separated the spectrum into three distinct regions of interest: aliphatic, alicyclic, and aromatic. The results showed that structural changes varied minimally with depth. Specifically, there was a slight increase in the signal from the aromatic core and a corresponding minor decrease in the aliphatic signal. These findings are consistent with decreasing molar volume and consequent increasing density with increasing reservoir depth.

2) Relaxation Dispersion experiments show the presence of two components, each exhibiting a significant disparity in the correlation times among their aliphatic, alicyclic, and aromatic regions. Hence the mobility in the aromatic group was consistently 2 to 3 orders of magnitude less than the aliphatic, and the alicyclic was either close to the aromatic or right in between the aromatic and alicyclic values. This hierarchy in mobility with structural environments, aligns with the steric congestion that would be encountered during the formation of aggregates via staggered π-π stacking. Notably, this mobility hierarchy is most pronounced in the major component, whereas in the minor components it was much less apparent due to their higher degrees of internal motion for all environments.

^{1}H relaxation dispersion experiments showed that for the aromatic, alicyclic and aliphatic there were two distinct time scales of motion, consistently in the same relative proportion

across all environments and solvents. The T_1/T_2 ratios in all environments increased with depth, and those in toluene were consistently larger than those in chloroform. The analysis was limited to a two-component owing to numerical stability concerns and the reported r_H values represent the lower limit for the average aggregate dimensions, as all internal motion cannot assumed to be queued.

3) DOSY NMR experiments provide complementary insights into the aggregate sizes of in both solvents. The diffusion constants suggest the existence of three distinctive aggregation states, referred to as sub nanoaggregate (0.3-0.8 nm), nanoaggregates (0.5-2.1 nm) and microaggregates (0.8-8.2 nm), within both solvents. Notably, the presence of large clusters is solely observed in toluene and not in $CDCl_3$. There is a consistent trend of increasing particle sizes with depth, with the aggregates consistently larger in toluene. For signals with r_H greater than 4 nm the maximum pulsed field gradient strength limits the cross-peak intensities. Consequently, the relative distribution between the larger and smaller aggregated can not be ascertained. It is worth noting that the DOSY has limited utility for particles larger than 4 nm; however, the T_1/T_2 ratios can accurately reflect them.

REFERENCES

1. Khormali, A.; Sharifov, A. R.; Torba, D. I., The control of asphaltene precipitation in oil wells. Petroleum Science and Technology 2018, 36 (6), 443-449.

2. Zuo, J. Y.; Mullins, O. C.; Mishra, V.; Garcia, G.; Dong, C.; Zhang, D., Asphaltene Grading and Tar Mats in Oil Reservoirs. Energy & Fuels 2012, 26 (3), 1670-1680.

3. Pomerantz, A. E.; Le Doan, T. V.; Craddock, P. R.; Bake, K. D.; Kleinberg, R. L.; Burnham, A. K.; Wu, Q.; Zare, R. N.; Brodnik, G.; Lo, W. C. H., Impact of laboratory-induced thermal maturity on asphaltene molecular structure. Energy & Fuels 2016, 30 (9), 7025-7036.

4. Pomerantz, A. E.; Seifert, D. J.; Bake, K. D.; Craddock, P. R.; Mullins, O. C.; Kodalen, B. G.; Mitra-Kirtley, S.; Bolin, T. B., Sulfur chemistry of asphaltenes from a highly compositionally graded oil column. Energy & Fuels 2013, 27 (8), 4604-4608.

5. Wu, Q.; Seifert, D. J.; Pomerantz, A. E.; Mullins, O. C.; Zare, R. N., Constant asphaltene molecular and nanoaggregate mass in a gravitationally segregated reservoir. Energy & Fuels 2014, 28 (5), 3010-3015.

6. Pomerantz, A. E.; Seifert, D. J.; Qureshi, A.; Zeybek, M.; Mullins, O. C., The molecular composition of asphaltenes in a highly compositionally graded column. Petrophysics-The SPWLA Journal of Formation Evaluation and Reservoir Description 2013, 54 (05), 427-438.

7. Cai, S.; Seu, C.; Kovacs, Z.; Sherry, A. D.; Chen, Y., Sensitivity Enhancement of Multidimensional NMR Experiments by Paramagnetic Relaxation Effects. Journal of the American Chemical Society 2006, 128 (41), 13474-13478.

8. da Silva Oliveira, E. C.; Neto, Á. C.; Júnior, V. L.; de Castro, E. V. R.; de Menezes, S. M. C., Study of Brazilian asphaltene aggregation by Nuclear Magnetic Resonance spectroscopy. Fuel 2014, 117, 146-151.

9. Fergoug, T.; Bouhadda, Y., Determination of Hassi Messaoud asphaltene aromatic structure from 1H & 13C NMR analysis. Fuel 2014, 115, 521-526.

10. Hauser, A.; AlHumaidan, F.; Al-Rabiah, H.; Halabi, M. A., Study on Thermal Cracking of Kuwaiti Heavy Oil (Vacuum Residue) and Its SARA Fractions by NMR Spectroscopy. Energy & Fuels 2014, 28 (7), 4321-4332.

11. Simmonds, D.; Banks, L.; Steiner, R.; Young, I., NMR anatomy of the brain using inversion-recovery sequences. Neuroradiology 1983, 25 (3), 113-118.

12. McDonald, G. G.; Leigh Jr, J. S., A new method for measuring longitudinal relaxation times. Journal of Magnetic Resonance (1969) 1973, 9 (3), 358-362.

13. Meiboom, S.; Gill, D., Modified spin-echo method for measuring nuclear relaxation times. Review of scientific instruments 1958, 29 (8), 688-691.

14. Bain, A. D.; Cramer, J., Slow chemical exchange in an eight-coordinated bicentered ruthenium complex studied by one-dimensional methods. Data fitting and error analysis. Journal of Magnetic Resonance, Series A 1996, 118 (1), 21-27.

15. Ferguson, R. C.; Marquardt, D. W., Computer analysis of NMR spectra: magnetic equivalence factoring. The Journal of Chemical Physics 1964, 41 (7), 2087-2095.

16. Chinelatto Júnior, L. S.; Cabral de Menezes, S. M.; Honorato, H. d. A.; Oliveira, M. C. K. d.; Marques, L. C. d. C., Dosy-Nmr as an Alternative Technique to Improve Asphaltenes Characterization. Energy & Fuels 2018.

17. Zdanowska-Fraczek, M.; Medycki, W., 35Cl NQR and 19F NMR relaxation studies of CClF2 group dynamics in N (CH3) 4H (ClF2CCOO) 2. Solid State Nuclear Magnetic Resonance 1996, 6 (2), 141-146.

18. Horsewill, A.; Tomsah, I., Bi-exponential nuclear spin-lattice relaxation in solid hexafluoroacetylacetone. Solid State Nuclear Magnetic Resonance 1993, 2 (1-2), 61-72.

19. Bloembergen, N.; Purcell, E. M.; Pound, R. V., Relaxation effects in nuclear magnetic resonance absorption. Physical review 1948, 73 (7), 679.

20. Levitt, M. H., Spin dynamics: basics of nuclear magnetic resonance. John Wiley & Sons: 2013.

21. Santos, F. J. V.; Nieto de Castro, C. A.; Dymond, J. H.; Dalaouti, N. K.; Assael, M. J.; Nagashima, A., Standard Reference Data for the Viscosity of Toluene. Journal of Physical and Chemical Reference Data 2005, 35 (1), 1-8.

22. Golubev, V.; Gurina, D.; Kumeev, R., Self-diffusion and heteroassociation in an acetone–chloroform mixture at 298 K. Russian Journal of Physical Chemistry A 2018, 92, 75-78.

23. Bellaire, D.; Kiepfer, H.; Münnemann, K.; Hasse, H., PFG-NMR and MD simulation study of self-diffusion coefficients of binary and ternary mixtures containing cyclohexane, ethanol, acetone, and toluene. Journal of Chemical & Engineering Data 2020, 65 (2), 793-803.

24. Johnson, C. S., Diffusion ordered nuclear magnetic resonance spectroscopy: principles and applications. Progress in Nuclear Magnetic Resonance Spectroscopy 1999, 34 (3), 203-256.

25. Eyssautier, J.; Levitz, P.; Espinat, D.; Jestin, J.; Gummel, J.; Grillo, I.; Barré, L., Insight into asphaltene nanoaggregate structure inferred by small angle neutron and X-ray scattering. The Journal of Physical Chemistry B 2011, 115 (21), 6827-6837.

CHAPTER 4

CHARACTERIZATION OF GREEN RIVER OIL SHALE BY NMR SPECTROSCOPY

4.1. Introduction

Oil shale is a sedimentary rock that has been a subject of interest for its potential as a source of oil and gas. This resource is becoming increasingly important because of its high energy content and the growing demand for fossil fuels. Oil shale is an abundant and widely available resource, primarily found in North America, making it a potentially attractive alternative to conventional oil reserves that are becoming depleted.[1] However, it is important to note that not all shale oil formations can be economically exploited through hydraulic fracturing or fracking. Sometimes, the geological structure of shale formations makes it difficult to extract oil efficiently. This may limit the production of oil from shale in such formations. But, with the advancements in technology for shale oil extraction and utilization, the interest in this resource as a new source of hydrocarbons for energy generation is growing.

The organic material in oil shale is called kerogen, a complex mixture of macromolecules. The formation of kerogen in sedimentary rocks involves several processes, such as the deposition of organic-rich sediments, compaction, burial, and chemical alteration.[2] As the organic-rich sediments are buried and compacted under the weight of overlying sediment, they undergo diagenesis, leading to kerogen formation. This process involves physical and chemical changes, including the breakdown of complex organic molecules and the rearrangement of carbon atoms to form simpler, more stable molecules.[3]

Over time, the kerogen can be transformed through a process called catagenesis, which involves increasing temperature and pressure. This transformation can lead to the conversion of kerogen into bitumen enriched in polar (NSO) compounds. Additional heating (~90-140°C), breaks C-C bonds in polar compounds and residual kerogen, yielding a hydrocarbon-rich liquid that is expelled from the source rock. Further thermal transformation results in the production of primarily condensate and then wet gas.[2] Catagenesis is complete when kerogen can no longer generate hydrocarbons, and metagenesis may occur, producing only methane. The factors that influence the transformation of kerogen into hydrocarbons include the composition of the original organic matter, the temperature and pressure conditions, and the geological history of the sedimentary basin. Figure 4.1 shows the kerogen decomposition kinetic model along with estimates of expelled fluid composition.

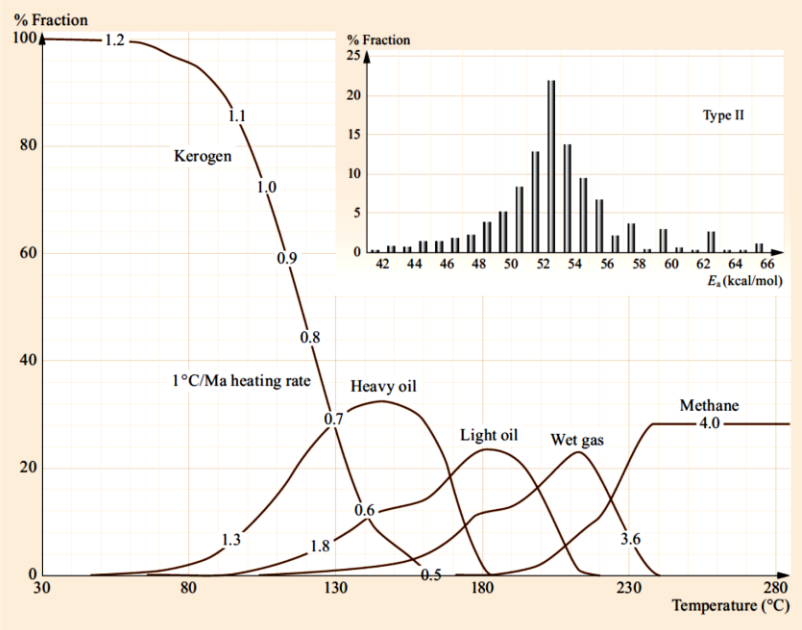

Figure 4.1. Kerogen decomposition kinetic model with predictions of generated fluid composition. (Reproduced with permission from Chang Samuel Hsu; Paul R. Robinson. *Springer Handbook of Petroleum Technology;* Springer International Publishing: **2017**, 359-375).

It has taken millions of years to go through the natural catagenesis processes required to convert it to oil and gas. Kerogen, however, can also be converted artificially to bitumen, from which oil can be generated by pyrolysis processes.

Pyrolysis is a process that transforms kerogen to oil by heating oil shale kerogen under anaerobic conditions, known as retorting. During retorting, the kerogen is crushed and then heated to a temperature of about 500-550°C in the absence of air. This causes the organic matter to thermally decompose into simpler hydrocarbons, such as oil and gas. The hydrocarbons are then extracted from the shale using various methods such as condensation, fractionation, or absorption. [4, 5]

Pyrolysis has been the traditional method used for large-scale production. However, this surface retort technology is not suitable for deposits located more than 250 meters below the surface. *In-situ* retorting has emerged as the most practical method for extracting oil from such resources. *In-situ* retorting involves drilling wells into the shale formation, heating the oil shale kerogen underground at temperatures of 300-350 °C for days to months. Then extracting the resulting liquid or gas through recovery wells. This method was used for commercial production in Sweden in the mid-20th century and has since been the subject of extensive theoretical modeling and laboratory experiments.[6] Field tests have been conducted by companies like Unocal and Shell, with the latter proving to be superior to surface retort methods in terms of oil quality and environmental impact. Currently, new *in-situ* field tests are being planned by American Shale Oil LLC[7] and ExxonMobil.[8]

Oil shale pyrolysis has been extensively studied, with most research focusing on the Mahogany (R-7) zone of the Green River Formation. While the Mahogany zone is one of the world's richest sources of oil shale kerogen, its proximity to potable water aquifers poses

challenges for *in-situ* oil and gas generation.[3] However, this study focuses on samples taken from the R-1 zone of the Garden Gulch Member, which is the deepest kerogen-rich layer of the Green River Formation. This zone is a desirable target for oil shale production operations because it is isolated from shallower freshwater aquifers, making it a promising option for future oil shale production.

Semi-open laboratory pyrolysis experiments were conducted on Green River Shale. This system differs from other pyrolysis systems, as it is capable of operating over a range of pressures, which is an important variable that can significantly affect the results of the pyrolysis process. The samples were subjected to various operating conditions, including a range of pressure, temperature which resulted in the production of various samples at different maturities. The study found systematic effects of maturity on the composition of the organic matter, particularly the kerogen and bitumen phases. Bitumen was the primary product from kerogen breakdown at relatively low maturities, while at higher maturities, the bitumen itself broke down to form the majority of the produced fluids. Furthermore, the pyrolysis process caused changes in the composition of the bitumen phase, such as altering the H/C ratio, aromaticity, alkane chain distribution, oxygenated functional group abundance, sulfur content, and sulfur speciation. In the current study, the asphaltenes from the Green River shale oil are analysed using solution-state NMR spectroscopy techniques to see how the structural composition of asphaltenes changes with maturity.

4.2. Experimental Section

4.2.1. Pyrolysis Experiment

Andrew *et al*.[4] conducted pyrolysis experiments to obtain asphaltene samples at various maturity levels. To pyrolyze the Green River samples, they developed a semi-open self-purge reactor that was designed to mimic *in-situ* oil shale processing. In this experiment, different conditions were applied, including increasing the temperature from room temperature to 180°C, followed by gradually raising the temperature to the highest temperature (300–435°C) over variable time periods (5–12.5 h). An automatic valve system released vapors generated while keeping pressure constant (1–5 MPa).[3]

The maturity of asphaltene samples is measured using EASY%R_O measurements. EASY%R_O value is based on vitrinite reflectance measurements used to estimate the thermal maturity of petroleum source rocks and bitumen.[9] The vitrinite reflectance is calculated by microscopic analysis of rock samples and is measured as a percentage of light reflected from a sample as its temperature increases. EASY%R_O is obtained using a numerical algorithm for calculating vitrinite reflectance based on temperature changes.[10]

Shale rocks, containing kerogen that naturally matures at 0.48% EASY%R_O, were subjected to pyrolysis experiments, producing a series of samples with increasing maturity levels ranging from 0.78% to 1.28% EASY%R_O. Subsequently, NMR experiments were conducted on five samples, each corresponding to different maturity levels: 0.48%, 0.78%, 0.95%, 1.19%, and 1.28% EASY%R_O. The distribution of organic products from the pyrolysis experiments is represented in Figure 4.2.

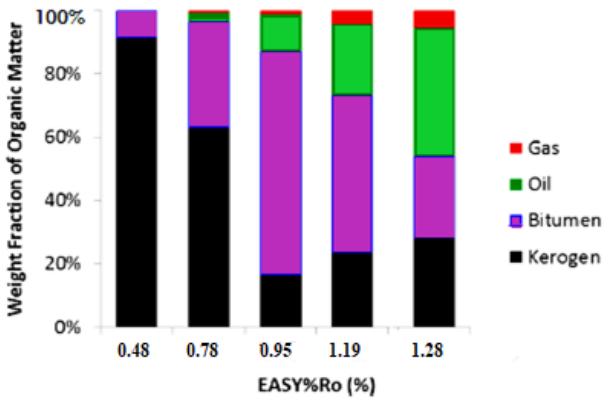

Figure 4.2. Organic products distribution from the pyrolysis experiments. (Reproduced with permission from Pomerantz, A. E.; Le Doan, T. V.; Craddock, P. R.; Bake, K. D.; Kleinberg, R. L.; Burnham, A. K.; Wu, Q.; Zare, R. N.; Brodnik, G.; Lo, W. C. H. *Energy & Fuels* **2016,** *30* (9), 7025-7036.)

4.2.2. Asphaltene Collection

Asphaltene samples were provided by Schlumberger-Doll Research, Cambridge, Massachusetts, USA. AMSO (American shale oil) is the codename for the asphaltene samples in this current study. The AMSO asphaltenes extraction process has been extensively discussed in the literature.[4] The elemental composition of the AMSO asphaltenes was determined using conventional combustion analysis.[4] The results of the elemental analysis of the asphaltene samples are shown in Figure 4.3.

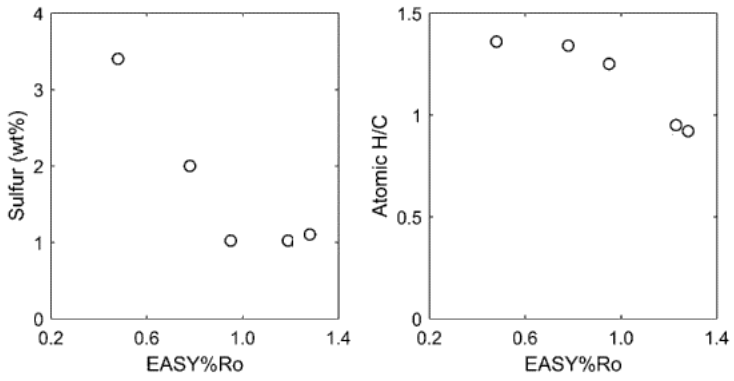

Figure 4.3. Elemental analysis of the asphaltene samples. (Reproduced with permission from Pomerantz, A. E.; Le Doan, T. V.; Craddock, P. R.; Bake, K. D.; Kleinberg, R. L.; Burnham, A. K.; Wu, Q.; Zare, R. N.; Brodnik, G.; Lo, W. C. H. *Energy & Fuels* **2016,** *30* (9), 7025-7036.)

As can be seen in this graph, both the sulfur concentration and the H/C ratio exhibit clear trends with increasing maturity. Initially, sulfur content decreases from 3.4 wt% to 1.0 wt% during maturation and then stabilises around 1.0 wt% at higher maturities. Conventional petroleum asphaltenes from different places have a wide range of sulfur levels, and these samples are all within that range.[11] The H/C ratios of pyrolyzed asphaltenes decline steadily from 1.36 at the lowest maturity to 0.92 at the highest maturity. As a point of contrast, the typical H/C ratio for petroleum asphaltenes extracted from traditional sources has been determined to be 1.14.[12]

4.2.3. Sample Preparation

For NMR analysis, asphaltene samples of 30 g/L concentration were used, and experiments were carried out at room temperature (25°C). The NMR samples were made using toluene-d_8 and $CDCl_3$ as solvents, which were purchased from Sigma-Aldrich and used as received. A small vial was used for the preparation of the solutions. First, 30 mg of asphaltene was

weighed out in a plastic weighing dish using an electronic analytical balance (Mettler Toledo, accuracy: 0.1 mg). The sample was then transferred into a small vial and dissolved in 1 mL (dispensed from a sealed 1-mL ampoule) of a deuterated solvent ($CDCl_3$ or toluene-d_8). A vial was used to ensure more effective mixing of the sample compared to using an NMR tube. The samples were treated with vortexing (VWR mini vortexer) for one minute in order to get thorough dissolution and to avoid the presence of particulates that would interfere with effective shimming. Subsequently the solution was transferred into the NMR tube using a glass Pasteur pipette. All the analyses were carried out using 5-mm NMR tubes, which were supplied by Wilmad Lab Glass. Based on the line width of the residual solvent signal, it was not deemed necessary to purge the samples with N_2 gas. The presence of oxygen was not controlled because the effect of oxygen on the relaxation rate was negligible. The influence of oxygen is only noticeable in systems with low molecular weight and solvents with extremely low viscosity. After the samples were prepared for NMR experiments, the outside of the tube was cleaned with acetone. In the NMR lab, Kimwipes were used to clean the bottom of the tube before placing it in a sample changer.

4.2.4. ^{1}H NMR Experiment

All NMR spectra were obtained using a Bruker Avance III HD 700 MHz NMR spectrometer operating at 16.4 T, equipped with a triple resonance Bruker TXO-Z (C/F-H-2H) probe equipped with a ^{2}H lock channel, automatic tuning and matching, and Z-gradient. Experiments were performed at room temperature, and the sample appeared to be completely dissolved. No evidence for phase inhomogeneity was found, since throughout the NMR investigations the reference signals always had a symmetric and narrow. Any phase inhomogeneity present on the microscopic scale would have resulted in difficulties

shimming the spectrum. The 1D ^{1}H NMR spectra were recorded with a 90° pulse width of 12.4 µs, and 128 transients. Choosing the appropriate recycle delay is essential, as discussed in Chapter 3, where 120 s was ascertained to give quantitative results. Any significantly longer delay than 120 s was deemed impracticable due to the length of time required to get an acceptable signal-to-noise ratio.

4.2.5. Relaxation Experiment

For ^{1}H T_1 and T_2 NMR measurements, samples were prepared in both solvents (toluene-d_8 and $CDCl_3$). The relaxation experiment used the same samples as were used in the ^{1}H NMR experiment. ^{1}H NMR relaxation data were obtained using a Bruker Avance III HD 700 MHz spectrometer operating in a four high power channels (HFXY) mode using a triple resonance Bruker TXO-Z (C/F-H-2H) probe equipped with a ^{2}H lock channel, automatic tuning and matching, Z-gradient, and VT capabilities. All spectra were obtained using a sweep width of 700 kHz, data points were zero-filled to 64k data points, unless stated otherwise. All relaxation data were acquired at room temperature. T_1 relaxation times were obtained using the inversion recovery pulse sequence[13] of the form {-RD-$p_1(180^0)$-τ-$p_2(90^0)$-aq(acquire)}; the phase cycles were: p_1: {x, -x}$_4$; p_2: {x_2, -x_2, y_2, -y_2}; aq: {x_2, -x_2, y_2, -y_2} and the recycle delay used was 120 s. The delay array used was 0.001, 0.35, 0.75, 1.5, 2, 2.2, 2.5, 2.7, 3, 3.2, 3.5, 4, 4.5, 5, 10, 20, 30, 45, 60, 75, 90, and 120 s with 8 scans for each delay.

T_2 relaxation data were obtained using the CPMG (Carr-Purcell-Meiboom-Gill) pulse sequence[14] of the form [–RD–p_1(90°)–{τ–p_2(180°)–τ}$_n$–aq(acquire)]; the phase cycles were: p_1: {x, x, -x, -x, y, y, -y, -y}; p_2: {y, -y, y, -y, x, -x, x, -x}; aq:{ x, x, -x, -x, y, y, -y, -y}; the time delay between the pulses was 2 ms and the recycle delay was 120 s. The delay

array was: 4, 6, 8, 10, 16, 20, 24, 36, 60, 70, 80, 120, 180, 250, 350, 450, 500, 750, 1000, and 1250 ms with 8 scans for each delay. Data were Fourier-transformed, baseline-corrected, and phased. The integration and deconvolution analysis were performed by MestRenova software (version 14.2.0).

4.2.6. Bi-exponential fits

The analysis of the bi-exponential behavior of the T_1 and T_2 curves is an important mathematical tool for NMR relaxation studies of complex samples. Commonly, the linear regression method is used to analyze T_1 and T_2 relaxation data as if they would follow mono-exponential behavior because it is a simple and straightforward way to model the decay of the magnetic signal over time. The basic premise of the linear regression method is that the logarithm of the signal intensity is linearly related to the time constant, which can be easily estimated by fitting a straight line to the logarithm of the signal intensity versus time data. The advantage of this method is that it is relatively simple to implement and provides quick and robust estimates of the T_1 or T_2 relaxation time constant.

However, when the T_1 or T_2 relaxation data exhibit a bi-exponential behavior, meaning that the relaxation is described by the sum of two exponential decays, the linear regression method is not appropriate. Using the linear regression method to analyze bi-exponential T_1 or T_2 relaxation data can result in a massive systematic error.[15] The current study uses the nonlinear fitting optimization method to analyze the relaxation curves properly. This nonlinear optimization was carried out with the Levenberg-Marquardt optimization method.[16]

4.2.7. Error Considerations

In this work, the amount of supplied sample was limited, allowing for the preparation of one NMR sample per asphaltene sample. In the case of ^{1}H NMR studies, the error for the relative method comes from the deconvolution of the peak fitting, and a residual error (RE) was obtained from (χ^2/N) values. In the case of relaxation studies, relative errors arise from the regression analysis with a regression error of around 1.5%.

4.3. Results and Discussion

Five asphaltene samples were studied with maturity levels of EASY%R_O values ranging from 0.48 to 1.28%. The isolated asphaltene samples are shown in Figure 4.4. Their colors change from brown to black as they mature. A darker black color indicates increased aromaticity and larger fused ring systems.[17,18]

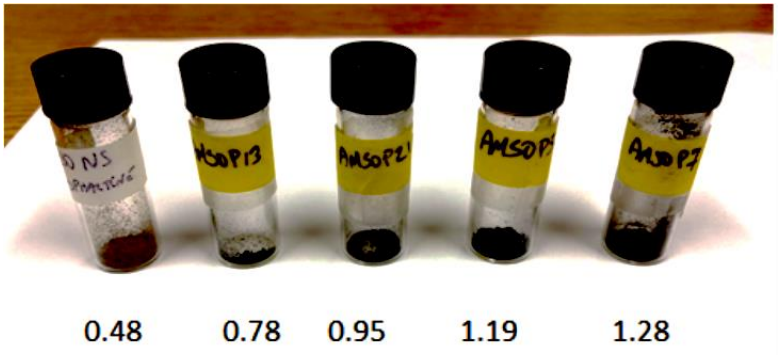

Figure 4.4. Photograph of asphaltenes samples with maturity (EASY%R_O). (Reproduced with permission from Pomerantz, A. E.; Le Doan, T. V.; Craddock, P. R.; Bake, K. D.; Kleinberg, R. L.; Burnham, A. K.; Wu, Q.; Zare, R. N.; Brodnik, G.; Lo, W. C. H. *Energy & Fuels* **2016,** *30* (9), 7025-7036.)

The ^{1}H NMR spectra of five asphaltenes with different maturities were recorded. All spectra are composed of overlapping signals. Instead of analyzing the full spectra, four regions of the first two samples, which were less mature and three regions for remaining sample containing signals of interest were primarily focused on, because limiting the region reduces the possibility of signal contamination from different structural environments with similar chemical shifts. Signals in specific chemical shift regions (aromatic, alkenyl, alicyclic, aliphatic) of the asphaltenes were deconvolved using the smallest number of deconvolution components, providing quantitative information about NMR parameters for each signal. The deconvolved components have their individual chemical shifts, line widths, signal intensities, areas, and Lorentzian/Gaussian (L/G) ratios. Figure 4.5 presents the ^{1}H NMR spectra of five asphaltenes samples, showing the main spectral zones assigned to each molecule.

a) b)

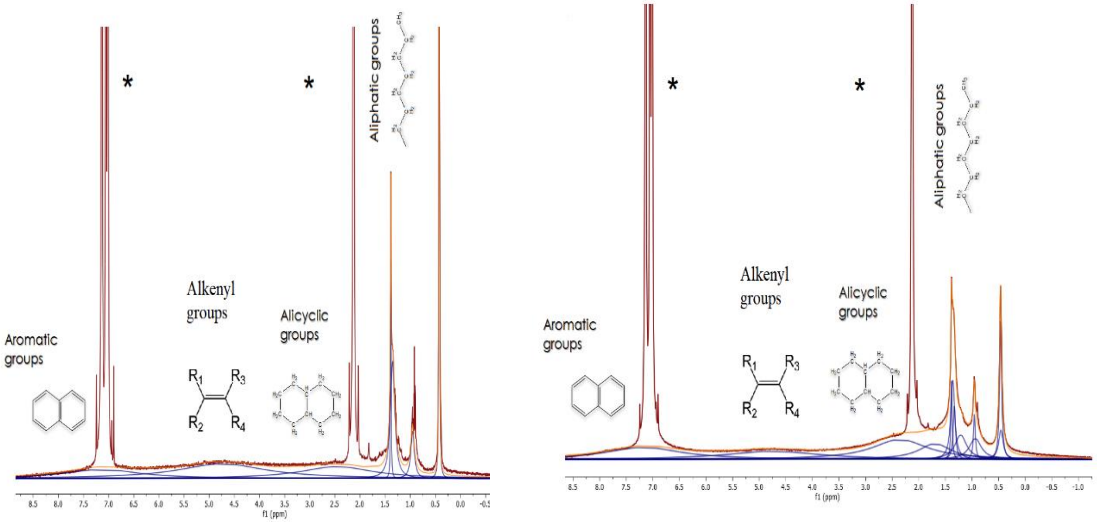

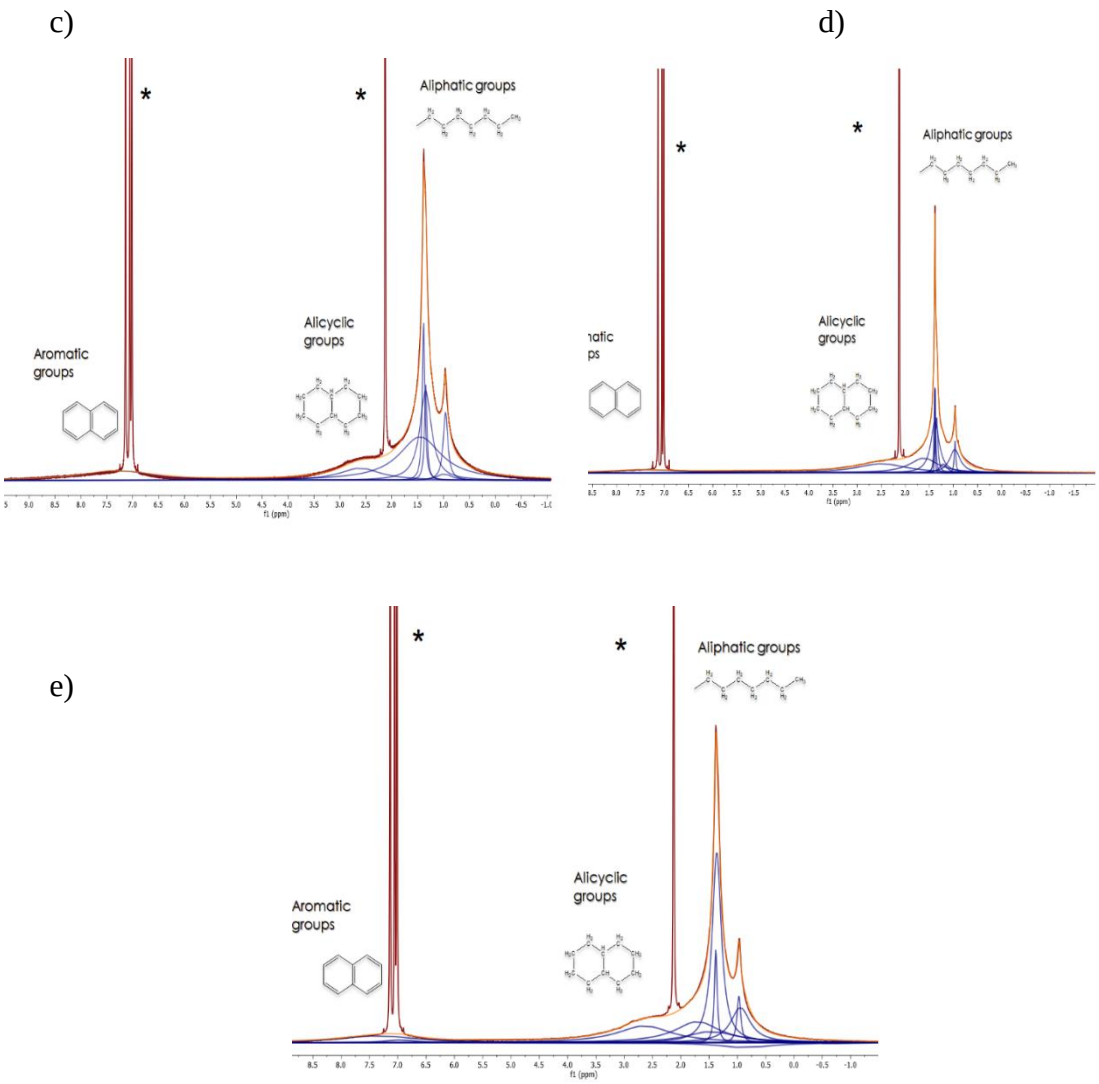

Figure 4.5. (a) 700 MHz ^{1}H NMR spectra of asphaltene samples, having EASY%Ro values of (a) 0.48; (b) 0.78; (c) 0.95; (d) 1.19; (e) 1.28. The maroon traces are the experimental spectra, the blue traces are the deconvoluted signals, and the orange traces are the sum of the deconvoluted components. All ^{1}H NMR spectra were recorded with an ambient temperature in toluene-d_8 (residual solvent signals are denoted by *) with a 90° pulse during acquisition with a recycle delay of 120 s and 32 scans.

In the present study, purely Lorentzian lineshapes were used to deconvolve the ^{1}H NMR spectra because the lineshapes were found to be homogenous in the solution state. If a Gaussian contribution to the lineshape were required, there would have been evidence that the lineshape changes with delay time during relaxation measurements. Deconvolution

involves determining each peak's areas, chemical shifts, and linewidths within the spectrum using Lorentzian basis functions. Table 4.1 lists typical deconvolution parameters associated with characteristic spectral areas and their functional groups.

Table 4.1. Chemical shift assignments for the fitted peaks of the ^{1}H NMR spectrum of asphaltene samples.

Functional group	Chemical shift (ppm)	Linewidth (Hz)
Aromatic hydrogens (H_{ar})	8.50-7.40	1500
Alkenyl hydrogens (H_{ake})	4.00-6.00	1400
Alicyclic hydrogens (H_{alc})	3.50-2.40	1400
Aliphatic chain	2.50-1.00	500, 150, 30

The composition of the different spectral environments (aromatic, alkenyl, alicyclic and aliphatic) in this study was determined using the relative method. In the relative method, the percentage of each region was obtained from the peak areas with respect to the sum of all asphaltene peak areas. The relative composition of each sample was calculated for spectra using a 120 s delay. The results are shown in Tables 4.2 and 4.3 and Figure 4.6.

Table 4.2. The deconvolution (peak-fitting) models used for the solution-state ^{1}H NMR spectra of asphaltene samples at ambient temperature in toluene-d_8 using a 120 s recycle delay. This deconvolution model used purely Lorentzian lineshapes.

δ(^{1}H) (ppm)	Width (Hz)	Area	δ(^{1}H) (ppm)	Width (Hz)	Area
0.48% EASY%Ro			0.78% EASY%Ro		
7.8	1500	12800	7.8	1500	16500
4.74	1400	16800	4.74	1400	13000
2.68	1400	13700	2.65	1400	17900
1.5	500	22500	1.45	500	29600
1.33	150	3680	1.33	150	3000
1.32	30	928	1.32	30	900
1.29	30	656	1.29	30	330
0.92	150	2260	0.92	150	2500
0.91	30	660	0.9	30	650
0.95% EASY%Ro			1.19% EASY%Ro		
7.5	1500	29900	7.5	1500	24200
2.65	1400	32500	2.7	1400	25900
1.4	500	52400	1.45	500	43700
1.33	150	5900	1.33	150	5300
1.32	30	900	1.32	30	1100
1.29	30	500	1.29	30	260
0.92	150	930	0.92	150	2200
0.9	30	710	0.91	30	460
1.28% EASY%Ro					
7.8	1500	30700			
2.65	1400	32900			
1.38	500	50300			
1.33	150	4860			
1.32	30	1290			
1.29	30	276			
0.92	150	4170			
0.91	30	600			

Table 4.3. Relative composition for the fitted peaks of the ^{1}H NMR spectra of asphaltene samples at ambient temperature in toluene-d_8 using a 120 s recycle delay.

EASY%R_O (%)	Total area	% Aromatic	% Alkenyl	% Alicyclic	% Aliphatic
0.48	74000	17.29 (± 0.03)	22.66 (± 0.02)	18.48 (± 0.03)	41.46 (± 0.02)
0.78	84500	19.52 (± 0.02)	15.38 (± 0.03)	21.18 (± 0.02)	43.76 (± 0.03)
0.95	124000	24.21 (± 0.02)		26.21 (± 0.03)	49.52 (± 0.02)
1.19	103000	23.68 (± 0.03)		25.43 (± 0.02)	50.91 (± 0.02)
1.28	125000	24.42 (± 0.02)		26.29 (± 0.02)	49.18 (± 0.02)

The relative composition of each sample was calculated, based on the peak areas determine by deconvolution (Table 4.3). Figure 4.6 shows that the aliphatic, alicyclic, and aromatic components of the AMSO samples increase until reaching 0.95% EASY%Ro while the opposite is true in the case of the alkenyl component, confirming that the composition of asphaltene changes during the pyrolysis process of green river oil shale. The relative composition is practically unchanged for samples with EASY%Ro values of 0.95% and higher. The sample with the EASY%Ro maturity of 1.19%, however, is somewhat lower in aromatic and alicyclic groups when compared to the samples with next lower and higher maturities. This slight off-trend behaviour of the 1.19% maturity sample has also been seen in other measurements (see below). According to the ^{1}H NMR spectra, the aromatic component contributes around 24%, the alicyclic component about 26%, and the aliphatic component above 49% for the three higher-maturity samples.

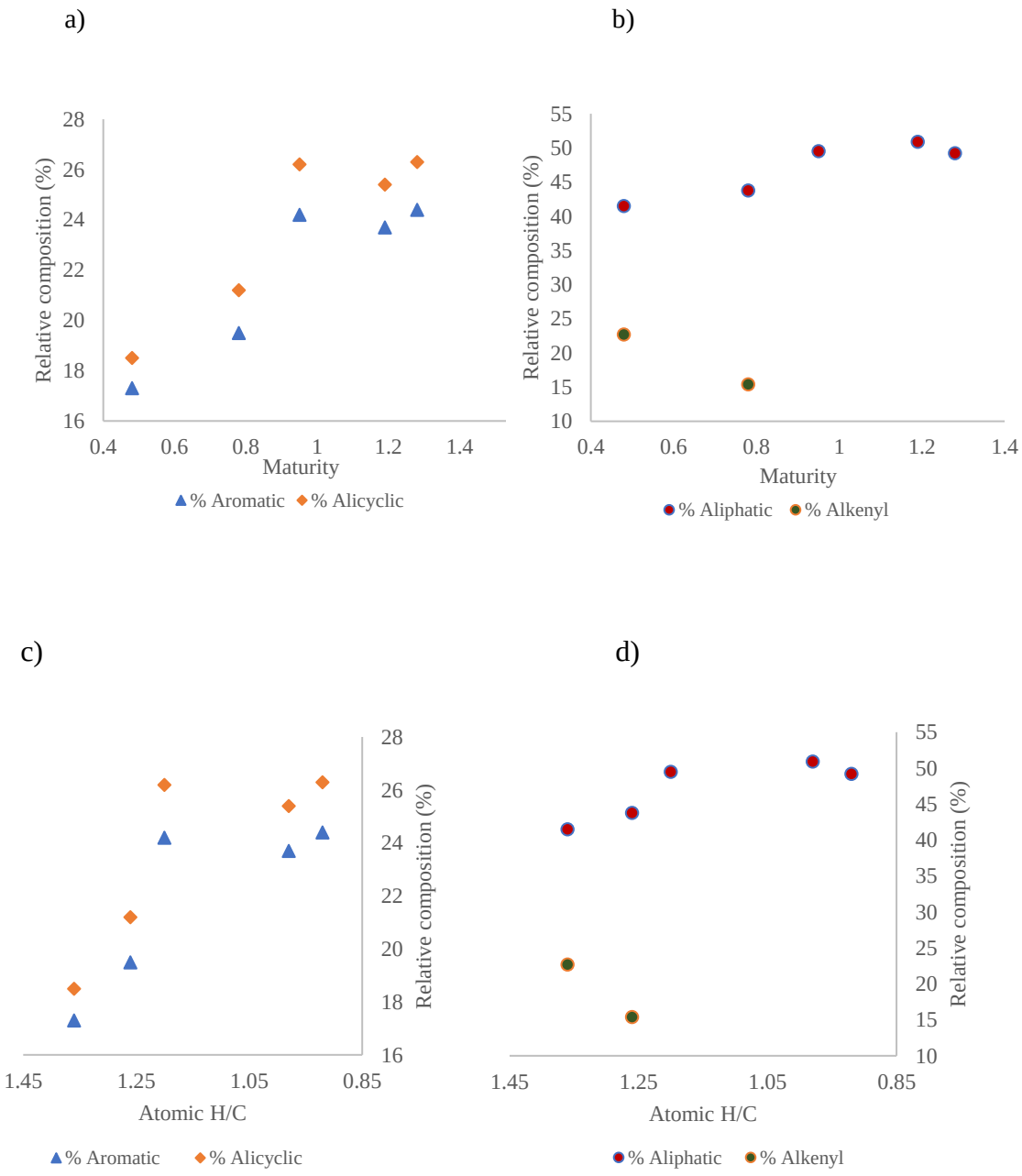

Figure 4.6. Effect of maturities and H/C ratios on asphaltenes molecular composition. Experiments were carried out in toluene-d_8 with a recycle delay of 120 s.

The early stages of pyrolysis, where H/C is above 1, are marked by an increase in the aromatic, alicyclic and aliphatic components, while the alkenyl component decreases. This suggest that the alkenyl groups are being consumed in the process of forming more and/or larger aromatic ring systems, and formation of alicyclic and aliphatic moieties. In the latter stages of pyrolysis, where H/C is below one, the alicyclic and aromatic components decrease and subsequently recover to the maximum values seen at H/C =1. The aliphatic components show the opposite trend. Furthermore, the alkenyl fraction decreases with decrease in H/C and essentially disappears past H/C = 1.25. The presence of the alkenyl fraction is thus a useful indicator of immaturity because it disappears after the early stages of pyrolysis. This observation is consistent with previous investigations using mass spectrometry,[4] where the average molecular weight of asphaltene samples was calculated using L^2MS and SALDI spectroscopy methods. The molecular weight rises from around 400 g/mol at low maturity to approximately 550 g/mol for maturities 0.95%, then decreases slightly for maturities increase >1.19% (535 g/mol).

4.3.1. T_1 and T_2 Relaxation Measurements

The T_1 and T_2 measurements were carried out for the five samples with EASY%R_O values of 0.48, 0.78, 0.95, 1.19 and 1.28%, using the inversion recovery (T_1) and CPMG (T_2) sequences. The T_1 and T_2 values were obtained from the experimental relaxation curves using the Levenberg-Marquardt algorithm[16]. The bi-exponential recovery curves for the T_1 determination for the 0.95% maturity sample are shown in Figure 4.7. The raw data obtained from the inversion recovery and CPMG experiments were normalized and plotted against time. (Figure 4.8).

Aromatic

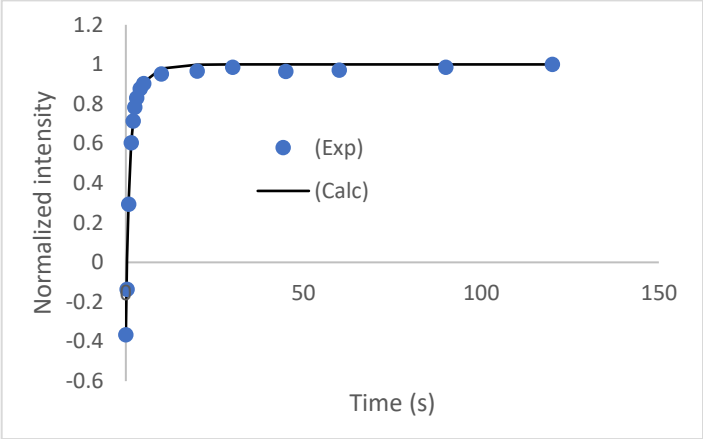

Alicyclic

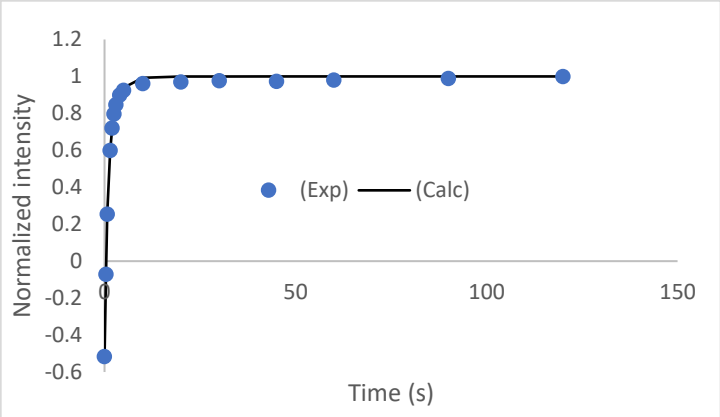

Aliphatic

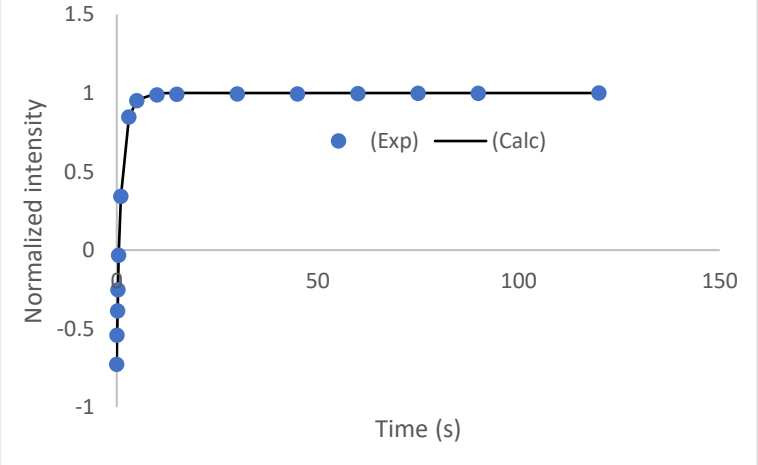

Figure 4.7. Non-linear regressive line-fitting of the T_1 data of the asphaltene sample (0.95% EASY%R_O) in toluene-d_8. The blue points are the inversion recovery data, and the black line shows the exponential recovery curve fitted to the data.

Aromatic

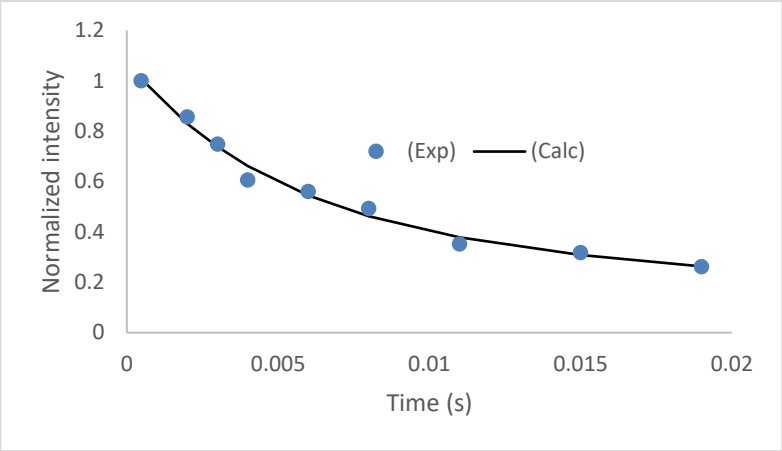

Alicyclic

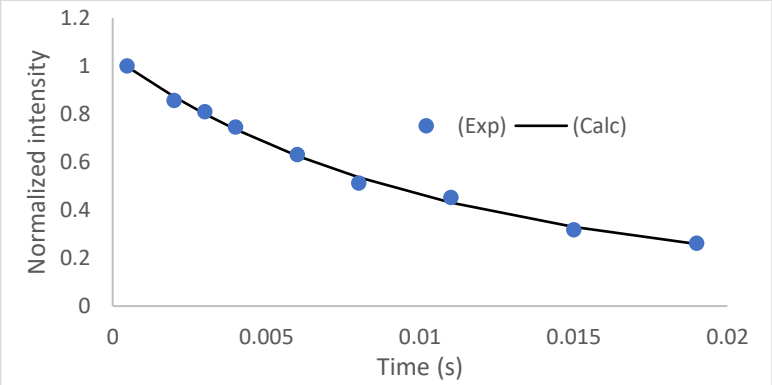

Aliphatic

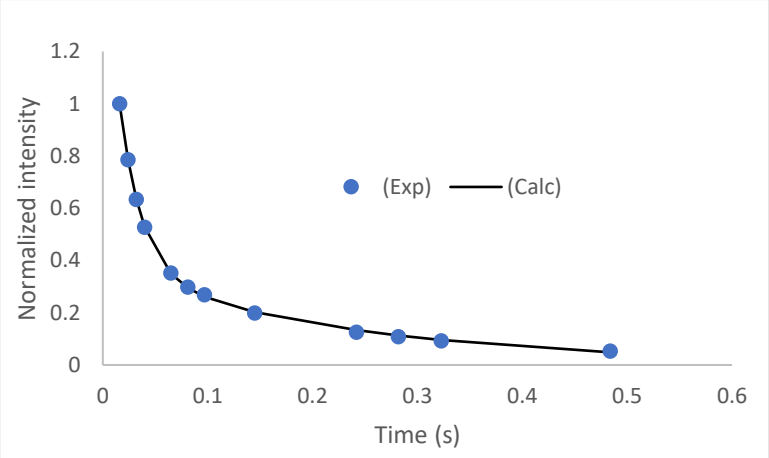

Figure 4.8. CPMG curve from the asphaltene sample (0.95% EASY%R_O) at 700 MHz. The blue data points are the CPMG data, and the black line shows the exponential decay curve fitted to the echo envelope.

Table 4.4 lists the T_1 and T_2 relaxation time constants of ^1H resonances of the asphaltene sample with maturity 0.95% EASY%R_O. Bi-exponential fitting gave two components in an approximate 3:1 ratio. The T_1/T_2 ratios were calculated by pairing the T_1 and T_2 values of components with similar percentage contributions. Shorter T_1 values were paired with shorter T_2 values for aliphatic groups, which have higher mobility, while for alicyclic and aromatic groups, shorter T_1 values were paired with longer T_2 values, consistent with their divergent behavior for longer correlation times (as shown in Figure 2.16 in Chapter 2).

Table 4.4. ^1H NMR relaxation times of asphaltene (0.95% EASY%R_O) in toluene-d_8. The values in parentheses represent the percentage of protons having the corresponding T_1 and T_2 values. The standard deviations for the T_1 and T_2 values are provided.

^1H ppm	Assignment	T_1 (s)	T_2 (ms)	T_1/T_2
1.5-0.8	aliphatic	0.43±0.04 (75±5.2%) 1.27±0.02 (25±4.5%)	21.6±0.8 (78±5.0%) 241±1.5 (22±4.2%)	20±0.8 5±0.15
3.5-2.4	alicyclic	2.58±0.04 (78±5.7%) 1.3±0.03 (22±5.0%)	5.1±0.07 (78±5.5%) 18.0±0.7 (22±4.8%)	505±10 72±2.8
8.5-7.5	aromatic	3.5±0.05 (80±5.8%) 1.28±0.03 (20±5.2%)	4.7±0.06 (80±5.5%) 20.0±0.8 (20±4.8%)	744±14 64±2.6

The variation of T_1/T_2 ratios with increasing maturity of asphaltene samples dissolved in toluene-d_8 and $CDCl_3$ are shown in Table 4.5 and Table 4.6, respectively. The relaxation analysis of all samples showed that each signal has two components: a major component with larger T_1/T_2 ratios and a minor component with smaller T_1/T_2 ratios, where their proportions remain the same between the structural environments and maturity. The difference in these T_1/T_2 ratios indicates that these environments have two distinct mobility regimes possibly corresponding to two aggregate phases differing in their internal motion.

The T_1/T_2 ratios of the aliphatic, alicyclic, and aromatic environments also show the effect of maturity on the degree of asphaltene aggregation in both mobility regimes.

Table 4.5. ^{1}H NMR relaxation measurements of asphaltene samples in toluene-d_8.

EASY%R_O	Toluene-d_8 (T_1/T_2)		
(%)	Aliphatic	Alicyclic	Aromatic
0.48	15.0±1.2 (70-85%) 3±0.06 (15-30%)	250±5.0 (70-85%) 53±1.3 (15-30%)	300±6.0 (70-85%) 50±1.5 (15-30%)
0.78	18.0±1.6 (70-85%) 4.5± 0.08 (15-30%)	380±7.6 (70-85%) 64±1.9 (15-30%)	580± 11.6 (70-85%) 58±1.9 (15-30%)
0.95	20.0±1.6 (70-85%) 5.0± 0.14(15-30%)	505±10 (70-85%) 72±2.1 (15-30%)	744±14 (70-85%) 64±2.0 (15-30%)
1.19	17.0±1.0 (70-85%) 4.0±0.10 (15-30%)	470±9.0 (70-85%) 65±2 (15-30%)	680±13 (70-85%) 56±1.8 (15-30%)
1.28	20.0±1.38 (70-85%) 5.0± 0.12(15-30%)	500±9.8 (70-85%) 70±2.1 (15-30%)	720±14.2 (70-85%) 68±2.1 (15-30%)

The values in parentheses represent the relative percentage of each signal having the corresponding T_1 and T_2. (See appendix for fitting curves)

Table 4.6. ^{1}H NMR relaxation measurements of asphaltene samples in $CDCl_3$.

EASY%R_O	$CDCl_3$ (T_1/T_2)		
(%)	Aliphatic	Alicyclic	Aromatic
0.48	13.0±0.6 (70-85%) 2.1±0.03 (15-30%)	85±1.7 (70-85%) 37±0.9 (15-30%)	96±1.9 (70-85%) 37±1.3 (15-30%)
0.78	15.0±0.8 (70-85%) 3.5± 0.03 (15-30%)	120±2.4 (70-85%) 49±1.9 (15-30%)	150± 3 (70-85%) 45±1.7 (15-30%)
0.95	17.0±1.0 (70-85%) 4.0± 0.03(15-30%)	170±3.4 (70-85%) 56±2.1 (15-30%)	220±4.4 (70-85%) 52±2.1 (15-30%)
1.19	16.0±0.8 (70-85%) 4.2±0.02 (15-30%)	140±2.8 (70-85%) 53±1.75 (15-30%)	190±3.8 (70-85%) 50±1.9 (15-30%)
1.28	17.5±0.9 (70-85%) 4.0± 0.02(15-30%)	160±3.2 (70-85%) 58±2.4 (15-30%)	210±4.2 (70-85%) 53±1.7 (15-30%)

The values in parentheses represent the relative percentage of each signal having the corresponding T_1 and T_2. (See appendix for fitting curves)

The T_1/T_2 ratios of asphaltenes with different maturities are significantly smaller compared to those found in natural reservoirs like the Manifa asphaltenes (Chapter 3). For instance, the T_1/T_2 ratio of the aromatic signal in Manifa was around 20,000 while in AMSO it was approximately 700. The molecular weight of asphaltenes from oil shale pyrolysis experiments was also lower than those found in typical reservoirs.[19, 20] The differences in T_1/T_2 ratio can be attributed to the varying conditions present in natural reservoirs, such as high pressure, moderate temperature, and geological time. Presumably these conditions would allow for ring growth, gradual aggregation, and subsequent clustering over time. On the other hand, *in-situ* pyrolysis attempts to mimic reservoir conditions, but the exact timescale cannot be precisely replicated. Thus, the composition, size, and aggregation of asphaltenes from the pyrolysis would be expected to differ from those found in natural reservoirs, which is reflected in the T_1/T_2 ratios when compared with values from natural reservoirs.

For AMSO asphaltene samples in toluene-d_8, the T_1/T_2 ratios of all regions (aliphatic, aromatic, alicyclic) increase with maturity from 0.48 to 0.95% as bitumen, being the primary product at this stage, increases accordingly. The major components of the aromatic T_1/T_2's increase with maturity similarly to the increase in aromatic content, which is consistent with increasing aromatization at the cost of alkenyl groups. Thus, the T_1/T_2's of the alkyl components would be expected to increase accordingly, which it does from 15 to 20 in toluene. Furthermore, the major component of alicyclic group's T_1/T_2 ratios increase from 250 to 505, as do aromatic ratios from 300 to 744. The larger ratio for the alicyclic groups indicates that they are more sterically constrained hence reflecting values closer to

the aromatics to the extent of congestion. Parallel behaviour is seen for the minor components in all environments.

The trend in T_1/T_2 of the major component of the aromatic reverses when maturity exceeds 0.95% when the pyrolysis reaction shifts to oil production where bitumen is consumed. At this stage the asphaltenes are portioned between both the oil and bitumen fraction, limiting the size of the aggregates that can form in the bitumen, resulting in smaller particles sizes and hence reducing the T_1/T_2 ratio. As the oil fraction increases and as the total amount of asphaltenes increases, a point is reached where the particles start to increase in size and the T_1/T_2 ratio once more start to increase.

Essentially the same behavior in the relaxation time ratio was observed in $CDCl_3$ but to a lesser extent. Also, the trend in the aliphatic and alicyclic are the same but attenuated with respect to the aromatic due to the influence additional internal motion. The trends in the minor components also mirror the behaviour seen for the major components.

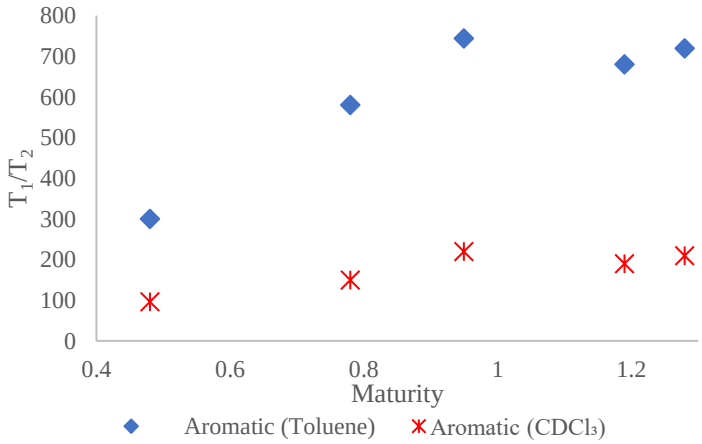

Figure 4.9. Relationship between T_1/T_2 ratios of aromatic signals in asphaltene spectra with varying maturities.

The ratio of T_1/T_2 is related to the rotational correlation time, τ_c, which can be calculated using Eq.4.1.[21]

$$\frac{T_1}{T_2} = \frac{1}{2}\frac{\left[10+37\omega^2\tau_c^2+12\omega^4\tau_c^4\right]}{\left[5+8\omega^2\tau_c^2\right]} \tag{4.1}$$

AMSO asphaltene samples show T_1/T_2 ratios ranging between 3 and 740 correspond to the correlation times of 0.5 to 7 ns in toluene and 2.1 to 210 in chloroform with correlation times of 0.2 to 3.9 ns.

The hydrodynamic radii, r_H, of the asphaltene aggregates are calculated via the equation used in Chapter 2 (Eq.2.27) at T = 298 K, and η(Toluene) = 0.56 mPa/s, and $\eta(CHCl_3)$ = 0.54 mPa/s. As shown in Figure 4.10, the hydrodynamic radius calculated using the correlation times of the major component of the aromatic signal in $CDCl_3$, and toluene-d_8 increases with sample maturity. The hydrodynamic radius increases with higher maturity from 2.0 nm to 2.4 nm in toluene-d_8, and 1.7 to 1.9 nm in chloroform, reflecting the increase in particle size in both solvents.

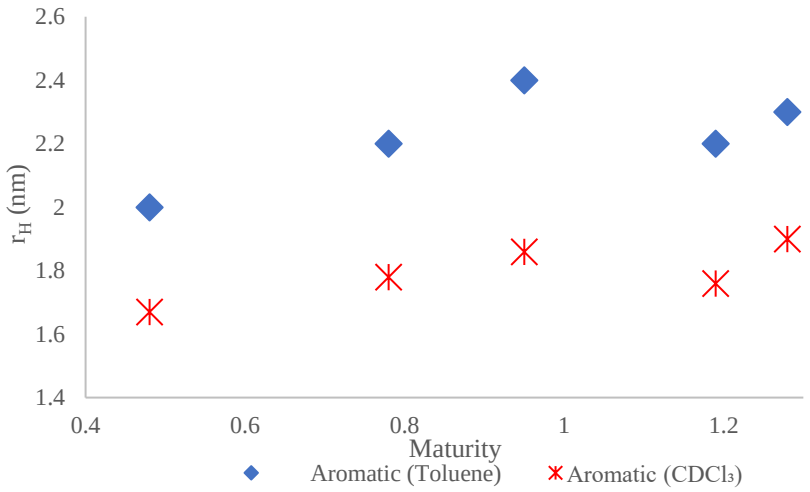

Figure 4.10. Relationship between hydrodynamic radii of aromatic signals in asphaltene at varying maturities, using a recycle delay of 120 s.

4.4. Conclusion

A study of asphaltenes isolated from pyrolyzed Green River oil shale was conducted using ^{1}H and relaxation NMR spectroscopy. This method was used to investigate the relationship between asphaltene maturity and aggregation. During the pyrolysis of Green River shale, asphaltene composition changes systematically with maturity. Asphaltenes alicyclic, aromatic, and aliphatic components initially increase with maturities at the expense of the alkenyl component, under conditions when pyrolysis generates bitumen as its primary product. Once oil starts being expelled from the bitumen there is an initial drop in alicyclic and aromatic and corresponding increase in the aliphatic component, that eventually returns to the original trend with maturity. Thus, at low maturity the aromatic regions grow initially by forming alicyclic and alkyl chain while alkenyls are consumed. Once oil expulsion kicks

in the trend is briefly reversed as the asphaltenes are partitioned to the oil seemingly favoring the larger aromatic systems.

Significant variation in aggregate size was observed with maturity, through the T_1/T_2 ratios in aliphatic, alicyclic, and aromatic environments. The bi-exponential behavior of all T_1/T_2 ratios was seen all samples and with all structural environments, where the proportion between major and minor component was invariant. This indicates that these environments have two different mobility regimes corresponding implying that the asphaltene particles is composed of two phases that differ in the density of aggregation. The results of the relaxation analysis showed that the size of the asphaltene particle increases with maturity up to EASY%Ro 0.95%, which comports with previous studies, where the molecular weight increased of varying maturities over the same range of EASY%Ro.[4] The hydrodynamic radius results confirmed that the asphaltene aggregates size increased with maturity. Further investigations revealed that aggregate size is significantly larger in toluene-d_8 than in $CDCl_3$.

REFERENCES

1. Wang, H.; Ma, F.; Tong, X.; Liu, Z.; Zhang, X.; Wu, Z.; Li, D.; Wang, B.; Xie, Y.; Yang, L., Assessment of global unconventional oil and gas resources. Petroleum Exploration and Development 2016, 43 (6), 925-940.

2. Hsu, C. S.; Robinson, P. R., Springer handbook of petroleum technology. Springer: 2017.

3. Le Doan, T.; Bostrom, N.; Burnham, A.; Kleinberg, R.; Pomerantz, A.; Allix, P., Green River oil shale pyrolysis: Semi-open conditions. Energy & Fuels 2013, 27 (11), 6447-6459.

4. Pomerantz, A. E.; Le Doan, T. V.; Craddock, P. R.; Bake, K. D.; Kleinberg, R. L.; Burnham, A. K.; Wu, Q.; Zare, R. N.; Brodnik, G.; Lo, W. C. H., Impact of laboratory-induced thermal maturity on asphaltene molecular structure. Energy & Fuels 2016, 30 (9), 7025-7036.

5. Burnham, A. K.; McConaghy, J. R., Semi-open pyrolysis of oil shale from the Garden Gulch Member of the Green River Formation. Energy & Fuels 2014, 28 (12), 7426-7439.

6. Ljungstrom, F. Electrothermal production of shale oil. 1953.

7. Kang, Z.; Zhao, Y.; Yang, D., Review of oil shale in-situ conversion technology. Applied Energy 2020, 269, 115121.

8. Symington, W.; Olgaard, D.; Otten, G.; Phillips, T.; Thomas, M.; Yeakel, J., ExxonMobil's Electrofrac Process for In Situ Oil Shale Conversion. ACS Symposium Series 2010, 1032.

9. Peters, K.; Hackley, P.; Thomas, J.; Pomerantz, A., Suppression of Vitrinite Reflectance by Bitumen Generated from Liptinite During Hydrous Pyrolysis of Artificial Source Rock. Organic Geochemistry 2018, 125.

10. Sweeney, J. J.; Burnham, A. K., Evaluation of a simple model of vitrinite reflectance based on chemical kinetics. AAPG bulletin 1990, 74 (10), 1559-1570.

11. Speight, J. G., Chemical and physical studies of petroleum asphaltenes. In Developments in petroleum science, Elsevier: 1994; Vol. 40, pp 7-65.

12. Welte, D.; Tissot, P., Petroleum formation and occurrence. Springer: 1984.

13. Simmonds, D.; Banks, L.; Steiner, R.; Young, I., NMR anatomy of the brain using inversion-recovery sequences. Neuroradiology 1983, 25 (3), 113-118.

14. Meiboom, S.; Gill, D., Modified spin-echo method for measuring nuclear relaxation times. Review of scientific instruments 1958, 29 (8), 688-691.

15. Bain, A. D.; Cramer, J., Slow chemical exchange in an eight-coordinated bicentered ruthenium complex studied by one-dimensional methods. Data fitting and error analysis. Journal of Magnetic Resonance, Series A 1996, 118 (1), 21-27.

16. Ferguson, R. C.; Marquardt, D. W., Computer analysis of NMR spectra: magnetic equivalence factoring. The Journal of Chemical Physics 1964, 41 (7), 2087-2095.

17. Ferralis, N.; Liu, Y.; Bake, K. D.; Pomerantz, A. E.; Grossman, J. C., Direct correlation between aromatization of carbon-rich organic matter and its visible electronic absorption edge. Carbon 2015, 88, 139-147.

18. Ruiz-Morales, Y., HOMO− LUMO gap as an index of molecular size and structure for polycyclic aromatic hydrocarbons (PAHs) and asphaltenes: A theoretical study. I. The Journal of Physical Chemistry A 2002, 106 (46), 11283-11308.

19. Pomerantz, A. E.; Hammond, M. R.; Morrow, A. L.; Mullins, O. C.; Zare, R. N., Two-step laser mass spectrometry of asphaltenes. Journal of the American Chemical Society 2008, 130 (23), 7216-7217.

20. Wu, Q.; Seifert, D. J.; Pomerantz, A. E.; Mullins, O. C.; Zare, R. N., Constant asphaltene molecular and nanoaggregate mass in a gravitationally segregated reservoir. Energy & Fuels 2014, 28 (5), 3010-3015.

21. Levitt, M. H., Spin dynamics: basics of nuclear magnetic resonance. John Wiley & Sons: 2013.

CHAPTER 5

ASPHALTENE AGGREGATION IN PETROPHASE 2017 ASPHALTENE SAMPLES

5.1. Introduction

Asphaltene aggregation is one of the most common challenges faced by the oil industry. The asphaltene fraction of crude oil represents the heaviest and most polar and aromatic compounds in crude oil.[1] The nature of asphaltene aggregation is still poorly understood due to the vast structural variation of asphaltenes. Understanding asphaltene structure on the nanoscale is an important step in developing strategies to improve crude oil production and minimize operational problems.

Asphaltene aggregation has been studied in the sonicated and crude PetroPhase 2017 Asphaltene samples using various physiochemical methodologies. The PetroPhase 2017 Asphaltene samples were produced by Marianny Y. Combariza's group at the Santander Industrial University in Colombia. They developed an efficient purification method for asphaltene,[2] and those samples were forwarded to a number of laboratories around the globe. The project aims to get a comprehensive view of a particular asphaltene sample from one source, employing as many experimental techniques as possible. For the first time, scientists participating in petroleum characterization have coordinated efforts to study the same asphaltene sample and get proper measurements that can be directly compared to each other.

The study by Giraldo-Dávila *et al.*[3] used thin-layer chromatography (TLC) to fractionate PetroPhase 2017 Asphaltene samples and analyze the resulting fractions by Fourier-

transform ion cyclotron resonance mass spectrometry (FT-ICR MS). The study involved the fractionation of PetroPhase 2017 asphaltenes on silica plates with an eluotropic series of mobile phases, which resulted in three distinct bands of compounds, including non-eluted compounds (NE), compounds eluted with toluene (T), and compounds eluted with dichloromethane/methanol (DM). The authors found that the NE fraction of asphaltenes, which contained high levels of heteroatomic moieties and was highly alkylated, had a quick aggregation rate and formed stable emulsions, while the DM and T fractions had slower aggregation rates and did not form stable emulsions. Furthermore, they found that the NE fraction aggregates through a supramolecular assembly mechanism and contains surfactant-like structures rather than structures just based on π stacking. Removing the NE compounds from the PetroPhase sample resulted in no aggregation or stable emulsion formation. However, the authors cautioned that these results only reflect asphaltenes of their TLC fractions and may not reflect the interactions of a mixture of compounds in a real precipitation or emulsion formation situation involving the entire crude oil. Therefore, further studies are necessary to address these issues.

Chacón-Patiño *et al.*[4] developed a method for studying PetroPhase 2017 Asphaltenes using extrography chromatography fractionation and mass spectrometry. The extrography method involved selectively removing asphaltene species with high monomer-ion yield and using polarity gradient solvent extraction to separate asphaltene fractions based on solubility. The resulting fractions were then analyzed using Fourier-transform ion cyclotron resonance mass spectrometry (FT-ICR MS). The study found that mass spectrometry of whole asphaltenes showed highly aromatic, alkyl-deficient, island-type structures. Extrography separation methods revealed that the earliest eluting fraction (acetone fraction) ionized most efficiently and matched the results obtained for the whole asphaltenes and

exhibited enrichment of island motifs. The later-eluting fractions (Tol/THF fraction), however, showed lower monomer-ion yields and were enriched in archipelago-type fragments. The authors concluded that the island model is not the dominant structure of asphaltenes, and that it coexists with abundant archipelago structures, with the ratios of each being sample-dependent.

The study by Putman *et al.*[5] investigated the aggregation behavior of PetroPhase 2017 Asphaltene samples using gel permeation chromatography (GPC) to separate the asphaltenes into different fractions. To analyze the composition of the different fractions, they used a combination of positive atmospheric pressure photoionization (APPI) and Fourier-transform ion cyclotron resonance mass spectrometry (FT-ICR MS). They also used inductively coupled plasma mass spectrometry (ICP-MS) to measure the amounts of certain elements in the fractions. According to the study, the earliest-eluting species were composed of more alkylated species, with a shift towards aromatic compounds as elution time increased. The authors found that increased aggregation was associated with a decrease in aromaticity and an increase in aliphatic species. The study also found that as aggregation decreased, the compositional range shifted toward more condensed aromatics in the high DBE (double bond equivalent) range, as well as an increase in lower DBE species, which suggests a shift in the sulfur moiety from thiophenic sulfur to sulfidic sulfur.

In the current study, ^{1}H NMR spectroscopy as well as relaxation measurements and DOSY spectroscopy were used to determine the aggregation behavior of the PetroPhase 2017 Asphaltene samples. The structural difference and aggregate size distribution was investigated for sonicated and crude samples.

5.1.1. Sonication process

In a laboratory setting, the sonication procedure is usually done with an ultrasonic bath or an ultrasonic probe. Sonication overcomes intermolecular interactions between molecules, allowing large aggregates to be broken down into smaller fragments. It is used to break up clumps of colloidal particles that are clustered together. Despite the fact that sonication is widely used in the pharmaceutical industry and research, the effects on asphaltenes are poorly understood.[6]

Kang *et al.*[7] conducted a study to examine the effects of ultrasonic processing on Athabasca asphaltene. They evaluated five different ultrasonic frequencies and four saturating gases in their experiment. The results showed a significant reduction in the number average molecular weight (NAMW) of the asphaltene samples after short treatment times, with the greatest reduction observed at a frequency of 358 kHz. The reduction in NAMW was fastest when the asphaltene was treated with a mixture of Ar/H_2 (50%/50% v/v) at a frequency of 205 kHz. On the other hand, saturating with hydrogen gases had minimal effect on the kinetics of NAMW reduction. The visible light absorption spectra of the asphaltene samples showed that the heptane soluble fractions increased by more than 50% after sonochemical treatment, which can be considered as an upgrading process.

Mousavi and Najafi *et al.*[8] studied asphaltene aggregation in Sarvak (oil fields of southwest Iran) oil samples that were exposed to ultrasonic waves at different time intervals using confocal microscopy. They found that ultrasonic waves prevent macrostructure aggregate formation. Because of using ultrasonic waves, they observed asphaltene aggregates decreased in size. After sonication, the average flock radius drops from 4.32 μm to 4.17 μm for asphaltene particles. The use of ultrasonic waves may reduce the aggregate's

average radius, as well as reduce the size of large particles. This study exemplifies the successful use of ultrasonic wave technology for reducing asphaltene precipitation problems.

5.2. Experimental section

5.2.1. Asphaltene Samples

The PetroPhase 2017 Asphaltene samples originate from Colombian heavy crude oil, and Marianny Y. Combariza's group at the Santander Industrial University isolated the samples by use of the standard ASTM D6560-12 method.[9,2] They employed Branson Ultrasonics at 22 kHz and 130 W to dilute 10 g crude oil in 400 ml of n-heptane for the sonicated sample. The mixture was then heated at 90°C under reflux for 60 minutes, then allowed to cool overnight. The asphaltenes were filtered and extracted with n-heptane in a Soxhlet extractor until the washing solvent was clear. The current NMR experiment used two types of samples: sonicated and parent crude asphaltene. The density of crude asphaltene is 0.894 g/cm^3 at 20°C.[10] DBE (double bond equivalent) values for PetroPhase 2017 Asphaltene samples range from 15 to 28, and the carbon number ranges from 25 to 40. The relative abundance of sulfur-containing compounds and vanadyl porphyrins in these asphaltenes is greater than 3.5%.[4]

5.2.2. Sample preparation

For NMR analysis, asphaltene samples of 30 g/L concentration were used, and experiments were carried out at room temperature (25°C). The NMR samples were made using toluene-d_8 as a solvent, which was purchased from Sigma-Aldrich and used as received. A small vial was used for the preparation of the solutions. First, 30 mg of asphaltene was weighed out in a plastic weighing dish using an electrical analytical balance (Mettler Toledo,

accuracy: 0.1 mg). The sample was then transferred into a small vial and dissolved in 1 mL of a deuterated toluene-d_8. A vial was used to ensure more effective mixing of the sample compared to using an NMR tube. The samples were treated with vortexing (VWR mini vortexer) for one minute to get thorough dissolution and to avoid the presence of particulates that would interfere with effective shimming. Subsequently the solution was transferred into the NMR tube using a glass Pasteur pipette. All the analyses were done with 5-mm NMR tubes, which were supplied by Wilmad Lab Glass. Based on the line width of the residual solvent signal, it was not deemed necessary to purge the samples with N_2 gas. The presence of oxygen was not controlled because the effect of oxygen on the relaxation rate was negligible. The influence of oxygen is only noticeable in systems with low molecular weight and solvents with extremely low viscosity.

After the samples were prepared for NMR experiments, the outside of the tube was cleaned with acetone. In the NMR lab, Kimwipes were used to clean the bottom of the tube before placing it in a sample changer.

5.2.3. ^{1}H NMR Experiment

All NMR spectra were obtained using a Bruker Avance III HD 700 MHz NMR spectrometer operating at 16.4 T, equipped with a triple resonance Bruker TXO-Z (C/F-H-2H) probe equipped with a ^{2}H lock channel, automatic tuning and matching, and Z-gradient. Experiments were performed at room temperature, and the sample appeared to be completely dissolved. No evidence for phase inhomogeneity was found, since throughout the NMR investigations the reference signals always had a symmetric and narrow line shape. Any phase inhomogeneity present on the microscopic scale would have resulted in

difficulties shimming the spectrum. The 1D ^{1}H NMR spectra were recorded with a 90° pulse width of 12.4 μs, 128 transients 60 s recycle delay and 64 scans.

5.2.4. Relaxation Experiment

For ^{1}H T_1 and T_2 NMR measurements, samples were prepared in toluene-d_8 solvent. The relaxation experiment used the same samples as were used in the ^{1}H NMR experiment. ^{1}H NMR relaxation data were obtained using a Bruker Avance III HD 700 MHz spectrometer operating in a four high power channels (HFXY) mode using a triple resonance Bruker TXO-Z (C/F-H-2H) probe equipped with a ^{2}H lock channel, automatic tuning and matching, Z-gradient, and VT capabilities. All spectra were obtained using a sweep width of 700 kHz, data points were zero-filled to 64k data points, unless stated otherwise. All relaxation data were acquired at room temperature. T_1 relaxation times were obtained using the inversion recovery pulse sequence[11] of the form {–RD–p_1(180°)–τ–p_2(90°)–aq(acquire)}; the phase cycles were: p_1: {x, –x}$_4$; p_2: {x_2, –x_2, y_2, –y_2}; aq: {x_2, –x_2, y_2, –y_2} and the recycle delay used was 60 s. The delay array used was 0.001, 0.35, 0.75, 1.5, 2, 2.2, 2.5, 2.7, 3, 3.2, 3.5, 4, 4.5, 5, 10, 20, 30, 45, and 60 s with 8 scans for each delay.

T_2 relaxation data were obtained using the CPMG (Carr-Purcell-Meiboom-Gill) pulse sequence[12] of the form [–RD–p_1(90°)–{τ–p_2(180°)–τ}$_n$–aq(acquire)]; the phase cycles were: p_1: {x, x, –x, –x, y, y, –y, –y}; p_2: {y, –y, y, –y, x, –x, x, –x}; aq:{ x, x, –x, –x, y, y, –y, –y}; the time delay between the pulses was 2 ms and the recycle delay was 60 s. The delay array was: 4, 6, 8, 10, 16, 20, 24, 36, 60, 70, 80, 120, 180, 250, 350, 450, 500, 750, 1000, and 1250 ms with 8 scans for each delay. Data were Fourier-transformed, baseline-corrected, and phased. The integration and deconvolution analysis were performed by MestRenova software (version 14.2.0).

5.2.5. Bi-exponential fits

The analysis of the bi-exponential behavior of the T_1 and T_2 spectra is an important mathematical tool for NMR relaxation studies of complex samples. Generally, the linear regression method is used to analyze T_1 and T_2 data in case of mono-exponential behavior. This method does not work for the bi-exponential behavior because of a massive systematic error. In this study the nonlinear Levenberg-Marquardt[13] optimization method was used.

5.2.6. DOSY Experiment

Proton diffusion ordered NMR (DOSY) experiments were performed on a Bruker Avance 700 MHz spectrometer, which operates at 16.4 T and uses a triple-resonance Bruker TXO-Z (C/F-H-2H) probe equipped with a ^{2}H lock channel and Z-gradient. Each sample was obtained by mixing 30 mg of asphaltene in 1 mL of toluene-d_8. For a DOSY experiment, a series of NMR spectra is generally collected in a stimulated echo as a function of pulsed-field gradient intensity. The intensity of each signal decreases at a rate determined by the diffusion coefficient. The stebpgp1s pulse sequence was used in the diffusion-ordered spectroscopy (DOSY) experiments.[14] Spectra were obtained with 32 scans in an increasing linear gradient ranging from 2% to 95% with a pulsed gradient time δ of 3.6 ms and diffusion times Δ of 50 -100 ms during the DOSY experiment. The spectra were subsequently processed using the Bruker Dynamics Suite with two processing methods. The initial method follows a standard procedure allowing for up to three components, while the second method employs an inverse Laplace transform. In the former method, nonlinear optimization is applied to derive $A_{\mathrm{diffusion}}(\delta, \Delta, D)$ from Equation 3.6 in Chapter 3, yielding diffusion constants, intensities for each component, and their respective 95% confidence limits.

5.2.7. Error Considerations

In this work, the amount of supplied sample was limited, allowing for the preparation of one NMR sample per asphaltene sample. In the case of ^{1}H NMR studies, the error for the relative method comes from the deconvolution of the peak fitting, and a residual error (RE) was obtained from (χ^2/N) values. In the case of relaxation studies, relative errors arise from the regression analysis with a regression error of around 1.5%.

5.3. Results and Discussion

One of the primary goals of this study is to investigate crude and sonicated PetroPhase 2017 Asphaltene samples to ascertain if sonication affects the asphaltene self-association process and possibly how. In this study, solution-state ^{1}H NMR spectroscopy was used to characterize the PetroPhase 2017 Asphaltene samples. Typical ^{1}H NMR spectra of crude and sonicated asphaltene samples are shown in Figure 5.1.

In the relative method, the percent contribution of each region was obtained from the peak areas (Table 5.1) with respect to the sum of all asphaltene peak areas as shown in Table 5.2. Extremely narrow components were not included in this deconvolution analysis since their contributions to the overall percent composition would be minimal. No significant changes in the contributions from each structural environment were observed between the sonicated and crude samples. This indicates that no significant structural changes are taking place in the individual asphaltene molecules. As sonication is a relatively low-energy phenomenon such changes were not expected.

a) Crude

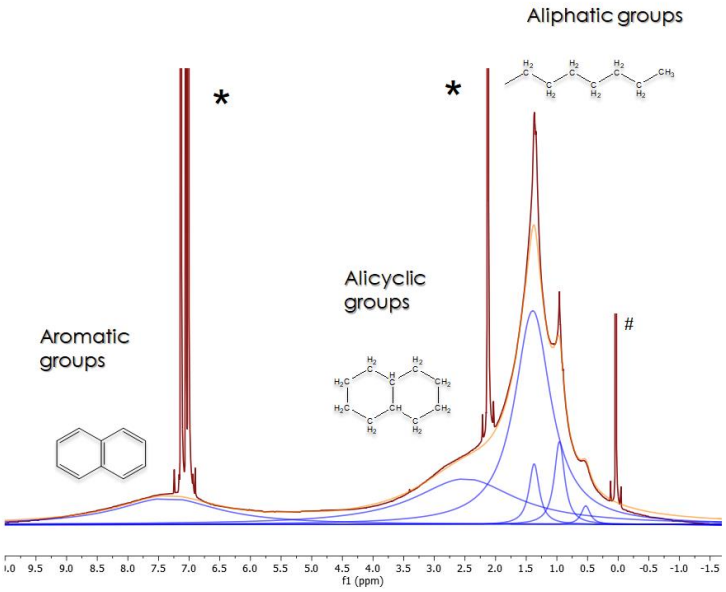

b) Sonicated

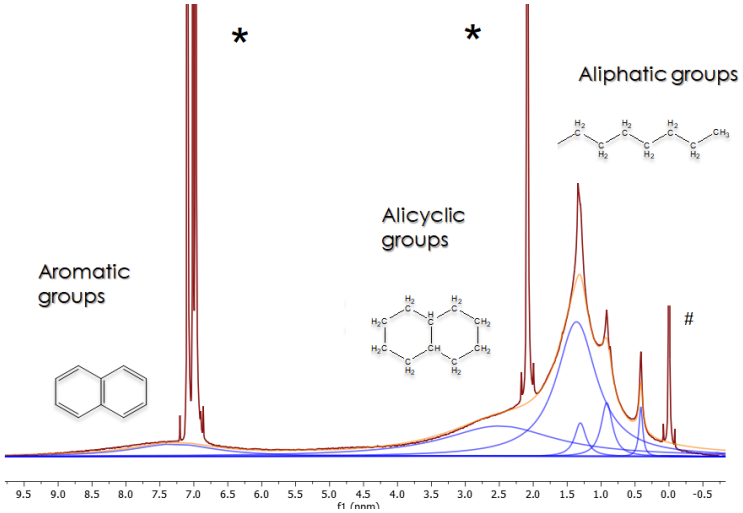

Figure 5.1. 700 MHz ^{1}H NMR spectra of (a) crude and (b) sonicated PetroPhase 2017 Asphaltene samples. The maroon traces are the experimental spectra, the blue traces are the deconvoluted signals, and the orange traces are the sum of the deconvoluted components. All ^{1}H NMR spectra were recorded at ambient temperature in toluene-d_8 (residual solvent signals are denoted by *) using TMS (denoted by #) as the internal reference with a 90° pulse during acquisition with a recycle delay of 60 s and 64 scans.

Table 5.1. The deconvolution (peak-fitting) models used for the solution-state ^{1}H NMR spectra of PetroPhase 2017 Asphaltene samples at ambient temperature in toluene-d_8 using a 60 s recycle delay. This deconvolution model used purely Lorentzian lineshapes.

δ(^{1}H) (ppm)	Width (Hz)	Area	δ(^{1}H) (ppm)	Width (Hz)	Area
Crude			Sonicated		
7.35	1400	20940	7.30	1250	15980
2.49	1400	25457	2.49	1400	19899
1.39	500	48355	1.36	500	37646
1.37	140	5680	1.31	140	3623
0.95	140	4370	0.92	140	3540

Table 5.2. Relative composition for the fitted peaks of the ^{1}H NMR spectra of crude and sonicated asphaltene samples. The percentage of relative errors were calculated from the residual error (χ^2/N) in the deconvolution analysis.

Structural parameter	Crude sample	Sonicated sample
% Aromatic	20.0 (± 0.05)	19.8 (± 0.04)
% Alicyclic	24.3 (± 0.04)	24.6 (± 0.05)
% Aliphatic	55.7 (± 0.05)	55.6 (± 0.05)

Professor Lamia Goual of the University of Wyoming studied Direct-Current (DC) Electrical Conductivity of the sonicated PetroPhase 2017 Asphaltene material (L. Goual, personal communication, June 05, 2017). She monitored aggregation behavior in the sonicated samples by DC conductivity measurements. DC conductivity depends on small-sized charge carriers undergoing charge-transfer reactions at the electrodes. Thus, increasing DC conductivity of asphaltenes with concentration results from the increase in the number of charge carriers and their mobility. When aggregation occurs the number of carriers is reduced, and they have reduced mobility despite carrying larger charges. The

net result is an inflection in the slope of the conductivity curve with concentration. The critical nanoaggregate concentration (CNAC) is typically on the order of mg/L for asphaltenes depending on the asphaltene type and solvent.[15] Goual and coworkers observed the critical nanoaggregate concentration (CNAC) around 100 mg/L. She also observed a secondary aggregation process at much higher concentrations, attributed to clustering of the nanoaggregates. This critical cluster concentration (CCC) occurred near 1000 mg/L for these asphaltenes.

The samples used in the current relaxation dispersion and DOSY experiments had a concentration of 30 g/L, which is much higher than the critical cluster concentration for the PetroPhase 2017 Asphaltene samples. Therefore, clusters are expected to predominate in the present solution samples of the PetroPhase 2017 Asphaltenes. If this is correct, one could surmise that most of the NMR signal arises from the clusters and the minority from the nanoaggregates.

The ^{1}H relaxation experiments were used to measure the ^{1}H relaxation times from which rotational correlation times were determined for the sonicated and the crude asphaltenes. To obtain T_1 and T_2 relaxation times, the experimental relaxation curves were fitted using the non-linear optimization via the Levenberg-Marquardt algorithm, allowing for two independent relaxation times and their relative contributions to the curve. (The curves are shown in Appendix 3). Tables 5.3 and 5.4 list the T_1 and T_2 relaxation time constants together with the assignment to the three ^{1}H chemical shift ranges for a toluene-d_8 solution of crude and sonicated PetroPhase 2017 Asphaltene, respectively, using a 60 s recycle delay.

Table 5.3. ^{1}H NMR Relaxation times of crude PetroPhase 2017 Asphaltene in toluene-d_8. The values in parentheses represent the percentage of protons having the corresponding T_1 and T_2. The standard deviations for both T_1 and T_2 have been calculated.

^{1}H ppm	assignment	T_1 (s)	T_2 (ms)	T_1/T_2
1.5-0.8	Aliphatic	0.62 ± 0.03 (55 ± 5.0%)	18.8 ± 0.9 (58 ± 4.5%)	33.0 ± 1.9
		1.92 ± 0.04 (45 ± 4.5%)	280 ± 2.0 (42 ± 4.5%)	7.0 ± 0.15
3.5-2.4	Alicyclic	3.30 ± 0.05 (58 ± 5.4%)	5.2 ± 0.05 (55 ± 4.5%)	660 ± 9.2
		0.81 ± 0.03 (42 ± 4.8%)	32.1 ± 1.0 (45 ± 4.2%)	25.0 ± 1.2
9.0-7.85	Aromatic	4.2 ± 0.05 (54 ± 5.5%)	4.3 ± 0.04 (58 ± 5.0%)	980 ± 17
		0.92 ± 0.03 (46 ± 5.5%)	30.0 ± 1.2 (42 ± 4.5%)	30.0 ± 1.5

Table 5.4. ^{1}H NMR Relaxation times of sonicated PetroPhase 2017 Asphaltene in toluene-d_8. The values in parentheses represent the percentage of protons having the corresponding T_1 and T_2. The standard deviations for both T_1 and T_2 have been calculated.

^{1}H ppm	assignment	T_1 (s)	T_2 (ms)	T_1/T_2
1.5-0.8	Aliphatic	0.57 ± 0.03 (56 ± 4.5%)	32.5 ± 1.1 (58 ± 5.5%)	17.5 ± 1.0
		1.48 ± 0.04 (44 ± 4.5%)	460 ± 3.0 (42 ± 4.7%)	3.2 ± 0.1
3.5-2.4	Alicyclic	2.38 ± 0.05 (55 ± 5.5%)	7.2 ± 0.07 (56 ± 4.5%)	330 ± 7.5
		0.8 ± 0.02 (45 ± 4.8%)	64.0 ± 1.5 (44 ± 4.8%)	12.5 ± 0.6
9.0-7.85	Aromatic	3.50 ± 0.05 (58 ± 5.5%)	6.3 ± 0.06 (60 ± 5.0%)	553 ± 10
		0.93 ± 0.03 (42 ± 5.5%)	60.0 ± 1.4 (40 ± 5.4%)	15.5 ± 0.7

The T_1 and T_2 relaxation data exhibited biexponential behavior for all three signal types in both samples. Furthermore, the major component consistently remains at a relative abundance of 55 to 60% between all environments and both samples. The T_1 and T_2 pairing is consistent with the divergence in relaxation behaviour between T_1 and T_2 with longer correlation times, *i.e.*, the longer T_1 is thus associated with the shorter T_2. The more internally mobile alkyl protons exhibit inherently shorter correlation times and thus cannot

exhibit the divergent relaxation behaviour to the same extent, as was discussed in Chapter 3. The T_1/T_2 ratios of the more abundant components were always larger than the corresponding minor component by as much as one order of magnitude. The consistent bimodal distribution of the T_1/T_2 ratios from the same structural environments indicates the presence of at least two phases with distinct motional timescales. The difference in mobility, especially for the alicyclic and aromatic components, is much less than with Manifa samples (see Chapter 3). For Manifa the ratios of the two corresponding T_1/T_2 values in toluene were 100 to 200, while for Petrophase 2017 they were 20 to 30. The aliphatic mobility ratios were essentially the same between the Manifa and Petrophase 2017 samples, being around 4, indicating that their mobilities are dominated by internal motion.

Consistent with the Manifa samples, the T_1/T_2 ratios of Petrophase 2017 vary dramatically between environments where the major components range over 1 to 2 orders of magnitude, while the minor components differ by 1 order of magnitude. In all cases, the T_1/T_2 values are always largest for the aromatics followed closely by the alicyclic, and the aliphatics were the smallest. This is consistent with the relative mobility expected for staggered π–π stacking aggregation geometries.

It should be noted that T_1/T_2 ratios for the crude signals are consistently twice as large compared to those of the sonicated signals for both major and minor components. The T_1/T_2 ratios of the aromatics, being the least mobile, most likely reflect the mobility of the whole aggregate. As even in this case the effect of internal motion cannot be ignored. The T_1/T_2 ratios of the major components for aromatics signals in each sample in toluene-d_8 is shown in Table 5.5. These were used to calculate the correlation times, and ultimately the hydrodynamic radii as previously described in Chapter 3 using Equations 3.3 and 3.4. The

major component of the crude and the sonicated sample gave correlation times of 8 and 6 ns with corresponding hydrodynamic radii of 2.4 and 2.1 nm, respectively.

Table 5.5. The lower limit of the T_1/T_2 ratios of aromatics and the corresponding lower limit to the r_H values for the crude and sonicated asphaltenes in toluene-d_8.

	Aromatic (major)	
Sample	T_1/T_2	r_H (nm)
Crude	980 ± 17	2.4 ± 0.1
Sonicated	553 ± 10	2.1 ± 0.1

Figure 5.2 shows the T_1/T_2 ratios for the crude and sonicated samples for all their structural environments. Focussing on the T_1/T_2 ratios of the major components, the ultrasonic waves substantially disrupt the aggregates, as reflected by consistently reducing the T_1/T_2 ratios in the sonicated samples for all the structural environments, however, most pronounced for the aromatic signals.

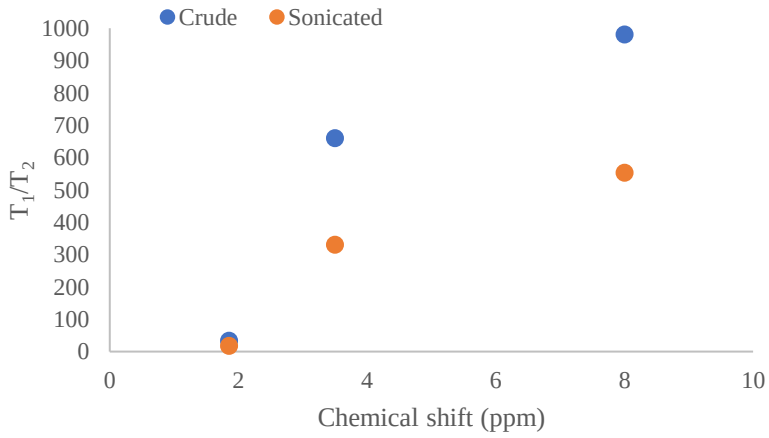

Figure 5.2. Changes in the T_1/T_2 ratios of PetroPhase 2017 Asphaltene samples with the chemical shift.

5.3.1. Measurement of diffusion coefficients

Crude and sonicated PetroPhase 2017 Asphaltenes were characterized by two-dimensional DOSY spectroscopy. The DOSY spectra of the two asphaltenes studied in deuterated toluene at a 30 g/L concentration are shown in Figure 5.3, including the spectra processed using inverse Laplace transform.

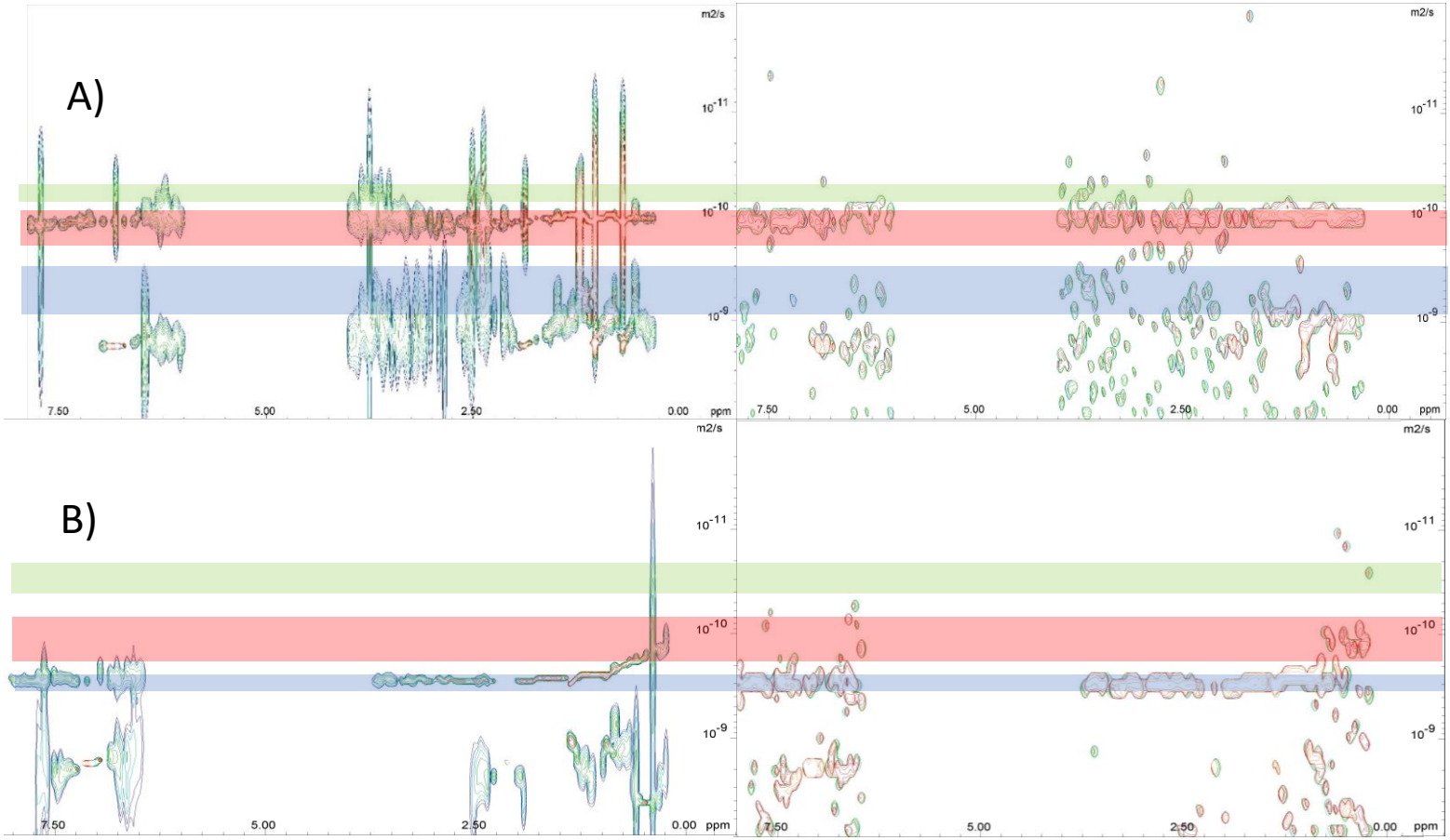

Figure 5.3. ^{1}H DOSY and the corresponding Inverse Laplace Transform (ILT) spectra of PetroPhase 2017 Asphaltene samples in toluene-d_8 (a) the crude and (b) the sonicated samples. X-axis represents the chemical shift in ppm and Y-axis represents the diffusion coefficient value in log form. The coloured horizontal lines indicate the components (green- red-, and purple-colored lines), characterized by their different diffusion coefficients.

From the graphs in Figure 5.3 three ranges in the diffusion constants were identified, referred to high, medium, and low, and indicated by color-coded boxes in Figure 5.3. The ranges of the three classes of diffusion coefficients (D), the corresponding adjusted diffusion coefficients (D*) and hydrodynamic radii (r_H) values are listed in Table 5.6. The DR and D* values have been defined in Chapter 3. The hydrodynamic radii are calculated via the equation used in Chapter 2 (Eq. 2.36).

Table 5.6. The diffusion coefficients (D), solvent diffusion coefficients (SD), relative diffusion coefficients (DR), adjusted diffusion coefficients (D*) and r_H values for PetroPhase 2017 Asphaltene samples in toluene-d_8. Assuming the self-diffusion constant for toluene is $D_o = 2.28 \times 10^{-9}$ m^2/s.

Sample	D (m^2/s) × 10^{-10}	SD (m^2/s) ×10^{-10}	D* (m^2/s) ×10^{-10}	r_H (nm) subnano, nano, micro
Sonicated	3.0-9.0	17.6	3.9-11.7	0.35-1.0
	0.9-2.0		1.2-2.6	1.6-3.4
	0.5-0.7		0.65-0.91	4.4-6.2
Crude	2.5-3.5	19.3	3.0-4.1	0.99-1.3
	0.7- 1.8		0.83-2.2	1.8-4.9
	0.2 ± 0.4		0.24-0.47	8.6-16.8

In Table 5.6, the presumed small aggregates are indicated in purple, the medium aggregates in red and the large aggregates (clusters) are green. When considering the diffusion data of the samples in toluene, the larger adjusted diffusion constants (D*), *i.e.*, 3.9-11.7 and 3.0-4.1 × 10^{-10} m^2/s, corresponding to the sonicated to crude samples, give hydrodynamic radii (r_H) values of 0.35-1.0 and 0.99-1.3 nm, respectively. For this category the r_H corresponds to suboptimal aggregates such as monomers, dimers, trimers, *etc*. The medium D* values range from 1.2-2.6 and 0.8-2.2 × 10^{-10} m^2/s for the sonicated and crude samples, with corresponding r_H values of 1.6-3.4 and 1.8-4.9 nm, respectively. The r_H values in the

medium category suggest that the optimal size is reached (the nanoaggregate unit), and the onset of clustering takes place. Finally, the lowest D* value range from 0.65-0.91 and 0.24-0.47 $\times 10^{-10}$ m^2/s, with corresponding r_H values of 4.4-6.2 and 8.6-17 nm, respectively, are clusters. As the D values for the crude sample are approaching 10^{-11} m^2/s the signal-to-noise ratio is significantly degraded compared to those of the others signals, which are comfortably in the 10^{-10} m^2/s range. Consequently, one would have less confidence in the values of the crude sample, especially in the estimated upper range of the particle size.

The DOSY results clearly indicate that the size distribution of the larger particles in the crude material are greatly reduced upon sonication, where the average radii were cut at least in half. The size distribution in the medium particles were also reduced substantially by 10 to 30 %. The size distribution for the smallest particles was reduced by about 20 % similarly to the medium particles.

According the small-angle X-ray scattering (SAXS) study by Eyssautier *et al.*[15], the nanoaggregate size is 1.7 nm (7 molecules), or 1.4 nm (6 molecules) according to similar work by Eyssautier *et al.*[16] Using 1.7 nm as the size of a nanoaggregate, the number of nanoaggregates in the clusters, based only on the lower limit for the large particle range observed by DOSY, would be 130 nanoaggregates per cluster for the crude and 17 for the sonicated samples. The medium-sized particles represent clusters of 1 to 24 nanoaggregates for the crude and 1 to 8 for the sonicated samples. The smallest particles are below the nanoaggregate size, with aggregation numbers from 1.4-3.1 molecules for the crude and 0.7-1.4 molecules for the sonicated sample.

The diffusion constants from DOSY for the sonicated sample can be directly compared to those determined by DC conductivity measurements by L. Goual *et al.* (L. Goual, personal

communication, June 05, 2017). They showed that at 0.010 mg/mL, well below the CNAC, D was 5.125×10^{-10} m^2/s, which was attributed to individual units or very small aggregates with r_H = 0.78 nm. The diffusion constants increased steadily with concentration up to 0.1 mg/mL at the CNAC where more stable aggregates form with aggregation numbers near 4, with D = 3.274×10^{-10} m^2/s and r_H = 1.22 nm. Further increasing the concentration to the onset of clustering at the CCC at 1.00 mg/ml, D = 2.506×10^{-10} m^2/s, with r_H = 1.59 nm, with corresponding aggregation number of 8. Past the CCC, the diffusion constants increased to 1.945×10^{-10} m^2/s with r_H = 2.05 nm at 5.0 mg/mL with aggregation number 18 to 20, involving 2 to 3 nanoaggregates.

According to Goual's work the optimal onset of nanoaggregate formation is 8 molecules with r_H at 1.59 nm, which corresponds to the transition from the small to medium sizes in this work. Simple extrapolation of D with concentration to 30 mg/mL would place D between 1.5 to 0.75×10^{-10} m^2/s, with r_H = 3 to 4 nm. This corresponds to the lower bound to the large particles in the sonicated sample in this work.

5.4. Conclusion

The literature review encompasses studies on PetroPhase 2017 Asphaltene samples, revealing that asphaltene aggregates exhibit different aggregation rates and structures. Some studies challenge the dominance of the island model for asphaltene structures by demonstrating the coexistence of island-type and archipelago-type structures. Additionally, studies highlight how changes in asphaltene aggregation are linked to variations in aromaticity and sulfur content. The current study employed NMR spectroscopic techniques to investigate aggregate and structural differences in PetroPhase 2017 Asphaltene samples,

both sonicated and crude, contributing to a deeper understanding of asphaltene behavior. Those methods allow us to make conclusions about how aggregation changes in the presence of ultrasonication. While the ^{1}H NMR results show, as expected, that no molecular structural changes occur upon sonication, according to this study, the aggregate sizes of asphaltenes decrease with sonication.

The T_1/T_2 ratios in aliphatic, alicyclic, and aromatic environments were determined fromT_1 and T_2 relaxation measurements using standard inversion recovery techniques and CPMG methods, respectively. The biexponential behavior of all T_1/T_2 ratios indicates that at least two environments with two different mobility regimes exist. Under sonication conditions, the T_1/T_2 ratio for the major component of the aromatic region decreased significantly from 980 to 553 giving hydrodynamic radii of 2.4 and 2.1 nm, respectively. The results of the relaxation analysis confirmed the prediction of previous studies[8] that the size of the asphaltene aggregate decreased upon sonication of the sample. The DOSY NMR spectra also showed that the sonication technique reduced asphaltene aggregate size. The diffusion constants reveal three distinct aggregation states: sub nanoaggregates, nanoaggregates, and microaggregates (clusters). The DOSY experiments support the previous findings that the size of aggregates is reduced substantially by sonication. The DOSY results are in excellent agreements with DC conductivity measurements by a collaborator. Importantly, it should be noted that the DOSY data do not precisely depict the relative composition of asphaltenes due to its restricted sensitivity and comparatively slower diffusion rates.

REFERENCES

1. Chacón-Patiño, M. L.; Rowland, S. M.; Rodgers, R. P., Advances in Asphaltene Petroleomics. Part 3. Dominance of Island or Archipelago Structural Motif Is Sample Dependent. Energy & fuels 2018, 32 (9), 9106-9120.

2. Giusti, P.; Bouyssière, B.; Carrier, H.; Afonso, C., 18th International Conference on Petroleum Phase Behavior and Fouling. ACS Publications: 2018.

3. Giraldo-Dávila, D.; Chacón-Patiño, M. L.; McKenna, A. M.; Blanco-Tirado, C.; Combariza, M. Y., Correlations between molecular composition and adsorption, aggregation, and emulsifying behaviors of petrophase 2017 asphaltenes and their thin-layer chromatography fractions. Energy & Fuels 2017, 32 (3), 2769-2780.

4. Chacón-Patiño, M. L.; Rowland, S. M.; Rodgers, R. P., Advances in Asphaltene Petroleomics. Part 2: Selective Separation Method That Reveals Fractions Enriched in Island and Archipelago Structural Motifs by Mass Spectrometry. Energy & Fuels 2018, 32 (1), 314-328.

5. Putman, J. C.; Moulian, R.; Smith, D. F.; Weisbrod, C. R.; Chacon-Patino, M. L.; Corilo, Y. E.; Blakney, G. T.; Rumancik, L. E.; Barrere-Mangote, C.; Rodgers, R. P., Probing aggregation tendencies in asphaltenes by gel permeation chromatography. Part 2: Online detection by Fourier transform ion cyclotron resonance mass spectrometry and inductively coupled plasma mass spectrometry. Energy & Fuels 2020, 34 (9), 10915-10925.

6. Rabbani, A.; Ghazanfari, M. H.; Amani, M., Asphaltene Formation Damage Stimulation by Ultrasound: An Analytical Approach Using Bundle of Tubes Modeling. Journal of Petroleum Engineering 2015.

7. Kang, N.; Hua, I.; Xiao, C., Impacts of Sonochemical Process Variables on Number Average Molecular Weight Reduction of Asphaltene. Industrial & engineering chemistry research 2006, 45 (15), 5239-5245.

8. Mousavi, S.; Najafi, I.; Ghazanfari, M.; Amani, M., Comparison of ultrasonic wave radiation effects on asphaltene aggregation in toluene–pentane mixture between heavy and extra heavy crude oils. Journal of energy resources technology 2012, 134 (2).

9. Standard, A., Standard Test Method for Determination of Asphaltenes (Heptane Insolubles) in Crude Petroleum and Petroleum Products. 2012.

10. Passade-Boupat, N.; Gingras, J.-P.; Desplobins, C.; Zhou, H., Could the asphaltene solubility class index be used as the "Wax Appearance Temperature" of asphaltenes? Illustration through the study of the polydispersity of PetroPhase 2017 asphaltenes. Energy & Fuels 2018, 32 (3), 2760-2768.

11. Simmonds, D.; Banks, L.; Steiner, R.; Young, I., NMR anatomy of the brain using inversion-recovery sequences. Neuroradiology 1983, 25 (3), 113-118.

12. Meiboom, S.; Gill, D., Modified spin-echo method for measuring nuclear relaxation times. Review of scientific instruments 1958, 29 (8), 688-691.

13. Ferguson, R. C.; Marquardt, D. W., Computer analysis of NMR spectra: magnetic equivalence factoring. The Journal of Chemical Physics 1964, 41 (7), 2087-2095.

14. Chinelatto Júnior, L. S.; Cabral de Menezes, S. M.; Honorato, H. d. A.; Oliveira, M. C. K. d.; Marques, L. C. d. C., Dosy-Nmr as an Alternative Technique to Improve Asphaltenes Characterization. Energy & Fuels 2018.

15. Eyssautier, J.; Levitz, P.; Espinat, D.; Jestin, J.; Gummel, J.; Grillo, I.; Barré, L., Insight into asphaltene nanoaggregate structure inferred by small angle neutron and X-ray scattering. The Journal of Physical Chemistry B 2011, 115 (21), 6827-6837.

16. Eyssautier, J. l.; Espinat, D.; Gummel, J. r. m.; Levitz, P.; Becerra, M.; Shaw, J.; Barré, L. c., Mesoscale organization in a physically separated vacuum residue: Comparison to asphaltenes in a simple solvent. Energy & fuels 2012, 26 (5), 2680-2687.

CHAPTER 6

STUDY OF FLUORINATED PROBES IN THE CHARACTERIZATION OF UG8 ASPHALTENE

6.1. Introduction

As established in the previous chapters, ^{1}H NMR spectroscopy including ^{1}H relaxation time determinations is a useful technique for studying asphaltene's structure and dynamic behavior and is at least as informative as ^{13}C NMR spectroscopy. However, relaxation time measurements are highly time-consuming because they need exceptionally long recycle delays to avoid systematic errors due to saturation. It is therefore necessary to develop a faster NMR method requiring minimal analysis. In principle, ^{19}F NMR spectroscopy offers this capability if appropriate small molecular probes can be found. In this study, we will evaluate a selection of small fluorinated molecular probes to test whether they can provide reliable dynamic and structural information compared to those obtained by parallel ^{1}H NMR measurements.

6.2.1. The effectiveness of using ^{19}F NMR spectroscopy

Fluorine-19 is an abundant spin-1/2 nucleus with a strong magnetic moment and no quadrupole moment therefore it offers excellent sensitivity comparable to that of ^{1}H for NMR spectroscopy in solution.[1] Fluorine-19 typically exhibits high resolution in solution similar to the resolution in ^{1}H NMR spectra of their nonfluorinated counterparts. As fluorine does not naturally occur in petroleum-associated materials, no interfering background signals will complicate the analysis and interpretation of the spectra. For

similar reasons, broad baseline distortions due to extremely wide background signals can be avoided in complex mixtures using ^{19}F NMR spectroscopy. The chemical shift of ^{19}F is strongly influenced the presence of local magnetic fields resulting from subtle structural changes in the electron density nearby. As the chemical shift range of ^{19}F is ~ 400 ppm as opposed to ~15 ppm for ^{1}H, small structural changes are readily detected.[2]

Fluorine-19 relaxation is governed primarily by dipole-dipole (DD) interactions, either between intermolecular ^{19}F's or intramolecularly with nearby protons, and the interaction with local diamagnetic fields resulting from chemical shift anisotropy (CSA). Furthermore, the two types of interactions can interfere with each other. In ^{19}F relaxation, CSA and DD-CSA cross-terms are expected to contribute significantly to relaxation, which is usually dominated by the DD mechanism, especially at high fields such as 16.5 T (700 MHz spectrometers). As a result, spin-lattice relaxation times for ^{19}F will be shorter than ^{1}H for longer correlation times. At lower field (100 MHz), the CSA has less impact on ^{19}F relaxation, and the DD mechanisms are dominant. At lower fields, however, the relaxation dispersion is relatively small, and the relaxation times are less sensitive by the timescale of motion past the T_1 minimum. As a result, higher fields are required to observe sufficient relaxation dispersion to serve as a reliable proxy for the correlation time past the T_1 minimum.

The theoretical details regarding the differences between ^{19}F and ^{1}H relaxation mechanisms will not be addressed in this thesis. That will be the subject of a separate investigation. The observations and analyses presented here will be mainly qualitative.

6.2.2. ^{19}F NMR spectroscopy using fluorinated probes

The uses of fluorinated molecular probes and selective fluorination are effective in the study of the structure and dynamics of macromolecular systems such as proteins and nucleic acids.[3,4] Fluorinated probes have been incorporated into proteins via two methods: (1) biosynthesis, in which fluorinated amino acids are added to the expression medium, and (2) chemical modification, in which fluorinated probes react with the target protein site.[5] The parameters of ^{19}F, such as chemical shifts and relaxation times, are highly sensitive to its surroundings, so this approach allows for monitoring protein conformational changes and transitory interactions. Kawahara *et al*.[6] used fluoroproline to study structural changes in collagen peptides. Such information is difficult to obtain by ^{1}H NMR spectroscopy; but, by incorporating the fluoroproline probe in peptides, Kawahara and his colleagues were able to use ^{19}F NMR to obtain more accurate and reliable measurements. They studied the collagen peptide conformational changes during collagen isomerism, association, and dissociation processes using ^{19}F-^{19}F exchange spectroscopy and ^{19}F-^{1}H HOESY and observed the transition of collagen peptides between triple-helical and single-coil states, which could not be explained using circular dichroism (CD) spectroscopy.

Liu *et al.*[7] studied the conformational changes in the G protein (receptor) and β-arrestin (ligand) binding using ^{19}F NMR spectroscopy. They determined the equilibrium of binding constant of the ligand, based on the changes in the chemical shift of ^{19}F labels located in the cytoplasmic region of the receptor. By analyzing the ^{19}F NMR signals, they have shown that β-arrestin-biased ligands primarily change the two main conformational states of the cytoplasmic ends of the helix VII region of the receptor. Fluorine-19 NMR spectroscopy was shown to be an extremely efficient tool for studying the structure-activity relationship

of proteins and ligands. These principles can be used to develop pharmacological ligands that are rationally designed. Rydzik *et al.*[8] observed conformational and binding behavior patterns between 1,1,1-trifluoro-3-bromo acetone (BFA) and metallo-β-lactamase using ^{19}F NMR spectroscopy. They determined the binding constants, the type of metallo-β-lactamase inhibitors, and a number of ligand binding modes.

Hoang *et al.*[9] employed the ^{19}F CPMG relaxation dispersion experiment to examine calcium-modulated conformational changes proteins and their binding process with fluorophenyl alanine ligands. It is difficult to observe line broadening or characteristic exchange in the ^{1}H relaxation of the protein because of its disordered side chains and density. Fluorine-19 CPMG relaxation dispersion experiments found that these protein's N- and C-termini behave differently during protein-ligand binding. The N-terminus of the protein is primarily responsible for accommodating the specific binding protein and ligand.

Shi *et al.*[10] used ^{19}F-labeled unnatural amino acids at specific positions in proteins to observe changes in chemical shifts and sidechain relaxation dispersion behavior using 1D ^{19}F NMR and T_1 and T_2 relaxation experiments. Internal motions of protein side chains are usually investigated using ^{13}C or ^{1}H relaxation NMR measurements. As proteins grow larger, however, it becomes increasingly challenging to obtain relaxation data because of two factors: first, resonance assignments become increasingly complex, and secondly, protein sidechains usually exhibit a relatively poor signal-to-noise ratio. In this study, in the presence of peptide ligand on the protein sidechain, the ^{19}F T_1/T_2 ratio decreased, and the remarkable increase in T_2 indicated a rise in internal motion. Proton relaxation experiments have never shown a comparable difference in the respective T_1/T_2 ratio.

Lu *et al.*[11] measured the ^{19}F longitudinal and transverse relaxation times of fluorosubstituted tryptophan amino acids and fluorotryptophan-labeled cyclophilin A proteins in solution. They calculated ^{19}F R_1 and R_2 relaxation rates in fluorotryptophans as free amino acids and as amino acids bound to proteins. The relaxation rates are nearly the same for both free amino acid and amino acid bound in protein, suggesting that protein motions have only a minor effect on dynamics of the fluorotryptophan ring.

A few examples of using ^{19}F NMR spectroscopy for asphaltene characterization can be found in the literature. Desando *et al.*[12] chemically derivatized asphaltenes by phase transfer methylation and trifluoroacetylation. They used ^{13}C and ^{19}F NMR spectroscopy to reveal a broad site distribution of different hydroxyls containing functional groups. Stapf *et al.*[13] investigated the asphaltene aggregates in crude oil using ^{19}F NMR spectroscopy and field cycled relaxometry. They used three types of reservoir oils in this study: low-viscosity oil (A_0) with no resin, waxy oil (W_0) with resin, and asphaltene oil (A13) with 13 wt% asphaltenes. As a probe, four fluorine-containing tracer molecules were used. Aromatic probes were hexafluorobenzene (C_6F_6) and octafluorotoluene (C_7F_8), whereas saturated alkane probes were perfluorooctane (n-C_8F_{18}) and perfluoropentadecane (n-$C_{15}F_{32}$). In the study, low concentrations of fluorinated tracer probes were added to crude oils, and the T_1/T_2 ratio was determined as a function of field strength. They observed significant variation in the ^{19}F relaxation times for aromatic and aliphatic probes in the three crude oils. The T_1/T_2 ratio of the aromatic probes C_6F_6 and C_7F_8 in an A13 oil was close to 100. In contrast, T_1/T_2 is only about 5 when using alkane probes octane-F_{18} and pentadecane-F_{32} in the same sample. The ^{19}F relaxation times ratios T_1/T_2 for oils A_0 and W_0 were examined using aromatic and saturated ^{19}F probes, and a range of values was observed up

to T_1/T_2 >7. In ^{1}H NMR data of crude oil, no comparable differences in this ratio have been found before. Benzene-F_6 and toluene-F_8 relaxation dispersion is strong in oil A13, but for oil A_0 and W_0, as well as the alkane probes in oil A13, relaxation dispersion is quite small. The main finding of this study is that aromatic probes have significantly higher T_1/T_2 values in the presence of asphaltenes in oil.

6.3. Materials and Methods

6.3.1. Samples

The asphaltene sample for this study was obtained by Schlumberger-Doll Research in Cambridge, Massachusetts, USA. The petroleum asphaltene sample has a codename of UG8, which is a Kuwaiti black oil. In the literature, the extraction procedure for the UG8 asphaltene has been discussed in detail.[14] Compared to coal asphaltene, UG8 petroleum asphaltene has a higher sulfur content and a higher H:C atomic ratio.[15] The elemental composition of asphaltenes can vary greatly depending on the source of the crude oil and the processing conditions. However, the typical elemental composition of UG8 asphaltenes consists of a high amount of carbon (C) at 81%, hydrogen (H) at 7%, nitrogen (N) at 1.02%, sulfur (S) at 8.94%, and trace amounts of oxygen (O) at 1.6%. The H:C atomic ratio in UG8 asphaltenes is 1.05.[15]

6.3.2. Probes for ^{19}F NMR spectroscopy

In this study, three commercially available fluorinated probes were used: $CFCl_3$, C_6F_6, and perfluorooctanoic acid (PFOA). $CFCl_3$ was used owing to its small size and ability to undergo strong dispersion interaction. C_6F_6 was chosen for its potential for π-π interactions. PFOA is a surfactant thus able to seek out interfaces between polar and non-polar environments. Sigma Aldrich supplied perfluorooctanoic acid (PFOA), $CFCl_3$, and

C_6F_6. The solvents, $CDCl_3$ and toluene-d_8, purchased from Sigma Aldrich (99.8%D). All materials and reagents were used without further purification or processing.

6.3.3. Sample preparation

The UG8 asphaltene samples were prepared as a stock solution in $CDCl_3$ and toluene-d_8 at a concentration of 15 mg/mL, using the same method described in Chapters 3 and 4. The serial dilution method was used to prepare three different concentrations (1.0, 5.0, and 15 mg/mL) of the stock solution in $CDCl_3$ and toluene-d_8 solvents. This involved measuring the calculated amount of the stock solution using a micropipette and adding the required volume of solvent using a volumetric pipette. The samples were then transferred into labeled, clean, and dry test tubes and mixed thoroughly to ensure homogeneity. To reduce evaporation, the solutions were prepared just when needed and stored in the freezer. For the ^{19}F NMR relaxation time measurements, the concentration of the fluorinated probe molecules was set to 4 mg/mL.

6.3.4. NMR spectroscopy

All NMR spectra were obtained using a Bruker Avance III HD 700 MHz NMR spectrometer operating at 16.4 T, equipped with a triple resonance Bruker TXO-Z (C-H-2H) probe equipped with a ^2H lock channel, automatic tuning and matching, and Z-gradient. For ^{19}F NMR spectra, a selective ^{19}F probe, equipped with a triple resonance Bruker TXO-Z (F-H-2H) probe equipped with a ^2H lock channel, automatic tuning and matching, and Z-gradient was used.

All relaxation data were acquired at room temperature. T_1 relaxation times were obtained using the inversion recovery pulse sequence[16] of the form{-RD-p_1(180°)-τ- p_2(90°)-

aq(acquire)}; the phase cycles were: p_1: {x, –x}$_4$; p_2: {x_2, –x_2, y_2, –y_2}; and aq: {x_2, –x_2, y_2, –y_2}.

T_2 relaxation data were obtained using the CPMG (Carr-Purcell-Meiboom -Gill) pulse sequence[17] of the form [–RD–p_1(90°)–{τ–p_2(180°)–τ}$_n$–aq(acquire)]; the phase cycles were: p_1: {x, x, –x, –x, y, y, –y, –y}; p_2: {y, –y, y, –y, x, –x, x, –x}; and aq:{ x, x, –x, –x, y, y, –y, –y}. The fixed delay in the CPMG train was 2 × 2.0 ms, which was looped up to 250 times. The recycle delay for ^{1}H relaxation measurements were set to 60 s, to avoid saturation effects (as determined in Chapter 3). However, the recycle delay for ^{19}F relaxation measurements was set to 10 s because the T_1 values for this experiment was close to 2 s. Thus, a recycle delay of 10 s should give reasonable quantitative spectra without unnecessarily long experiments. Data were Fourier-transformed, baseline-corrected, and phased. The integration and deconvolution analysis were performed by MestRenova software (version 14.2.0).

6.3.5. Exponential fits

The ^{1}H relaxation data shows a bi-exponential behavior and requires a nonlinear optimization method known as the Levenberg-Marquardt optimization method[18] for proper analysis. On the other hand, the ^{19}F relaxation data exhibits mono-exponential behavior and are analyzed using the linear regression method.

6.3.6. DOSY experiment

^{1}H diffusion ordered NMR (DOSY) experiments were performed on a Bruker Avance 700 MHz spectrometer, which operates 16.4 T and equipped with a triple resonance Bruker TXO-Z (C/F-H-2H) probe equipped with a ^{2}H lock channel and Z-gradient. The DOSY experiment used the same samples as the samples were used in the ^{1}H relaxation experiment. A DOSY experiment is usually collected using a spin-echo as a function of pulsed-field gradient intensity. The diffusion coefficient determines the rate at which each signal intensity decreases.[19] The stebpgp1s pulse sequence was used in the diffusion ordered spectroscopy (DOSY) experiments.[19] Spectra were obtained with 32 scans in an increasing linear gradient ranging from 2% to 95% with a pulsed gradient time δ of 3.6 ms and diffusion times Δ of 50 -100 ms during the DOSY experiment. The spectra were subsequently processed using the Bruker Dynamics Suite with two processing methods. The initial method follows a standard procedure allowing for up to three components, while the second method employs an inverse Laplace transform. In the former method, nonlinear optimization is applied to derive $A_{\mathrm{diffusion}}(\delta, \Delta, D)$ from Equation 3.6 in Chapter 3, yielding diffusion constants, intensities for each component, and their respective 95% confidence limits.

6.4. Results and Discussion

6.4.1. ^{1}H NMR relaxation of UG8 asphaltene at different concentrations in $CDCl_3$ and toluene-d_8

NMR relaxation experiments were conducted on solutions of UG8 to determine its ^{1}H T_1 and T_2 values with concentrations of 1, 5 and 15 mg/mL. The T_1 and T_2 of the UG8

asphaltene at various concentrations in $CDCl_3$ are shown in Table 6.1. The T_1 and T_2 relaxation times are sensitive to internal motion as well by whole-body motion, the former would predominate for isolated molecular entities and opposed to the latter which would prevail for large densely-packed colloidal aggregates.

The T_1 and T_2 relaxation data show a biexponential pattern for all three signal types in all concentrations. In every instance, the major component constituted approximately 70 to 80% of the total. The T_1 and T_2 pairing is consistent with the divergence in relaxation behaviour between T_1 and T_2 with longer correlation times, *i.e,* when T_1 is longer, T_2 is shorter. The alkyl protons, typically with the highest internal mobility, demonstrate shorter correlation times and did not show such dramatic differences in relaxation behavior, as explained in Chapter 3.

Table 6.1. ^{1}H NMR relaxation times of UG8 asphaltene in $CDCl_3$.

Concentration (mg/mL)	Aliphatic		Alicyclic		Aromatic	
	T_1 (s)	T_2(ms)	T_1 (s)	T_2 (ms)	T_1 (s)	T_2 (ms)
1	0.91 ± 0.03 (70 ± 4.5%)	410 ± 3.0 (68 ± 4.0%)	1.85 ± 0.05 (75 ± 5.5%)	112 ± 0.89 (75 ± 5.0%)	2.76 ± 0.06 (70 ± 5.5%)	94.8 ± 0.9 (70 ± 4.5%)
	1.20 ± 0.04 (30 ± 3.5%)	980 ± 5.5 (32 ± 3.5%)	0.88 ± 0.02 (25 ± 4.0%)	195 ± 1.2 (25 ± 4.5%)	1.47± 0.03 (30 ± 4.5%)	203 ± 1.3 (30 ± 5.0%)
5	0.95 ± 0.02 (75 ± 3.5%)	91.4 ± 0.9 (68 ± 4.0%)	2.15 ± 0.06 (78 ± 5.5%)	40.5 ± 0.5 (75 ± 5.8%)	3.14 ± 0.06 (75 ± 5.5%)	48.0 ± 0.7 (72 ± 4.5%)
	1.75 ± 0.03 (25 ± 3.5%)	502 ± 3.50 (32 ± 3.5%)	0.99 ± 0.03 (22 ± 4.0%)	89.2 ± 0.9 (25 ± 4.5%)	1.65 ± 0.03 (25 ± 4.5%)	79.2 ± 0.9 (28 ± 5.0%)
15	1.10 ± 0.03 (75 ± 3.5%)	48.8 ± 0.82 (70 ± 4.0%)	3.15 ± 0.06 (78 ± 5.5%)	26.1 ± 0.4 (75 ± 5.8%)	3.23 ± 0.05 (75 ± 5.5%)	22.8 ± 0.6 (70 ± 4.5%)
	2.18 ± 0.04 (25 ± 3.5%)	350 ± 2.50 (30 ± 3.5%)	1.07 ± 0.04 (22 ± 4.0%)	37.0 ± 0.5 (25 ± 4.5%)	1.65 ± 0.03 (25 ± 4.5%)	35.2 ± 0.8 (30 ± 5.0%)

Generally, the T_1/T_2 ratio is used to estimate the average correlation time in each structural environment. The T_1/T_2 ratios of the UG8 asphaltene at various concentrations are shown in Figure 6.1 and Table 6.2.

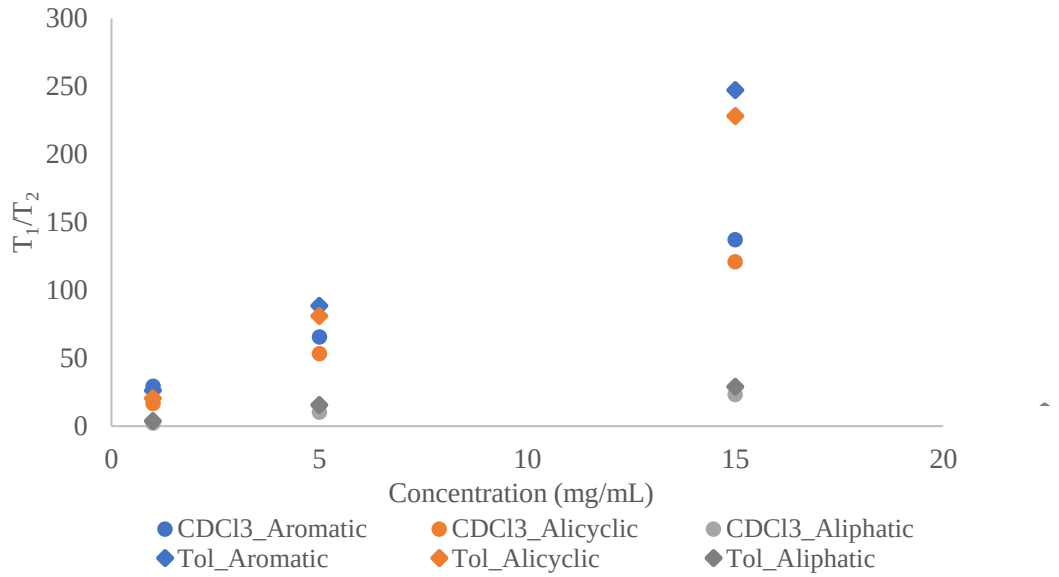

Figure 6.1. The relationship between T_1/T_2 (major component) for selected signals in the ^1H spectrum of UG8 asphaltene with concentration using a 60 s delay in $CDCl_3$ and toluene-d_8.

Table 6.2. T_1/T_2 ratios of UG8 asphaltene with different concentrations using 60 s delay in $CDCl_3$ and toluene-d_8. The values in parentheses represent the percentage of protons having the corresponding T_2 and T_1.

Concentration (mg/mL)	$CDCl_3$ (T_1/T_2)			Toluene-d_8 (T_1/T_2)		
	Aliphatic	Alicyclic	Aromatic	Aliphatic	Alicyclic	Aromatic
1	2.2 ± 0.09 (65-75%)	16 ± 0.4 (70-80%)	29 ± 0.8 (65-75%)	3.8 ± 0.2 (70-80%)	20 ± 0.8 (70-80%)	26 ± 0.8 (70-80%)
	1.9 ± 0.07 (25-35%)	4.5 ± 0.2 (20-30%)	7.2 ± 0.3 (25-35%)	1.5 ± 0.06 (20-30%)	6.5 ± 0.2 (20-30%)	8.6 ± 0.5 (20-30%)
5	10 ± 0.4 (70-80%)	53 ± 1.8 (75-85%)	65 ± 2.0 (70-80%)	15 ± 0.7 (65-75%)	81 ± 2.2 (65-75%)	89 ± 2.6 (65-75%)
	3.5 ± 0.2 (20-30%)	11 ± 0.4 (15-25%)	20 ± 0.6 (20-30%)	4.3 ± 0.2 (25-35%)	18 ± 0.5 (25-35%)	22 ± 0.7 (25-35%)
15	23 ± 0.9 (70-80%)	120 ± 3.6 (70-80%)	140 ± 4.2 (65-75%)	29 ± 1.0 (70-80%)	230 ± 5.1 (70-80%)	250 ± 6.3 (70-80%)
	6.5 ± 0.5 (20-30%)	29 ± 0.6 (20-30%)	40 ± 1.2 (25-35%)	7.6 ± 0.7 (20-30%)	40 ± 1.2 (20-30%)	46 ± 1.3 (20-30%)

The T_1/T_2 ratio approaches 1 at the limit of very rapid reorientational motion with τ_c well below the T_1 minimum, where $\tau_c \approx \omega_o^{-1}$. Higher ratios occur for τ_c values beyond the T_1 minimum and thus infers much slower motion. The bi-exponential T_1 and T_2 relaxation data for all three types of signals of interest, corresponding to aliphatic, alicyclic, and aromatic environments, result in two T_1/T_2 ratios for each, with one being much larger than the other. The difference in these ratios indicates that each of these environments have two distinct mobility regimes corresponding to two states, either differing in their degree of aggregation, and/or in their degrees of freedom of internal motion. The larger ratios, which represent the more abundant component, are plotted against concentration in Figure 6.1. The T_1/T_2 ratios of all three environments show the effect of asphaltene concentration on aggregation and/or on internal motion. All these measurements were carried out with a 60 s recycle delay, which was deemed sufficient to avoid saturation effects.

The critical nanoaggregate concentration (CNAC) is defined as the concentration at which nanoaggregates stop growing, which is at 0.13 mg/mL for UG8 in toluene. UG8 asphaltene also forms secondary aggregates near 5 mg/mL, which is its critical cluster concentration (CCC).[20] The lowest concentration of 1 mg/mL in this study being higher than the CNAC and well below the CCC suggests that nanoaggregates predominate, as proposed by Lisitza *et al.*[21] At this concentration, the larger T_1/T_2 ratio likely result from increasing nanoaggregate contribution. This trend in the relaxation time ratios persists with concentration from the CNAC to beyond the CCC in both solvents and in all structural environments.

At medium concentration (5 mg/mL) where clustering starts taking place, the major component of aliphatic ratios has changed from 2.2 to 10 ($CDCl_3$ solution) with respect to

1 mg/mL; the alicyclic and aromatic T_1/T_2 ratios increase to much larger values, *i.e.*, 53 and 65 from 16 and 29, respectively. This trend is consistent with increasing restriction of internal mobility for alicyclic and aromatic environments upon increasing aggregate size. This specific trend would be expected in the case of π–π stacking as the alicyclic rings increasingly impinge on the densely packed aromatic cores with increasing aggregate concentration. The increase in the T_1/T_2 ratios upon increasing concentration are much less pronounced in the minor-component ratios for the aliphatic, alicyclic, and aromatic environments, suggesting the lack of stacking or some other sort of binding causes these to be less dense and thus retaining higher internal mobility. In other words, one could consider the major component more densely packed than the minor components.

At high concentration (15 mg/mL), well above the CCC, the T_1/T_2 ratio of the major aromatic component approaches 140 in $CDCl_3$, suggesting a higher degree of aggregation between nanoaggregates, *i.e.*, clusters have formed. In contrast, the ratio of the minor component of the aromatic resonances reaches 40, still indicating a high degree of internal motion, however, much diminished than at lower concentrations. This suggests that upon clustering the mobile component exhibits some steric pressure; however, the diminished differentiation between the three structural environments remains essentially the same.

Apart from generally being larger, the same behavioral trends for the T_1/T_2 were observed in toluene-d_8 solutions for both major and minor components in all three structural environments. As one significant difference, the rate of increase is larger for both the alicyclic and aromatic signals resulting in the final values in toluene being larger by a factor of two when compared to $CDCl_3$. The higher values in toluene over chloroform imply

higher mobility of the aggregates in chloroform and thus the clustering is less compact than in toluene. Thus, solvent strongly influences the degree of clustering.

Recall that T_1/T_2 ratios for the major components are typically much smaller for the aliphatic signals compared to their alicyclic and aromatic counterparts as they exhibit additional modes of internal motion. If one were to assume that the environment of the major component is the most densely packed, one would expect the T_1/T_2 ratio of the aromatic signal to be best at representing the lower limit of timescale of the reorientational motion for the whole aggregate. Based on these ratios, the rotational correlation time can be used to estimate a minimum value for hydrodynamic radii of the aggregates using Equations 3.3 and 3.4 from Chapter 3. The calculated rotational correlation times and hydrodynamic radii are listed in Table 6.3. The increase in aggregate size is readily appreciated in chloroform where the hydrodynamic radius increases from 1.48 nm at 1 mg/mL, typical of a small nanoaggregate, to 1.70 nm at 5 mg/mL, corresponding to full sized aggregates, to 1.94 nm at 15 mg/mL, corresponding to an average clustering number near 2. The same is seen for toluene where r_H increases from 1.45 to 2.13 nm over the same concentration range, indicating clustering of up to 3 nanoaggregates at the highest concentration. In addition, the average aggregate size is consistently larger in toluene than in chloroform at and over 5 mg/mL.

The T_1/T_2 ratios for the aromatic major components of UG8 at 15 mg/mL are comparable to those of the PetroPhase 2017 sample (see Chapter 5), despite them being twice as large considering they were obtained at twice the concentration. The Manifa asphaltene relaxation-time ratios (see Chapter 3) do stand far apart from the PetroPhase 2017 and UG8 sample, even when considering that they were obtained at 50 mg/mL, being 80 times larger.

This suggest that the degree of clustering depends strongly on the asphaltene type, however the nanoaggregate sizes are more consistent between all three sample types.

Table 6.3. T_1/T_2 ratios of aromatics, correlation times (τ_c) and r_H values of UG8 asphaltenes.

Solvent	Conc (mg/mL)	T_1/T_2 Major	τ_c (ns)	r_H (nm)	T_1/T_2 Minor	τ_c (ns)	r_H (nm)[a]
$CDCl_3$	1	29	1.78	1.48	7.2	0.82	*1.14*
	5	65	2.69	1.70	20	1.46	*1.39*
	15	140	3.98	1.94	40	2.1	*1.57*
Toluene	1	26	1.68	1.45	8.6	0.91	*1.18*
	5	89	3.16	1.79	22	1.54	*1.41*
	15	250	5.32	2.13	46	2.26	*1.60*

[a]Hydrodynamic radii were calculated based on the T_1/T_2 ratios at the minor component. These radius values are not meaningful in the proposed core/shell model, but would represent particle sizes, if the minor component were to represent an aggregate state.

6.4.2. DOSY NMR spectroscopy of UG8 asphaltene at different concentrations

Diffusion-ordered spectroscopy (DOSY) experiments were conducted on the UG8 asphaltene samples at different concentrations, providing valuable insights into their translational diffusion coefficients and size information. These experiments were performed using three different concentrations (1, 5, 15 mg/mL) of UG8 asphaltenes in deuterated chloroform and toluene. The aliphatic ^{1}H NMR signals were used to identify components with different diffusion coefficients. Figure 6.2 shows the DOSY spectra of UG8 asphaltene in deuterated toluene and chloroform, including spectra processed using the inverse Laplace transform.

The graphs in Figure 6.2 show four different groups of cross peaks whose corresponding diffusion-constant ranges were tabulated in Tables 6.4 and 6.5. These groupings correspond to ranges in diffusion coefficients that are high, medium, low, and very low in magnitude.

As part of the DOSY processing the amplitude factors for 150-200 peaks were fit to allow for up two contributions from three diffusions components. Typical errors in the diffusion constants ranged from 0.1 to 0.5 x 10^{-10} m^2/s. Some peaks had extremely wide errors as two components could not be resolved; correspondingly, an upper and lower value was used based on the width.

a)

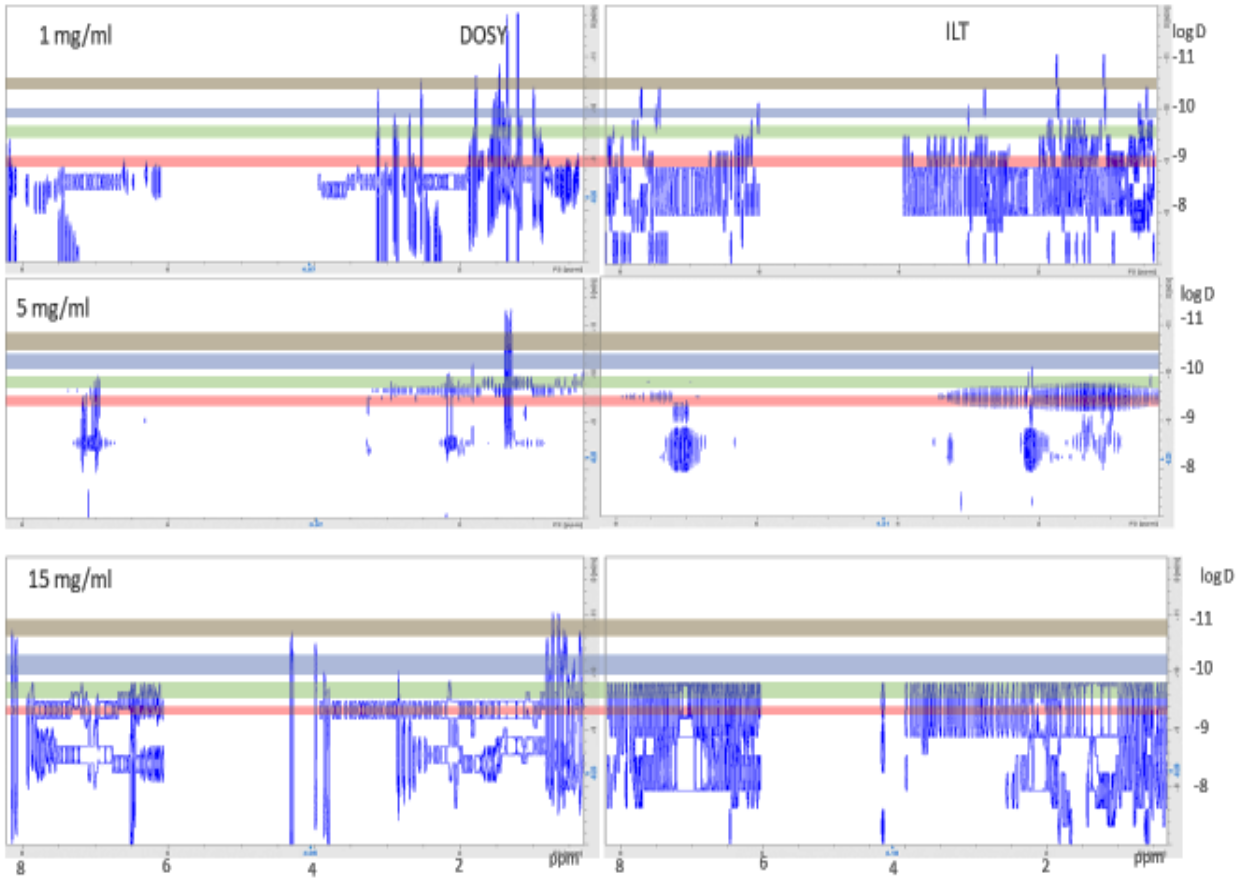
1 mg/ml
DOSY
ILT
log D
-11
-10
-9
-8
5 mg/ml
log D
-11
-10
-9
-8
15 mg/ml
log D
-11
-10
-9
-8
8
6
4
2
ppm
8
6
4
2
ppm

b)

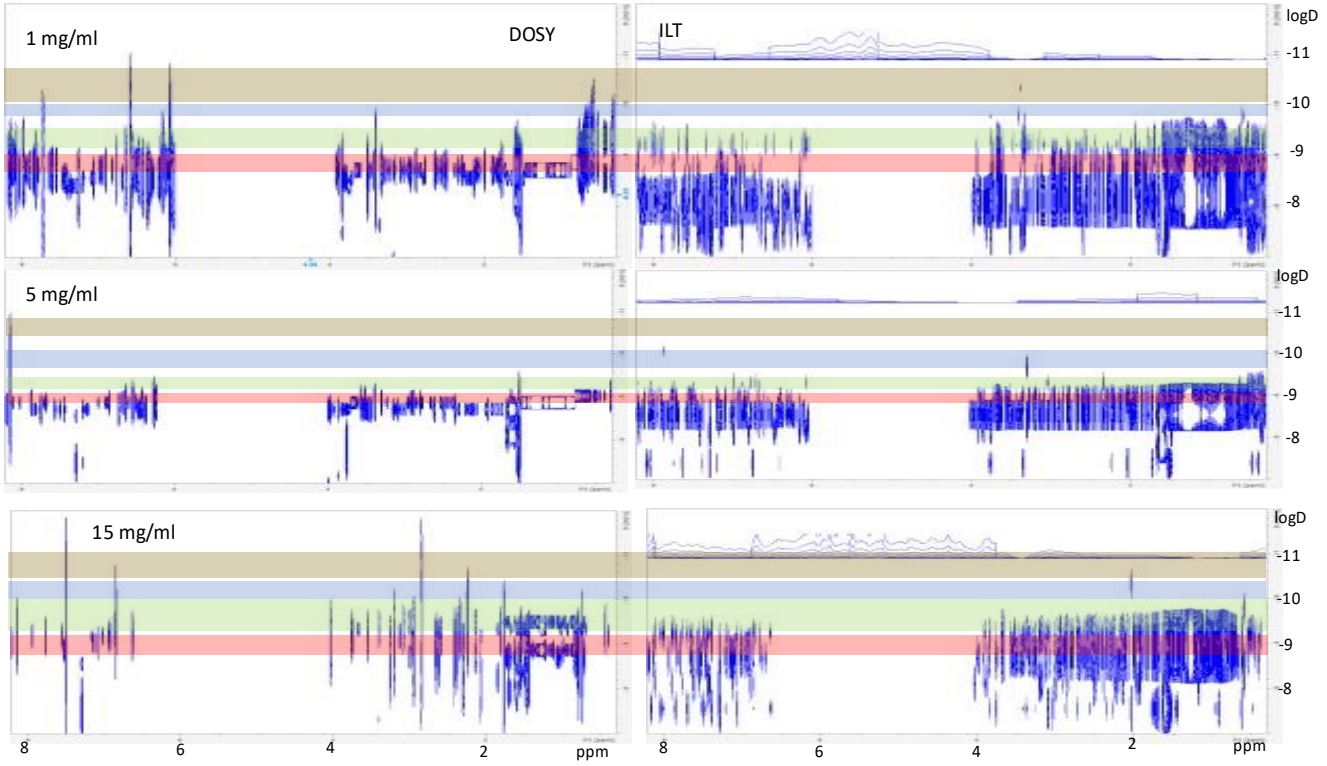

Figure 6.2. ^{1}H DOSY and the corresponding Inverse Laplace Transform (ILT) spectra of UG8 asphaltene in a) toluene-d_8 and b) $CDCl_3$ at different depth. X-axis represents the chemical shift in ppm and Y-axis represents the diffusion coefficient value in log form. The coloured horizontal lines indicate the components (red-, green-, purple-, and brown-colored boxes), characterized by their different diffusion coefficients.

The diffusion-coefficient ranges are indicated by colored boxes, and the solvent diffusion coefficients (black line) is also indicated. In Table 6.4, the presumed sub-nanoaggregates are represented in red, the nanoaggregates in green, the micro-aggregates (small clusters) in purple and the macro-aggregates (large clusters) in brown. The hydrodynamic radii and the adjusted diffusion coefficients (D*) of the UG8 asphaltenes are calculated via the equations used in Chapter 3 (Eq. 3.4 and 3.5) at T = 298 K, and η(toluene) = 0.56 mPa/s, and $\eta(CHCl_3)$ = 0.54 mPa/s. The adjusted diffusion coefficients (D*) and r_H values with increasing concentration of UG8 asphaltenes dissolved in toluene-d_8 and $CDCl_3$ are listed in Tables 6.4 and 6.5, respectively. The same color coding is used for the components in the Table as in Figure 6.2.

Table 6.4. The diffusion coefficients (D), solvent diffusion coefficients (SD), relative diffusion coefficients (DR), adjusted diffusion coefficients (D*), r_H values, and approximate estimation of the relative contribution for UG8 asphaltenes in toluene-d_8. The self-diffusion constant for toluene is taken as $D_o = 2.28 \times 10^{-9}$ m^2/s. The error analysis for the individual data points in the range in D is based on the three-component fit performed in the dynamic center during the DOSY analysis.

Concentration (mg/mL)	D (m^2/s) $\times 10^{-10}$	SD (m^2/s) $\times 10^{-10}$	D* (m^2/s) $\times 10^{-10}$	r_H (nm) sub-nano, nano, micro, macro	Estimated Contribution
1	8.5-12.0 ± 0.3	18.0 ± 0.1	10.8-15.2 ± 0.4	0.27-0.37 ± 0.01	Major
	2.0-3.0 ± 0.2		2.5-3.8 ± 0.3	1.1-1.6 ± 0.3	Medium
	0.9-1.5 ± 0.2		1.1-1.9 ± 0.3	2.1-3.7 ± 0.3	Minor
	0.20-0.40 ± 0.1		0.25-0.53 ± 0.13	8-16 ± 4	Trace
5	3.0-4.0 ± 0.2	18.0 ± 0.2	3.8-5.1 ± 0.3	0.76-1.0 ± 0.06	Medium
	1.2-2.0 ± 0.2		1.5-2.5 ± 0.3	1.6-3.4 ± 0.4	Medium
	0.40-0.80 ± 0.2		0.51-1.0± 0.3	4-8 ± 2	Minor
	0.17-0.38 ± 0.1		0.22-0.48 ± 0.13	8-18 ± 4	Trace
15	3.7-4.5 ± 0.3	18.7 ± 0.1	4.5-5.5 ± 0.4	0.71-0.86 ± 0.06	Trace
	1.4-2.7 ± 0.2		1.7-3.3 ± 0.2	1.2-2.4 ± 0.1	Minor
	0.50-0.90 ± 0.2		0.70-1.10 ± 0.3	3.7-5.8 ± 2	Medium
	0.12-0.22 ± 0.1		0.15-0.27 ± 0.12	15-27 ± 12	Major

Table 6.5. The diffusion coefficients (D), solvent diffusion coefficients (SD), relative diffusion coefficients (DR), adjusted diffusion coefficients (D*), r_H values, and approximate estimation of the relative contribution for UG8 asphaltenes in $CDCl_3$. The self-diffusion constant for chloroform is taken as $D_o = 3.96 \times 10^{-9}$ m^2/s. The error analysis for the individual data points in the range in D is based on the three-component fit performed in the dynamic center during the DOSY analysis.

Concentration (mg/mL)	D (m^2/s) $\times 10^{-10}$	SD (m^2/s) $\times 10^{-10}$	D* (m^2/s) $\times 10^{-10}$	r_H sub-nano, nano, micro, macro	Estimated Contribution
1	9.0-20.0± 0.5	25.5 ± 0.2	14.0-31.0 ± 0.8	0.13-0.28 ± 0.01	Major
	3.0-7.0 ± 0.2		4.7-10.9 ± 0.3	0.36-0.83 ± 0.02	Medium
	1.0-2.0 ± 0.1		1.6-3.1± 0.2	1.3-2.4 ± 0.12	Minor
	0.2-1.0 ± 0.1		0.31-1.6 ± 0.2	2.4-12.6 ± 0.2	Trace
5	9.0-14 ± 0.5	20.0 ± 0.1	18-28 ± 1	0.14-0.22 ± 0.01	Medium
	4.0-7.0 ± 0.2		8--14 ± 1	0.28-0.50 ± 0.04	Medium
	0.7-2.0 ± 0.2		1.4-4.0 ± 1.2	1.0-2.8 ± 0.8	Minor
	0.13-0.40 ± 0.1		0.26-0.79 ± 0.2	5-15 ± 4	Trace
15	6.0-13 ± 0.5	19.5 ± 0.1	12-26 ± 1	0.15-0.32 ± 0.01	Minor
	1.0-5.0 ± 0.2		2.0-10.2 ± 0.4	0.38-1.95 ± 0.08	Medium
	0.4-1.0 ± 0.2		0.8-2.0 ± 0.4	2-5 ± 1	Medium
	0.1-0.4 ± 0.1		0.2-0.8 ± 0.2	5-20 ± 5	Minor

The DOSY cross-peaks intensities varied greatly between groups in both solvents, where the lowest D values ($< 10^{-10}$ m^2/s) have particularly low intensities as compared to those at middle and higher D values. Qualitative estimates of the magnitude of the contribution of each grouping are also given in the Tables as major, medium, minor, and trace.

Conductivity measurements on UG8 in toluene show that there is a rapid increase from 31 - 155 mg/L, where the CNAC is reached, after which it increases further at about half the

previous rate ending at 860 mg/L falling well short of the CCC estimated to be around 5000 mg/L (L. Goual, personal communication). The diffusion coefficient calculated from the conductivities starting at 31 mg/L is 28×10^{-10} m^2/s (r_H = 0.14 nm) monotonically decreases to 10×10^{-10} m^2/s (0.40 nm). These correspond closely to those of the sub-nano grouping from the current DOSY measurements in toluene. The conductivities past CNAC decrease rapidly giving corresponding diffusion constants of 6.0×10^{-10} m^2/s (r_H = 0.66 nm) at 200 mg/L to 4.0×10^{-10} m^2/s (r_H = 0.99 nm) at 860 mg/L, which is 6-7 times the CNAC while still well below the CCC. In this region one would expect the sub-nano population to decline significantly and the nano population starting to predominate. The diffusion constants in this region are converging to those in the nano category for the DOSY measurement in toluene.

Upon closer inspection of the DOSY results for the four categories do not align between the solvents. Consider the spectra of samples with 1 mg/mL UG8 concentration. The first two ranges in chloroform (0.13 to 0.28 nm and 0.36 to 0.83 nm) and the first (0.27 to 0.37 nm) in toluene seem to correspond, and thus are considered sub-nano. The third category in chloroform (1.3-2.4 nm) is most comparable to the second and third in toluene (1.1 to 1.6 nm and 2.5-3.8 nm) where the lower values are considered nano, while the upper values would be micro. The fourth group in chloroform (2.4 to 12.6 nm) starting in the micro and ending in the macro categories. In toluene the fourth group falls in the macro range.

In the sub-nano category, the hydrodynamic radii (r_H) correspond to suboptimal aggregates such as monomers, dimers, trimers, *etc*., having r_Hs smaller than 1.2 nm. The nanoaggregates range from 1.3 to 2.0 nm. The r_H's in the micro category surpasses the

optimal aggregate size, from 2.0 – 5.0 nm, which corresponds to the onset of clustering from 2 to 40 aggregates (based on the ratio of the hydrodynamic volumes). The macro group considered sizes above 5 nm with cluster ranging from 40 to 4000.

Even though it seems that the particle sizes in the four categories increase with concentration in both solvents, their relative contributions also change dramatically with concentration. These observations at this stage are at best qualitative, where newer DOSY methods need to be developed to provide uniform amplitudes for diffusion constants down to 10^{-11} m^2/s.

In summary, it can be said that the particle sizes increase with concentration in both solvents, where sizes are consistently larger in toluene. These results are consistent with those from the T_1/T_2 ratios; however, there are some notable differences. The relaxation dispersion results show only two categories, mainly because of the limitation of a biexponential analysis. The hydrodynamic radii derived from the T_1/T_2 of the major component in toluene range from 1.45 to 2.13 nm, indicating clustering between 1 and 4 nanoaggregates. This is akin to the DOSY results for the nano and micro categories, but not identical, where r_H increases from 1.1 to 2.0 nm and 2.0 to 5.8 nm. The hydrodynamic radii calculated from the T_1/T_2 values in toluene for the minor component fall within the 1.18 to 1.6 nm range, which would be in line with the nano- and sub-nano categories of the DOSY results.

If the major and minor components in T_1/T_2 were to correspond to different particle size distributions, one would expect that the major component should be dominated by the micro and the minor by the nanoaggregates. This would imply that the relative %

contribution of the two components should change with concentrations and solvent. Instead, the % contribution are eventually invariant with concentration and solvent which casts doubt on the assumption that the major and minor reflect contributions from particles with different size distributions.

6.4.3. ^{19}F NMR spectroscopy

The ^{19}F NMR spectra of solutions of the potential probe molecules perfluorooctanoic acid (PFOA), $CFCl_3$, and C_6F_6 were recorded in $CDCl_3$ (Figure 6.3). These fluorinated molecules are commercially available. Ribiero *et al.*[23] applied ^{19}F, ^{19}F COSY to derive a complete set of NMR analyses of a perfluorinated alkyl chain in DMSO-d_6 solvent. Their analyses were used to assign the ^{19}F NMR spectrum for PFOA in Figure 6.3(a). The trifluoromethyl (CF_3; C_ω) group is assigned to the signal at –80 ppm. The $C_\varepsilon F_2$ group adjoining to the CF_3 group is usually the most upfield in linear perfluorinated chains and the group shows at –126 ppm. $C_\varepsilon F_2$ has the strongest shielding due to the γ-gauche shielding effect. γ-gauche is a net shielding effect caused by a gauche arrangement between a carbon atom and its ^{19}F neighbor, and it has a relatively short internuclear distance.[23] The γ -gauche shielding effect occurs for half the ^{19}F nuclei in PFOA chains with *cis-cis* helical structure. In the region around –118 ppm, a triplet has been assigned to $C_\alpha F_2$. This is because of the deshielding effect of the nearby carboxyl group. The remaining fluoromethylene (CF_2) groups were identified based on the intensity of cross peaks in 2D COSY spectroscopy in D_2O solvent.[24]

Another probe used in this experiment is $CFCl_3$, neat $CFCl_3$ being the standard reference compound for ^{19}F chemical shifts (0 ppm). Chemical shifts of fluorine are slightly different depending on the chlorine isotopes present in $CFCl_3$, resulting in the characteristic isotopic

pattern (Figure 6.5(b)). Hexafluorobenzene (C_6F_6) was chosen to represent an aromatic environment. The ^{19}F NMR signal is known to occur near –162 ppm, and this solvent is frequently used as an internal secondary reference as shown in Figure 6.5(c).

(a) PFOA $C_\omega F_3$-$C_\varepsilon F_2$-$C_\lambda F_2$-$C_\delta F_2$-$C_\gamma F_2$-$C_\beta F_2$-$C_\alpha F_2$-COOH

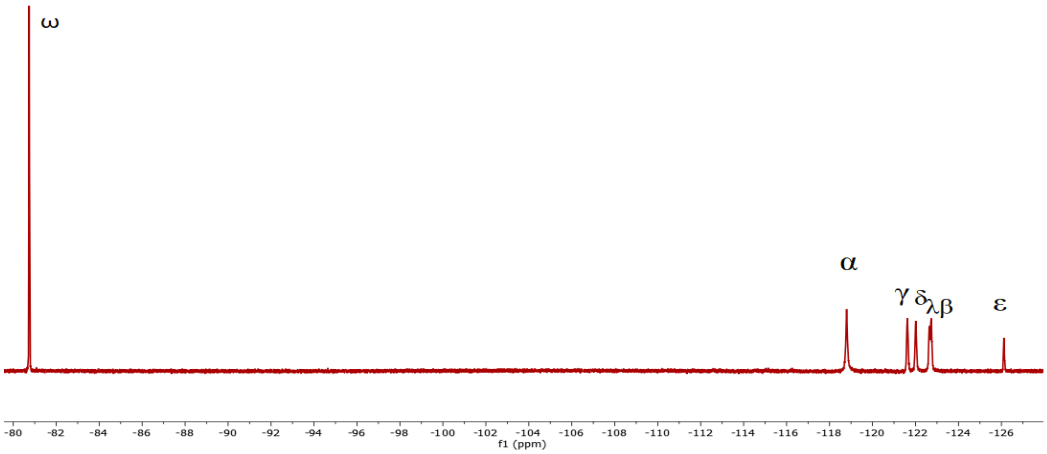

(b) $CFCl_3$

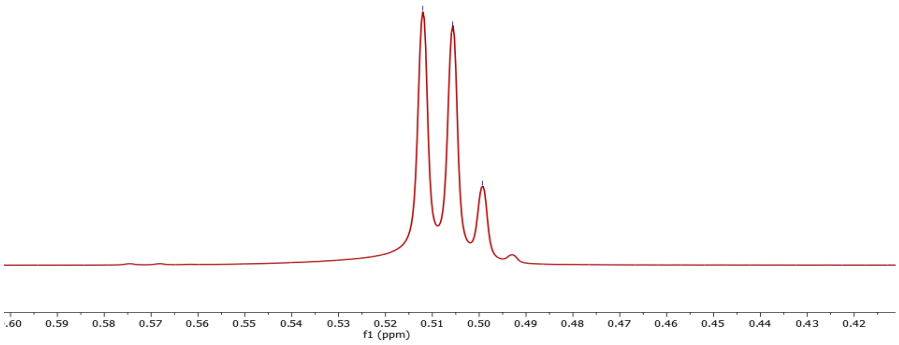

(c) C_6F_6

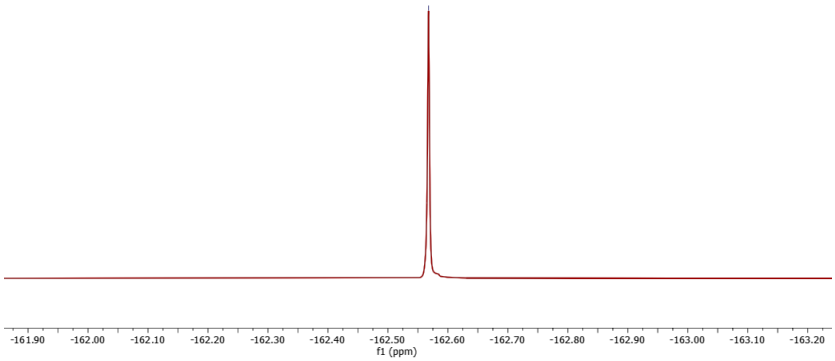

Figure 6.3. ^{19}F NMR spectra for (a) PFOA, (b) $CFCl_3$ and (c) C_6F_6 in $CDCl_3$.

6.4.4. ^{19}F Relaxation experiments of PFOA with UG8 at various ratios in $CDCl_3$ and in toluene-d_8

Fluorine-19 T_1 and T_2 relaxation times were determined for all signals of PFOA in the presence and absence of UG8. Table 6.6 shows the spin-lattice relaxation time (T_1) as a function of asphaltene concentration in $CDCl_3$. The ^{19}F relaxation experiments exhibits only mono-exponential behavior, not biexponential as seen in ^1H relaxation of UG8.

Table 6.6. ^{19}F spin-lattice relaxation time (T_1) of PFOA at different ratios with UG8 asphaltene in $CDCl_3$. The standard deviations for the T_1 values are provided.

UG8 Conc.	UG8:PFOA[a]	T_1 (s)				
mg/mL		$C_\omega F_3$	$C_\alpha F_2$	$C_{\gamma,\delta} F_2$	$C_{\lambda,\beta} F_2$	$C_\varepsilon F_2$
0	-	1.74 ± 0.03	0.85 ± 0.02	0.79 ± 0.02	0.82 ± 0.03	1.20 ± 0.03
1	1:6.66	1.50 ± 0.05	0.63 ± 0.03	0.65 ± 0.04	0.65 ± 0.05	0.92 ± 0.05
5	1:1.33	1.23 ± 0.03	0.56 ± 0.02	0.53 ± 0.03	0.55 ± 0.04	0.85 ± 0.03
15	1:0.45	0.76 ± 0.03	0.49 ± 0.04	0.42 ± 0.05	0.43 ± 0.02	0.64 ± 0.04

[a] The UG8:PFOA molar ratios were calculated using PFOA molecular weight of 414.07 g/mol and UG8 average molecular weight of 700 g/mol. Three different concentrations of UG8 (1, 5, and 15 mg/mL) were used, with the amount of PFOA being the same for all three samples.

In the presence of UG8, the ^{19}F T_1 relaxation time for all the signals of PFOA are shorter and decrease with increasing UG8 concentration. The T_1 of the $C_\omega F_3$ group is significantly longer than that of the CF_2 groups, which can be attributed to the additional degree of rotational freedom and the much shorter correlation times τ_c of the terminal $C_\omega F_3$ group of PFOA compared to the others while being in the fast motion regime when $\tau_c < 1/\omega_o$. The T_1 for $C_\varepsilon F_2$ will function similarly to that of the $C_\omega F_3$, as it is adjacent to $C_\omega F_3$ and thus will have its τ_c shortened by end chain motion. The $C_\alpha F_2$ behaves similarly to $C_\varepsilon F_2$ as its τ_c will also be shortened by chain motion near the carboxyl end. All the main chain signals $C_\beta F_2$, $C_\lambda F_2$, $C_\delta F_2$ and $C_\gamma F_2$ have consistently similar relaxation times, both in the presence or absence of UG8, indicating that they all belong to the same motional regime. Therefore, most of this analysis will be based on these signals.

With the introduction of UG8, T_1 decreases monotonically with increasing UG8 concentration. If a probe were effective, one would expect the changes in T_1 of the probe to be commensurate with those seen in ^1H of UG8. The ^{19}F T_1 values of PFOA decrease when UG8 concentration increases as binding between PFOA and UG8 restricts motion of

PFOA, causing its τ_c to lengthen to a maximum determined by the τ_c of the asphaltene, depending on the strength of the binding interaction. As τ_c is lengthened, both the T_1 and T_2 times will decrease while in the fast motion regime $\tau_c < 1/\omega_o$. In the slow-motion regime ($\tau_c > 1/\omega_o$), however, the T_1 will increase and the T_2 will decrease when τ_c lengthens. The reduction in the T_1 for the $C_\omega F_3$ group is more dramatic as it is the most mobile having the shortest τ_c of all the ^{19}F environments in PFOA. A more modest reduction in the T_1 for the $C_\varepsilon F_2$ group is anticipated. A similar result is expected for the $C_\alpha F_2$, especially if the carboxyl group is expected to have a dominant role in binding to the asphaltene aggregates. It turns out that the trend in the $C_\alpha F_2$ T_1 is the same as that for the remaining main chain CF_2 groups implying that the binding may be dominated by dispersion forces between the main chain of PFOA and most likely the asphaltene sidechains. The persistence of the higher T_1 values of the $C_\omega F_3$ suggests that the end of the chain remains the most mobile. The similar trend in the T_2 data lends credence to this interpretation.

Table 6.7 shows the ^{19}F spin-spin relaxation (T_2) as a function of asphaltene concentration. Again, the T_2 values are always longer in the free molecule. Upon the introduction of UG8, a decrease in T_2 is observed. Also, the T_2 of the $C_\omega F_3$ remains longer than the others, reflecting the additional degree of motion. Since the τ_c of all groups increases as they bind to asphaltene, the T_2 decrease monotonically with increasing UG8 concentration.

Table 6.7. ^{19}F spin-spin relaxation time (T_2) of PFOA at different ratios with UG8 asphaltene in $CDCl_3$. The standard deviations for the T_2 values are provided.

UG8 Conc.	UG8: PFOA	T_2 (s)				
mg/ml		$C_\omega F_3$	$C_\alpha F_2$	$C_{\gamma,\delta} F_2$	$C_{\lambda,\beta} F_2$	$C_\varepsilon F_2$
0	-	1.30 ± 0.04	0.35 ± 0.02	0.15 ± 0.01	0.14 ± 0.009	0.21 ± 0.02
1	1:6.66	0.57 ± 0.03	0.14 ± 0.02	0.084 ± 0.02	0.093 ± 0.009	0.12 ± 0.009
5	1:1.33	0.25 ± 0.05	0.053 ± 0.007	0.027 ± 0.004	0.033 ± 0.005	0.042 ± 0.005
15	1:0.45	0.094 ± 0.02	0.035 ± 0.006	0.011 ± 0.003	0.011 ± 0.002	0.024 ± 0.003

The ^{19}F T_1/T_2 ratios for PFOA with and without UG8 in $CDCl_3$ are given in Table 6.9, which range from 1 and 40 with increasing UG8 concentration. A ratio near 1 in the standard PFOA sample is consistent with a free molecule in solution with high mobility. Figure 6.4 shows the plot the T_1/T_2 ratios for the fluorine environments in PFOA with increasing concentration of UG8 in $CDCl_3$. Note that T_1/T_2 ratios for the $C_\beta F_2$, $C_\lambda F_2$, and $C_\delta F_2$, $C_\gamma F_2$ groups are consistently higher than for the $C_\omega F_3$ group. This is in line with the end groups being considerably more mobile than the main chain and $C_\varepsilon F_2$ groups. These results support the contention that binding is dominated by an interaction involving the main chain and UG8. Furthermore, the uniformity of the T_1/T_2 ratios of all the CF_2 groups could also be attributed to PFOA taking on a helical backbone configuration, which is common for perfluorinated alkanes. The CF_2 chemical shift changes upon binding may provide more support for this hypothesis.

Table 6.8. ^{19}F T_1/T_2 ratios for PFOA in different concentrations of UG8 asphaltene in $CDCl_3$.

UG8 Conc.	UG8: PFOA	T_1/T_2				
mg/mL		$C_\omega F_3$	$C_\alpha F_2$	$C_{\gamma,\delta} F_2$	$C_{\lambda,\beta} F_2$	$C_\varepsilon F_2$
0	-	1.3 ± 0.04	3.2 ± 0.11	5.4 ± 0.2	5.8 ± 0.2	5.6 ± 0.2
1	1:6.66	2.6 ± 0.09	4.2 ± 0.14	7.6 ± 0.3	7.3 ± 0.26	7.6 ± 0.3
5	1:1.33	4.5 ± 0.21	11 ± 0.4	20 ± 0.7	20 ± 0.8	20 ± 0.8
15	1:0.45	8.0 ± 0.32	16 ± 0.6	39 ± 1.5	39 ± 1.3	29 ± 1.2

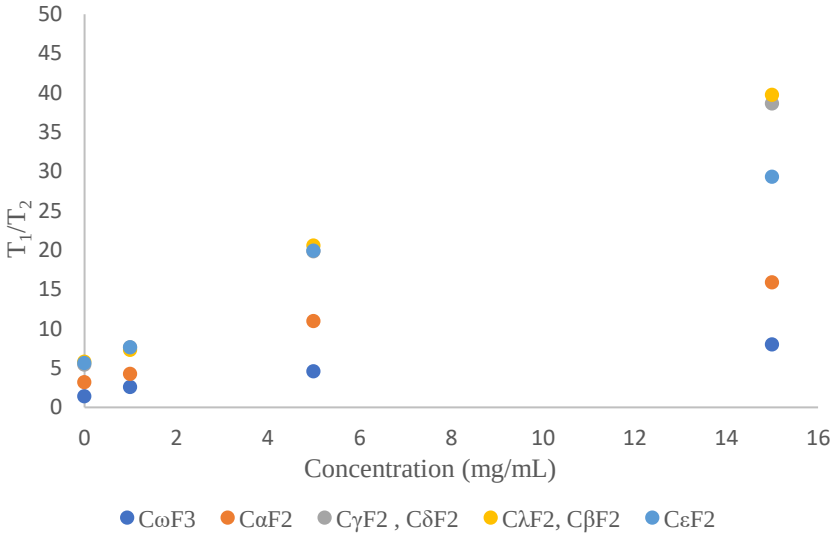

Figure 6.4. Ratios of the ^{19}F relaxation times T_1/T_2 for PFOA with different concentration of UG8 asphaltene in $CDCl_3$.

The T_1/T_2 ratios were determined for PFOA in toluene-d_8 (Table 6.9, Figure 6.5). The same trend in T_1 and T_2 values with respect to the UG8 concentration was observed when comparing the results with those from $CDCl_3$. Different ways in which various solvents influence the aggregation of asphaltenes have been investigated.[27] The greater relaxation dispersion in toluene when compared to $CDCl_3$ is qualitatively consistent with the ^1H

relaxation dispersion results; however, the relative changes appear to be different between the two solvents.

Table 6.9. ^{19}F relaxation times T_1/T_2 for PFOA in different concentrations of UG8 asphaltene in toluene-d_8.

UG8 Conc.	UG8: PFOA	T_1/T_2				
mg/ml		$C_\omega F_3$	$C_\alpha F_2$	$C_{\gamma,\delta} F_2$	$C_{\lambda,\beta} F_2$	$C_\varepsilon F_2$
0	-	2.2 ± 0.09	3.4 ± 0.15	5.8 ± 0.2	7.1 ± 0.3	5.4 ± 0.25
1	1:6.66	2.6 ± 0.1	4.2 ± 0.15	8.6 ± 0.34	8.4 ± 0.34	8.2 ± 0.36
5	1:1.33	6 ± 0.24	14 ± 0.5	21 ± 0.84	21 ± 0.9	22 ± 1.0
15	1:0.45	12 ± 0.5	25 ± 1.0	41 ± 1.7	45 ± 2.0	40 ± 1.6

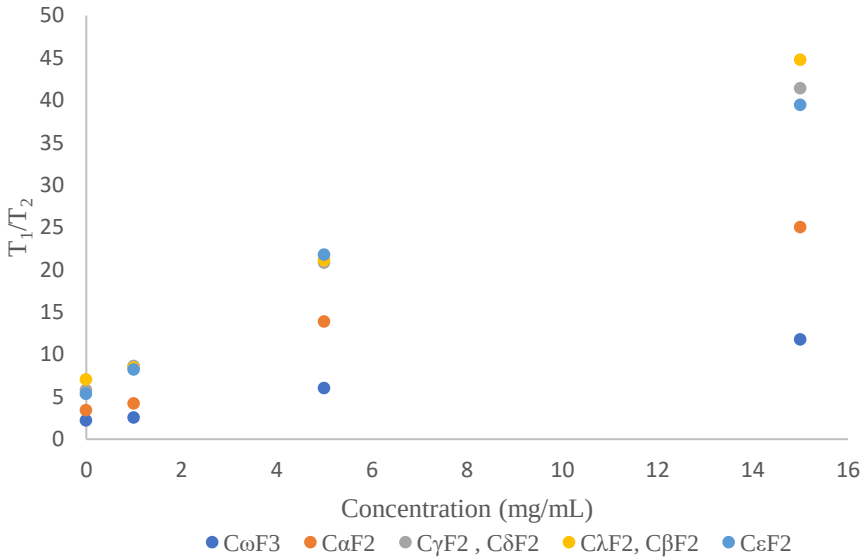

Figure 6.5. The ratio of the ^{19}F relaxation times T_1/T_2 for PFOA in different concentrations of UG8 in toluene-d_8.

Table 6.10 summarises the ^1H relaxation parameters of the aromatic signals from UG8 with increasing concentration in $CDCl_3$ and toluene-d_8, together with the ^{19}F relaxation parameters of the main chain signals of PFOA with increasing concentration in both

solvents. When comparing the ^{19}F and ^{1}H relaxation data directly, the ^{1}H T_1/T_2 ratios of the aromatic minor signal clearly correspond closest to the ^{19}F T_1/T_2 ratios of the main chain signals with increasing concentration in both solvents. Additionally, the magnitude of the ^{1}H T_1/T_2 ratios for the aromatic major signal is larger than those of ^{19}F. This means that ^{19}F is only detecting one component of ^{1}H signals. This observation is in disagreement with the interpretation of the two components in ^{1}H NMR spectrum representing separate particle-size distributions. It seems more likely that the ^{19}F is interacting with the outer layer of the aggregates, which is the more mobile environment – the minor ^{1}H component. The dense, less mobile interior/core does not appear to be reached by the probe, which is represented by the major ^{1}H component.

Table 6.10. ^{1}H relaxation times for UG8 and ^{19}F relaxation times for main chain of PFOA in different concentrations of UG8 in $CDCl_3$ and toluene-d_8.

	^{1}H				^{19}F	
	$CDCl_3$		Toluene-d_8		$CDCl_3$	Toluene-d_8
	Aromatic		Aromatic		$C_{\gamma,\delta}F_2$	$C_{\gamma,\delta}F_2$
Concentration (mg/mL)	T_1/T_2 (major)	T_1/T_2 (minor)	T_1/T_2 (major)	T_1/T_2 (minor)	T_1/T_2	T_1/T_2
1	29	7.2	26	8.6	7.6	8.6
5	65	20	89	22	20	21
15	140	40	250	46	39	41

6.4.5. ^{19}F Relaxation experiments with increasing concentration of PFOA

The ^{19}F relaxation measurements were repeated, but with double the concentration of PFOA and the same concentration of UG8 (Tables 6.11 and 6.12). Accordingly, the ratios of UG8 to PFOA are twice those in the previous tables.

Table 6.11. ^{19}F T_1/T_2 ratios for PFOA in $CDCl_3$. The values in parentheses represent the change in T_1/T_2 when the PFOA concentration is doubled.

UG8 Conc.	UG8:PFOA molar ratio	T_1/T_2				
mg/mL		$C_\omega F_3$	$C_\alpha F_2$	$C_{\gamma,\delta} F_2$	$C_{\lambda,\beta} F_2$	$C_\varepsilon F_2$
1	1:13.3	3.0 (+0.4)	5.0 (+0.6)	8.0 (+0.4)	7.8 (+0.5)	7.8 (+0.2)
5	1:2.66	6.5 (+2.0)	13 (+2.0)	23 (+3.0)	23 (+3.0)	21 (+1.0)
15	1:0.90	9.2 (+1.2)	18 (+2.0)	45 (+6.0)	46 (+7.0)	33 (+3.0)

Table 6.12. T_1/T_2 ratio for PFOA in toluene-d_8. The values in parentheses represent the change in T_1/T_2 when the PFOA concentration is doubled.

UG8 Conc.	UG8:PFOA molar ratio	T_1/T_2				
mg/mL		$C_\omega F_3$	$C_\alpha F_2$	$C_{\gamma,\delta} F_2$	$C_{\lambda,\beta} F_2$	$C_\varepsilon F_2$
1	1:13.3	3.1 (+0.5)	5.8 (+1.6)	9.6 (+1.0)	9.8 (+1.4)	8.9 (+0.7)
5	1:2.66	9.0 (+3.0)	18 (+4.0)	28 (+7.0)	30 (+9.0)	24 (+2.0)
15	1:0.90	13 (+1.6)	30 (+5.0)	55 (+14)	59 (+14)	43 (+3.0)

The T_1/T_2 ratios increase slightly when the amount of PFOA is doubled in both solvents. However, when the UG8 concentration is 15 mg/mL and thus the UG8: PFOA ratio is 1:0.90, the increase is most pronounced, especially for the main chain signals. The increase in the T_1/T_2 ratios is always higher in toluene than in $CDCl_3$. This suggests that the probe binds more strongly in toluene than in $CDCl_3$, penetrating more deeply into the particle further into the far less mobile interior.

6.4.6. ^{19}F chemical shift analysis of PFOA with UG8

The ^{19}F chemical shifts of the PFOA and UG8 systems were determined in $CDCl_3$ and toluene-d_8. Fluorine-19 chemical shifts are highly sensitive to their surroundings, so PFOA has different chemical shifts in $CDCl_3$ than in toluene-d_8 (Table 6.13). Changing the solvent significantly influences the immediate electronic environment surrounding of the fluorine nuclei leading to profoundly different chemical shifts. The effect of solvent on the chemical shift is through the paramagnetic shielding term which is strongly affected by external fields. Hence, several factors come into play including solvent polarity, dipole-dipole interaction, steric effects and London dispersion forces.[28] Toluene influences neighboring nuclei through its π-electron density, which can lead to strong shielding or deshielding effect depending on the relative orientation of its π-plane to the solute. $CDCl_3$ has an electric dipole and large electron density from the chlorines leading to strong dipole and London dispersion forces perturbing the electron density surrounding nearby solute nuclei.

Table 6.13. ^{19}F NMR Chemical Shifts (ppm) of PFOA

^{19}F Nuclei	Toluene-d_8	$CDCl_3$	D_2O	CD_3OD
Carbon ID	δ (ppm)	δ (ppm)	δ (ppm)	δ (ppm)
PFOA			literature value[22]	literature value[24]
$C_\omega F_3$	–86.1	–80.8	–80.9	–80.8
$C_\alpha F_2$	–123.8	–118.8	–117.9	–118.6
$C_{\gamma,\delta} F_2$	–126.9	–121.7	–121.9	–121.4
$C_{\lambda,\beta} F_2$	–127.8	–122.1	–122.2	–122.4
$C_\varepsilon F_2$	–131.3	–126.1	–126.2	–125.7

The experimental shifts are compared to those in D_2O and CD_3OD in Table 6.13. Note that D_2O, CD_3OD and $CDCl_3$ have similar chemical shifts, but those in toluene are quite distinct. This suggest that toluene-d_8 interacts more strongly with PFOA than $CDCl_3$. As toluene is an effective solvent for asphaltenes, correspondingly the probe is expected to be compatible to the asphaltene particle surface.

When the ratio of UG8 to PFOA increases, the incremental changes in chemical shift are subtle for all groups and solvents. Tables 6.14 and 6.15 shows the ^{19}F NMR chemical shifts of perfluorooctanoic acid (PFOA) and asphaltene (UG8) at various ratios. Not all the chemical shift trends are the same for each signal. In both solvents, the main chain CF_2 groups increase monotonically. The increases in toluene are larger than in chloroform which is consistent with stronger binding. In both solvents the chemical shifts of the end chain $C_\omega F_3$ increase more slowly and then decreases suddenly when UG8 concentration reaches and exceeds 5 mg/mL. This is also seen for $C_\varepsilon F_2$ and $C_\alpha F_2$ groups but not to the same extent $C_\omega F_3$. This behaviour is consistent with the chain ends being less exposed to the asphaltene interior staying closer to the surface allowing them to be more mobile as the T_1/T_2 ratios suggest. Thus, it seems that binding occurs primarily via interaction between the main chain and UG8.

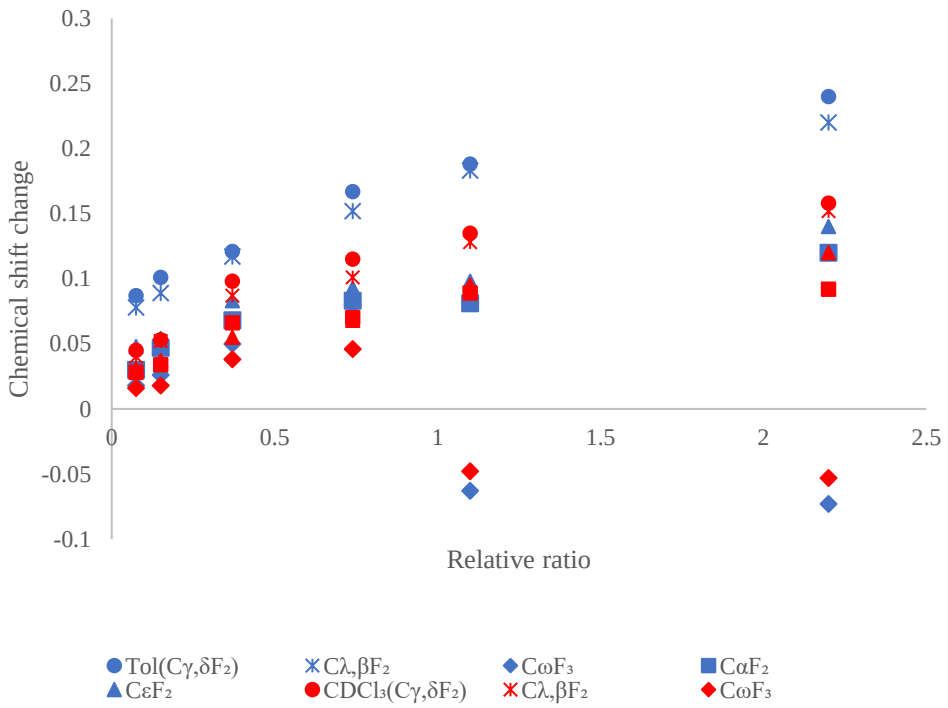

Figure 6.6. Changes in the chemical shift of PFOA with UG8 concentrations in $CDCl_3$ and toluene-d_8

Table 6.14. The ^{19}F chemical shifts (ppm) of PFOA and changes in the presence of UG8 ($\Delta\delta$) for various UG8/PFOA ratios in toluene-d_8

^{19}F Nuclei	δ_{free} (ppm)	$\Delta\delta$ (ppm)					
Carbon ID	PFOA	1:13.3 UG8/PFOA	1:6.66 UG8 /PFOA	1:2.66 UG8/PFOA	1:1.33 UG8 /PFOA	1:0.90 UG8/PFOA	1:0.45 UG8/PFOA
UG8 Conc. (mg/ml)		1	1	5	5	15	15
$C_\omega F_3$	–86.1	0.018	0.026	0.05	0.08	–0.063	–0.073
$C_\alpha F_2$	–123.8	0.03	0.047	0.068	0.083	0.081	0.12
$C_{\gamma,d}F_2$	–126.9	0.087	0.101	0.121	0.167	0.188	0.24
$C_{l,\beta}F_2$	–127.8	0.078	0.089	0.117	0.152	0.183	0.22
$C_\varepsilon F_2$	–131.3	0.048	0.054	0.083	0.093	0.098	0.14

Table 6.15. The ^{19}F chemical shifts (ppm) of PFOA and changes in the presence of UG8 ($\Delta\delta$) for various UG8/PFOA ratios in $CDCl_3$

^{19}F Nuclei	δ_{free} (ppm)	$\Delta\delta$ (ppm)					
Carbon ID	PFOA	1:13.3 UG8 /PFOA	1:6.66 UG8 /PFOA	1:2.66 UG8/PFOA	1:1.33 UG8/PFOA	1:0.9 UG8/PFOA	1:0.45 UG8/PFOA
UG8 Conc. (mg/ml)		1	1	5	5	15	15
$C_\omega F_3$	–80.8	0.016	0.018	0.038	0.046	–0.048	–0.053
$C_\alpha F_2$	–118.9	0.028	0.034	0.066	0.07	0.089	0.092
$C_{\gamma,\delta}F_2$	–121.7	0.045	0.053	0.098	0.115	0.135	0.158
$C_{\lambda,\beta}F_2$	–122.1	0.04	0.052	0.087	0.101	0.128	0.152
$C_\varepsilon F_2$	–126.1	0.031	0.037	0.055	0.068	0.095	0.12

6.4.7. ^{19}F Relaxation experiments of fluorine probes (C_6F_6 and $CFCl_3$) with UG8 at various ratios in $CDCl_3$ and toluene-d_8

For C_6F_6, ^{19}F T_1/T_2 ratios were determined in both solvents. The ratios T_1/T_2 ranged between 1 and 8. Table 6.16 and Figure 6.7 show the T_1/T_2 ratio for the C_6F_6 probe in varying concentrations of UG8 in $CDCl_3$ and toluene-d_8.

Table 6.16. ^{19}F relaxation times for C_6F_6 in different concentrations of UG8 asphaltene in $CDCl_3$ and toluene-d_8.

	$CDCl_3$			Toluene-d_8		
Concentration (mg/mL)	T_1	T_2	T_1/T_2	T_1	T_2	T_1/T_2
0	1.71 ± 0.06	1.20 ± 0.07	1.42 ± 0.07	1.92 ± 0.08	0.82 ± 0.07	2.32 ± 0.1
1	1.2 ± 0.05	0.61 ± 0.05	2.1 ± 0.1	1.51 ± 0.07	0.54 ± 0.05	2.91 ± 0.13
5	0.9 ± 0.04	0.33 ± 0.03	3.3 ± 0.16	0.82 ± 0.05	0.18 ± 0.03	4.55 ± 0.25
15	0.41 ± 0.04	0.09 ± 0.02	5.1 ± 0.26	0.44 ± 0.03	0.054 ± 0.007	8.14 ± 0.4

a) b)

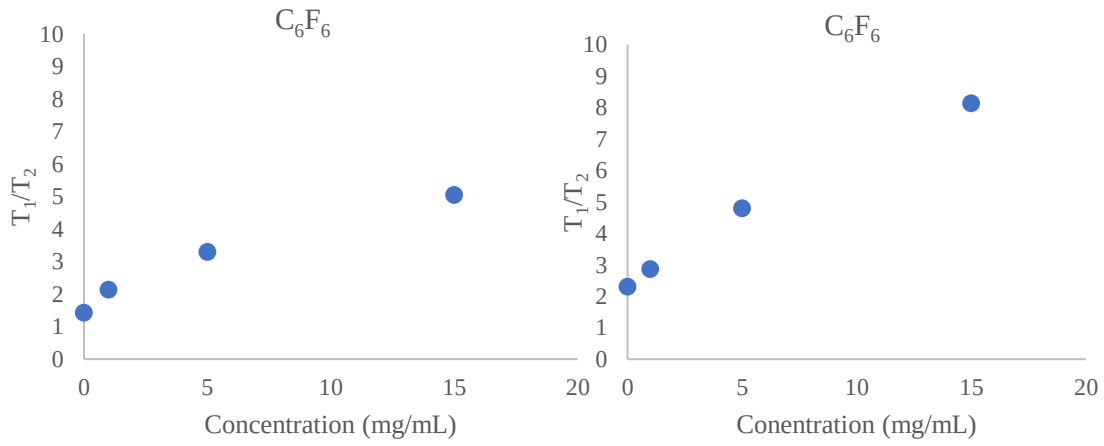

Figure 6.7. Ratio of the ^{19}F relaxation times T_1/T_2 for C_6F_6 in different concentrations of UG8 asphaltene in (a) $CDCl_3$ and (b) toluene-d_8.

The T_1/T_2 ratio of C_6F_6 increases with the concentration of UG8, which is stronger in toluene solvent. However, these trends are significantly smaller than those for PFOA. The T_1 and T_2 values of C_6F_6 are very similar to those of the free molecule, resulting in shorter correlation times. Therefore, C_6F_6 is not an effective probe since it does not interact well with UG8.

Previous studies, however, have demonstrated that C_6F_6 is an excellent probe.[13] A dramatic change in the T_1/T_2 ratio was observed when the asphaltene concentration was varied in the model oils. Fluorine relaxometry was used at a magnetic field strength of 7.05 T in a model oil with a 13% asphaltene content, and the T_1/T_2 ratio was on the order of 100. Hence, our results seem to be inconsistent with those from the literature. What might happen with the model oil is that it contains a resin component. Resins play a major role in stabilizing asphaltene particles, which are always associated with asphaltene. Therefore, the mobility of resins reflects asphaltene mobility. Most likely, this probe will interact with resin in oil rather than with asphaltene itself. Therefore, C_6F_6 cannot interact with asphaltene directly without resins, as model oil can.

Table 6.17 and Figure 6.8 show the relaxation data when the $CFCl_3$ probe is used, and the T_1/T_2 ratios range between 1 and 2. There is almost no change in the T_1/T_2 ratios of $CFCl_3$ with increasing UG8 concentration in both solvents, as it behaves as small molecules with very short correlation times. As a result, this finding shows that $CFCl_3$ does not function as a probe for the structure of the asphaltene system.

Table 6.17. ^{19}F relaxation times for $CFCl_3$ in different concentrations of UG8 asphaltene in $CDCl_3$ and toluene-d_8.

	$CDCl_3$			Toluene-d_8		
Concentration (mg/mL)	T_1	T_2	T_1/T_2	T_1	T_2	T_1/T_2
0	2.2 ± 0.03	1.08 ± 0.03	1.9 ± 0.07	2.02 ± 0.03	0.83 ± 0.03	2.4 ± 0.09
1	2.2 ± 0.02	1.12 ± 0.03	2 ± 0.05	2.02 ± 0.02	0.85 ± 0.02	2.4 ± 0.08
5	2.05 ± 0.02	1.09 ± 0.04	1.9 ± 0.07	1.98 ± 0.02	0.78 ± 0.03	2.5 ± 0.08
15	2.16 ± 0.02	1.05 ± 0.04	2.1 ± 0.08	1.99 ± 0.03	0.76 ± 0.02	2.6 ± 0.07

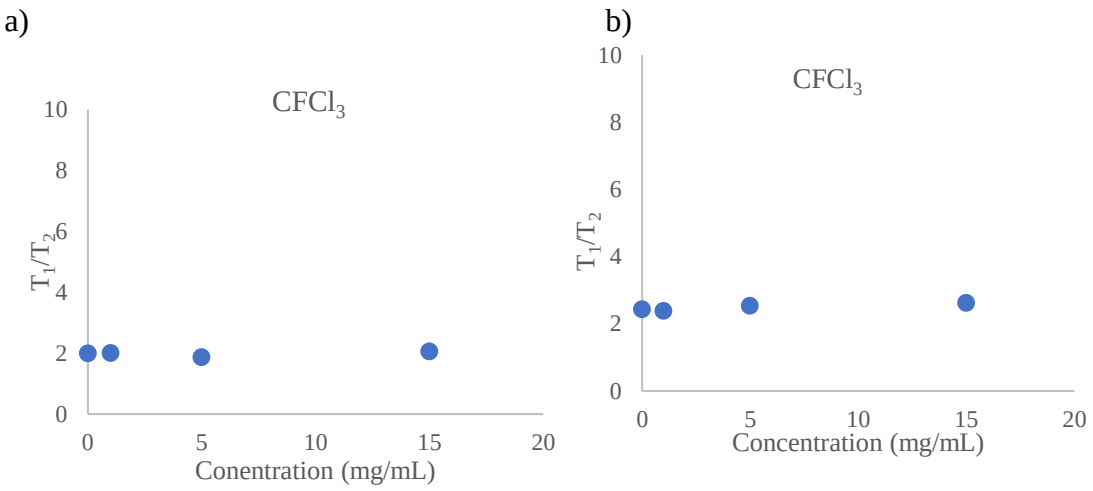

Figure 6.8. Ratio of the ^{19}F relaxation times T_1/T_2 for $CFCl_3$ in different concentrations of UG8 asphaltene in (a)$CDCl_3$ and (b) toluene-d_8.

6.5. Conclusions

The relaxation dynamics of UG8 asphaltene were studied by ^{1}H and ^{19}F NMR spectroscopy. In comparing the relaxation behavior of ^{19}F and ^{1}H NMR resonances it is evident that significant differences in their relaxation behavior exist between different probes and solvents.

For $CFCl_3$, relaxation dispersion is very small in toluene and $CDCl_3$ solvents in the presence of UG8. It behaves as a small molecule with very short correlation times. Therefore, $CFCl_3$ does not function as a probe for the structure of the asphaltene system. The C_6F_6 is expected to have strong interactions with UG8, but the relaxation dispersion was found not to be significant. It is most likely that this probe will interact with asphaltene in crude oil rather than directly with asphaltene in an organic solvent. When PFOA is used, UG8 and PFOA bind more strongly than any the other tested probe. However, the nature of the solvent has a significant impact on the binding. The relative changes in the T_1/T_2 ratios suggest that the PFOA and UG8 have weaker binding in toluene-d_8 than in $CDCl_3$. This is also supported by chemical shift and linewidth analysis. Therefore, PFOA is an effective probe in an asphaltene system.

The study conducted ^{1}H DOSY and ^{1}H relaxation dispersion NMR experiments to gain insights into aggregate sizes in both solvents. While DOSY data may not precisely represent asphaltene composition due to sensitivity and diffusion rate limitations, T_1/T_2 ratios accurately reflect the composition between a mobile and a rigid environment.

The relaxation studies of the ^{1}H signals of UG8 and of ^{19}F resonances of PFOA in the presence of UG8 support a core/shell model of nanoaggregates of the UG8 asphaltene. The two components of the biexponential behaviour of ^{1}H relaxation can be assigned to a

denser, more rigid core and a less dense, more mobile shell of aggregates. The relaxation behaviour of the PFOA probe mirrors that of the ^{1}H UG8 signals of the minor more mobile component, suggesting that PFOA can only bind to the less dense shell, and does not penetrate into the dense core.

REFERENCES:

1. Gerig, J., Fluorine NMR of proteins. Progress in Nuclear Magnetic Resonance Spectroscopy 1994, 26, 293-370.

2. Dolbier Jr, W. R., Guide to fluorine NMR for organic chemists. John Wiley & Sons: 2016.

3. Danielson, M. A.; Falke, J. J., Use of 19F NMR to probe protein structure and conformational changes. Annual review of biophysics and biomolecular structure 1996, 25 (1), 163-195.

4. Marsh, E. N. G.; Suzuki, Y., Using 19F NMR to probe biological interactions of proteins and peptides. ACS chemical biology 2014, 9 (6), 1242-1250.

5. Kitevski-LeBlanc, J. L.; Prosser, R. S., Current applications of 19F NMR to studies of protein structure and dynamics. Progress in Nuclear Magnetic Resonance Spectroscopy 2012, 62, 1-33.

6. Kawahara, K.; Nemoto, N.; Motooka, D.; Nishi, Y.; Doi, M.; Uchiyama, S.; Nakazawa, T.; Nishiuchi, Y.; Yoshida, T.; Ohkubo, T.; Kobayashi, Y., Polymorphism of Collagen Triple Helix Revealed by 19F NMR of Model Peptide [Pro-4(R)-Hydroxyprolyl-Gly]3-[Pro-4(R)-Fluoroprolyl-Gly]-[Pro-4(R)-Hydroxyprolyl-Gly]3. The Journal of Physical Chemistry B 2012, 116 (23), 6908-6915.

7. Liu, J. J.; Horst, R.; Katritch, V.; Stevens, R. C.; Wüthrich, K., Biased signaling pathways in β2-adrenergic receptor characterized by 19F-NMR. Science 2012, 335 (6072), 1106-1110.

8. Rydzik, A. M.; Brem, J.; van Berkel, S. S.; Pfeffer, I.; Makena, A.; Claridge, T. D.; Schofield, C. J., Monitoring Conformational Changes in the NDM-1 Metallo-β-lactamase by 19F NMR Spectroscopy. Angewandte Chemie 2014, 126 (12), 3193-3197.

9. Hoang, J.; Prosser, R. S., Conformational Selection and Functional Dynamics of Calmodulin: A 19F Nuclear Magnetic Resonance Study. Biochemistry 2014, 53 (36), 5727-5736.

10. Shi, P.; Wang, H.; Xi, Z.; Shi, C.; Xiong, Y.; Tian, C., Site-specific ^{19}F NMR chemical shift and side chain relaxation analysis of a membrane protein labeled with an unnatural amino acid. Protein Sci 2011, 20 (1), 224-228.

11. Lu, M.; Ishima, R.; Polenova, T.; Gronenborn, A. M., 19F NMR relaxation studies of fluorosubstituted tryptophans. Journal of Biomolecular NMR 2019, 73 (8), 401-409.

12. Desando, M. A.; Lahajnar, G.; Ripmeester, J. A.; Zupancic, I., The low temperature oxidation of Athabasca oil sand asphaltene observed from 13C, 19F, and pulsed field gradient spin-echo proton NMR spectra. Fuel 1998, 78 (1), 31-45.

13. Stapf, S.; Ordikhani-Seyedlar, A.; Mattea, C.; Kausik, R.; Freed, D. E.; Song, Y.-Q.; Hürlimann, M. D., Fluorine tracers for the identification of molecular interaction with porous asphaltene aggregates in crude oil. Microporous and Mesoporous Materials 2015, 205, 56-60.

14. Hortal, A. R.; Hurtado, P.; Martínez-Haya, B.; Mullins, O. C., Molecular-Weight Distributions of Coal and Petroleum Asphaltenes from Laser Desorption/Ionization Experiments. Energy & Fuels 2007, 21 (5), 2863-2868.

15. Andrews, A. B.; Edwards, J. C.; Pomerantz, A. E.; Mullins, O. C.; Nordlund, D.; Norinaga, K., Comparison of Coal-Derived and Petroleum Asphaltenes by 13C Nuclear Magnetic Resonance, DEPT, and XRS. Energy Fuels 2011, 25 (7), 3068-3076.

16. Simmonds, D.; Banks, L.; Steiner, R.; Young, I., NMR anatomy of the brain using inversion-recovery sequences. Neuroradiology 1983, 25 (3), 113-118.

17. Meiboom, S.; Gill, D., Modified spin-echo method for measuring nuclear relaxation times. Review of scientific instruments 1958, 29 (8), 688-691.

18. Ferguson, R. C.; Marquardt, D. W., Computer analysis of NMR spectra: magnetic equivalence factoring. The Journal of Chemical Physics 1964, 41 (7), 2087-2095.

19. Chinelatto Júnior, L. S.; Cabral de Menezes, S. M.; Honorato, H. d. A.; Oliveira, M. C. K. d.; Marques, L. C. d. C., Dosy-Nmr as an Alternative Technique to Improve Asphaltenes Characterization. Energy & Fuels 2018.

20. Zeng, H.; Song, Y.-Q.; Johnson, D. L.; Mullins, O. C., Critical Nanoaggregate Concentration of Asphaltenes by Direct-Current (DC) Electrical Conductivity. Energy & fuels 2009, 23 (3), 1201-1208.

21. Freed, D. E.; Lisitza, N. V.; Sen, P. N.; Song, Y.-Q., Molecular Composition and Dynamics of Oils from Diffusion Measurements. Springer New York: New York, NY, pp 279-299.

22. da Silva Oliveira, E. C.; Neto, Á. C.; Júnior, V. L.; de Castro, E. V. R.; de Menezes, S. M. C., Study of Brazilian asphaltene aggregation by Nuclear Magnetic Resonance spectroscopy. Fuel 2014, 117, 146-151.

23. Ribeiro, A. A., 19F, 13C single-and two-bond 2D NMR correlations in perfluoroheptanoic acid. Journal of fluorine chemistry 1997, 83 (1), 61-66.

24. Reo, N. V. Hepatic Metabolism of Perfluorinated Carboxylic Acids: A Nuclear Magnetic Resonance Investigation; WRIGHT STATE UNIV DAYTON OH: 1990.

25. Nanny, M. A.; Maza, J. P., Noncovalent interactions between monoaromatic compounds and dissolved humic acids: A deuterium NMR T1 relaxation study. Environmental science & technology 2001, 35 (2), 379-384.

26. Kovacs, H.; Kowalewski, J.; Maliniak, A.; Stilbs, P., Multinuclear relaxation and NMR self-diffusion study of the molecular dynamics in acetonitrile-chloroform liquid mixtures. The Journal of Physical Chemistry 1989, 93 (2), 962-969.

27. Budd, N.; Joshi, N.; Russell, C.; Paille, A.; Li, Q. In The Remediation of Oilfield Asphaltenic Deposits: Near-Well-Bore Application, SPE International Conference and Exhibition on Formation Damage Control, OnePetro: 2018.

28. Evdokimov, I. N.; Eliseev, N. Y.; Akhmetov, B. R., Asphaltene dispersions in dilute oil solutions. Fuel 2006, 85 (10-11), 1465-1472.

29. Shortridge, M. D.; Hage, D. S.; Harbison, G. S.; Powers, R., Estimating Protein−Ligand Binding Affinity Using High-Throughput Screening by NMR. Journal of combinatorial chemistry 2008, 10 (6), 948-958.

CHAPTER 7

CONCLUSIONS AND FUTURE WORK

7.1. Conclusions

This thesis research utilized solution-state NMR spectroscopic techniques to study the molecular structure and aggregation behavior of several different asphaltenes. The different asphaltenes ranged from various sources, *i.e.*, Manifa samples obtained from different well depths in the Manifa oil field in Saudi Arabia, AMSO samples having different maturity levels originating from American shale oil, Columbian PetroPhase 2017 Asphaltene samples subjected to ultrasonication treatment, and UG8 samples obtained from a Kuwaiti black oil deposit.

A detailed and thorough quantitative ^{1}H NMR protocol was developed to replace time-consuming NMR methods, such as ^{13}C NMR spectroscopy, and to improve the reliability and validity of compositional and dynamic information obtained. The first was achieved via a deconvolution model for the ^{1}H NMR spectra to quantify the relative abundance of aromatic, alicyclic, aliphatic, and, in some cases, alkenyl components, effectively addressing the distortions due to signal overlap. Another important finding is the need for extended recycle delays of 120 s to reduce saturation effects. A recycle day of 5 s, which has been widely reported in the literature, was shown to provide erroneous information. The ^{1}H T_1-T_2 relaxation dispersion method was utilized to examined how asphaltene aggregation behavior is affected by changing solvents, concentration, and sample sources. The corresponding T_1/T_2 ratios of the aromatic signals allowed for estimates of correlation times (τ_c) associated with their reorientational dynamics of the asphaltene aggregates,

which in turn gave their hydrodynamic radii (r_H). All relaxation dispersion analyses required the contribution from two components, one that is highly mobile with smaller ratios and one that is rigid with larger ratios. The relative contributions of these two components vary depending on the nature of the asphaltenes source. Variations in solvent polarity give insight into the nature of the interactions leading to aggregation and clustering, but were invariant within each type of asphaltene, regardless of the solvent and/or processing method. These findings were further validated through the corroborative use of DOSY NMR techniques. DOSY NMR experiments provide complementary insights into the aggregate sizes of asphaltenes.

The study focused on a range of asphaltene samples, namely Manifa, AMSO, PetroPhase 2017 Asphaltene, and Petroleum asphaltene (UG8), each exhibiting distinct and varied structural properties and are known to the exhibit diverse aggregation behaviour. A notable observation was the significantly larger T_1/T_2 ratio observed for the Manifa asphaltenes as compared to the other samples. These larger T_1/T_2 ratios correlated with higher molecular weight, indicating slower reorientational dynamics and suggesting the presence of very large aggregates. In contrast, AMSO and other asphaltene samples behaved differently, as characterized by substantially lower T_1/T_2 ratios. The lower T_1/T_2 ratios indicate the presence of smaller asphaltene aggregate arrangements limited to mostly nano-aggregates and their small clusters. Furthermore, the perseverance of bi-exponential relaxation behavior emphasized the predominance of two domains of distinct mobility for each structural environment.

First, the Manifa asphaltenes were studied using solution-state ^{1}H NMR, relaxation dispersion, and DOSY to investigate structural composition and aggregation behavior. The

^{1}H NMR experiments involved extended recycle delays (120 s) to prevent signal saturation and were analyzed using the generalized deconvolution model. The results showed minor structural changes with increasing depth, characterized by a slight increase in the aromatic core signal and a minor decrease in the aliphatic signal. Relaxation Dispersion experiments revealed two components with significant differences in mobility among aliphatic, alicyclic, and aromatic regions. This hierarchy in mobility aligns with the steric congestion expected during aggregate formation via staggered π-π stacking. T_1/T_2 ratios increased with depth, with higher values in toluene compared to chloroform.

DOSY experiments provided insights into aggregate sizes, revealing three states: sub nanoaggregates (0.3-0.8 nm), nanoaggregates (0.5-2.1 nm), and microaggregates (0.8-8.2 nm). Large clusters were observed only in toluene, with a consistent trend of increasing particle sizes with well depth. It is worth noting that the DOSY technique has limitations when dealing with aggregates larger than 4 nm as a consequence of instrumental limitations on the pulsed field gradient strength; therefore, no quantification of the relative abundances of the different aggregates can be obtained by for the larger particles using DOSY.

The subsequent investigation focused on American shale oil (AMSO) as another source of asphaltenes extracted from pyrolyzed material to study the relationship between asphaltene maturity and aggregation behavior. This study also used deconvolution analysis to resolve ^{1}H NMR spectra and analyze changes in asphaltene composition during pyrolysis at different maturity levels. The results revealed systematic variations in asphaltene composition with increasing maturity during pyrolysis. Initial increases in aliphatic, alicyclic, and aromatic components at the expense of alkenyl constituent highlight the complexity of these transformations. The study underscores that asphaltene particles

exhibit significant variations in size with increasing maturity, as evidenced by T_1/T_2 ratios across different structural environments. The bi-exponential behavior observed in these ratios suggests the presence of two distinct phases within asphaltene particles, that attain a variety of aggregated states. Importantly, this research validates the notion that asphaltene particle size increases with maturity up to EASY%Ro 0.95%, aligning with prior studies that observed an increase in molecular weight across this maturity range. The confirmation of increased asphaltene aggregate size with maturity, coupled with the discrepancy between toluene-d_8 and $CDCl_3$, underlines the crucial role of solvent on influencing asphaltene aggregation.

As part of a group of laboratories around the world studying one asphaltene that was obtained from an inter-laboratory study originating in Columbia, the PetroPhase 2017 Asphaltene in the crude and sonicated form was subjected to comprehensive analyses through ^1H, relaxation, and DOSY NMR spectroscopy. The concentration of the solutions used in this study significantly exceeded the critical cluster concentration, suggesting that the PetroPhase 2017 Asphaltenes are primarily in their clustered states. While ^1H NMR results suggest no molecular structural changes during sonication, the study reveals a reduction in asphaltene aggregate sizes due to ultrasonication. Utilizing relaxation NMR spectroscopic techniques, it was found that PetroPhase 2017 Asphaltenes formed the smallest cores compared to other asphaltene types in this research. This is very interesting in light of these samples having been determined to have a high archipelago fraction and exhibiting the smallest major-minor ratio in the relaxation dispersion results. Notably, the T_1/T_2 ratios (980) of the rigid component observed in the aromatic region indicate slower reorientational dynamics, resulting in a hydrodynamic radius of approximately 2.4 nm.

Interestingly, under sonication, the T_1/T_2 ratio for the major component in the aromatic region significantly decreased to 553, corresponding to smaller hydrodynamic radii of around 2.1 nm. This indicates the effective reduction of asphaltene aggregation due to sonication. The relaxation analysis consistently confirmed that asphaltene aggregate size decreased following the sonication process. This observation was further supported by the DOSY NMR results, which consistently demonstrated a decrease in asphaltene aggregate size upon sonication. These findings are in excellent agreement with DC conductivity measurements conducted by a collaborator.

The final chapter provided insight into the feasibility of ^{19}F NMR spectroscopy being a facile replacement for ^{1}H methods. Despite the latter being less demanding of instrument time, they remain time consuming in data analysis. The ^{19}F nucleus as an NMR probe presents the advantage of not having a natural background NMR signal in asphaltenes and was therefore studied with convenience. This study aimed to examine whether fluorinated molecular probes were able to provide reliable comparable structural and aggregation information on asphaltenes compared ^{1}H NMR methods. Initially, the UG8 asphaltenes were studied by ^{1}H relaxation methods and DOSY at concentrations from nearby CNAC to the CCC and to well above the CCC. Upon increasing concentration, the UG8 asphaltenes form nanoaggregates, which eventually coalesce to form microaggregates. Fluorine-19 NMR spectroscopy and ^{19}F T_1 and T_2 relaxation experiments were used to measure relaxation dispersion in the fluorinated probe in the presence of UG8. The T_1/T_2 ratios increase with increasing UG8 concentration reflecting the changes in UG8 aggregation states. One remarkable finding was the consistent presence of mono-exponential relaxation

at all concentrations, and the relaxation dispersion values corresponding only the minor component of the ^{1}H UG8 ratios.

Testing of other probes such as C_6F_6 and $CFCl_3$ yielded no significant T_1/T_2 ratio changes upon the introduction of UG8. Thus, C_6F_6 and $CFCl_3$ would not function well as probes for observing aggregation for asphaltenes. This is at odds with previous studies using C_6F_6 which observed large dispersion values on model oils. This discrepancy was attributed to the probe not interacting directly with the asphaltene but rather through another component closely associate with the asphaltene component in crude oil.

When the PFOA was added to asphaltene solutions, interactions were observed, as shown by the high ^{19}F T_1/T_2 ratio. The relative changes in the T_1/T_2 ratios with increasing PFOA concentration suggest that PFOA binds more strongly to UG8 in toluene-d_8 than in $CDCl_3$. This was also supported by observation of the ^{19}F NMR chemical shifts of PFOA in the two solvents with changing UG8: PFOA ratio. Thus, it was concluded that PFOA is an effective probe for asphaltene aggregation and that it binds to the aggregate surface. The latter finding suggests that the minor component in the ^{1}H relaxation dispersion corresponds to the surface and the major to interior of the aggregate particles.

Asphaltenes source and extraction method significantly influence its structure, aggregation, and hydrodynamic radius. This thesis used solution-state NMR spectroscopy to study different sources of asphaltene aggregation on a molecular level in terms of structure, connectivity, and dynamics. The NMR spectroscopic evidence was presented for a particular feature: extremely long recycle delays were needed for all the ^{1}H NMR experiments to prevent signal saturation. One of the primary objectives of the thesis was to demonstrate that relaxation techniques were able to shed light on the nature of aggregation

and dynamics. Relaxation analysis confirmed the complex nature of the asphaltene phase composition. Two potential explanations exist for the presence of two components with different T_1/T_2 ratios in asphaltene samples. The first explanation suggests a core-shell structure in which the more mobile component forms the outer, less dense 'shell,' and the less mobile component constitutes the denser core of asphaltene nanoparticles. Furthermore in both mobility regimes the relaxation dispersion values increased dramatically from the aliphatic, to the alicylic, and ultimately to the aromatic environments. This lends strong support to the notion of structural hierarchy, as invoked by the "island" model, indicating that two distinct sets of T_1/T_2 ratios for each environment exists, possibly corresponding to two asphaltene unit sizes: nanoaggregates and clusters. DOSY NMR experiments provide complementary insights into the aggregate sizes in both solvents. Because of the invariance of the relative components within each type of asphaltene, the core-shell model seems to be the most plausible explanation. Changes in aggregate size that were observed by significantly different T_1/T_2 ratios between solvents should have resulted in significant changes in relative contributions of a more mobile nanoaggregate versus less mobile cluster. Since this is not observed for any of the four sample types, it is surmised that two components in the relaxation dispersion measurements are correlated to the dense core of a nanoaggregate and its less dense, more mobile shell. These nanoaggregates are sufficiently stable to be detected on the NMR time scale. Larger aggregates, such as clusters that are formed by these nanoaggregates will manifest in longer T_1/T_2 ratios. Core-shell models have been proposed based on SAXS, WAXS and SANS measurements,[1,2] but they have not clearly been attributed to nanoaggregate structures. Core-shell structures of nanoaggregates could also account for inclusion of archipelago-type asphaltene components, as they could potentially interact peripherally to the aromatic cores of

nanoaggregates, through T-shaped interactions. Such archipelago-type components will then be part of the less dense shell.

The study of the interaction between asphaltene and fluorinated molecular probes was done with ^{19}F NMR spectroscopy, showing that PFOA is an effective probe because it interacts effectively with UG8 asphaltene. However, it is important to acknowledge that the ^{19}F NMR studies performed in this thesis are preliminary, and further investigations are required to fully exploit the information obtained.

Moving forward, several potential avenues for future research exist in this field. These include:

1) Exploring the interaction of other fluorinated probes with different asphaltene samples: Further investigation using a range of fluorinated probes and various asphaltene sources would provide a broader understanding of their applicability in characterizing asphaltene structure and aggregation behavior. This would help identify probes that exhibit strong and specific interactions with asphaltene, enhancing our ability to study their properties.
2) Investigating the influence of solvents on ^{19}F NMR behavior: Examining how different solvents affect the ^{19}F NMR spectra and relaxation properties of asphaltenes would provide insights into solvent-dependent effects on asphaltene-probe interactions. This investigation can help optimize solvent selection for future studies and provide a deeper understanding of the solvents impact on asphaltene behavior.

7.2. Future Directions

The current asphaltene studies have led to more questions than answers. In this thesis, several interesting observations pertaining to asphaltene aggregation have been made, for example, the existence of at least two components in the NMR relaxation dispersion measurements with different motional regimes. While the percentages of these components may vary between different types of asphaltenes, they remain consistent within asphaltene samples of one origin.

The hypothesis coming out of the thesis research is that the two components correspond to different environments, *i.e.*, core and shell, in a nanoaggregate of stacked asphaltenes, where parallel layers of asphaltenes are stacked on top of each other, with some weak interactions occurring perpendicular to the stacks, involving island or archipelago-like structures (Figures 7.1 and 7.2).

This new interpretation introduces complexities in understanding the relationship between the components and asphaltene aggregation behavior. To further explore this concept and validate the proposed explanation, further studies are proposed, involving thorough investigations using ^{1}H T_1/T_2, ^{1}H DOSY, and ^{19}F DOSY NMR spectroscopy, while varying asphaltene concentrations and employing different solvents.

Measuring diffusion constants by DOSY presents challenges owing to limitations imposed by the spectrometer's hardware specifications. These limitations made it difficult to achieve uniform dephasing conditions for all signals of interest. For future research in this field, it is imperative to explore improved techniques and methodologies to overcome these limitations.

a. **b.**

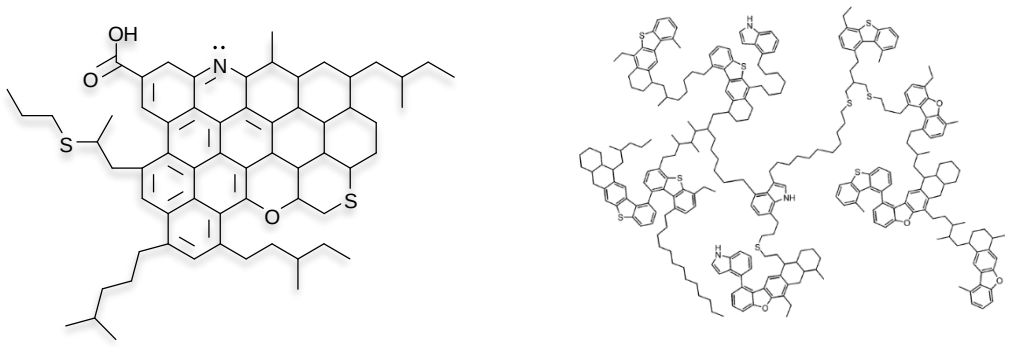

Figure 7.1. Archetypical structures of the asphaltene molecular unit for a) the island and b) the archipelago models.

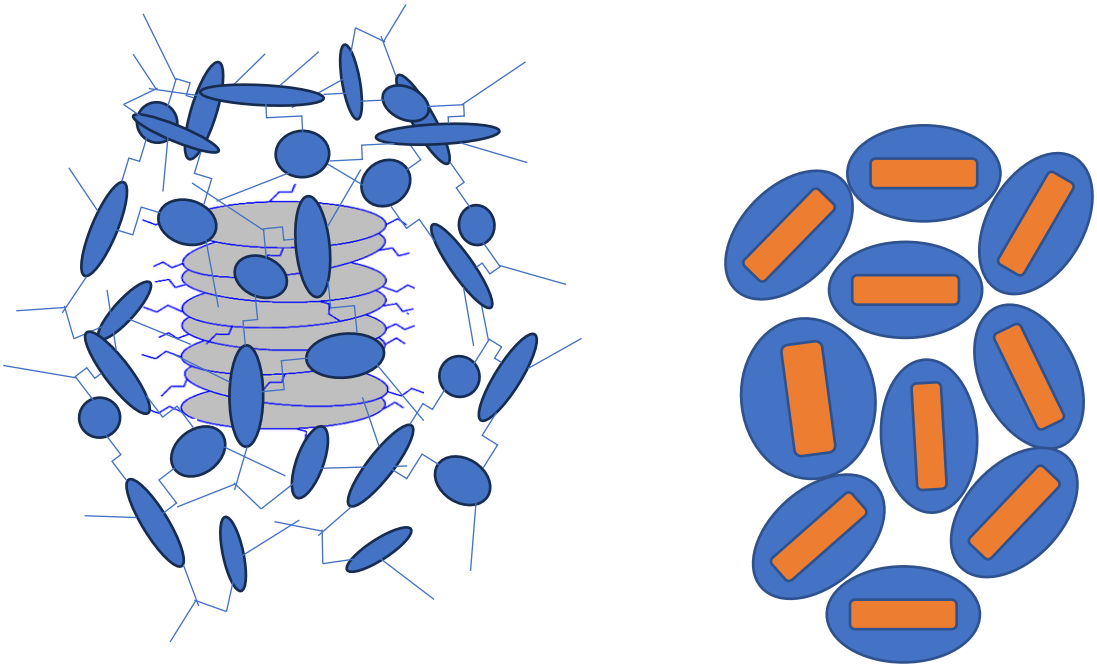

Figure 7.2. Left: Schematic describing the proposed core shell model for the nanoaggregate with island molecules densely stacked in the interior and archipelago molecules on the surface. Right: Schematic describing the proposed model for a cluster of core-shell nanoaggregates.

Several possible directions for future studies are proposed.

1) Concentration variations for T_1 and T_2 measurements: It will be informative to investigate T_1 and T_2 relaxation times at lower concentrations, particularly around and below the CNAC. This is crucial to test the validity of the core-shell model for nanoaggregates. If the model holds true, the biexponential behavior observed at higher concentrations will change in terms of relative percentage of the minor and major components and at sufficiently low concentrations changing to essentially monoexponential relaxation behaviour.

2) Aligning ^{1}H T_1/T_2 experiments with ^{1}H DOSY experiments: This approach requires conducting both experiments meticulously for a range of identical samples, solvents, and concentrations under the same conditions. Comparing the results can directly connect the size-related data from DOSY with the dynamics-related information from ^{1}H T_1/T_2 experiments. This alignment will deepen the understanding of asphaltene behavior and provide a robust validation method. It will confirm that the particle sizes determined by DOSY match the relaxation times measured in ^{1}H T_1/T_2 experiments, thereby strengthening the reliability of both measurements and their conclusions.

3) Model compounds: Model compounds can be used as valuable tools for mimicking specific aspects of asphaltene behavior, such as aromaticity or the presence of polar functional groups. To advance this study area, it is important to find model compounds with chemical structures and properties like asphaltenes. However, it is important to note that their ability to fully replicate the entire range of asphaltene aggregation behavior is

limited due to their smaller degree of aggregation. The relaxation dispersion method can be employed to address this limitation and gain insights into the smaller degree of aggregation exhibited by model compounds. Alternatively, one could study the incorporation of these model compounds into asphaltenes aggregates. In this manner, various model compounds differing in sidechain length, core size, and polarity, can offer valuable insights into the impact of these factors on nanoaggregate formation.

4) Variable-temperature studies: This thesis did not study the effect of temperature on asphaltene aggregation behavior. In future studies, temperature would be an important parameter to be considered. Previous studies examined the effect of temperature on asphaltene solubility and precipitation.[3] According to the results, asphaltene solubility increases, and precipitation decreases with increasing temperature. Higher temperatures disturb the stability of large aggregates and reduce the subsequent aggregation and particle growth of asphaltene, resulting in less precipitation. To further understand the influence of temperature on asphaltene aggregation behavior, relaxation experiments should be conducted at different temperatures and concentrations. By studying the relaxation behavior at varying temperatures, it is possible to investigate how changes in temperature affect the aggregation behavior of asphaltene. If the invariance in minor/major component ratios is maintained, especially at high concentrations, it could provide strong support for the core-shell model.

5) Broadened range of diffusion constants: One of the limitations of DOSY NMR is its restricted range of measurable diffusion constants. This limitation is typically due to hardware constraints, such as the strength and duration of gradient pulses and the available observation time. Advanced spectrometer and probe design can offer stronger gradient

pulses, longer observation times, and improved gradient strength control. This expanded range enables the measurement of diffusion constants spanning several orders of magnitude accurately.

6) Fluorine-19 diffusion measurements: Subsequent studies on the interaction between fluorinated probes and asphaltene including, ^{19}F diffusion measurements are important. Fluorine-19 DOSY NMR spectroscopy is a useful technique as it can measure both weak and strong interactions between a probe and asphaltene. The experiment can be used to confirm binding if a significant change in probe diffusion coefficient is observed after asphaltene is added to the solution. In addition, strong binding can be determined by the ^{19}F and ^{1}H DOSY having similar translational diffusion coefficients. That method would be an effective way to determine whether the probe will be useful or not.

7) Multidimensional NMR spectroscopy: Two-dimensional (2D) NMR spectroscopy can be used in asphaltene characterization to verify ^{1}H relaxation dispersion results with 2D cross relaxation measurements. The NOESY and ROESY experiments are homonuclear two-dimensional correlation techniques and is used to determine the cross relaxation between two protons which are close together in space. The comparison between cross-relaxation rates from both methods is ideal for distinguishing between signals from nanoaggregates and clusters. Hence, multidimensional NMR techniques such as NOESY and ROESY could be used to analyze the aggregation behavior of asphaltenes, and these experiments would be the next step in the project.

8) $T_{1\rho}$ measurements in solution: Extend the research to include $T_{1\rho}$ measurements in solution. The $T_{1\rho}$ relaxation time has the advantage of being able to control the sensitivity to slow motion via the spin-locking power. Overdetermining relaxation parameters can

enhance the precision and reliability of the correlation times. By using multiple methods, such as T_1, T_2, and $T_{1\rho}$, you can gain a more comprehensive understanding of asphaltene behavior and nanoaggregate structures in various conditions.

REFERENCES

1. Eyssautier, J.; Levitz, P.; Espinat, D.; Jestin, J.; Gummel, J.; Grillo, I.; Barré, L., Insight into asphaltene nanoaggregate structure inferred by small angle neutron and X-ray scattering. The Journal of Physical Chemistry B 2011, 115 (21), 6827-6837.

2. Eyssautier, J. l.; Espinat, D.; Gummel, J. r. m.; Levitz, P.; Becerra, M.; Shaw, J.; Barré, L. c., Mesoscale organization in a physically separated vacuum residue: Comparison to asphaltenes in a simple solvent. Energy & fuels 2012, 26 (5), 2680-2687.

3. Maqbool, T.; Srikiratiwong, P.; Fogler, H. S., Effect of Temperature on the Precipitation Kinetics of Asphaltenes. Energy & Fuels 2011, 25 (2), 694-700.

APPENDIX 1

Bi-exponential fitting for the T_1 and T_2 data in Chapter 3. The raw data obtained from the relaxation experiment was normalized and plotted against time. Tables showing the ^1H T_1 and T_2 values measured for Manifa asphaltenes, along with the corresponding percentages of long and short T_1 and T_2 and provides the standard deviation of each data point in the fit.

8070.9 ft -Toluene-d_8

T_1 -Aliphatic

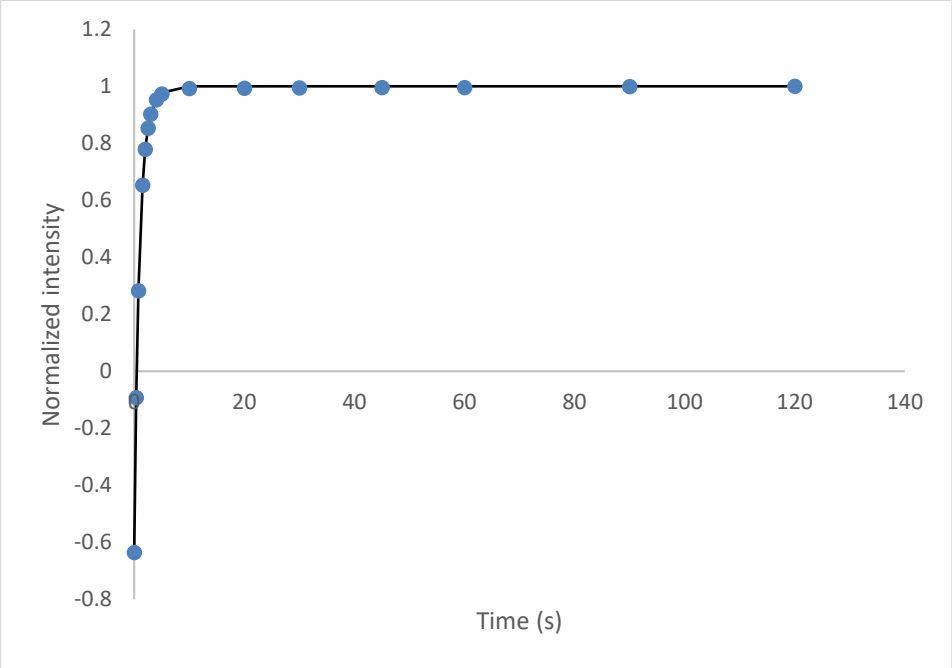

Alicyclic

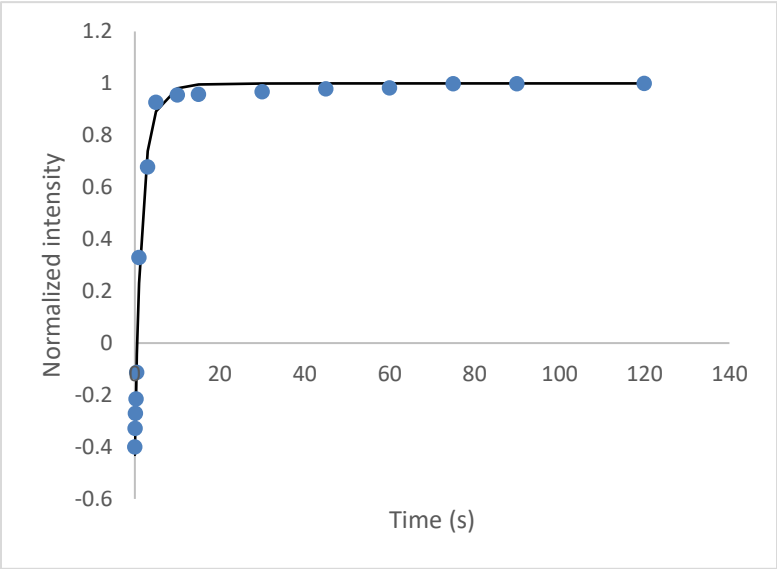

Aromatic

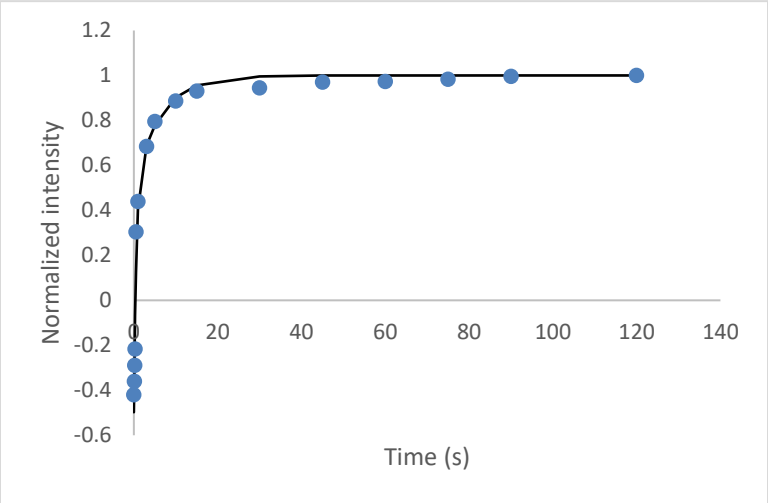

T_2- Aliphatic

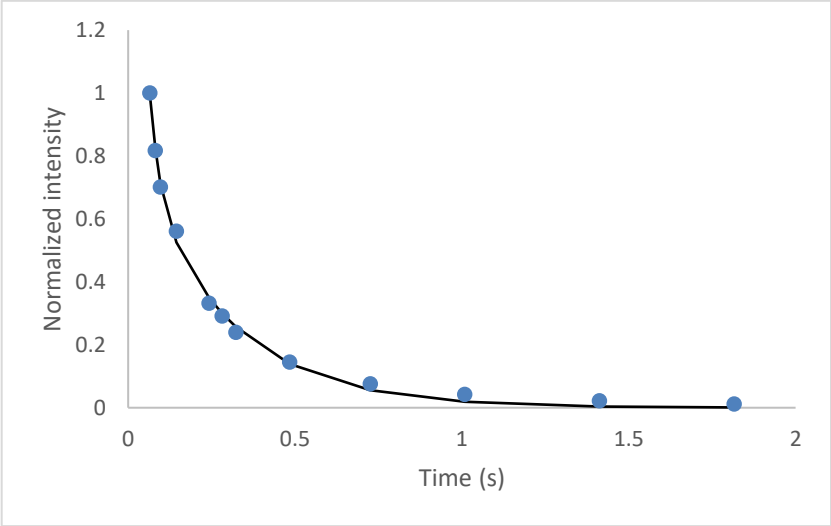

Alicyclic

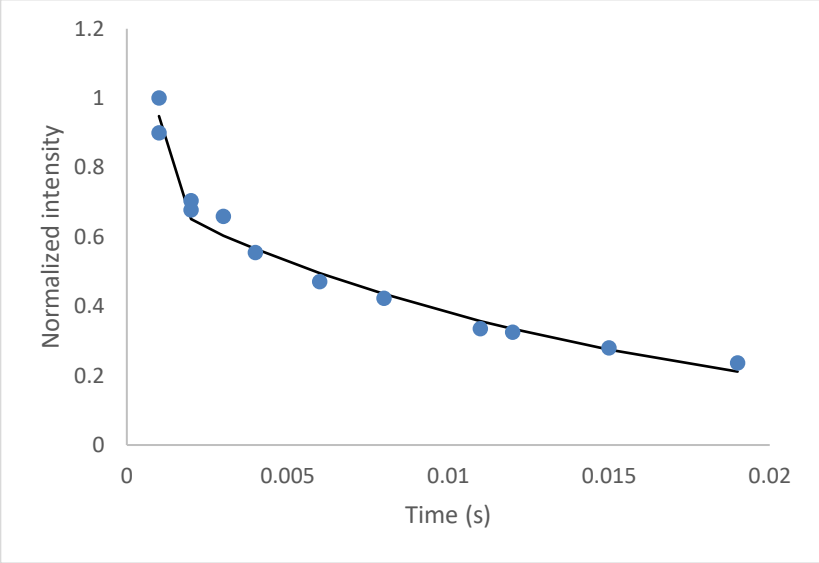

Aromatic

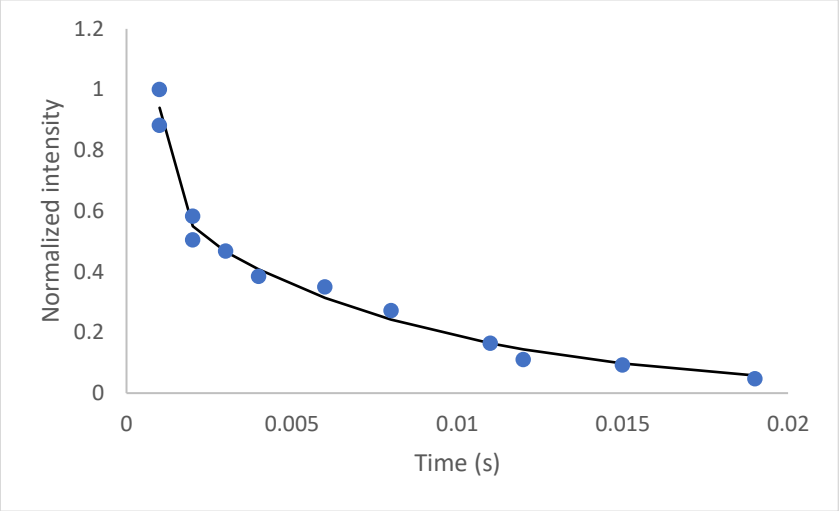

Table A1. ^{1}H NMR Relaxation times of reservoir depth (8070.9 ft) asphaltene in toluene-d_8. The values in parentheses represent the percentage of protons having the corresponding T_2 and T_1.

^{1}H ppm	assignment	T_1 (s)	T_2 (ms)	T_1/T_2
1.5-0.8	aliphatic chain CH_2/ CH_3	0.51±0.02 (65±4.5%)	29.9±0.9 (70±4.0%)	17±1.0
		1.40±0.05 (35±3.5%)	264±1.5 (30±4.5%)	5.2±0.18
3.5-2.4	alicyclic attached to aromatics	3.15±0.05 (65±5.5%)	0.28±0.01 (68±5.0%)	11250±430
		1.30±0.03 (35±4.5%)	15.2±0.6 (32±4.0%)	82±3.7
9.5-7.5	aromatic CH	6.14±0.05(73±5.8%)	0.34±0.01 (75±5.5%)	18050±720
		1.30±0.04 (27±4.4%)	15.1±0.5 (25±4.0%)	85±3.8

8026.3 ft-Aliphatic T_1

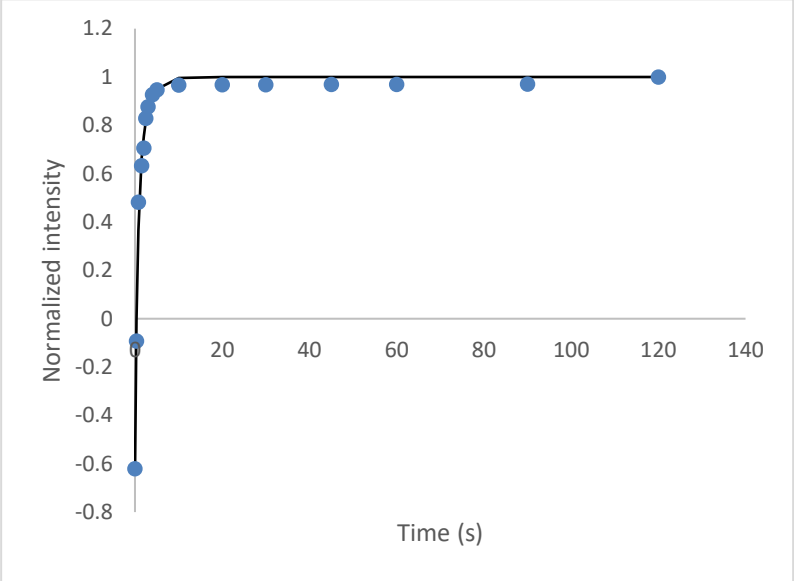

Aromatic

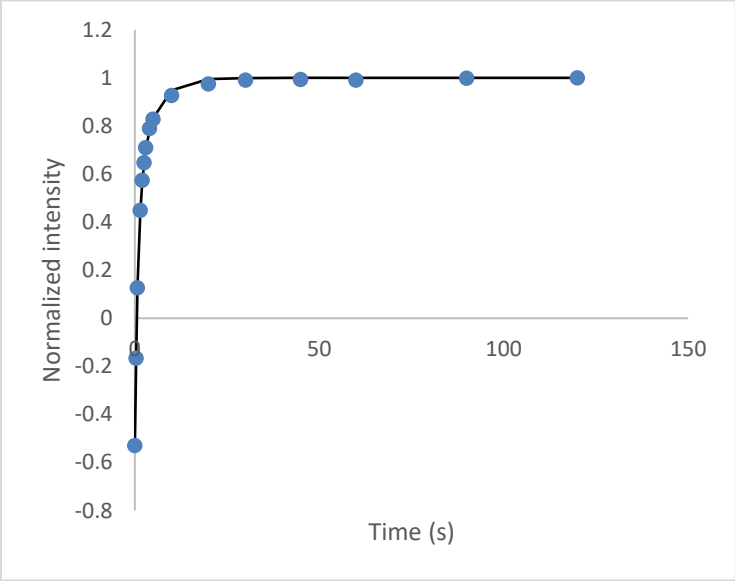

Alicyclic

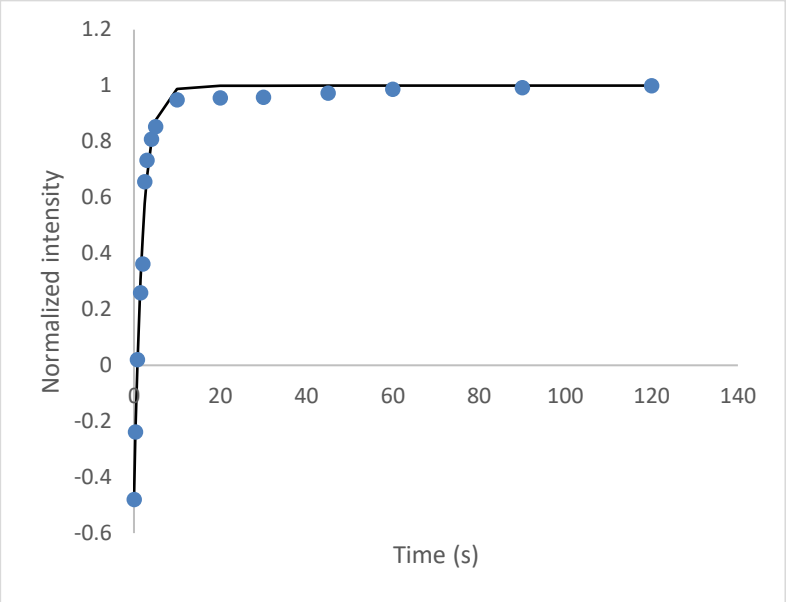

Aliphatic-T_2

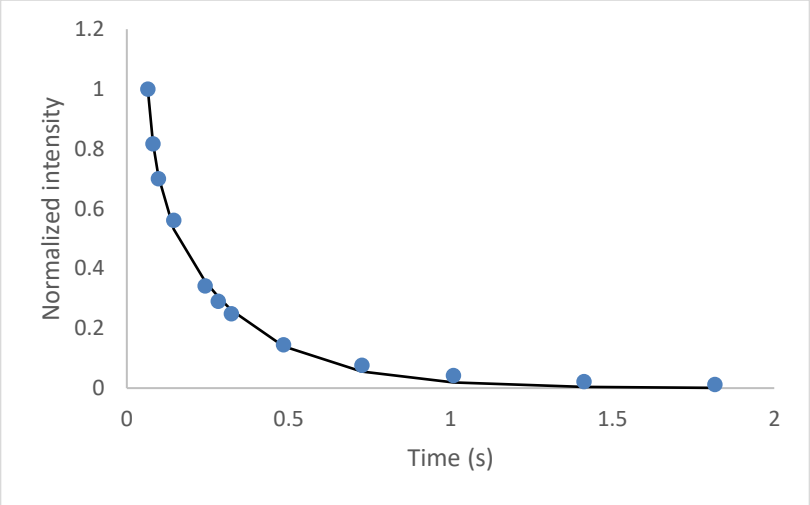

Alicyclic

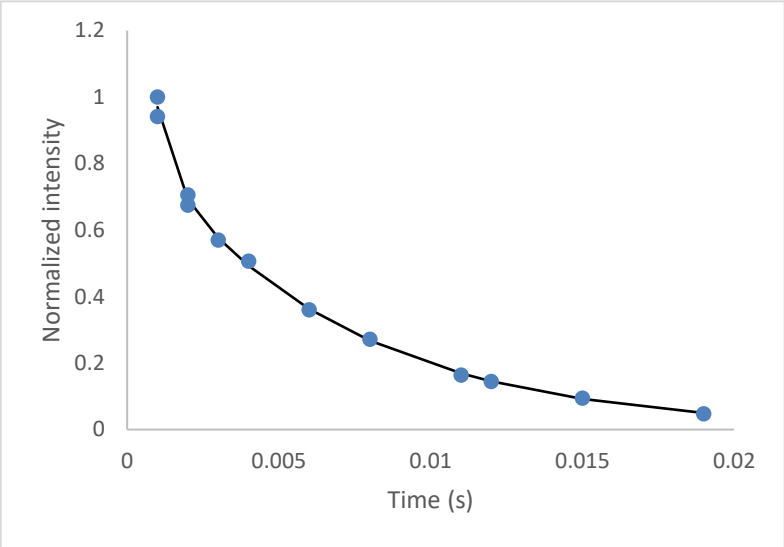

Aromatic

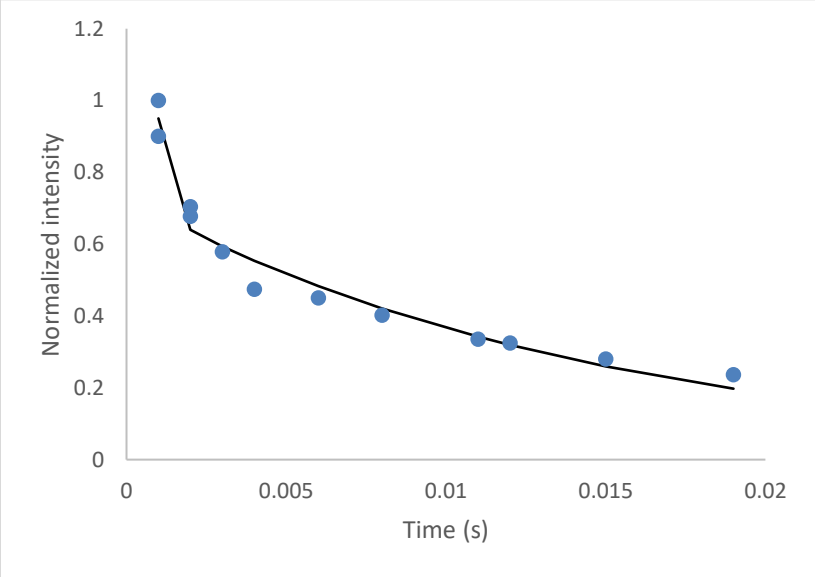

Table A2. ^{1}H NMR Relaxation times of reservoir depth (8026.3 ft) asphaltene in toluene-d_8. The values in parentheses represent the percentage of protons having the corresponding T_2 and T_1.

^{1}H ppm	assignment	T_1 (s)	T_2 (ms)	T_1/T_2
1.5-0.8	aliphatic chain	0.46±0.02 (70±4.5%)	28.1±0.8 (68±4.0%)	16.8±0.86
		1.20±0.03 (30±3.5%)	254±1.5 (32±3.0%)	4.7±0.12
3.5-2.4	alicyclic	2.91±0.06 (68±5.5%)	0.32±0.01 (70±5.0%)	9000±327
		1.23±0.04 (32±4.0%)	16.2±0.6 (30±4.5%)	76±3.7
9.5-7.5	aromatic CH	4.81±0.07 (70±5.8%)	0.29±0.01 (72±4.5%)	16500±610
		1.23±0.04 (30±3.5%)	15.1±0.5 (28±4.5%)	81±3.8

7963.5 T_1-Aromatic

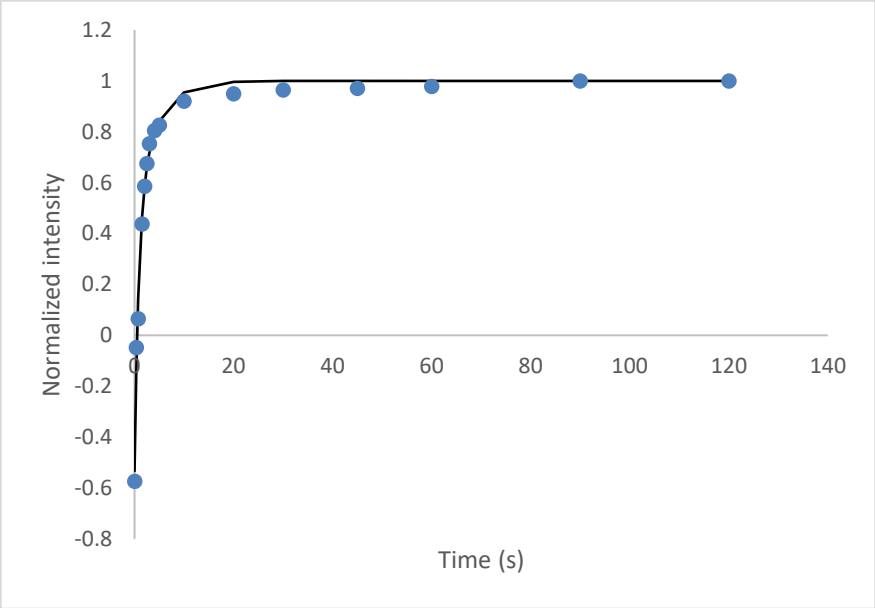

Alicyclic

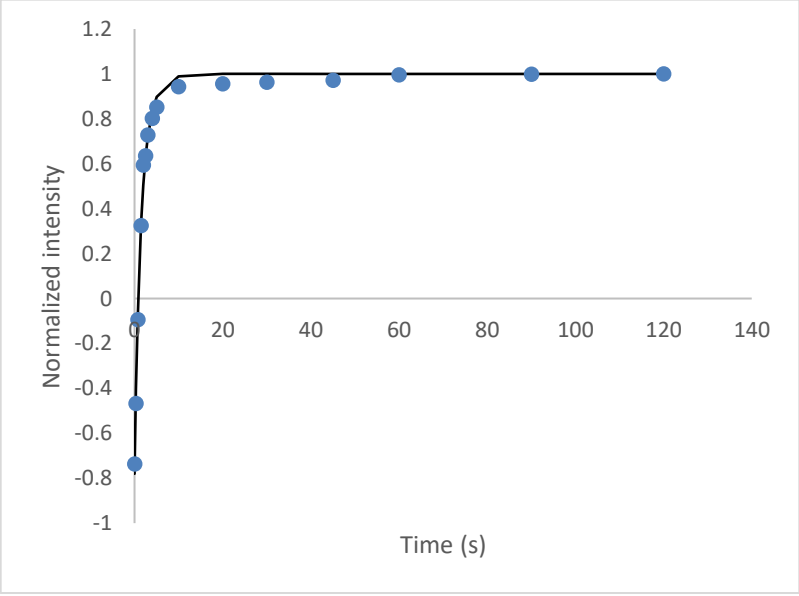

Aliphatic

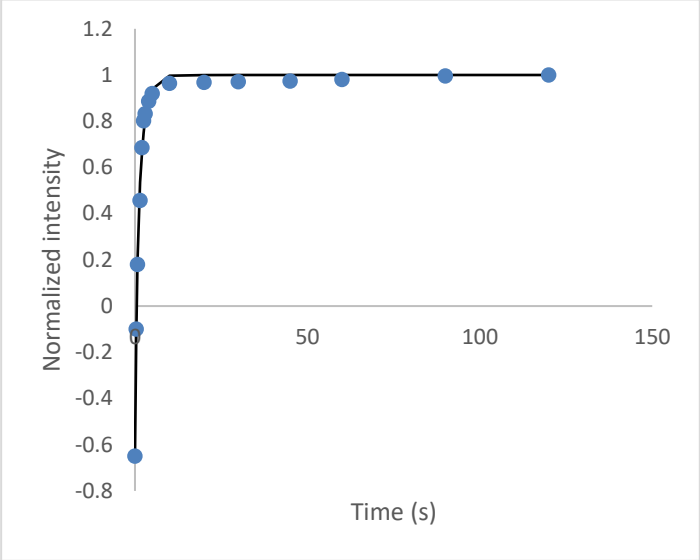

T_2-Alicylcic

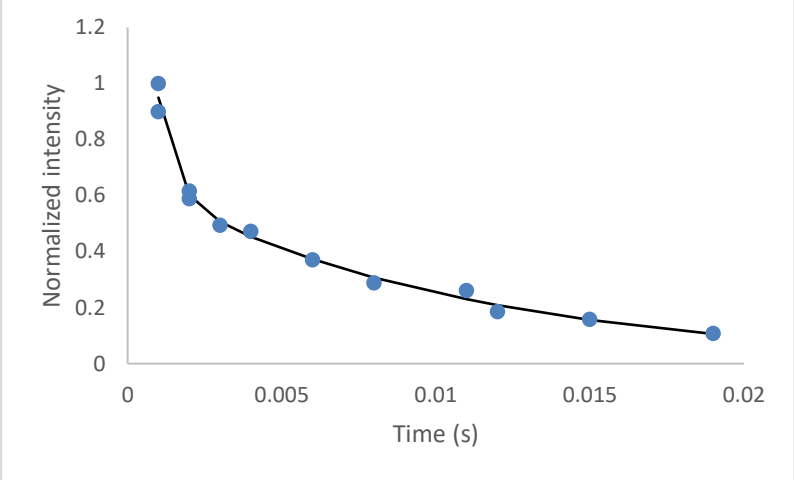

Aromatic

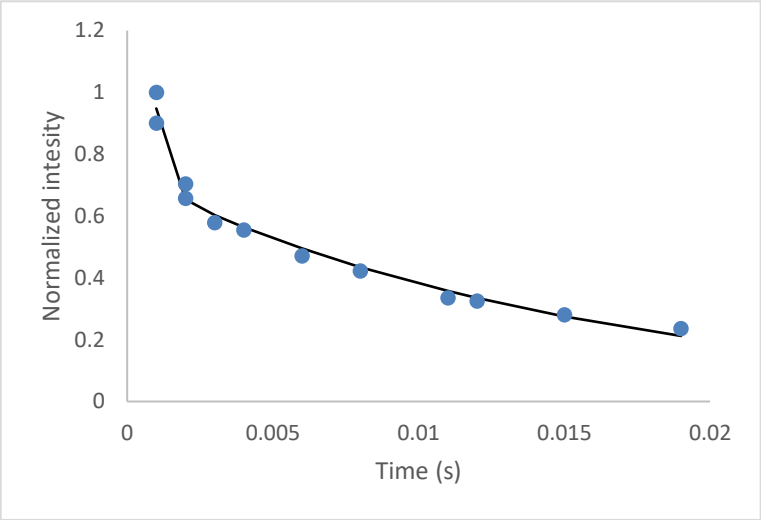

Aliphatic

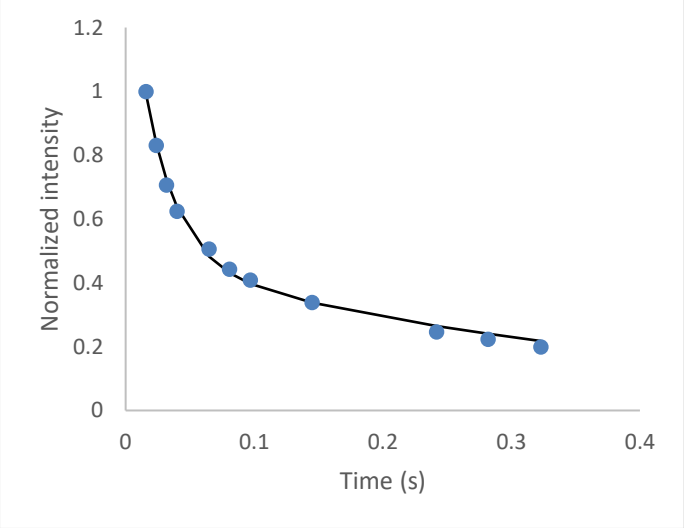

Table A3. ^{1}H NMR Relaxation times of reservoir depth (7963.5 ft) asphaltene in toluene-d_8. The values in parentheses represent the percentage of protons having the corresponding T_2 and T_1.

^{1}H ppm	assignment	T_1 (s)	T_2 (ms)	T_1/T_2
1.5-0.8	aliphatic chain	0.40±0.02 (70±3.5%) 1.20±0.03 (30±3.5%)	25.8±0.9 (68±4.0%) 414±3.50 (32±3.5%)	15.5±0.83 2.9±0.07
3.5-2.4	alicyclic	2.40±0.06 (68±5.5%) 1.21±0.03 (32±4.0%)	0.32±0.01 (65±5.8%) 17.5±0.7 (35±4.5%)	7500±290 69±3.2
9.5-7.5	aromatic CH	4.04±0.06 (70±5.5%) 1.30±0.03 (30±4.5%)	0.27±0.01 (72±4.5%) 18.5±0.8 (28±5.0%)	15000±570 70±3.3

7767.6 ft- Aromatic-T_1

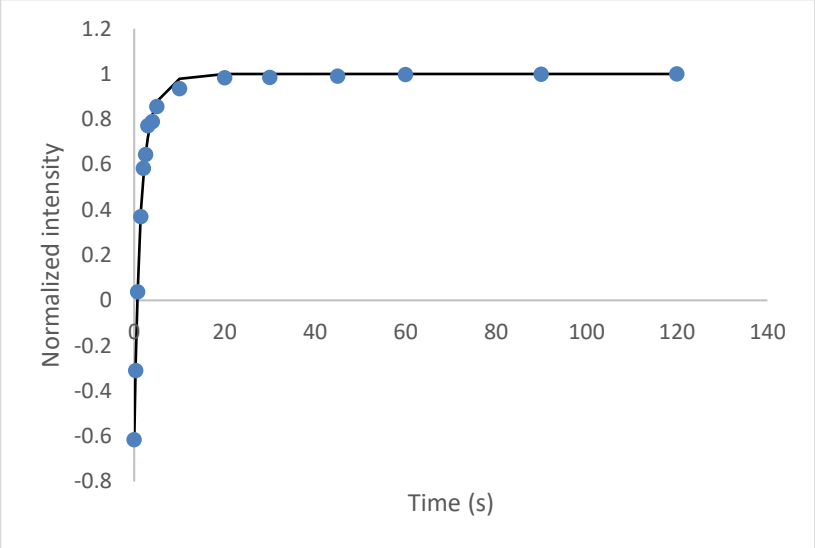

Alicyclic

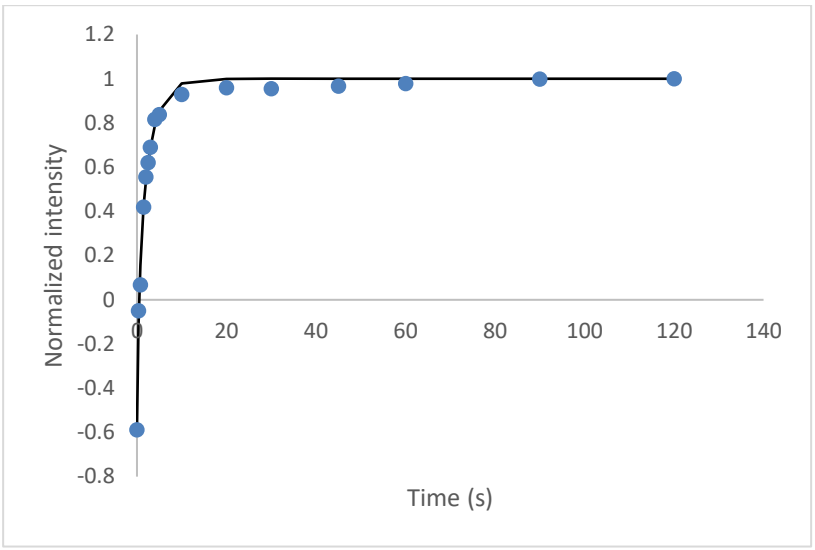

Aliphatic

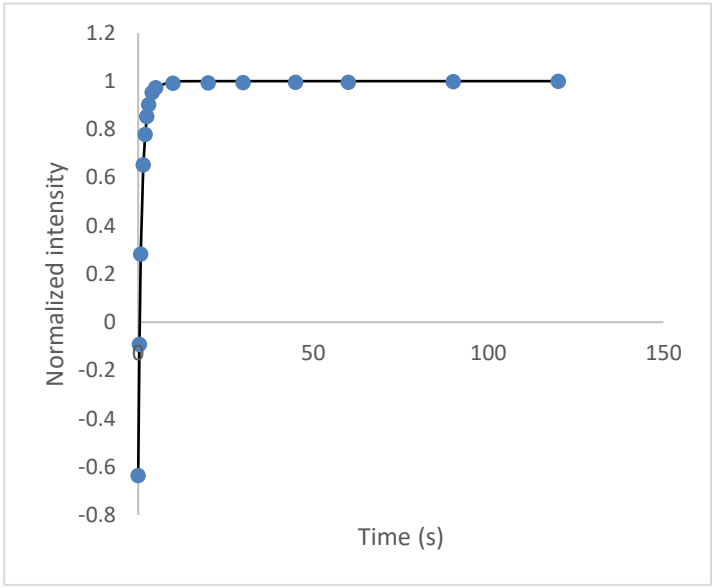

Aliphatic-T_2

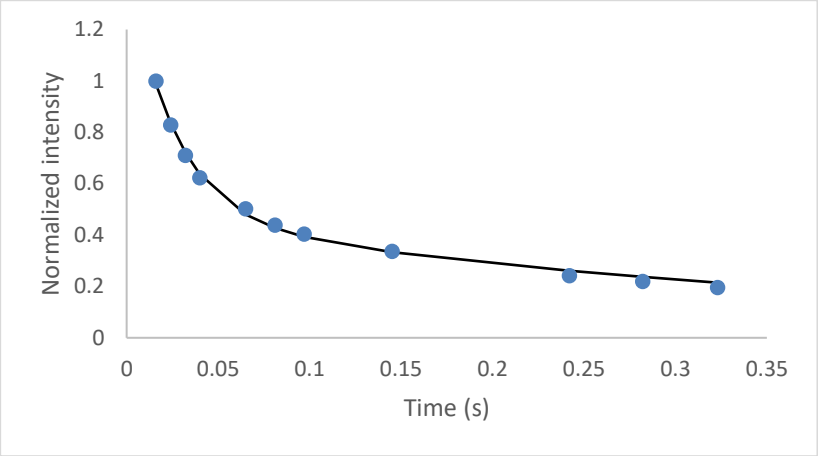

Aromatic

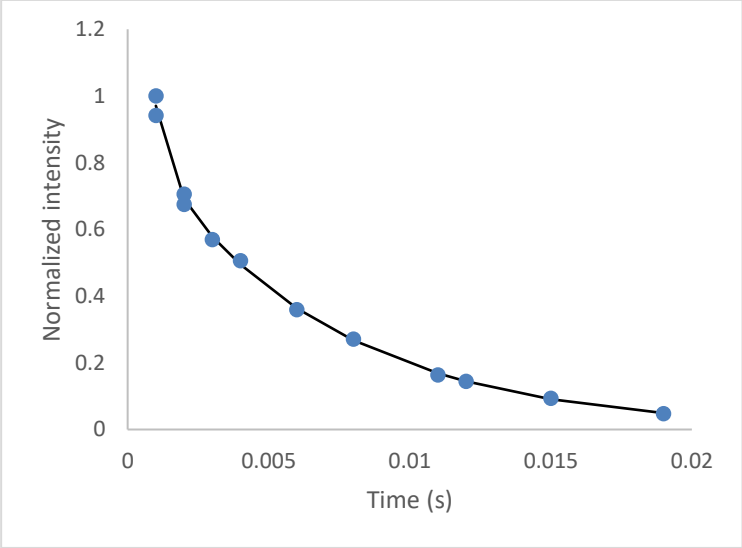

Alicyclic

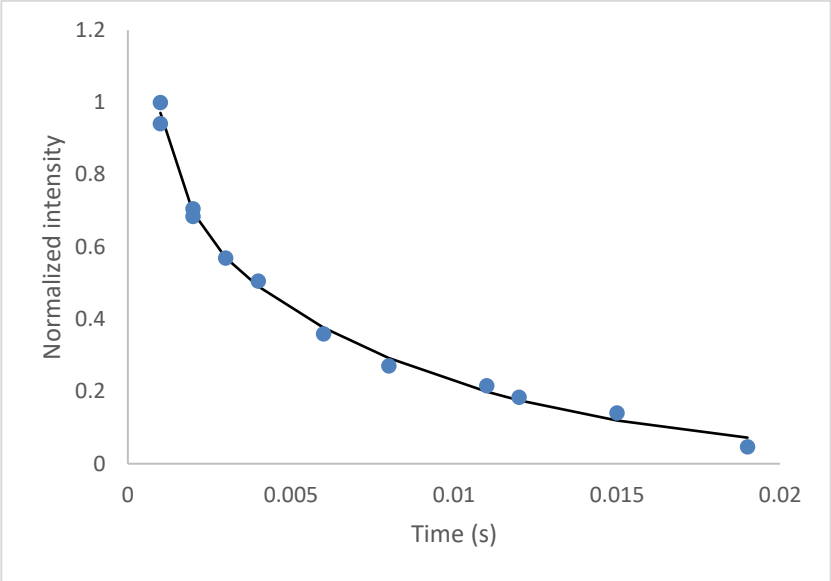

Table A4. ^{1}H NMR Relaxation times of reservoir depth (7767.6 ft) asphaltene in toluene-d_8. The values in parentheses represent the percentage of protons having the corresponding T_2 and T_1.

^{1}H ppm	assignment	T_1 (s)	T_2 (ms)	T_1/T_2
1.5-0.8	aliphatic chain	0.42 ± 0.02 (70 ± 4.5%)	29 ± 0.7 (68 ± 5.5%)	13.8 ± 0.72
		1.50 ± 0.03 (30 ± 3.5%)	330 ± 2.5 (32 ± 3.7%)	4.5 ± 0.12
3.5-2.4	alicyclic	2.60 ± 0.04 (70 ± 4.5%)	4.4 ± 0.05 (70 ± 4.5%)	590 ± 12
		1.56 ± 0.03 (30 ± 3.5%)	17.3 ± 0.75 (30 ± 3.5%)	90 ± 4.2
9.5-7.5	aromatic	3.10 ± 0.04 (65 ± 4.5%)	0.28±0.03 (65 ± 4.5%)	11000 ± 650
		1.20±0.05 (35 ± 4.5%)	13.3 ± 0.8 (35 ± 4.5%)	90 ± 4.3

Table A5. ^{1}H NMR Relaxation times of reservoir depth (8070.9 ft) asphaltene in $CDCl_3$. The values in parentheses represent the percentage of protons having the corresponding T_2 and T_1.

^{1}H ppm	assignment	T_1 (s)	T_2 (ms)	T_1/T_2
1.5-0.8	aliphatic chain	0.38±0.02 (65±4.5%)	29.2±0.9 (68±3.5%)	13±0.78
		1.20±0.04 (35±3.5%)	650±4.2 (32±4.0%)	1.8±0.06
3.5-2.4	alicyclic	2.38±0.05 (70±5.5%)	0.48±0.02 (65±5.8%)	5000±225
		1.24±0.03 (30±5.0%)	19.0±0.8 (35±3.5%)	65±3.0
9.5-7.5	aromatic CH	3.50±0.06 (72±5.8%)	0.35±0.02 (68±5.5%)	10000±390
		1.25±0.04 (28±4.5%)	18.3±0.9 (32±4.0%)	68±3.1

Table A6. ^{1}H NMR Relaxation times of reservoir depth (8026.3 ft) asphaltene in $CDCl_3$. The values in parentheses represent the percentage of protons having the corresponding T_2 and T_1.

^{1}H ppm	assignment	T_1 (s)	T_2 (ms)	T_1/T_2
1.5-0.8	aliphatic	0.40 ± 0.02 (70 ± 4.5%)	30 ± 0.7 (68 ± 5.5%)	13.2 ± 0.70
		1.45 ± 0.03 (30 ± 3.5%)	453 ± 3.0 (32 ± 3.7%)	3.2 ± 0.09
3.5-2.4	alicyclic	2.54 ± 0.04 (70 ± 4.5%)	5.08 ± 0.05 (70 ± 4.5%)	500 ± 10
		1.48 ± 0.03 (30 ± 3.5%)	16.8 ± 0.75 (30 ± 3.5%)	88 ± 4.2
9.5-7.5	aromatic	2.8 ± 0.04 (65 ± 4.5%)	0.29±0.03 (65 ± 4.5%)	9800 ± 500
		1.20 ± 0.03 (35 ± 4.5%)	13.3 ± 0.8 (35 ± 4.5%)	90 ± 4.5

Table A7. ^{1}H NMR Relaxation times of reservoir depth (7963.5 ft) asphaltene in $CDCl_3$. The values in parentheses represent the percentage of protons having the corresponding T_2 and T_1.

^{1}H ppm	assignment	T_1 (s)	T_2 (ms)	T_1/T_2
1.5-0.8	aliphatic	0.38 ± 0.02 (68 ± 3.5%)	31.6 ± 0.7 (68 ± 5.5%)	12.0 ± 0.65
		1.35 ± 0.03 (32 ± 4.0%)	750 ± 4.5 (32 ± 3.5%)	1.8 ± 0.04
3.5-2.4	alicyclic	2.4 ± 0.03 (65 ± 4.5%)	5.85 ± 0.06 (70 ± 4.5%)	410 ± 10
		1.35 ± 0.02 (35 ± 4.5%)	16.8 ± 0.80 (30 ± 3.5%)	80 ± 3.2
9.5-7.5	aromatic	2.2 ± 0.04 (65 ± 4.5%)	0.26 ± 0.03 (70 ± 4.5%)	8200 ± 400
		1.15 ± 0.05 (35 ± 4.5%)	13.0 ± 0.9 (30 ± 3.5%)	88 ± 3.5

Table A8. ^{1}H NMR Relaxation times of reservoir depth (7767.6 ft) asphaltene in $CDCl_3$. The values in parentheses represent the percentage of protons having the corresponding T_2 and T_1.

^{1}H ppm	assignment	T_1 (s)	T_2 (ms)	T_1/T_2
1.5-0.8	aliphatic	0.32 ± 0.02 (68 ± 3.5%)	32.0 ± 0.80 (68 ± 5.5%)	10.0 ± 0.6
		1.0 ± 0.03 (32 ± 4.0%)	830 ± 5.0 (32 ± 3.5%)	1.2 ± 0.04
3.5-2.4	alicyclic	1.8 ± 0.04 (65 ± 4.5%)	9.0 ± 0.08 (70 ± 4.5%)	200 ± 4.0
		1.2 ± 0.02 (35 ± 4.5%)	16.4 ± 0.85 (30 ± 3.5%)	73 ± 3.2
9.5-7.5	aromatic	2.0 ± 0.04 (65 ± 4.5%)	0.32 ± 0.03 (70 ± 4.5%)	6200 ± 300
		1.0 ± 0.03 (35 ± 4.5%)	14.2 ± 0.95 (30 ± 3.5%)	70 ± 3.5

APPENDIX 2

Bi-exponential fitting for the T_1 and T_2 data in Chapter 4. The raw data obtained from the relaxation experiment was normalized and plotted against time. Tables showing the ^1H T_1 and T_2 values measured for AMSO asphaltenes, along with the corresponding percentages of long and short T_1 and T_2 and provides the standard deviation of each data point in the fit.

0.48% EASY%R_O in Toluene-d_8

T_1 -Aliphatic

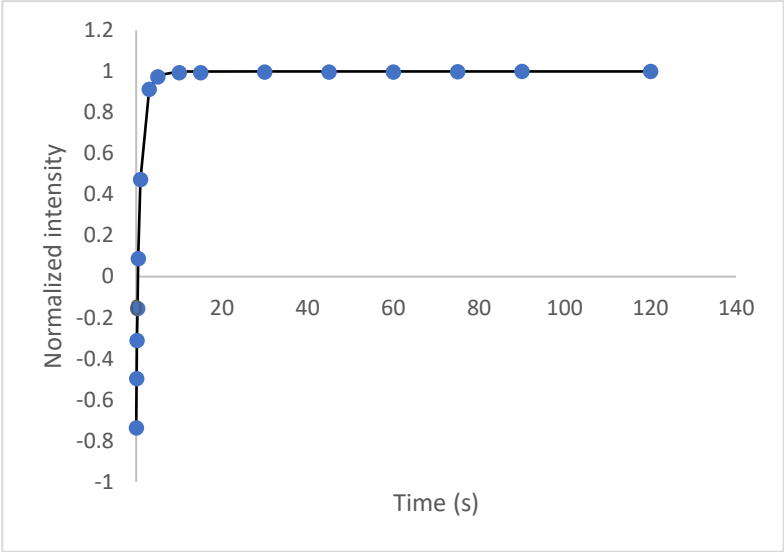

T_1 -Alicyclic

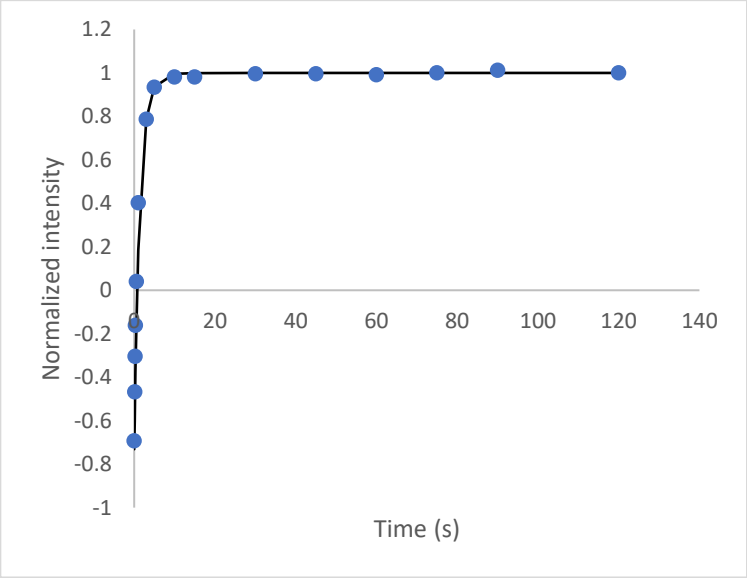

T_1 -Aromatic

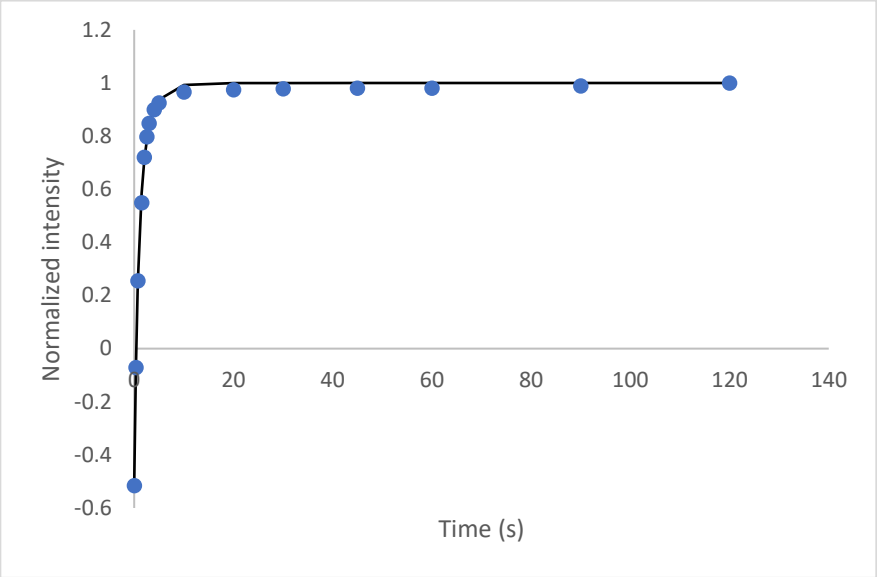

T_2 -Aliphatic

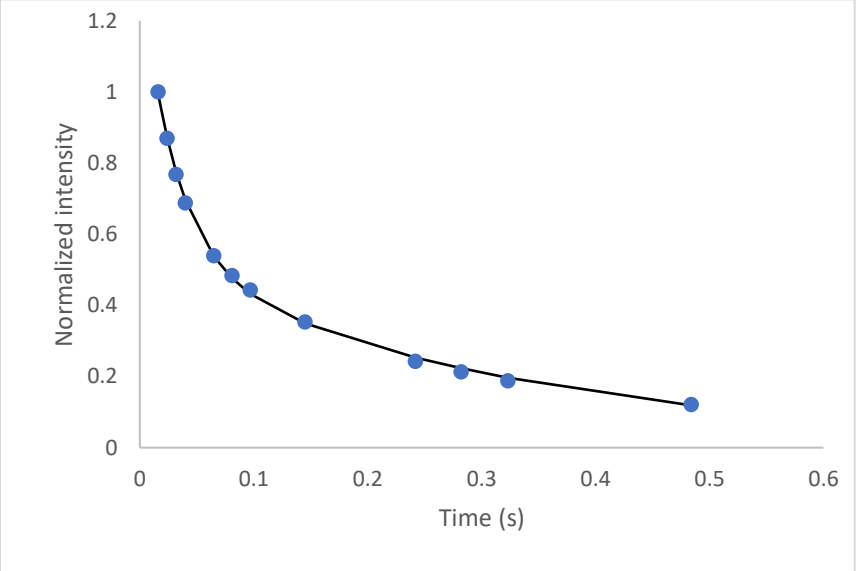

T_2-Alicyclic

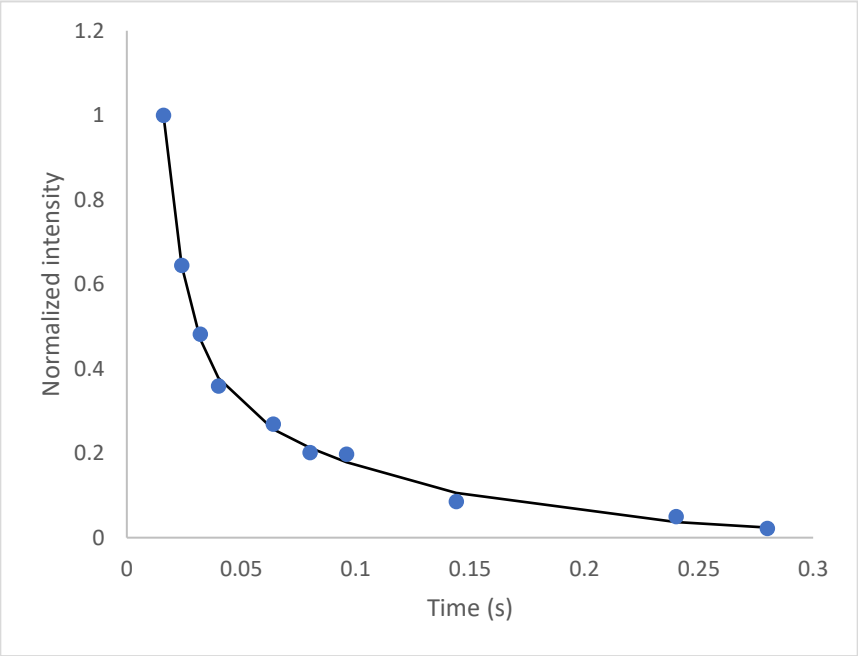

T_2-Aromatic

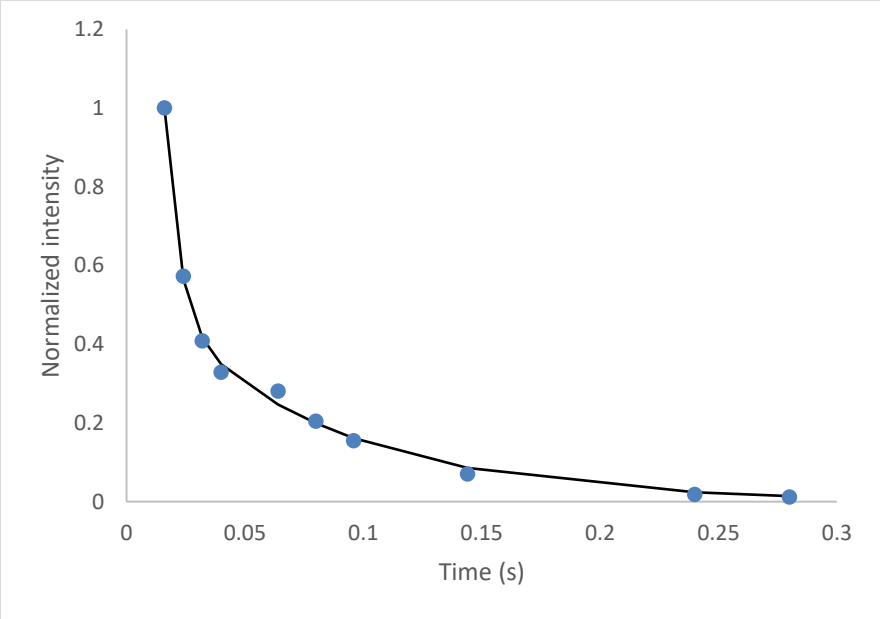

Table B1. ^{1}H NMR relaxation times of asphaltene (0.48% EASY%R_O) in toluene-d_8. The values in parentheses represent the percentage of protons having the corresponding T_1 and T_2 values. The standard deviations for the T_1 and T_2 values are provided.

^{1}H ppm	Assignment	T_1 (s)	T_2 (ms)	T_1/T_2
1.5-0.8	aliphatic chain	0.30±0.04 (75±5.2%) 1.1±0.02 (25±4.5%)	20.0 ±0.8 (78±5.0%) 366.6±1.5 (22±4.2%)	15±0.8 3±0.15
3.5-2.4	alicyclic	1.8 ±0.04 (78±5.7%) 0.9 ±0.03 (22±5.0%)	7.2 ±0.07 (78±5.5%) 16.9±0.7 (22±4.8%)	250±10 53 ±2.8
8.5-7.5	aromatic	2.1±0.05 (80±5.8%) 1.1±0.03 (20±5.2%)	7.0 ± 0.06 (80±5.5%) 22.0 ±0.8 (20±4.8%)	300±14 50±2.6

0.78% EASY%R_O in Toluene-d_8
T_1 -Aliphatic

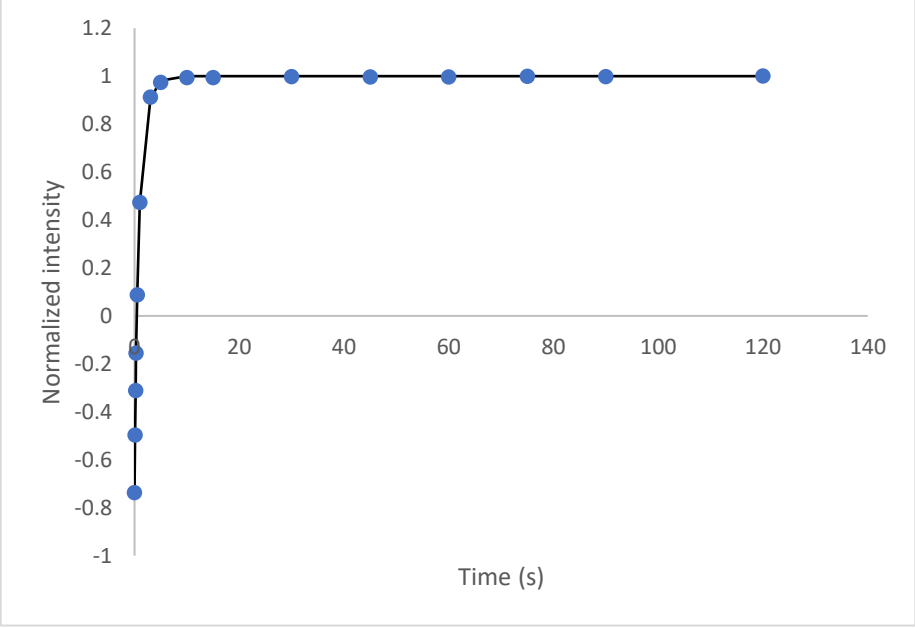

T_1 -Alicyclic

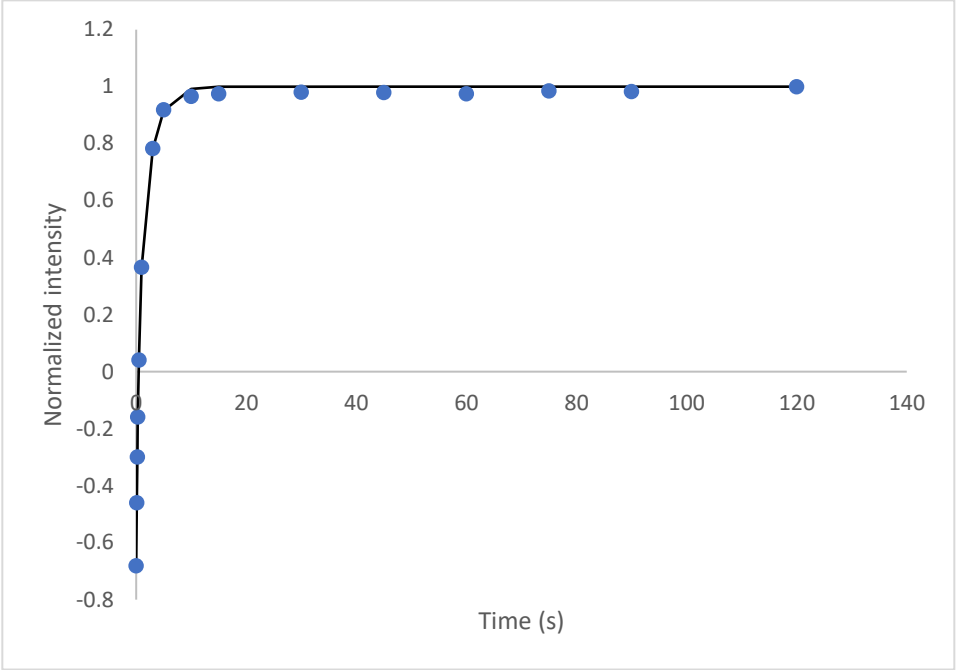

T_1-Aromatic

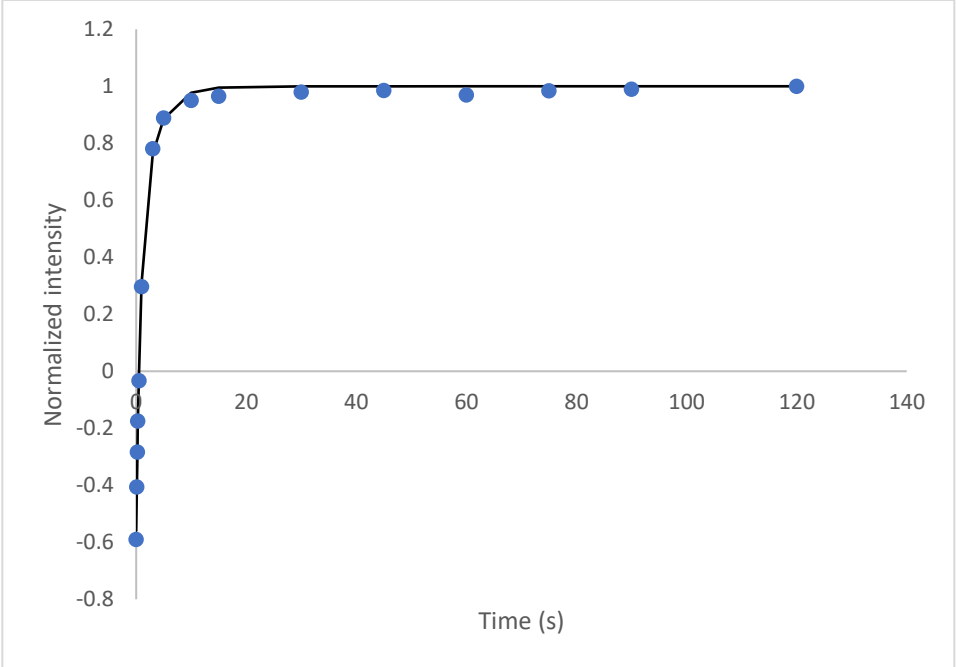

T_2-Aliphatic

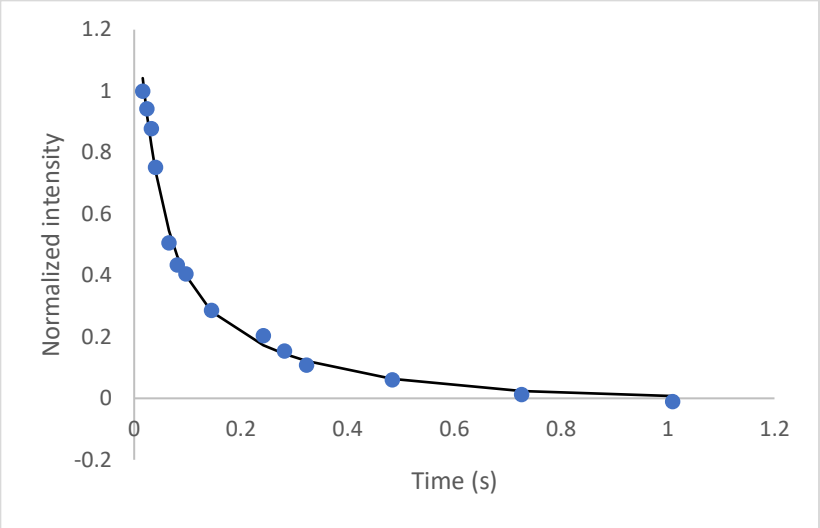

T_2-Alicyclic

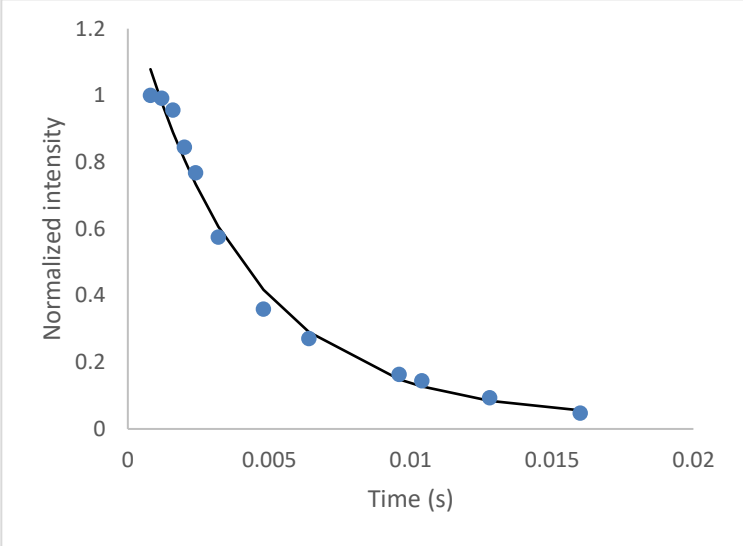

T_2-Aromatic

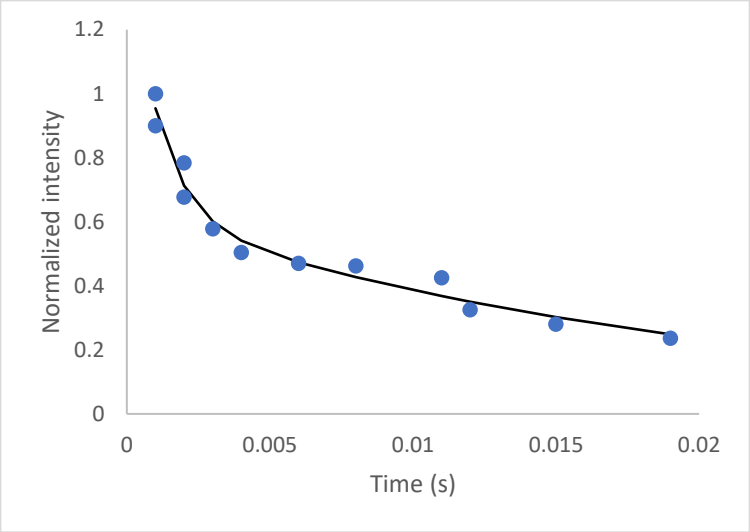

Table B2. ^{1}H NMR relaxation times of asphaltene (0.78% EASY%R_O) in toluene-d_8. The values in parentheses represent the percentage of protons having the corresponding T_1 and T_2 values. The standard deviations for the T_1 and T_2 values are provided.

^{1}H ppm	Assignment	T_1 (s)	T_2 (ms)	T_1/T_2
1.5-0.8	aliphatic chain	0.38±0.04 (75±5.2%)	21.1±0.8 (78±5.0%)	18±0.8
		1.2±0.02 (25±4.5%)	266.6±1.5 (22±4.2%)	4.5±0.15
3.5-2.4	alicyclic	2.16±0.04 (78±5.7%)	5.7±0.07 (78±5.5%)	380±10
		1.1±0.03 (22±5.0%)	17.0±0.7 (22±4.8%)	64 ±2.8
8.5-7.5	aromatic	2.8±0.05 (80±5.8%)	4.8±0.06 (80±5.5%)	580±14
		1.2±0.03 (20±5.2%)	20.7±0.8 (20±4.8%)	58±2.6

1.19% EASY%R_O in Toluene-d_8
T_1-Aliphatic

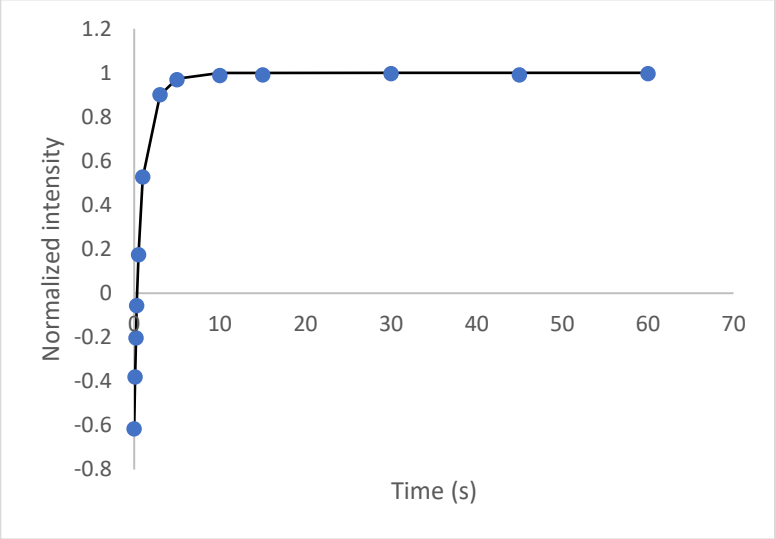

T_1-Alicyclic

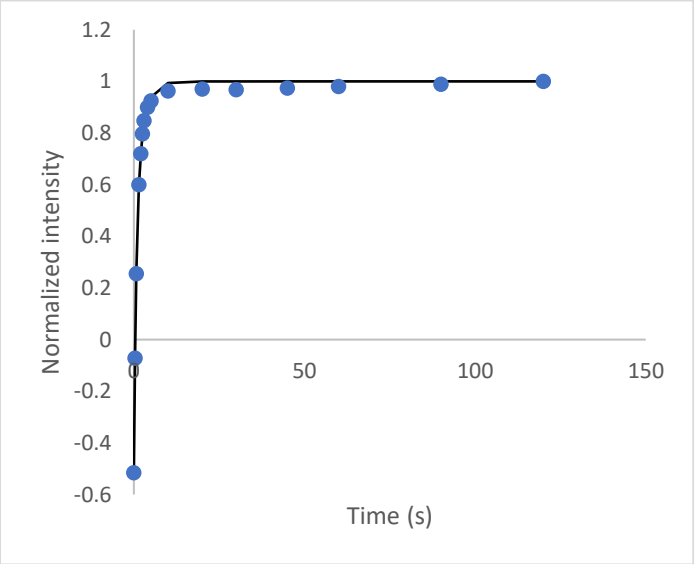

T_1-Aromatic

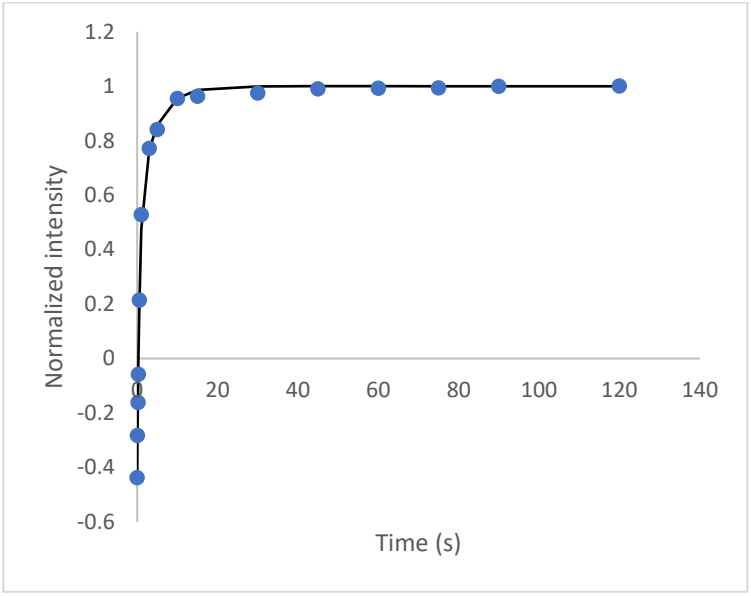

T_2-Aliphatic

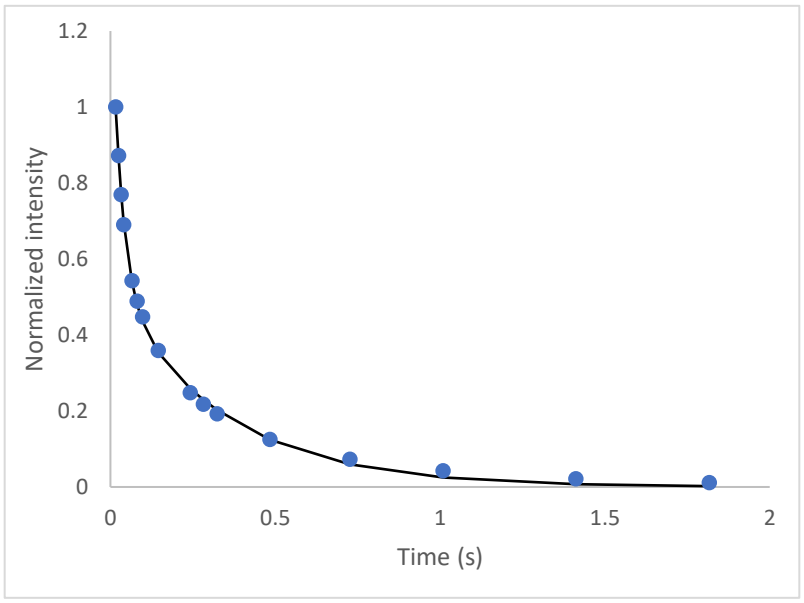

T_2-Alicyclic

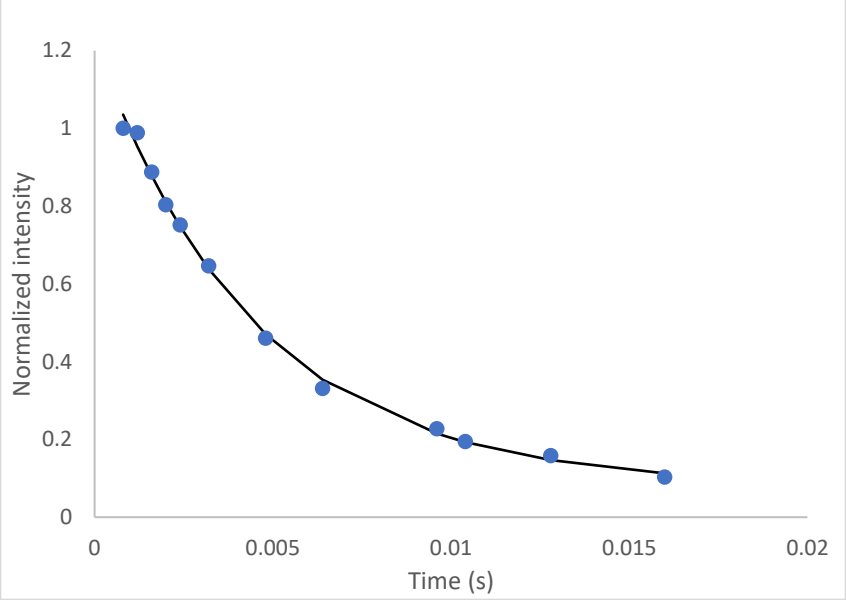

T_2-Aromatic

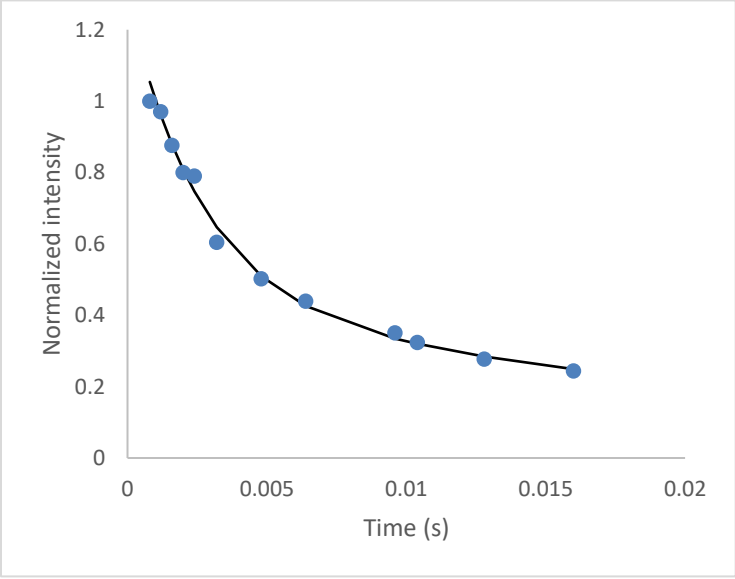

Table B3. ^{1}H NMR relaxation times of asphaltene (1.19% EASY%R_O) in toluene-d_8. The values in parentheses represent the percentage of protons having the corresponding T_1 and T_2 values. The standard deviations for the T_1 and T_2 values are provided.

^{1}H ppm	Assignment	T_1 (s)	T_2 (ms)	T_1/T_2
1.5-0.8	aliphatic	0.38±0.04 (75±5.2%)	22.3±0.8 (78±5.0%)	17±0.8
		1.3±0.02 (25±4.5%)	325±1.5 (22±4.2%)	4.0 ±0.15
3.5-2.4	alicyclic	2.3 ±0.04 (78±5.7%)	4.9±0.07 (78±5.5%)	470±10
		1.1±0.03 (22±5.0%)	16.9 ±0.7 (22±4.8%)	65 ±2.8
8.5-7.5	aromatic	3.0 ±0.05 (80±5.8%)	4.4 ±0.06 (80±5.5%)	680±14
		1.2±0.03 (20±5.2%)	21.4 ±0.8 (20±4.8%)	56±2.6

1.28% EASY%R_O in Toluene-d_8

T_1-Aliphatic

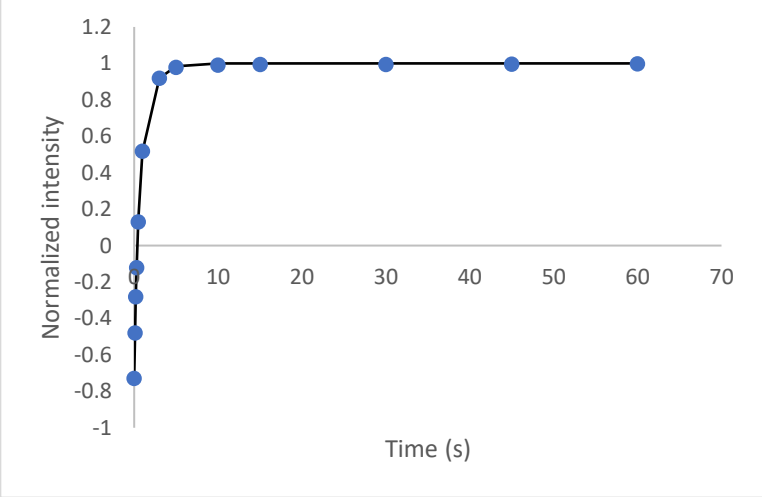

T_1-Alicyclic

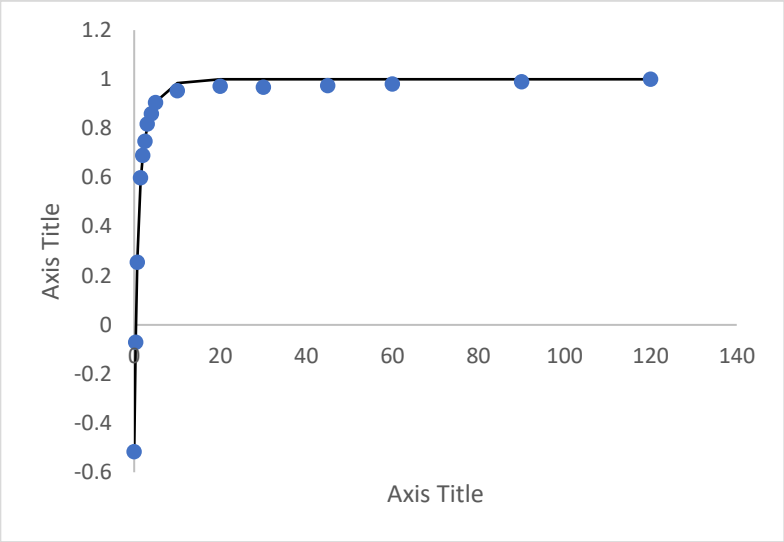

T_1- Aromatic

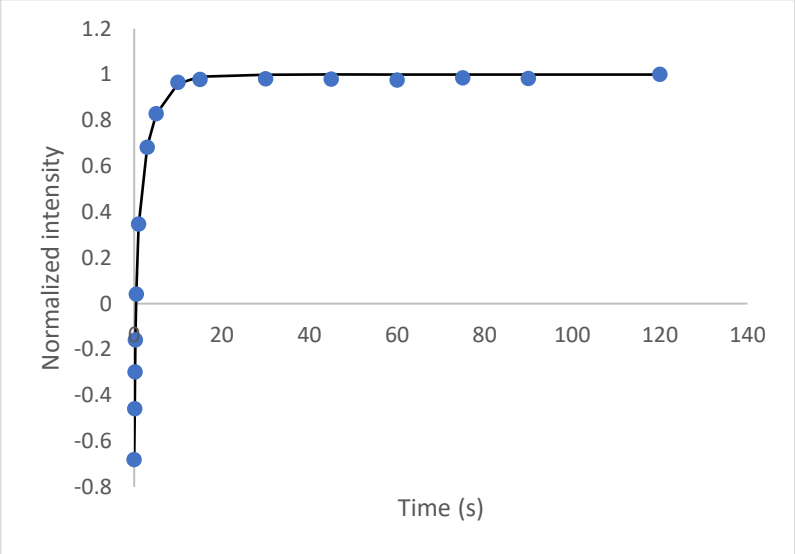

T_2- Aliphatic

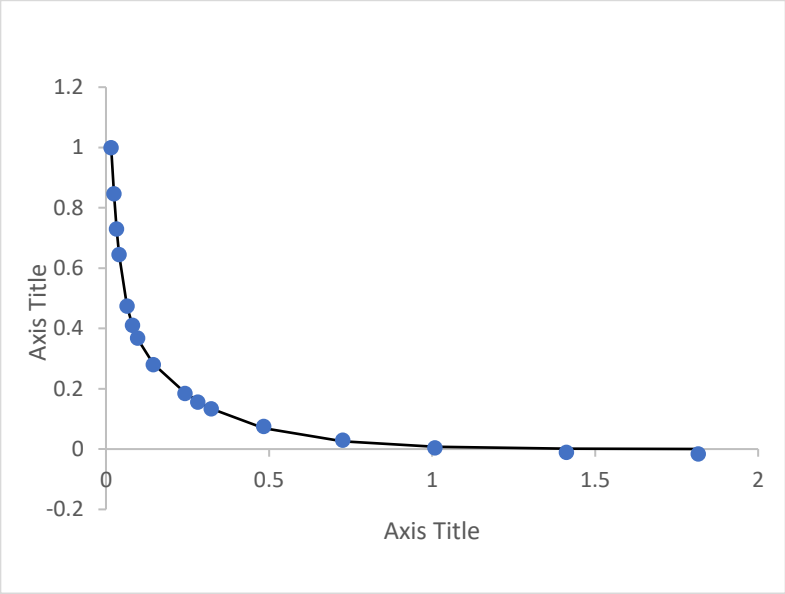

T_2- Alicyclic

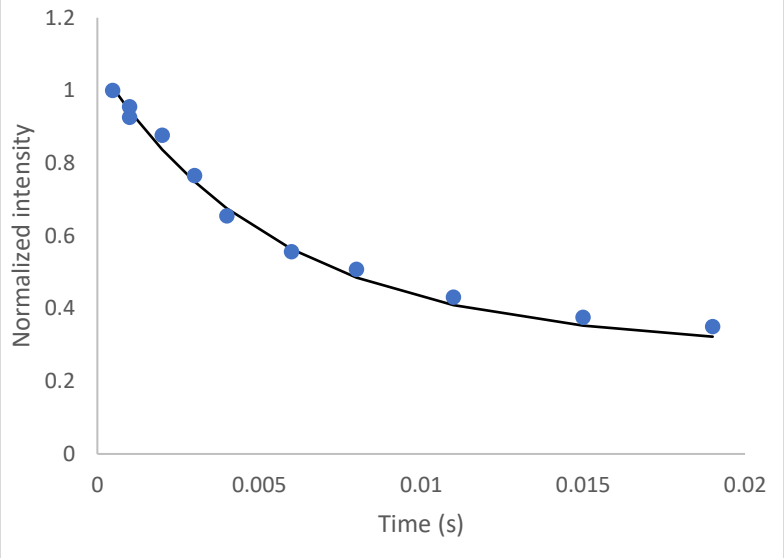

T_2- Aromatic

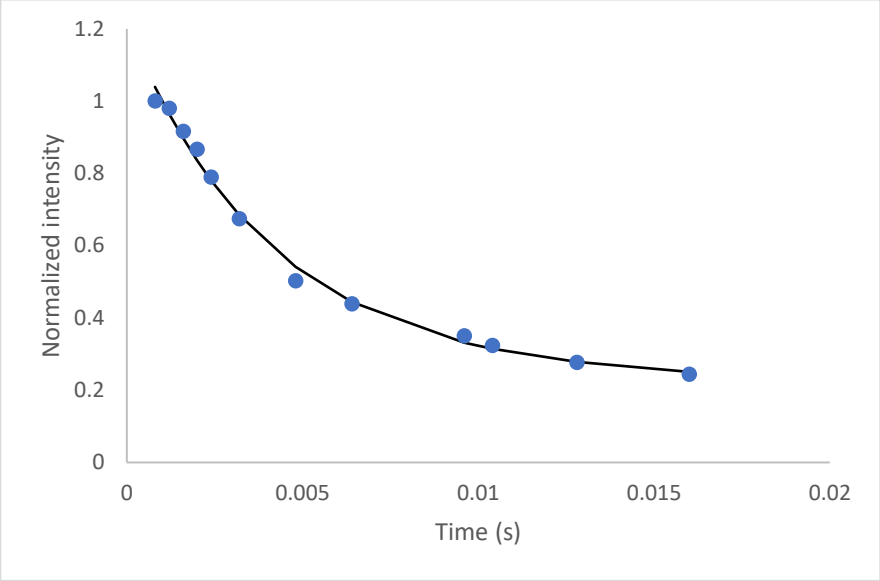

Table B4. ^{1}H NMR relaxation times of asphaltene (1.28% EASY%R_O) in toluene-d_8. The values in parentheses represent the percentage of protons having the corresponding T_1 and T_2 values. The standard deviations for the T_1 and T_2 values are provided.

^{1}H ppm	Assignment	T_1 (s)	T_2 (ms)	T_1/T_2
1.5-0.8	aliphatic	0.42 ±0.04 (75±5.2%) 1.25±0.02 (25±4.5%)	21.0±0.8 (78±5.0%) 250±1.5 (22±4.2%)	20±0.8 5±0.15
3.5-2.4	alicyclic	2.52±0.04 (78±5.7%) 1.3±0.03 (22±5.0%)	5.0±0.07 (78±5.5%) 17.1±0.7 (22±4.8%)	500±10 70±2.8
8.5-7.5	aromatic	3.3±0.05 (80±5.8%) 1.2±0.03 (20±5.2%)	4.6 ±0.06 (80±5.5%) 17.6±0.8 (20±4.8%)	720±14 68±2.6

Table B5. ^{1}H NMR relaxation times of asphaltene (0.48% EASY%R_O) in $CDCl_3$. The values in parentheses represent the percentage of protons having the corresponding T_1 and T_2 values. The standard deviations for the T_1 and T_2 values are provided.

^{1}H ppm	Assignment	T_1 (s)	T_2 (ms)	T_1/T_2
1.5-0.8	aliphatic	0.28 ± 0.05 (75±5%)	21.0 ±0.9 (78±5.0%)	13 ± 0.6
		1.0 ± 0.03 (25±5%)	476.6±1.8 (22±4.2%)	2.1 ± 0.08
3.5-2.4	alicyclic	1.4 ± 0.05 (78±5.7%)	16.5 ± 0.7 (75±5.5%)	85 ± 2.1
		0.9 ± 0.04 (22±5.0%)	24.3 ± 0.8 (25±4.8%)	37 ± 0.9
8.5-7.5	aromatic	1.6 ± 0.05 (78±5.8%)	16.6 ± 0.8 (75±5.5%)	96 ± 2.2
		1.0 ± 0.04 (22±5.2%)	27.0 ±0.9 (25±4.8%)	37 ± 1.3

Table B6. ^{1}H NMR relaxation times of asphaltene (0.78% EASY%R_O) in $CDCl_3$. The values in parentheses represent the percentage of protons having the corresponding T_1 and T_2 values. The standard deviations for the T_1 and T_2 values are provided.

^{1}H ppm	Assignment	T_1 (s)	T_2 (ms)	T_1/T_2
1.5-0.8	aliphatic	0.31 ±0.04 (75±5.2%)	20.6 ±0.8 (78±5.0%)	15.0 ± 0.8
		1.1±0.02 (25±4.5%)	314.3 ± 1.5 (22±4.2%)	3.5 ± 0.15
3.5-2.4	alicyclic	1.7 ±0.04 (78±5.7%)	14.2 ± 0.07 (78±5.5%)	120 ± 2.4
		0.9 ±0.03 (22±5.0%)	18.4 ± 0.7 (22±4.8%)	49 ± 1.9
8.5-7.5	aromatic	2.0 ± 0.05 (80±5.8%)	13.3 ± 0.06 (80±5.5%)	150 ± 3
		1.0 ± 0.03 (20±5.2%)	22.2 ± 0.8 (20±4.8%)	45 ± 1.7

Table B7. ^{1}H NMR relaxation times of asphaltene (0.95% EASY%R_O) in $CDCl_3$. The values in parentheses represent the percentage of protons having the corresponding T_1 and T_2 values. The standard deviations for the T_1 and T_2 values are provided.

^{1}H ppm	Assignment	T_1 (s)	T_2 (ms)	T_1/T_2
1.5-0.8	aliphatic	0.35 ± 0.04 (75±5.2%)	20.6 ± 0.8 (78±5.0%)	17 ± 1.0
		1.1 ± 0.02 (25±4.5%)	275 ± 1.5 (22±4.2%)	4.0 ± 0.15
3.5-2.4	alicyclic	2.0 ±0.04 (78±5.7%)	11.8 ± 0.07 (78±5.5%)	170 ± 3.4
		1.0 ± 0.03 (22±5.0%)	17.8 ± 0.7 (22±4.8%)	56 ± 2.1
8.5-7.5	aromatic	2.1 ±0.05 (80±5.8%)	9.5 ± 0.06 (80±5.5%)	220 ± 4.4
		1.0 ± 0.03 (20±5.2%)	19.2 ± 0.8 (20±4.8%)	52 ± 2.1

Table B8. ^{1}H NMR relaxation times of asphaltene (1.19% EASY%R_O) in $CDCl_3$. The values in parentheses represent the percentage of protons having the corresponding T_1 and T_2 values. The standard deviations for the T_1 and T_2 values are provided.

^{1}H ppm	Assignment	T_1 (s)	T_2 (ms)	T_1/T_2
1.5-0.8	aliphatic	0.32 ±0.04 (75±5.2%)	20.0 ±0.8 (78±5.0%)	16.0 ± 0.8
		1.2 ± 0.02 (25±4.5%)	285.7 ± 1.5 (22±4.2%)	4.2 ± 0.2
3.5-2.4	alicyclic	1.8 ±0.04 (78±5.7%)	12.8 ± 0.07 (78±5.5%)	140 ± 2.8
		0.9 ±0.03 (22±5.0%)	16.9 ± 0.7 (22±4.8%)	53 ± 1.75
8.5-7.5	aromatic	1.9 ± 0.05 (80±5.8%)	10 ± 0.06 (80±5.5%)	190 ± 3.8
		1.0 ± 0.03 (20±5.2%)	20 ± 0.8 (20±4.8%)	50 ± 1.9

Table B9. ^{1}H NMR relaxation times of asphaltene (1.28% EASY%R_O) in $CDCl_3$. The values in parentheses represent the percentage of protons having the corresponding T_1 and T_2 values. The standard deviations for the T_1 and T_2 values are provided.

^{1}H ppm	Assignment	T_1 (s)	T_2 (ms)	T_1/T_2
1.5-0.8	aliphatic	0.35 ± 0.04 (75±5.2%)	20.0 ± 0.8 (78±5.0%)	17.5 ± 0.9
		1.0 ± 0.02 (25±4.5%)	250 ± 1.5 (22±4.2%)	4.0 ± 0.2
3.5-2.4	alicyclic	1.9 ±0.04 (78±5.7%)	11.9 ± 0.07 (78±5.5%)	160 ± 3.2
		1.0 ± 0.03 (22±5.0%)	17.2 ± 0.7 (22±4.8%)	58 ± 2.4
8.5-7.5	aromatic	2.0 ±0.05 (80±5.8%)	9.5 ± 0.06 (80±5.5%)	210 ± 4.2
		1.0 ± 0.03 (20±5.2%)	18.9 ± 0.8 (20±4.8%)	53 ± 1.7

APPENDIX 3

Bi-exponential fitting for the T_1 and T_2 data in Chapter 5. The raw data obtained from the relaxation experiment was normalized and plotted against time.

Crude

Aliphatic -T_1

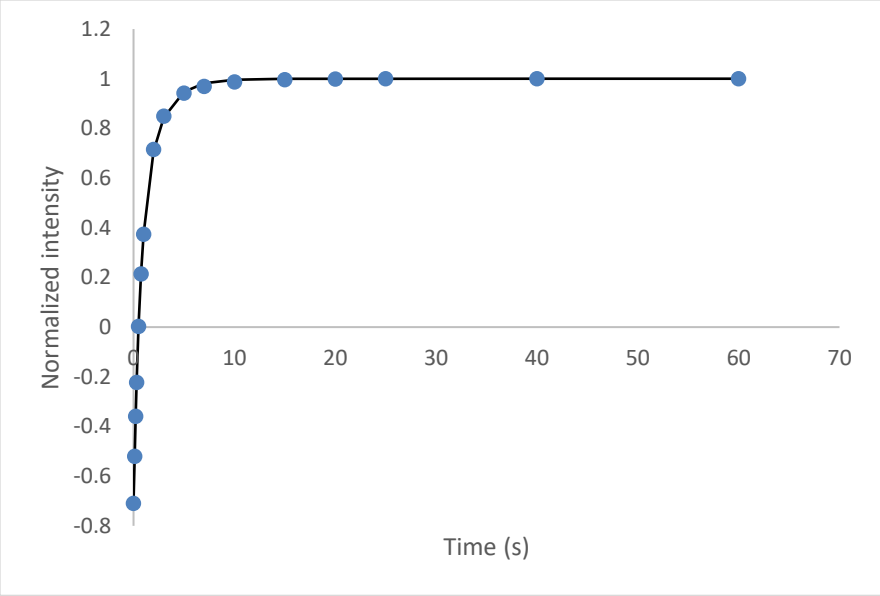

Aromatic

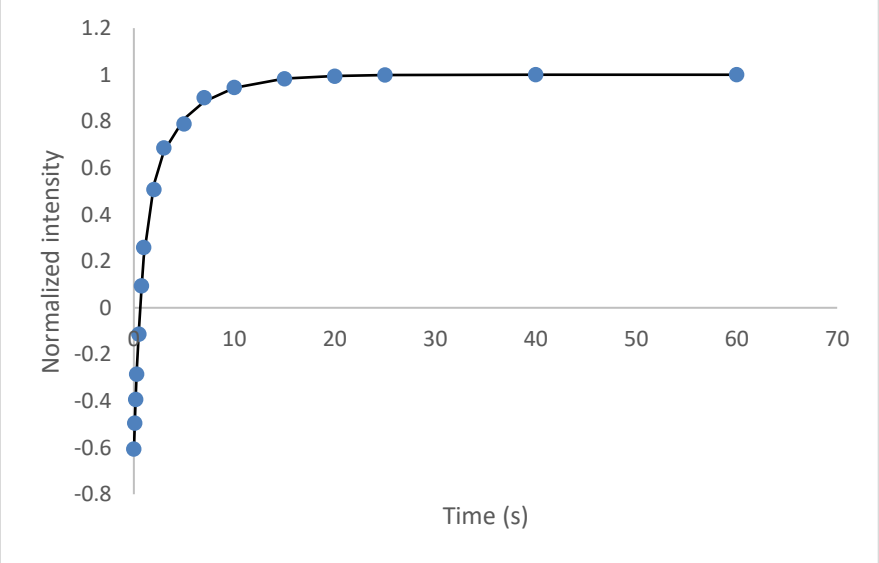

Alicyclic

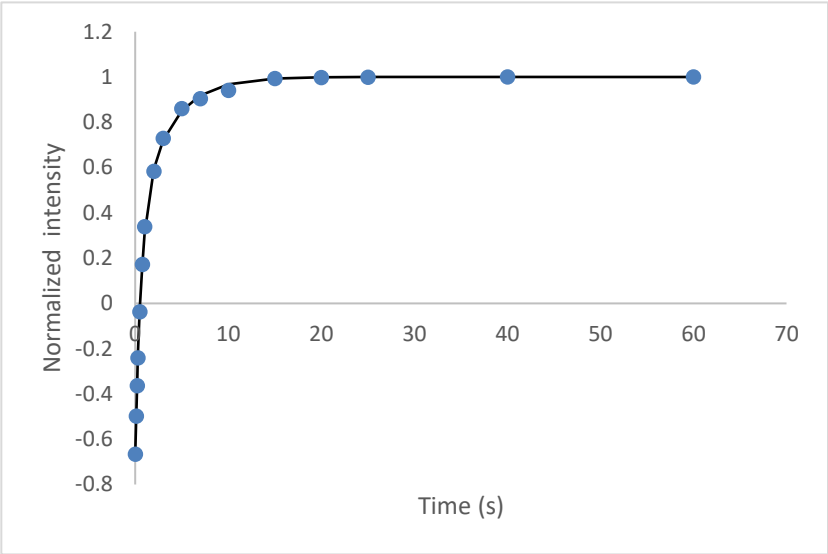

T_2-Aliphatic

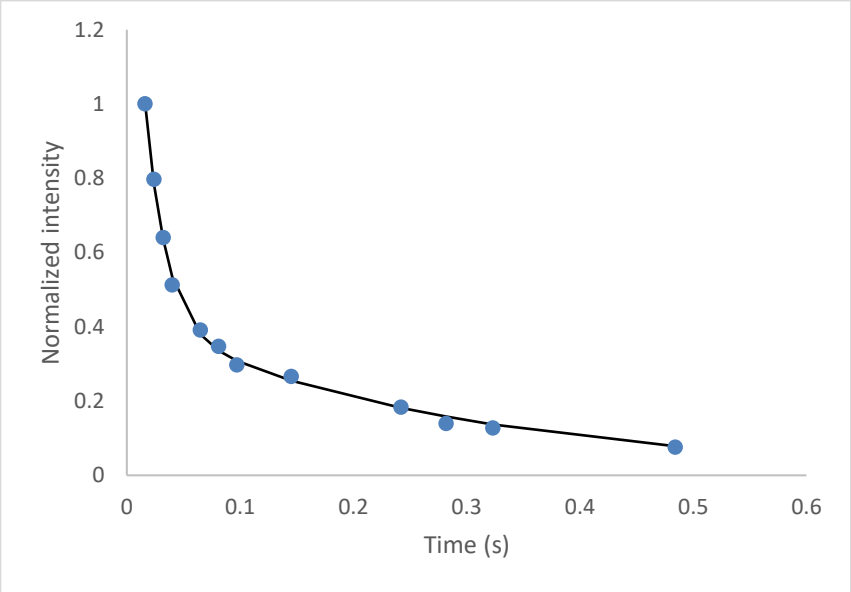

T_2-Alicyclic

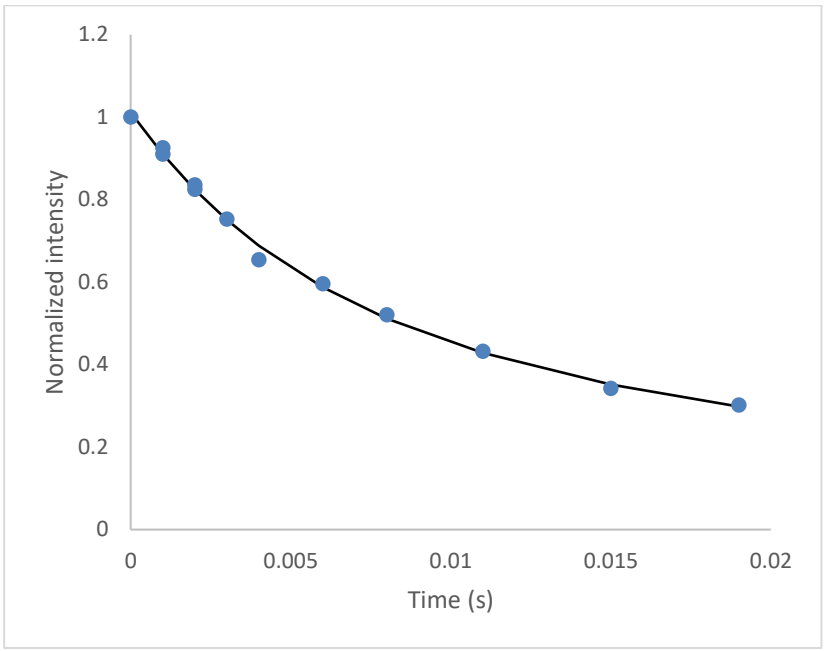

T_2-Aromatic

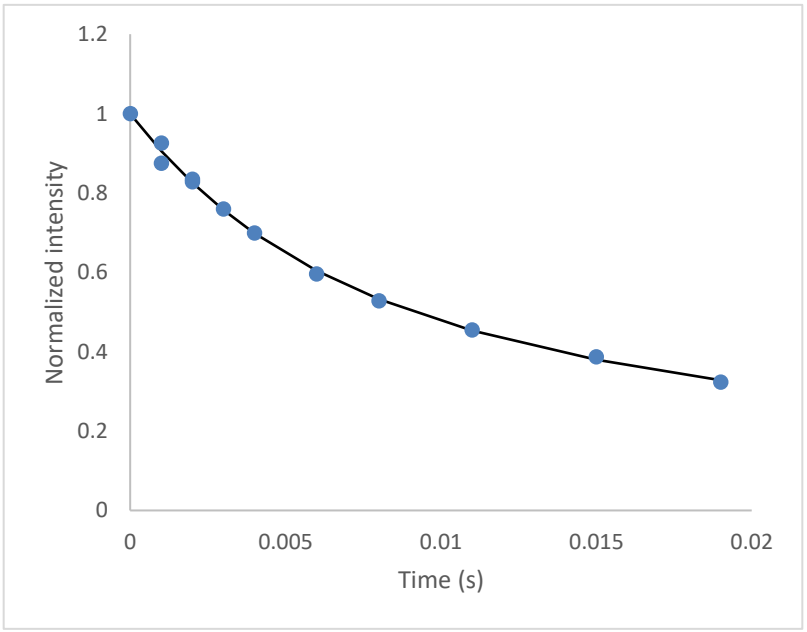

Sonicated

T_1-Alliphatic

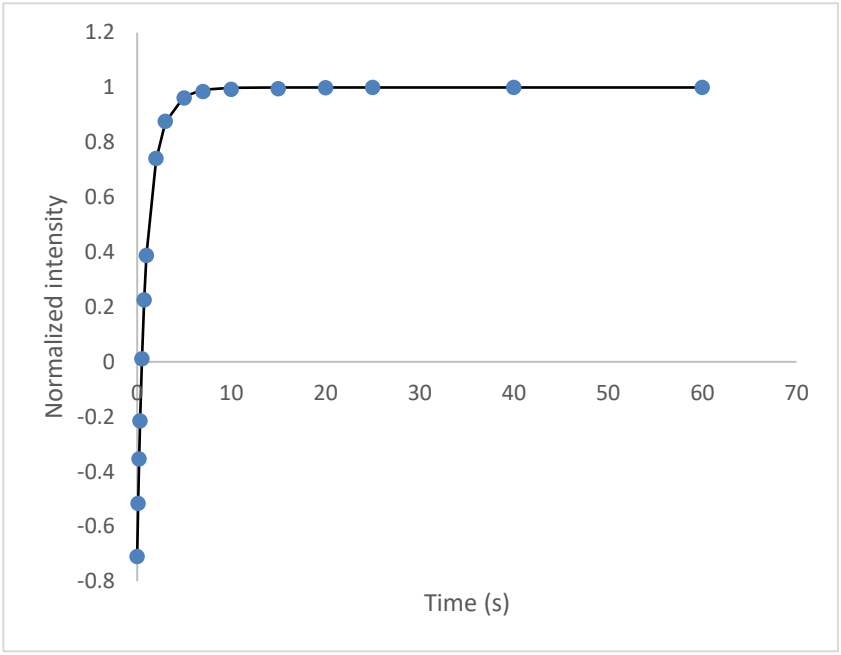

Alicyclic

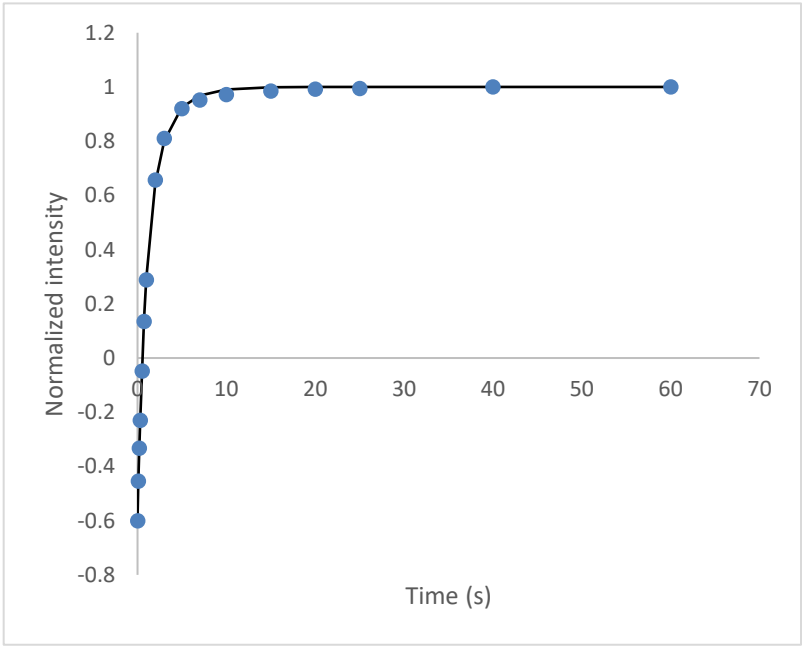

Aromatic

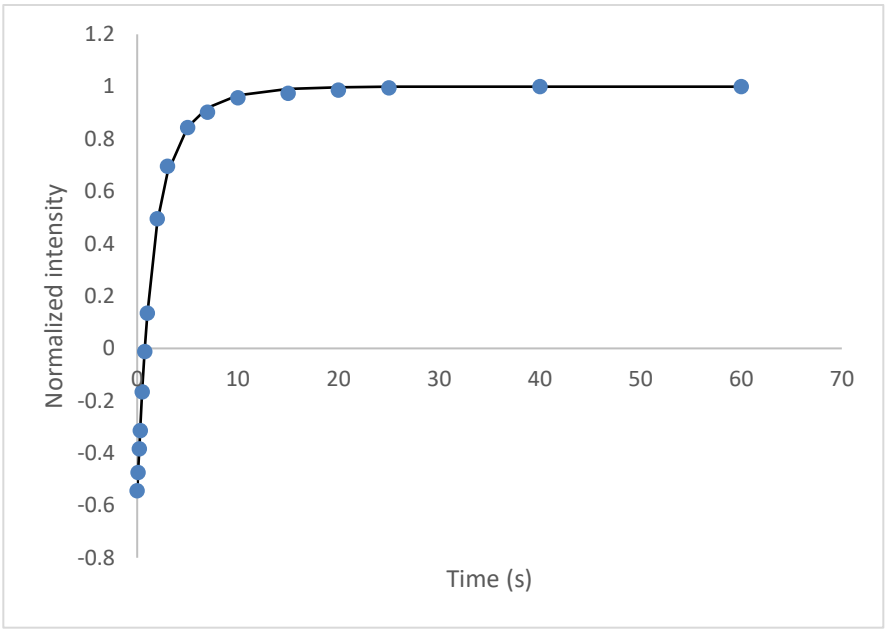

T_2-Aliphatic

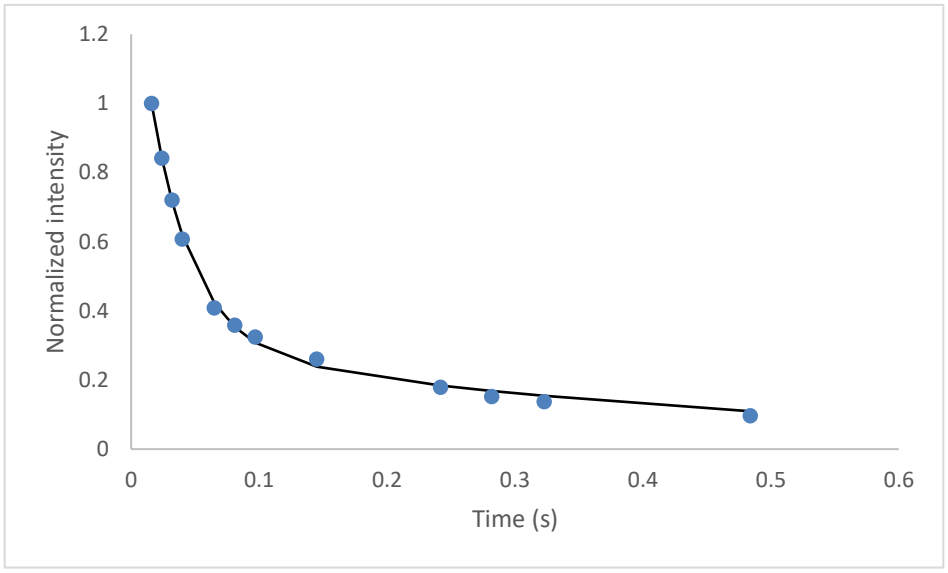

T_2-Alicyclic

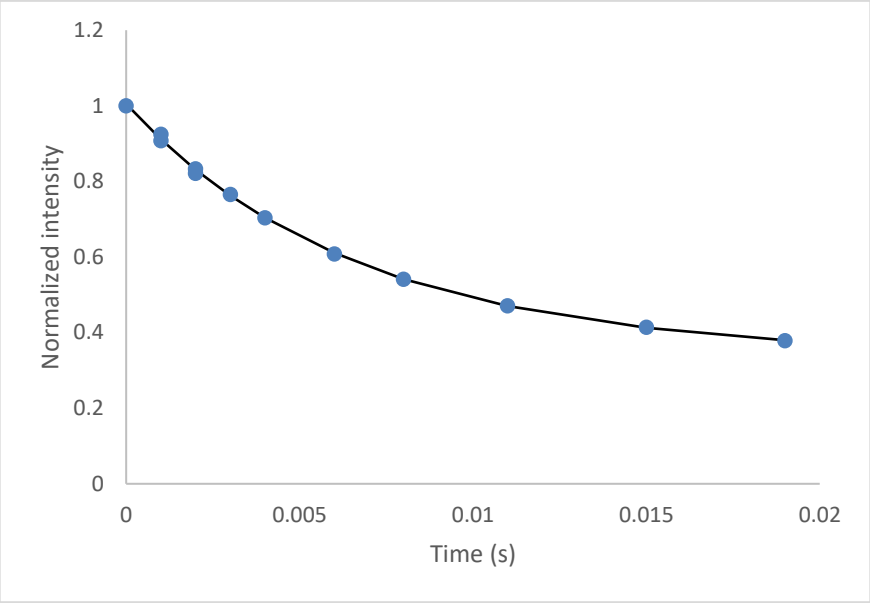

T_2-Aromatic

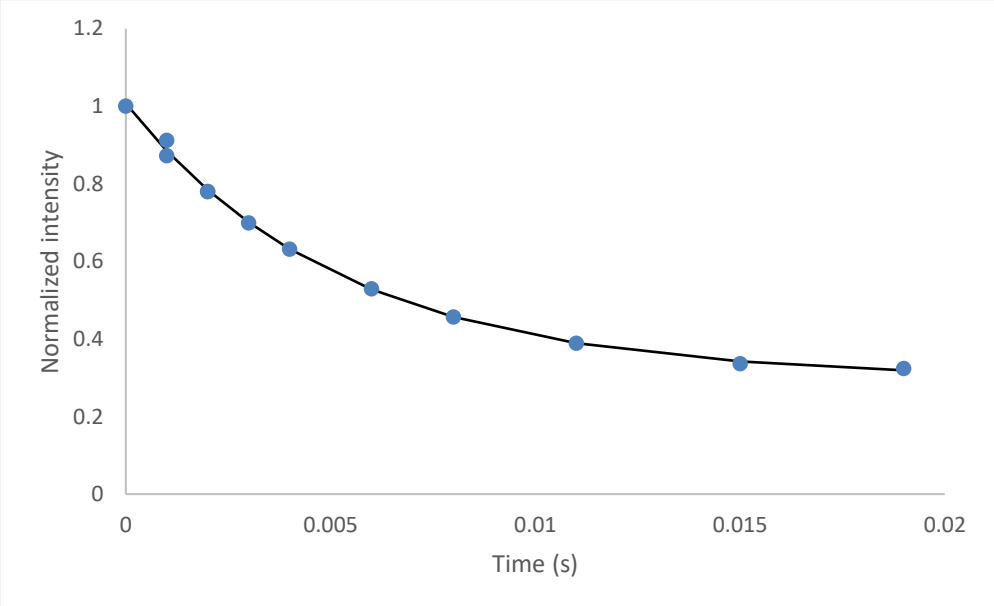

APPENDIX 4

Bi-exponential fitting for the T_1 and T_2 data in Chapter 6. The raw data obtained from the relaxation experiment was normalized and plotted against time. Tables showing the ^1H T_1 and T_2 values measured for UG8 asphaltenes, along with the corresponding percentages of long and short T_1 and T_2 and provides the standard deviation of each data point in the fit.

1 mg/mL-$CDCl_3$

T_1-Aliphatic

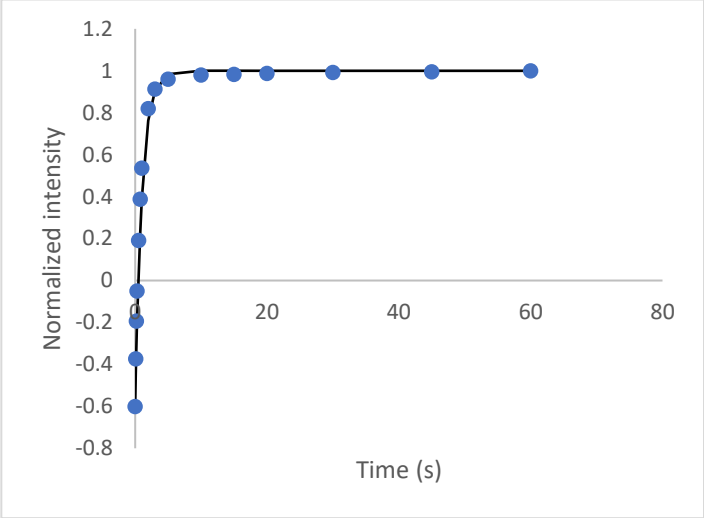

T_1-Alicyclic

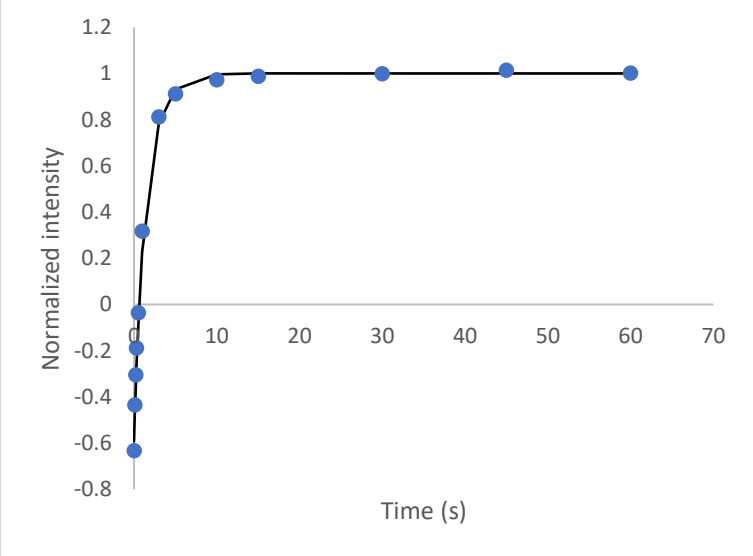

T_1-Aromatic

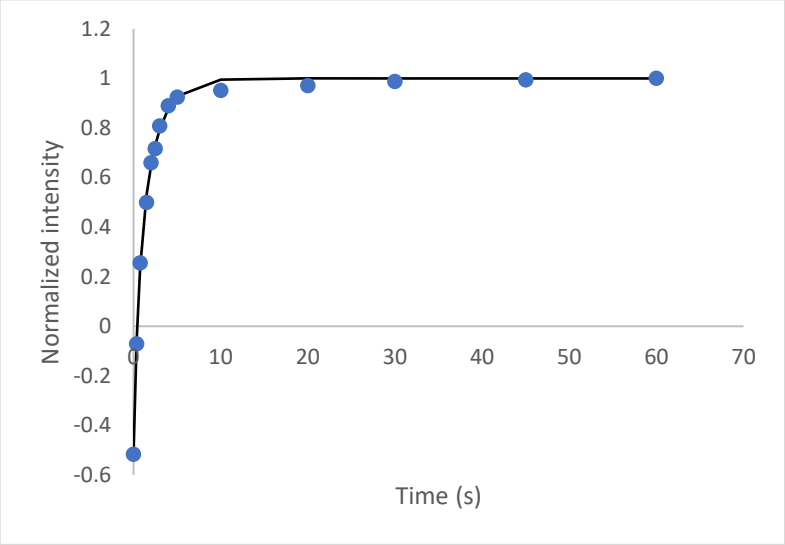

T_2-Aliphatic

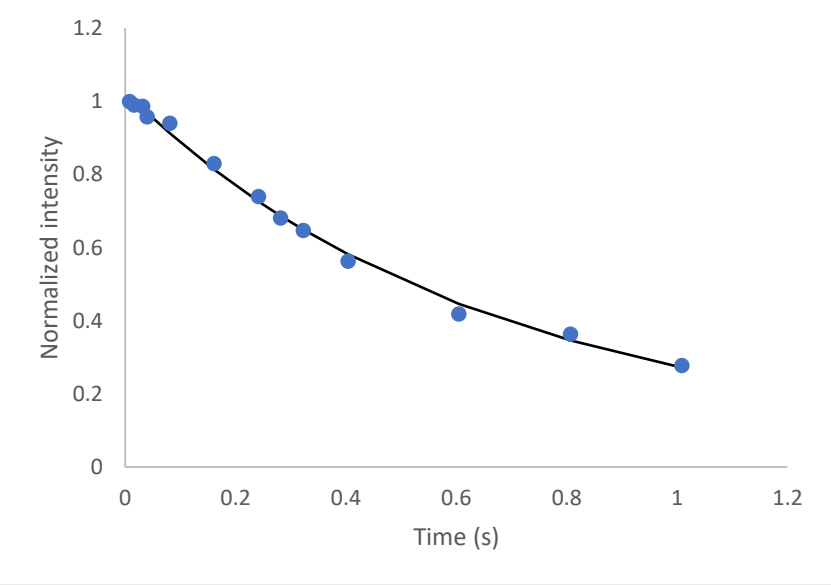

T_2-Alicyclic

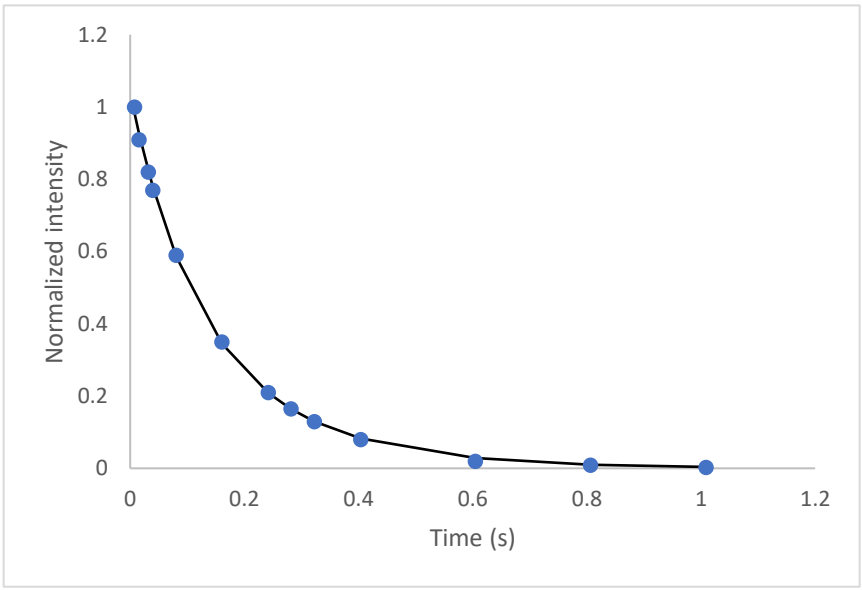

T_2-Aromatic

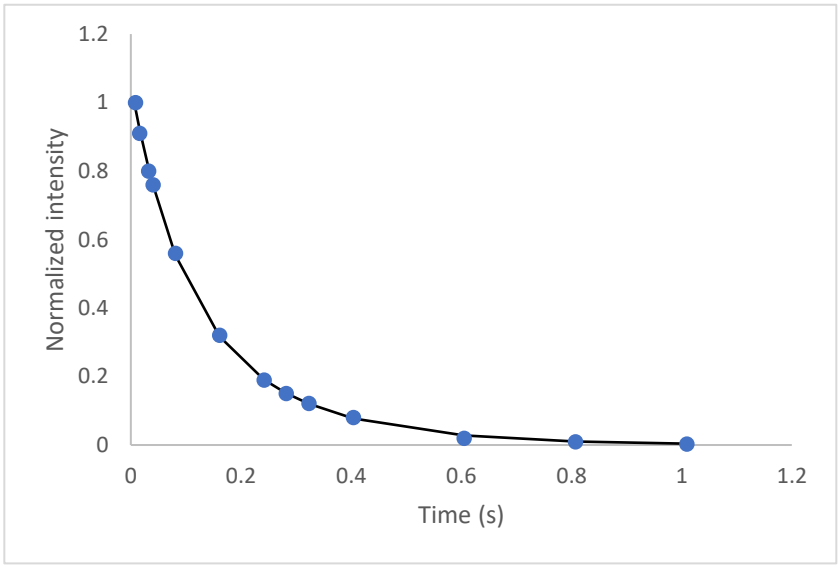

5 mg/mL-$CDCl_3$

T_1-Aliphatic

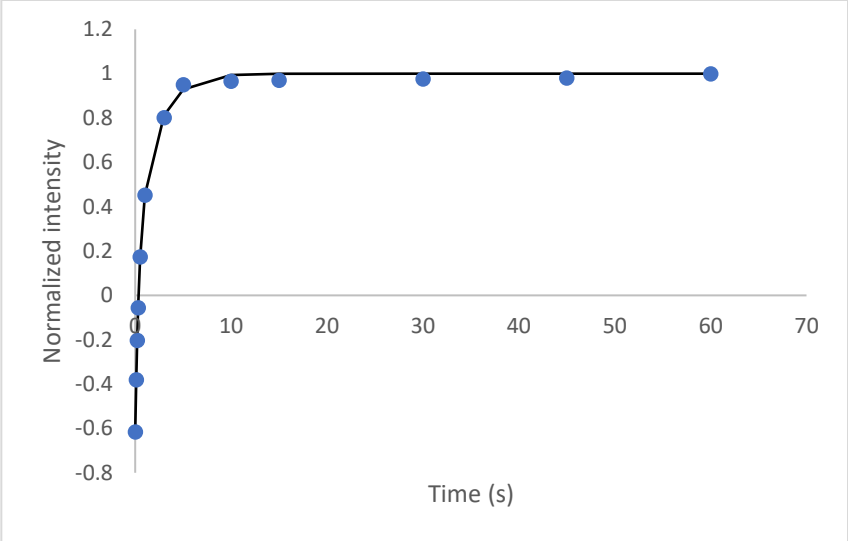

T_1-Alicyclic

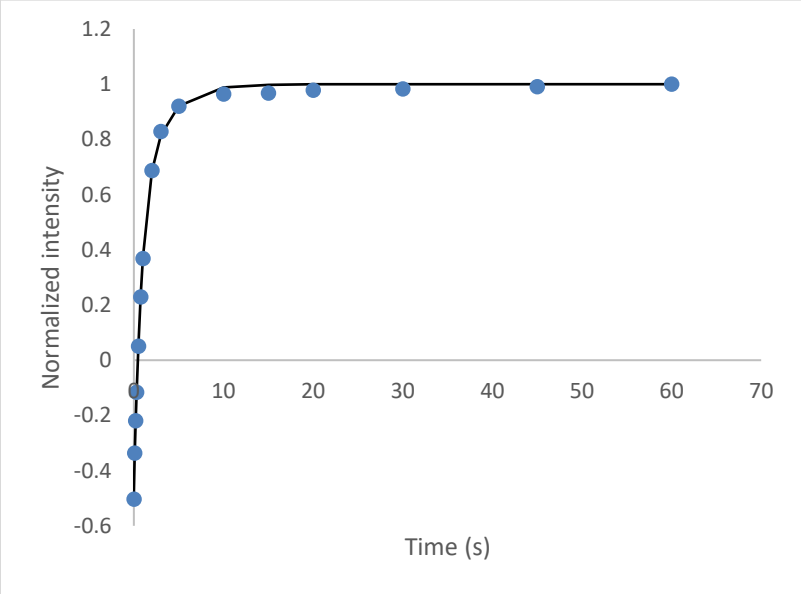

T_1-Aromatic

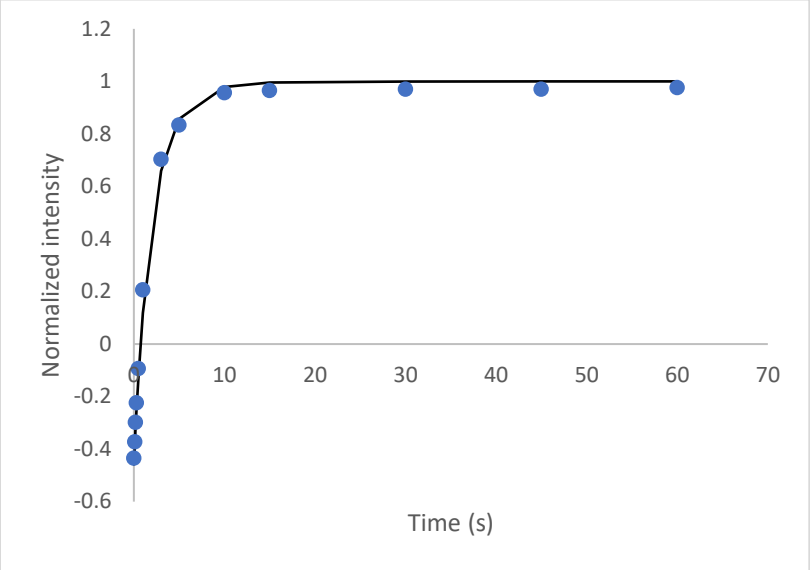

T_2-Aliphatic

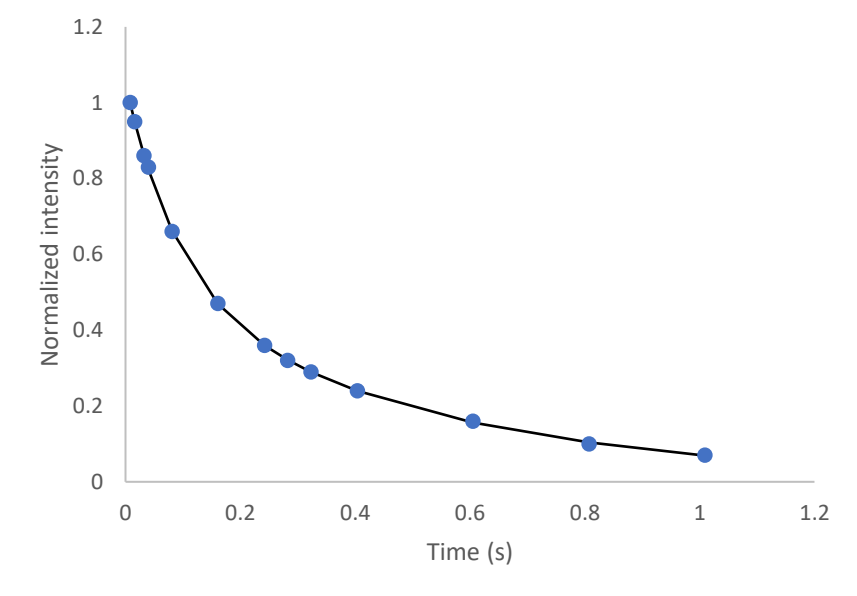

T_2-Alicyclic

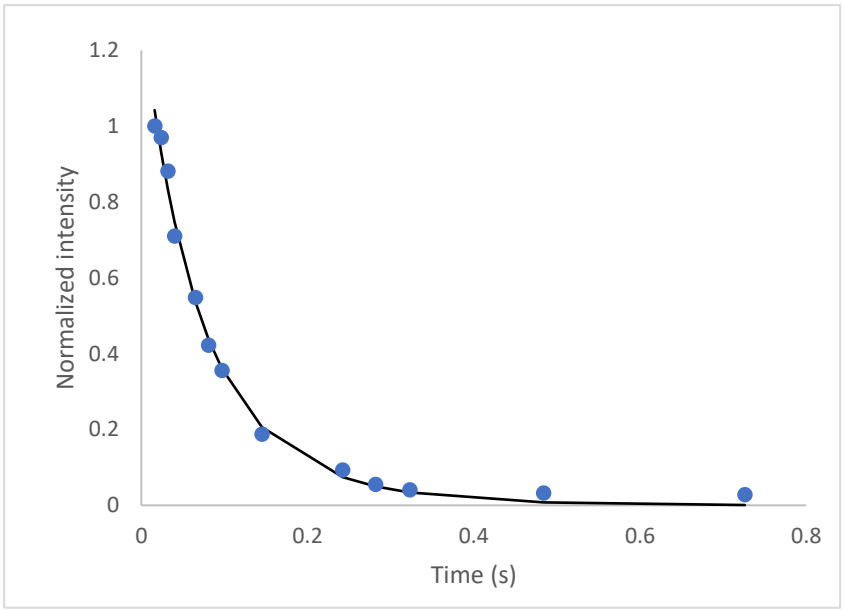

T_2-Aromatic

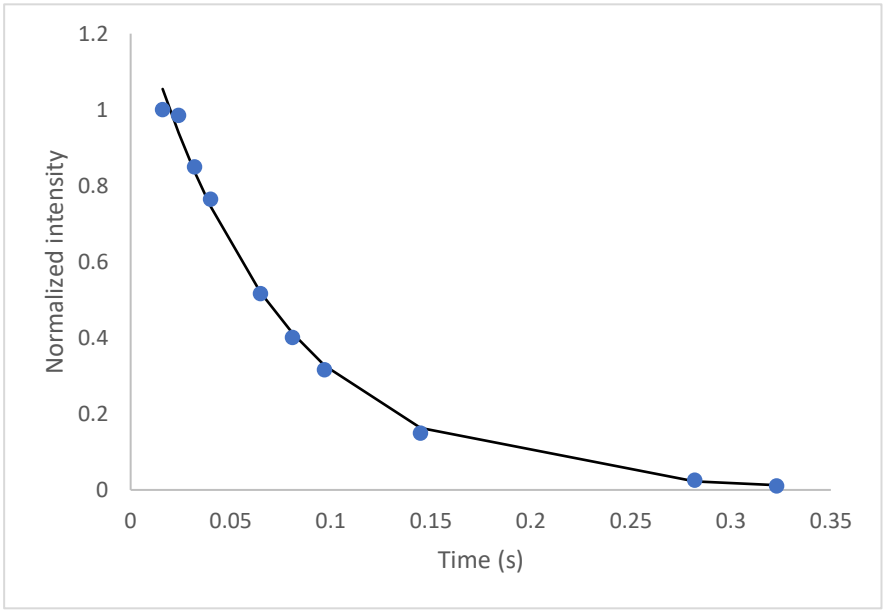

15 mg/mL-$CDCl_3$

T_1-Aliphatic

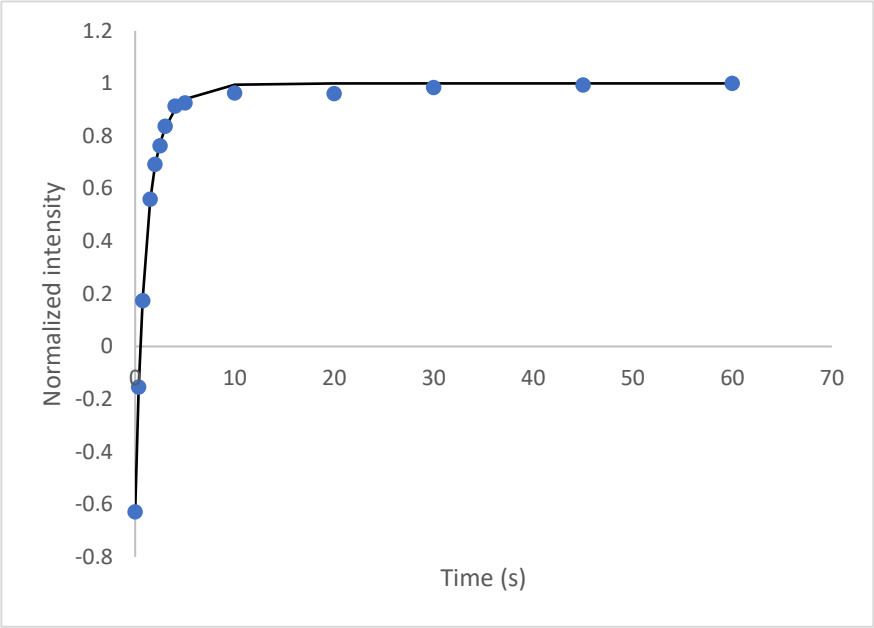

T_1-Alicyclic

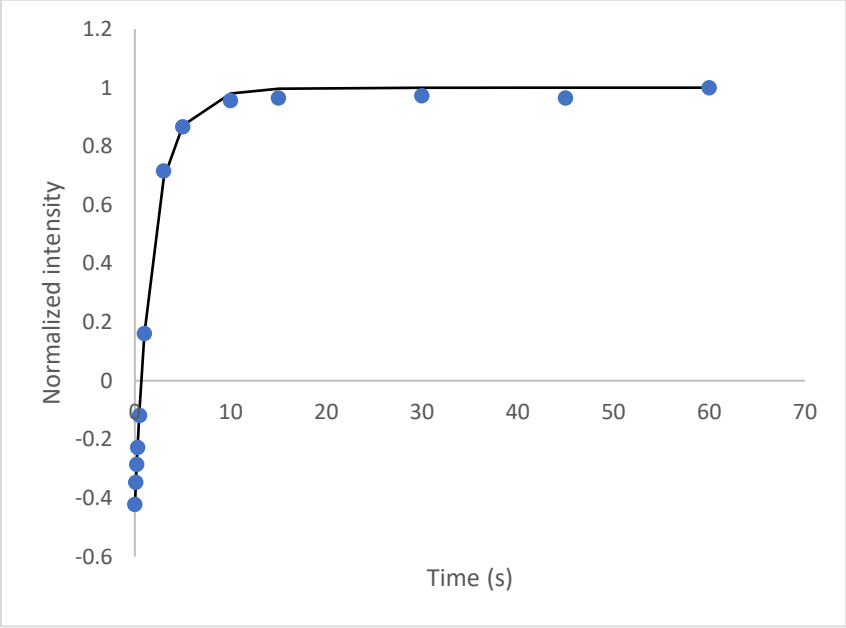

T_1-Aromatic

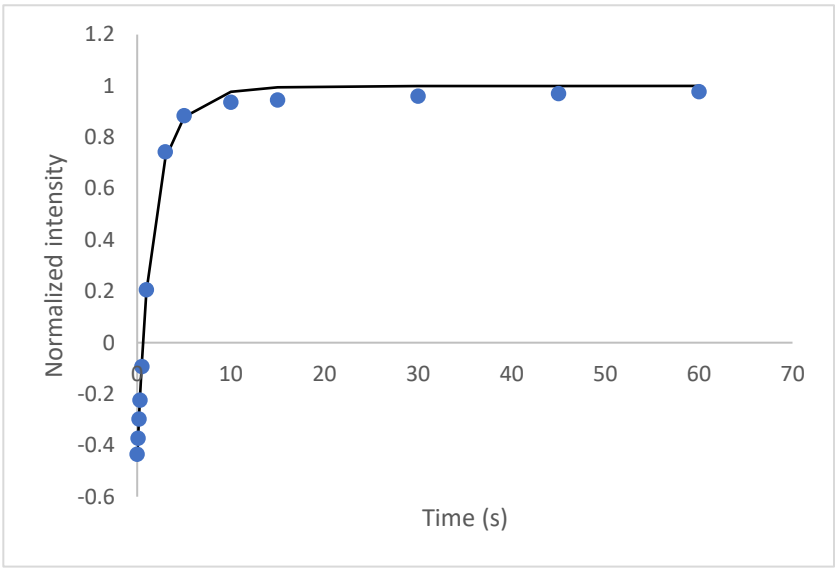

T_2-Aliphatic

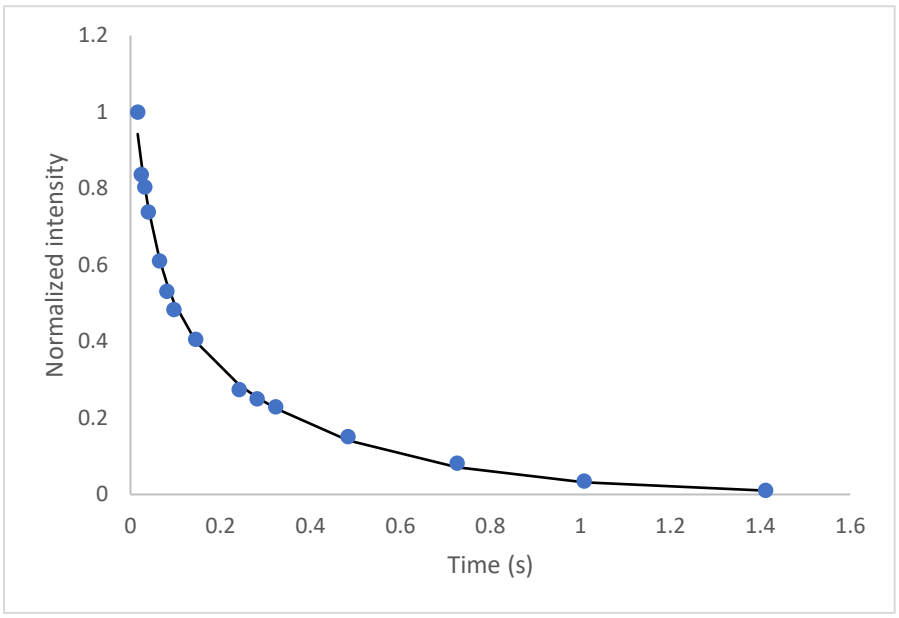

T_2-Alicyclic

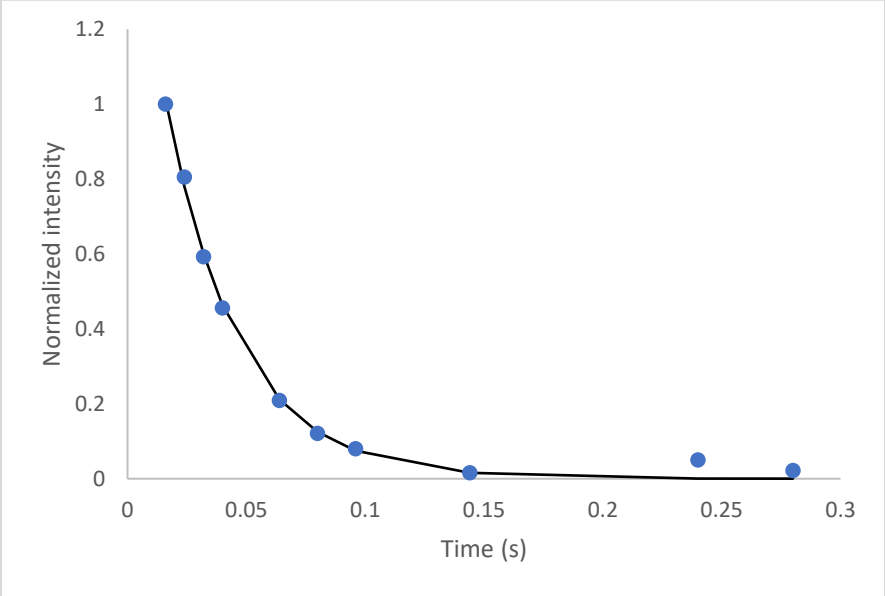

T_2-Aromatic

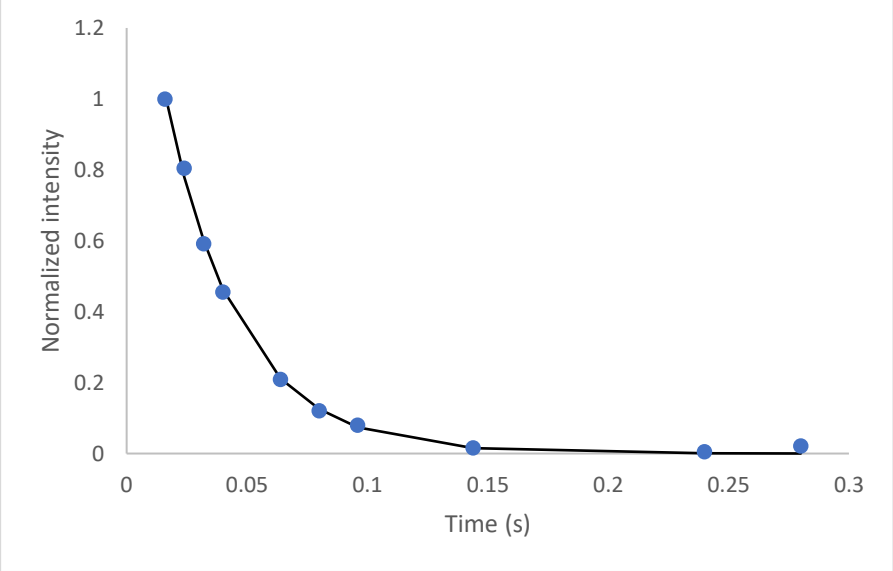

Table D1. ^{1}H NMR relaxation times of UG8 asphaltene in Toluene.

Concentration (mg/mL)	Aliphatic		Alicyclic		Aromatic	
	T_1 (s)	T_2(ms)	T_1 (s)	T_2 (ms)	T_1 (s)	T_2 (ms)
1	0.93 ± 0.03 (70 ± 4.5%)	240 ± 2.5 (68 ± 4.0%)	1.87 ± 0.06 (75 ± 5.5%)	91 ± 0.90 (75 ± 5.0%)	1.89 ± 0.05 (70 ± 5.5%)	72 ± 1.0 (70 ± 4.5%)
	1.33 ± 0.04 (30 ± 3.5%)	880 ± 5.5 (32 ± 3.5%)	1.11 ± 0.03 (25 ± 4.0%)	171 ± 1.3 (25 ± 4.5%)	1.34± 0.04 (30 ± 4.5%)	158 ± 1.4 (30 ± 5.0%)
5	0.98 ± 0.03 (70 ± 5.0%)	65 ± 0.85 (68 ± 4.0%)	3.78 ± 0.05 (70 ± 5.5%)	46.7 ± 0.7 (70 ± 5.8%)	4.26 ± 0.07 (75 ± 5.5%)	48.0 ± 0.8 (70 ± 4.5%)
	1.94 ± 0.04 (30 ± 4.5%)	427 ± 3.0 (32 ± 3.5%)	1.23 ± 0.04 (30 ± 4.0%)	69.2 ± 0.8 (30 ± 4.5%)	1.27 ± 0.04 (25 ± 4.5%)	58.6 ± 1.0 (30 ± 5.0%)
15	1.21 ± 0.04 (75 ± 3.5%)	41.1 ± 0.9 (70 ± 4.0%)	4.29 ± 0.07 (75 ± 5.5%)	18.7 ± 0.5 (75 ± 5.8%)	4.33 ± 0.06 (78 ± 5.5%)	17.5 ± 0.8 (75 ± 4.5%)
	2.20 ± 0.05 (25 ± 3.5%)	287 ± 2.0 (30 ± 3.5%)	1.45 ± 0.03 (25 ± 4.0%)	36.5 ± 0.6 (25 ± 4.5%)	1.47 ± 0.03 (22 ± 4.5%)	32.2 ± 0.9 (25 ± 5.0%)

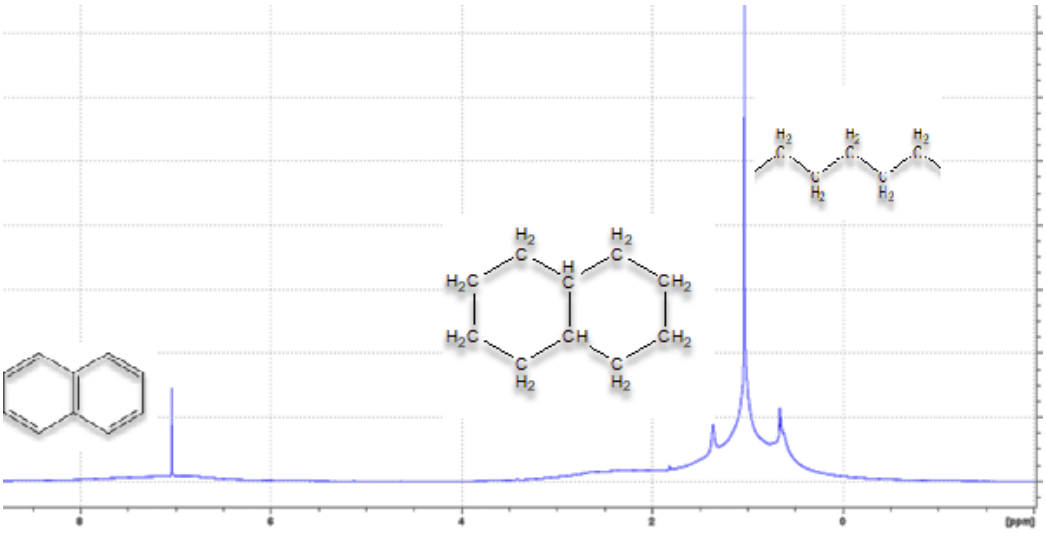

Figure D1. 700 MHz ^{1}H NMR spectra of UG8 asphaltene sample.